

Detection of Mycobacterial Siderophores and Implications for Diagnostics

Nicholas S. McBride

Dissertation for the degree of Doctor of Philosophy
Department of Chemical Engineering and Biotechnology



University of Cambridge
Queens' College

Detection of Mycobacterial Siderophores and Implications for Diagnostics by Nicholas S. McBride

Summary

Mycobacterium tuberculosis (*Mtb*) is a pervasive human pathogen that continues to kill 1.8 million people every year. Acquisition of iron within the host is vital to the pathogenicity of *Mtb* and to accomplish this it produces siderophores called mycobactins and carboxymycobactins. This dissertation has sought to build a simple assay for detection and quantification of mycobacterial siderophores that has potential applications in tuberculosis (TB) diagnosis. This assay has been tested and was successfully able to detect mycobactin spiked into a biological specimen. Furthermore, the theoretical level of mycobactin production that occurs in the lungs of infected patients was estimated. Samples were obtained from infected animal models of TB and human patients and tested for presence of mycobactin and carboxymycobactin. These data provided information regarding the potential use of siderophores as diagnostic biomarkers for TB.


Declaration of Originality

I, Nicholas S. McBride, declare that this dissertation is wholly my own work and has not been previously submitted for the attainment of any other academic degree. Any information herein that has been derived from the published or unpublished work of others has been duly attributed within the text and list of references.

I would like to thank collaborators Tobin J. Dickerson and Petr Čapek of the Scripps Research Institute for their synthesis of mycobactins, tandem mass spectrometry, isolation of antibodies, and determination of their binding constants, all of which are evaluated in Chapter 6. I would also like to thank Valentina Dona of the National Institute of Allergy and Infectious Diseases for carrying out the biological assays for synthetic mycobactin that are evaluated in Chapter 6 and Craig Saperstein of the University of Cambridge for the molecular modelling image that appears as Figure 77.

Statement of Length

This dissertation contains 48,888 words and 77 figures including appendices, bibliography, footnotes, tables and equations. This is in accordance with the limits set forth by the Engineering Degree Committee that PhD dissertations are not to exceed 65,000 words and not to contain more than 150 figures.

Signed: 

Nicholas S. McBride

Locations of Research

This dissertation was carried out as a joint research project under the NIH Oxford Cambridge Scholars Program with research time split between two institutions.

All work involving live *Mycobacterium tuberculosis* cultures and clinical samples was carried out at the Tuberculosis Research Section of the Laboratory of Clinical Infectious Diseases, National Institute of Allergy and Infectious Diseases (NIAID), National Institutes of Health (NIH) in Bethesda, MD, United States under the mentorship of Dr. Clifton E. Barry III and utilizing the biosafety level three (BSL3) facilities available there as required for containment of airborne infectious agents. This includes the work presented in chapters 2, 5, and portions of 6.

All electrochemical work, as well as bovine urine sample collection and processing was carried out at the Cambridge Analytical Biotechnology Laboratory of the Department of Chemical Engineering and Biotechnology (formerly the Institute of Biotechnology), University of Cambridge in Cambridge, United Kingdom under the supervisorship of Professor Elizabeth (Lisa) A. H. Hall. This includes the work presented in chapters 3, 4, and portions of 6.

Primary funding for this work was provided by the Tuberculosis Research Section and the NIH Oxford Cambridge Scholars Program with supplementation for consumables used in Cambridge by the Cambridge Analytical Biotechnology Laboratory. In total, 808 days have been spent at the NIH, and 905 days have been spent at the University of Cambridge.

Acknowledgements

In addition to my two supervisors who have been a regular source of inspiration and corrective reasoning, I would like to thank some of the many other individuals who have helped and supported me along the way:

Amit	For the advice and sometimes even convincing me to leave the lab for a beer.
Brett	For late night writing sessions with cats.
Bridgette	For guiding us through the NIH maze.
Caroline	For always keeping things together on the homefront.
Craig	For his molecular modeling voodoo.
Dave	For many conversations of both organic and human chemistry advice.
Donna	For expertly helping me to exercise my body and clear my head.
Duncan	Whose knowhow about cows speaks volumes.
Ellene	One friend I got to see on both sides of the Atlantic.
Estelle	For introducing me to the world of electrochemistry.
Eugene	I finally found out what 'pastoral support' means.
Golnaz	For being the cheerful face of the lab.
Helena	For her solid advice all along the way and encouragement when no one else would.
Jacqui	For always being a helpful and happy presence in the lab and teaching me all about mice.
Jamie	For arguing with me for hours on end to believe in myself.
Jenny	For bringing me out running all the way to Budapest.
John H.	Whose sagely advice is calming in the most stressful situations.
John L.	For the advice he gives from his considerable stockpile of HPLC/HRMS experience.
Justin	As a constant source of unflappable inspiration and knowledge.
Kapil	For bringing the biosuit dance party after hours and hours of plates.
Katinka	For showing the light at the end.
Kelly	Sushi and wine times!
Laura	For her mentorship in the new world of clinical microbiology.
Lef	My good friend and ally for my entire academic career.
Lindsey	For always having a kind word.
Marta	As a voice of reason, a calm in the storm.
Matt	For all the writing support.
Michael	For always taking the time to answer my questions, no matter how basic or incomprehensibly obfuscated.
Mikey I.	For ambles to H St. and ample couch space.
My family, Mom, Dad, and Amanda	For supporting me all the way through despite probably not understanding what on earth I'm doing.

My undergrad advisors: Rick, George, and Glenn	For convincing me that I'd never want to settle for anything less.
Pawel	For all the good times and all the slightly less-good chemical syntheses.
Richard	For showing my novice self the ups and downs of protein expression.
Sabrina, Kris, and Janette	The ones who saved me when I was stranded in a foreign airport.
Safwan	For all manner of eye-opening conversations about this crazy world that we inhabit.
The old housemates: Carissa, Jen, and Rogier	For making me feel at home whenever I'm in Cambridge.
TJ	For making DC fun!
Toby and Petr	For their prowess in siderophore synthesis.
Tucker and Sanaya	As the most amazing friends who have always been there for me.
Valentina	For her support both moral and material; my closest research peer.
Zsófi	For her love and support through the end times.

Table of Contents

Detection of Mycobacterial Siderophores and Implications for Diagnostics	1
Summary	2
Declaration of Originality	3
Statement of Length	3
Locations of Research	4
Acknowledgements	5
Table of Contents	7
Table of Figures	10
Table of Tables	13
Abbreviations and Symbols	14
1 Introduction	16
1.1 Tuberculosis	16
1.1.1 Anatomy of the Infection	17
1.1.2 Treatment	19
1.1.3 Diagnostics	19
1.1.3.1 Current Diagnostics	19
1.1.3.2 Future Techniques and Potential Biomarkers	20
1.2 Siderophores and Mycobactin	21
1.2.1 Structure	23
1.2.2 Biosynthesis	27
1.2.3 Function in Iron-acquisition by Mtb	30
1.2.3.1 Current Model of Mycobacterial Iron Trafficking	32
1.2.3.2 Immunology of Mycobactin	34
1.3 Therapeutic Applications of Mycobactins	36
1.3.1 Chelation Therapy	36
1.3.2 Mycobactins as Anti-Cancer Agents	37
1.3.3 Antimicrobial Potential of Mycobactins and Their Analogues	38
1.4 Imaging Applications of Siderophores	40
1.5 Use of Mycobactin to Detect and Identify Mycobacteria	41
1.6 Research Objectives	42
2 Production of Mycobactin <i>In Vitro</i>	45
2.1 Materials and Methods	46
2.1.1 Culture of Mycobacterium tuberculosis	46
2.1.1.1 Low-Iron Media	46
2.1.1.1.1 Effects of Different Media Preparations	47
2.1.1.2 Siderophore Production	47
2.1.1.3 Correlation of Optical Density and Cell Mass	47
2.1.1.4 Extraction of Mycobactin from Culture	48
2.1.2 HPLC Analysis	49
2.1.2.1 HPLC/DAD/MSD Instrumentation	49
2.1.2.2 Techniques Used for Mtb Culture Extracts	49
2.1.2.3 HPLC/DAD Quantification of Mycobactin	50
2.2 Results	51
2.2.1 Comparison of Media Preparation Methods	51
2.2.2 Absorbance and Mass Spectrum Identification of Mycobactins	52
2.2.3 Siderophore Production Growth Curves	54
2.2.4 Identification and Quantification of Siderophore Species	55
2.2.5 Abundance of Different Mycobactin Species	57
2.3 Conclusion	61
2.3.1 The Role of Mycobactin in <i>Mtb</i> Pathogenesis	61
2.3.2 Species of Mycobactins Produced	64
2.3.3 Physiological Range of Mycobactin Production	64

2.3.4	Implications for Development of an Assay for Mycobactin	66
3	A Simple Electrochemical Assay for Mycobactin	67
3.1	Methods	68
3.1.1	Instrumentation	68
3.1.2	Electrode Pretreatment	68
3.1.3	Electrochemical Techniques.....	69
3.1.3.1	Cyclic Voltammetry.....	69
3.1.3.2	Amperometric Titration	69
3.1.4	Deferration and Referration of Mycobactin.....	69
3.2	Results and Discussion.....	71
3.2.1	Cyclic Voltammetry of Mycobactin	71
3.2.1.1	Aqueous Cyclic Voltammetry.....	71
3.2.1.2	Nonaqueous Cyclic Voltammetry.....	74
3.2.1.2.1	Coupled Chemical Reaction After Reduction to Ferrous Mycobactin	76
3.2.1.2.2	Referration of DFMJ in Nonaqueous Solvent	78
3.2.1.2.3	Thermodynamic Stability of the Complex.....	80
3.2.1.2.4	Calculation of the Heterogeneous Electron Transfer Rate Constant	82
3.2.2	Chronoamperometry.....	83
3.2.3	Electrochemical Limit of Detection	85
3.3	Conclusions.....	87
4	Proof-of-Concept Application of the Assay.....	89
4.1	Materials and Methods.....	90
4.1.1	Bovine Urine Samples	90
4.1.2	Preparatory Chromatographic Concentration of Mycobactin	91
4.1.3	Spiking of Samples.....	91
4.1.4	Effects of Sample Processing.....	91
4.2	Results and Discussion.....	92
4.2.1	Chromatographic Collection and Elution of Mycobactin	92
4.2.2	Effects of Sample Processing.....	93
4.2.3	Application of the Assay for Monitoring Mycobactin in Urine	96
4.3	Conclusions.....	97
5	Evaluation of Siderophore Contents of Different Biological Media	99
5.1	Materials and Methods.....	100
5.1.1	Samples.....	100
5.1.1.1	Infected Animal Samples	100
5.1.1.2	Clinical Samples.....	101
5.1.2	HPLC/HRMS Instrumentation	102
5.1.3	Extraction of Mycobactins from Biological Media for HPLC/HRMS Analysis.....	103
5.1.4	HPLC Method Development.....	104
5.1.4.1	Optimisation of HPLC Conditions	104
5.1.4.2	Adaptation to High-Sensitivity HPLC/HRMS System.....	109
5.2	Results and Discussion.....	110
5.2.1	Limit of Detection in Urine and Plasma.....	110
5.2.2	Analysis of Clinical Tuberculosis Samples.....	113
5.3	Conclusions.....	115
6	Further Development of Mycobactin Assays.....	117
6.1	Materials and Methods.....	119
6.1.1	Cloning of Lcn2.....	119
6.1.2	NTA Immobilisation Ligand.....	119
6.1.2.1	Synthesis of NTA Immobilisation Ligand	119
6.1.2.2	Deposition of NTA onto the Electrode Surface	120
6.1.3	Synthesis of Mycobactins.....	120
6.1.3.1	Synthesis of Mycobactin T Using the Reported “Minimal Protecting Group Strategy” ..	120
6.1.3.2	Revised Synthesis of Mycobactins.....	124

6.1.4	Evaluation of Synthetic Mycobactins.....	127
6.1.4.1	Radiolabelling of Mycobactins	127
6.1.4.2	Uptake by Mtb in Liquid Culture.....	127
6.1.4.3	Growth Rescue Assay	128
6.1.4.4	Uptake by Mtb Within Infected Macrophages.....	128
6.1.5	Production of Anti-Mycobactin Antibodies and Determination of Binding Constants.....	129
6.2	Results and Discussion.....	129
6.2.1	Capture Ligand Development.....	129
6.2.1.1	Deposition of NTA onto the Electrode Surface	129
6.2.1.2	Cloning of Lcn2	130
6.2.2	Synthetic Mycobactins	131
6.2.2.1	Minimal Protecting Group Product.....	131
6.2.2.2	Revised Synthetic Product.....	135
6.2.2.3	Biological Activity of Synthetic Mycobactins.....	137
6.2.2.3.1	Uptake by Mtb in Liquid Culture and Growth Rescue Assay.....	137
6.2.2.3.2	Uptake by Mtb Within Infected Macrophages	139
6.2.3	Evaluation of Anti-Mycobactin Antibodies	140
6.3	Conclusions.....	141
7	Future Implications	143
7.1	Tuberculosis Diagnostic Potential of Mycobactin and Carboxymycobactin	143
7.1.1	Bovine Tuberculosis.....	143
7.2	Other Applications of the Mycobactin Assay	144
7.2.1	Companion Diagnostic for Therapeutic Administration of Mycobactins	144
7.2.2	Biosensor for Industrial Siderophore Production	145
7.3	The Role of <i>In Vivo</i> Mycobactin Reduction in Iron Trafficking	145
7.4	Electrode Surface Engineering.....	146
7.5	Conclusions.....	148
	References.....	149
	Appendix 1: Matlab Programs for Processing Electrochemical Data	160
	High-Speed Cyclic Voltammogram PicoScope Data Processing 'PicoScope_binning_v11.m'	160
	Appendix 2: Mycobactin Masses for HRMS Screening.....	163

Table of Figures

Figure 1: Global incidence (bubble temperature map) and prevalence (bubble size) of TB by country and population. Data from the World Health Organization (WHO, 2007) visualised by Gapminder World, powered by Trendalyzer from www.gapminder.org.	17
Figure 2: Schematic diagram of the mycobacterial cell wall.	19
Figure 3A: Structure of mycobactin with coordination ligands shown in red ⁴⁹ , and chiral centres in blue. B: Mycobactin T from <i>M. tuberculosis</i>	24
Figure 4: Mycobactin T before and after binding iron.	27
Figure 5: Schematic of mycobactin biosynthesis.	28
Figure 6: Model of mycobacterial iron acquisition; not drawn to scale.	33
Figure 7: DDM analogue shown bound to the CD1a T cell antigen display protein.	34
Figure 8: Lcn2 bound to ferric carboxymycobactin T; rendered from Protein Data Bank (PDB) accession code 1X8U ¹²⁷ using Chimera ¹³⁴	35
Figure 9A: Salicyl-AMP, the natural product of MbtA. B: Salicyl-AMS, the MbtA bisubstrate inhibitor. C: 2-Phenyl-salicyl-AMS, optimised inhibitor ¹⁶³	40
Figure 10: Correlation of wet cell mass per volume with 650 nm absorbance values, n = 3.	48
Figure 11: Graphical representation of the solvent gradients that were used for HPLC/MS analysis.	50
Figure 12: Standard curve of A ₄₅₀ peak area vs. FeMJ concentration.	50
Figure 13A: Growth curves of <i>Mtb</i> H37Rv in differently prepared GAST media; blue indicates that both the water and the Casitone solution were Chelex 100 treated and media was mixed in plastic bottles, red indicates that only the water was Chelex 100 treated and media was mixed in plastic bottles, green indicates no Chelex 100 treatment with media mixed in plastic bottles, and yellow indicates no Chelex 100 treatment with media mixed in glass bottles. B: Total wet cell masses from each culture condition at day 16.	52
Figure 14: FeMJ standard eluting under the ISOYJ70 method.	53
Figure 15A: Absorbance spectrums of mycobactin J (FeMJ) containing either unsaturated or saturated acyl moieties. B: comparable absorbance spectrums captured from HPLC elution of mycobactin T extracted from <i>Mtb</i> culture (FeMT). Spectrums were normalised at 450 nm, then plotted with a maximum absorbance of unity.	53
Figure 16: Mass spectrum of FeMJ; note the M – 2 peak indicating the presence of ⁵⁴ Fe at the natural isotopic composition of 5.8 percent.	54
Figure 17: Batch A was inoculated with <i>Mtb</i> that had been subcultured twice in low-iron GAST; batch B was inoculated with <i>Mtb</i> that had been subcultured seven times in low-iron GAST.	55
Figure 18: Mycobactin yield from culture extracts.	56
Figure 19A: Chromatogram of mycobactins comparing the pellet extracts from batches A and B using the ISOYJ70 HPLC method. B: Relative abundance of each species of detected mycobactin.	58
Figure 20: Chromatogram of mycobactins comparing the pellet and supernatant of extract B using the MYCEX HPLC method.	61
Figure 21: New model of mycobacterial iron acquisition; not drawn to scale.	63
Figure 22: Mycobactin J shown with pK _a values for its iron-chelating ligands based upon measurements of a similarly-structured water-soluble analogue ¹⁹⁹	70
Figure 23A: Spectrophotometric titration for ferric chloride into deferrated MJ (DFMJ) in methanol. B: Plot of 450 nm absorbance versus ferric chloride concentration for both addition of ferric chloride to DFMJ and ferric chloride alone.	71
Figure 24: Cyclic voltammograms of FeMJ and DFMJ in 50 percent ethanol, 0.1 M potassium chloride, 0.2 V/s scan rate.	72
Figure 25: Cyclic voltammograms of DFMJ and referrated DFMJ in PBS buffered 50 percent ethanol, 0.1 M potassium chloride, 0.2 V/s scan rate.	73
Figure 26: Cyclic voltammograms of FeMJ on either AuE or GCE in 50 percent ethanol, 0.1 M potassium chloride, 0.2 V/s scan rate.	74
Figure 27A: Cyclic voltammogram of FeMJ (640 μM); 0.2 V/s in DMSO with 0.1 M LiCl. B: Background-corrected CVs of FeMJ at varying scan rates showing oxidation and reduction peaks.	75
Figure 28: Plot of i _p /v ^{1/2} versus v ^{1/2} shown for both the reduction and oxidation peaks of FeMJ.	76
Figure 29: FeMJ i _a /i _c ratios on GCE in DMSO with 0.1 M LiCl.	77
Figure 30: Referration of DFMJ by titration with Fe(acac) ₃ at 0.2 V/s in DMSO, 0.1 M LiCl.	78
Figure 31: Cyclic voltammetry of Fe(acac) ₃ at 0.2 V/s in DMSO, 0.1 M LiCl.	79

Figure 32A: E_p versus $\ln v$; dashed lines indicate bounds of the lower concentration data, while solid lines indicate bounds of the higher concentration data for either the reduction or oxidation peak; light dotted lines are linear trend lines for the low and high scan rate oxidation data, the intersection of which indicates the critical scan rate (v_c). B: The same plot, but for a constant concentration of DFMJ referred to by a titration of $\text{Fe}(\text{acac})_3$. C: The same plot, but for a constant 0.5 mM concentration of FeMj and addition of excess $\text{Fe}(\text{acac})_3$	81
Figure 33: β_w vs. scan rate for different concentrations of FeMj	82
Figure 34: Amperometric titration of FeMj at -0.6 V versus Ag/Ag^+ . The areas with spikes of noise correspond to periods of stirring with a magnetic stir bar following addition of FeMj . No FeMj was added to the cell during the first two stirring events to serve as controls.	84
Figure 35: Ratio of the measured current (i) over background current (i_0) at -0.8 V from CV data to approximate steady-state values.	84
Figure 36A: Titration of FeMj by cyclic voltammogram at 0.2 V/s in DMSO, 0.1 M LiCl . B: CV peak current versus FeMj concentration.....	86
Figure 37: Titration of DFMJ into a 300 μM solution of $\text{Fe}(\text{acac})_3$ at 0.2 V/s in DMSO, 0.1 M LiCl	87
Figure 38: Effectiveness of Sep-Pak tC_{18} separation of FeMj from water when FeMj is initially solubilised in either DMSO or methanol (MeOH). A: spectrophotometric absorbance after elution in diethyl ether, drying, and dissolution in methanol; solutions were diluted to give the stated concentrations given 100 percent theoretical retention. B: absorbance of the undiluted flow-through of the initial 25 mL sample.	93
Figure 39: Analysis of Sep-Pak tC_{18} eluates from the bovine urine samples from a single urine pool and treated as defined in Table 10; spectrophotometric absorbance in 0.75 mL methanol (A) and CV analysis in 0.1 mL DMSO, 0.1 M LiCl at 0.2 V/s scan rate (B) are shown.....	95
Figure 40: Spectrophotometric absorbance of bovine urine Sep-Pak tC_{18} eluates in 0.75 mL methanol; C1-C3 refer to samples take from three individual cows with and without the addition of 2 μM FeMj	96
Figure 41: Mean cyclic voltammogram of standardised bovine urine eluates; the grey area indicates the range of standard deviation.....	97
Figure 42: HPLC/HRMS injection configuration.	103
Figure 43: Comparison of chloroform versus ethyl acetate extraction of mycobactins from human urine via in-house LC/DAD; the three prominent absorbance peaks indicate the elution of FeSCM , FeMj , and FeSMT respectively.	105
Figure 44: Comparison of different stationary phases for LC elution resolution. The y-axis measures the time between the elution of the mycobactin compounds indicated in the legend as a measure of resolution.....	106
Figure 45: Optimisation of three mass spectrometry parameters; A: fragmentation voltage, B: drying gas flow rate, and C: capillary voltage. Signal was optimised to give the greatest total ion current (TIC) for a bolus injection of FeMj	106
Figure 46: Solvent gradient profiles that were tested to optimise sensitivity for carboxymycobactins and mycobactins. Buffer A consisted of aqueous 0.1 percent formic acid, while buffer B consisted of acetonitrile with 0.1 percent formic acid.....	107
Figure 47: Results from elution of the test compounds using the solvent gradients displayed above. All elutions were done on a C_{18} -PFP column except for the NMHFLO1 method, which was tested on C_6 -phenyl and C_{18} core-shell columns as indicated. Note that the saturated form of FeMj is only present in trace quantities in the control samples, whereas FeSCM , FeMj , and FeSMT are present in equimolar quantities.....	108
Figure 48: The limit of detection for the test compound is shown to be in the range of 50-500 fmol using the NMC18PF9 solvent profile; the 50 pmol standard (not to scale) is shown in gray to indicate the expected elution times of the standard compounds FeSCM , FeMj , and FeSMT	109
Figure 49: Elution of mycobactins extracted from <i>Mtb</i> culture using the optimised NMC18PF9 LC/MSD method.....	109
Figure 50: Combined ion chromatograms of FeSCM , FeMj , and FeSMT (2.5 pmol) eluting at 20°C and 60°C.	110
Figure 51A: HPLC/HRMS chromatogram of extract from human urine spiked with 50 fmol of FeSCM , FeMj , and FeSMT . B: An enlarged plot of the FeSCM ion signal alone to give detail.	111
Figure 52: HPLC/HRMS chromatogram of extract from human plasma spiked with 2 pmol of FeSCM , FeMj , and FeSMT	112
Figure 53A: Lateral flow device design that could be used for concentrating mycobactin from a sample into a small volume for electrochemical analysis. B: Example of a specific receptor (Lcn2) for mycobactin bound to the electrode surface.	118

Figure 54: Structure of synthetic mycobactins. A: Synthetic mycobactin T (SMT). B: Synthetic carboxymycobactin (SCM).	119
Figure 55: Synthesis of 4-aminophenyl-NTA.	120
Figure 56: Retrosynthetic analysis of mycobactin T 1a and mycobactin S 1b. In mycobactin T, the stereocentre is of the <i>R</i> configuration and in mycobactin S, this stereocentre is of the <i>S</i> configuration.	121
Figure 57: Synthesis of oxazoline fragment 4. Reagents and conditions: (a) (i) BnBr, K ₂ CO ₃ , MeOH/DCM 1:1, reflux, overnight, 88%; (ii) NaOH, dioxane/water, reflux, 2 h, 93%; (iii) L-serine-OBn, EDC, DCM, RT, overnight, 89%; (b) (i) Burgess's reagent, THF, reflux, 30 min, 66%; (ii) H ₂ , 10% Pd/C, MeOH, 2 h, 99%.	121
Figure 58: Synthesis of unprotected hydroxamic acid fragments. Reagents and conditions: (a) (i) PhCHO, KOH, MS, MeOH, overnight, RT; (ii) m-CPBA, MeOH, 0 °C to RT, 5 h; (iii) TFA/DCM, 1:1, RT, 1 h; (iv) PhCHO, EtOAc, 0 °C to RT, 2 days, 66% over 4 steps; (b) NH ₂ OH·HCl, MeOH, 65 °C, 20 min, 87%; (c) (i) EDC/HOAt, NaHCO ₃ , CH ₃ CN, DMF, RT, 48 h, 50%; (ii) H ₂ , Pd/C, MeOH, 2 h, 97%; (d) SOCl ₂ , MeOH, 0 °C to RT, 12 h, 83%; (e) (i) nonadecanoyl chloride, NaHCO ₃ , DCM, RT, overnight; (ii) 6% DIPEA in MeOH, RT, 2 days, 76% over 2 steps; (f) H ₂ , Pd/C, MeOH, RT, 2 h, 95%.	122
Figure 59: Assembly of fragments using the reported "minimal protecting group" strategy. Reagents and conditions: (a) EDC/HOAt, DCM, RT, 6 h, 49%; (b) Ba(OH) ₂ , THF/water, RT, 1 h, 95%; (c) EDC·HCl/HOAt and catalytic DMAP, DMF, RT, 4 h; (d) EDC/HOAt, DMAP (cat.), DMF, RT, 16 h, 55% over 2 steps.	123
Figure 60: Assembly of benzyl protected fragments. Reagents and conditions: (a) EDC/HOAt, catalytic DMAP, DMF, RT, 16 h.	124
Figure 61: Synthesis of cyclic and linear benzyl hydroxamate fragments. Reagents and conditions: (a) Na ₂ [Fe(CN) ₅ NO], water, pH 9.5, 60 °C, 6 h, 86% (crude); (b) (i) NH ₂ OBn·HCl, EDC, THF/water, pH 4, 2 h, 45%; (ii) I ₂ , PPh ₃ , imidazole, THF, RT, 1 h, 80%; (c) Cs ₂ CO ₃ , DMF, 70 °C, 2 h, 74%; (d) 33% HBr in AcOH, DCM, rt, 30 min, 86%; (e) (i) CH ₂ N ₂ in Et ₂ O, MeOH, rt, 30 min; (ii) I ₂ , PPh ₃ , imidazole, THF, RT, 1 h, 50% over 2 steps; (f) 2 or 3, K ₂ CO ₃ , acetone, 70 °C, 2 h, 79%; (g) 33% HBr in AcOH, DCM, RT, 30 min, 98%.	125
Figure 62: Assembly of benzyl protected fragments. Reagents and conditions: (a) EDC/HOAt, DCM, RT, 5 h, 71%; (b) Ba(OH) ₂ , THF/water, RT, 1 h, 90%; (c) EDC/HOAt, DMF, RT, 4 h, 63%; (d) PPh ₃ , DIAD, THF, RT, 16 h, 45%; (e) H ₂ , Pd/C, MeOH or EtOH/EtOAc, 40 psi, 16 h; for 26a and mycobactin S 1b, * = (<i>S</i>), for 26b and mycobactin T 1a, * = (<i>R</i>), 95%.	126
Figure 63: Diazonium electrodeposition mechanism for 4-aminophenyl-NTA.	130
Figure 64A: Deposition of the diazonium ion onto a GCE surface at -0.4 V versus Ag/AgCl. B: CVs of potassium ferricyanide at pH 7.5 and 1.0 indicate the successful functionalisation of the electrode surface by slowing of the electrochemical process at pH 7.5; 0.1 M potassium chloride, 0.2 V/s scan rate.	130
Figure 65A: SDS-PAGE of insoluble and soluble fractions of Lcn2-pET28b BL21 <i>E. coli</i> cell lysate after induction with IPTG. B: SDS-PAGE of the Lcn2 purification shows Lcn2 with the expected molecular weight of 22.8 kDa.	131
Figure 66A: Contrasting absorbance spectra of the minimal protecting group products, and authentic FeMJ and FeMT. Spectra were normalised to their respective maxima at either 450 nm or 500 nm. B: Desferri mpSCM was ferrated using ferric chloride, then sodium hydroxide was titrated into the solution to observe the peak shift under re-alkalinisation.	133
Figure 67: Cyclic voltammetric analysis of minimal protecting strategy products. All analytes at 1 mM concentration, 0.1 M potassium chloride in 50 percent aqueous ethanol, 0.2 V/s scan rate.	133
Figure 68: HPLC chromatogram of mpSMT elution under the NM_MYCO3 protocol (see Section 2.1.2.2). Addition of ferric chloride to mpSMT gave rise to a doubled elution peak; the elution of authentic FeMJ is shown for comparison of elution times.	134
Figure 69: Structure of the minimal protecting group product mpSMT; not mycobactin.	135
Figure 70: UV-visible spectra of FeSMT and FeSCM exhibited the same absorbance profile as natural FeMT and FeMJ.	135
Figure 71: HPLC chromatogram of SMT elution under the NM_MYCO3 protocol (see Section 2.1.2.2). Addition of ferric acetylacetonate (Fe(acac) ₃) produces only a single peak.	136
Figure 72: HPLC chromatogram of FeSMT eluting alongside mycobactins extracted from <i>Mtb</i> culture (NM_MYCO3 protocol, see Section 2.1.2.2).	136
Figure 73: MS/MS spectra of the miscoupled product (mpSMT) (red, arrow points to <i>m/z</i> = 758.5092) and authentic mycobactin T (SMT) (blue, arrow points to <i>m/z</i> = 717.4797). In both cases, the parent peak has <i>m/z</i> = 844.5432. Figure provided by Tobin J. Dickerson and Petr Čapek.	137

Figure 74: Comparison of <i>Mtb</i> H37Rv and $\Delta mbtB$ uptake of 80 nM Fe ⁵⁵ labelled FeSMT. Based on data collected by Valentina Dona.	138
Figure 75: Growth rescue of $\Delta mbtB$ by FeSMT (A), FeSMS (B), or FeSCM (C). Based on data collected by Valentina Dona.	138
Figure 76: 80 nM (A) or 400 nM (B) ⁵⁵ Fe labelled FeSMT uptake into <i>Mtb</i> within macrophages infected with strain H37Rv or $\Delta mbtB$. Based on data collected by Valentina Dona.	140
Figure 77: Hypothetical molecular model of mycobactin T bound to a hydrophobic groove etched in the surface of a graphite electrode. Molecular modelling and image were generously contributed by Craig Saperstein using PyMOL version 1.5.0.1 ²³⁷ and Avogadro version 1.0.3 (avogadro.openmolecules.net).....	147

Table of Tables

Table 1: Siderophore classes isolated from different organisms of the Actinobacteria and Proteobacteria phylums.	22
Table 2: Mycobactins and nocardial siderophores with similar known structures. The substituents are given, as well as the chirality of each stereo centre denoting either the D/L configuration of its parent amino acid, or the R/S absolute configuration where appropriate and known.	24
Table 3: Isocratic 70% acetonitrile method (ISOYJ70F).	49
Table 4: MYCEX method.	49
Table 5: NM_MYCO3 method.	50
Table 6: Predicted mass spectrum of the protonated ion of FeMJ containing an unsaturated acyl chain (ChemDraw).	54
Table 7: Total mycobactin yields from extractions A and B.	56
Table 8: Detailed mycobactin yield information for each chromatographic peak; yields are given as percentage of total mycobactin detected. The general structure of mycobactin T is given for reference with the substituents of structural variation highlighted in blue and iron coordination ligands in red; a $\Delta 20$ fatty acyl moiety is shown for example.	56
Table 9: FeMJ i_a/i_c ratios on GCE in DMSO with 0.1 M LiCl.	77
Table 10: Bovine urine processing method validation; addition of FeMJ gave a final concentration of 5 μ M FeMJ. The steps highlighted in red were performed at the University of Cambridge Department of Veterinary Medicine due to biosafety category 2 requirements, whereas steps highlighted in green were performed at the Department of Chemical Engineering and Biotechnology.	92
Table 11: HPLC/HRMS limit of detection for siderophores spiked into either urine or plasma.	112
Table 12: List of animal and human clinical samples analysed by HPLC/HRMS.	114
Table 13: Binding constants for two monoclonal antibodies for different species of synthetic mycobactin as measured by competitive ELISA. Data provided by Petr Čapek (personal communication).	140
Table 14: Carboxymycobactin masses.	163
Table 15: Mycobactin T masses.	164

Abbreviations and Symbols

AcOH	Acetic acid
ACUC	Animal Care and Use Committee
ADC	Albumin dextrose complex
AuE	Gold electrode
BANG	BioAerosol Nebulising Generator
BCG	Bacillus Calmette-Guérin
BSA	Bovine serum albumin
BSL3	Biosafety level three
CAS	Chrome azurol S-shuttle solution
Casitone	Pancreatic digest of casein
Cbz	Carbobenzyloxy
CFU	Colony-forming units
CV	Cyclic voltammogram
<i>D</i>	Diffusion coefficient
DAD	Diode array detector
DCM	Dichloromethane
DDM	Dideoxymycobactin (also didehydroxymycobactin)
DFMJ	Desferri mycobactin J
DIAD	Diisopropyl azodicarboxylate
DIPEA	N,N-Diisopropylethylamine
DMAP	4-Dimethylaminopyridine
DMF	Dimethylformamide
DMSO	Dimethyl sulfoxide
DOTS	Directly observed treatment, short-course
<i>E. coli</i>	<i>Escherichia coli</i>
E^0_{complex}	Standard potential for reduction of the complex
E_{aq}	Standard potential for reduction in solution
EDC	Ethyl(dimethylaminopropyl) carbodiimide
ELISA	Enzyme-linked immunosorbent assay
E_p	Peak potential
$E_{p/2}$	Potential at half peak height
<i>F</i>	Faraday constant
FBS	Fetal bovine serum
FDG	Fludeoxyglucose
Fe(acac) ₃	Ferric acetylacetonate
Fe(CN) ₆	Ferricyanide
FeCM	Ferric carboxymycobactin
FeMJ	Ferric mycobactin J
FeMT	Ferric mycobactin T
FeSCM	Ferric synthetic carboxymycobactin
FeSMS	Ferric synthetic mycobactin S
FeSMT	Ferric synthetic mycobactin T
GAST	Low-iron glycerol alanine salts Tween medium
GCE	Glassy carbon electrode
HIV	Human immunodeficiency virus
HOAt	1-hydroxy-7-azabenzotriazole
HPLC/HRMS	High performance liquid chromatography/high resolution mass spectrometry
HPLC/MS	High performance liquid chromatography/mass spectrometry
<i>i</i>	Current
i_0	Background current
i_p	Peak current
i_{pa}	Anodic peak current
i_{pc}	Cathodic peak current
IPTG	Isopropyl-β-D-thio-galactoside

IRB	Institutional Review Board
k_s	Heterogeneous electron transfer rate constant
LAM	Lipoarabinomannan
LC	Liquid chromatography
Lcn2	Lipocalin 2 (also siderocalin and neutrophil gelatinase-associated lipocalin)
LSC	Liquid scintillation counter
<i>m</i> -CPBA	<i>meta</i> -Chloroperoxybenzoic acid
<i>M.</i>	<i>Mycobacterium</i>
M7H9	Middlebrook 7H9 media
MAIS	<i>M. avium</i> , <i>M. intracellulare</i> , and <i>M. scrofulaceum</i> group
mbtA-N (including mbtB)	Mycobactin biosynthesis protein A-N
MIC ₉₉	Minimum concentration of 99% growth inhibition
MOI	Multiplicity of infection
mpSCM	Minimal protecting group strategy synthetic 'carboxymycobactin' product
mpSMT	Minimal protecting group strategy synthetic 'mycobactin T' product
MS	Mass spectrometry
MS/MS	Tandem mass spectrometry
MSD	Electrospray quadrupole mass detector
<i>Mtb</i>	<i>Mycobacterium tuberculosis</i>
<i>n</i>	Number of electrons transferred
NAAT	Nucleic acid amplification test
NIAID	National Institute of Allergy and Infectious Diseases
NIDDK	National Institute of Diabetes and Digestive and Kidney Diseases
NIH	National Institutes of Health
NMR	Nuclear magnetic resonance spectroscopy
NTA	Nitrilotriacetic acid
OD ₆₅₀	Optical density at 650 nm
PBS	Phosphate buffered saline
PET	Positron emission tomography
PFP	Pentafluorophenyl
PPh ₃	Triphenylphosphine
PTFE	Polytetrafluoroethylene
<i>R</i>	Universal gas constant
RPMI	Roswell Park Memorial Institute medium
RT	Room temperature
S/N	Signal to noise ratio
SCM	Synthetic carboxymycobactin
SDS-PAGE	Sodium dodecyl sulfate polyacrylamide gel electrophoresis
SMS	Synthetic mycobactin S
SMT	Synthetic mycobactin T
SMT-C ₆	Synthetic mycobactin T with C ₆ alkyl tail
<i>T</i>	Absolute temperature
TB	Tuberculosis disease
THF	Tetrahydrofuran
TLC	Thin layer chromatography
TOF	Time-of-flight
UV	Ultra-violet
WHO	World Health Organization
XPS	X-ray photoelectron spectroscopy
β^{II}	Formation constant for the complex with Fe ²⁺
β^{III}	Formation constant for the complex with Fe ³⁺
β_v and β_w	Apparent transfer coefficients
ν	Scan rate

1 Introduction

Mycobactins are vital iron-harvesting molecules secreted by mycobacteria. These unique natural products have garnered much attention over the past 100 years because of their importance to the growth and pathogenesis of *Mycobacterium tuberculosis* (*Mtb*), the etiological agent of tuberculosis (TB). Despite this, there is currently no simple assay for detection and quantification of mycobactin. The research described in this dissertation has been directed toward the development of an electrochemical assay to detect these siderophores and investigation of its potential application and problems in TB diagnostics.

1.1 Tuberculosis

TB has ravaged humanity from before the beginning of history and has been implicated in the deaths of millions, ranging from *Homo erectus*¹ and Neolithic settlers² to Immanuel Kant and Erwin Schrödinger. In the most highly developed areas of the world the incidence of TB has finally been reduced yet the bacterium continues to infect fully one-third of the global population and kill 1.8 million people every year³. Areas with particularly high TB burdens include Sub-Saharan Africa and Southeast Asia, as can be seen in Figure 1.

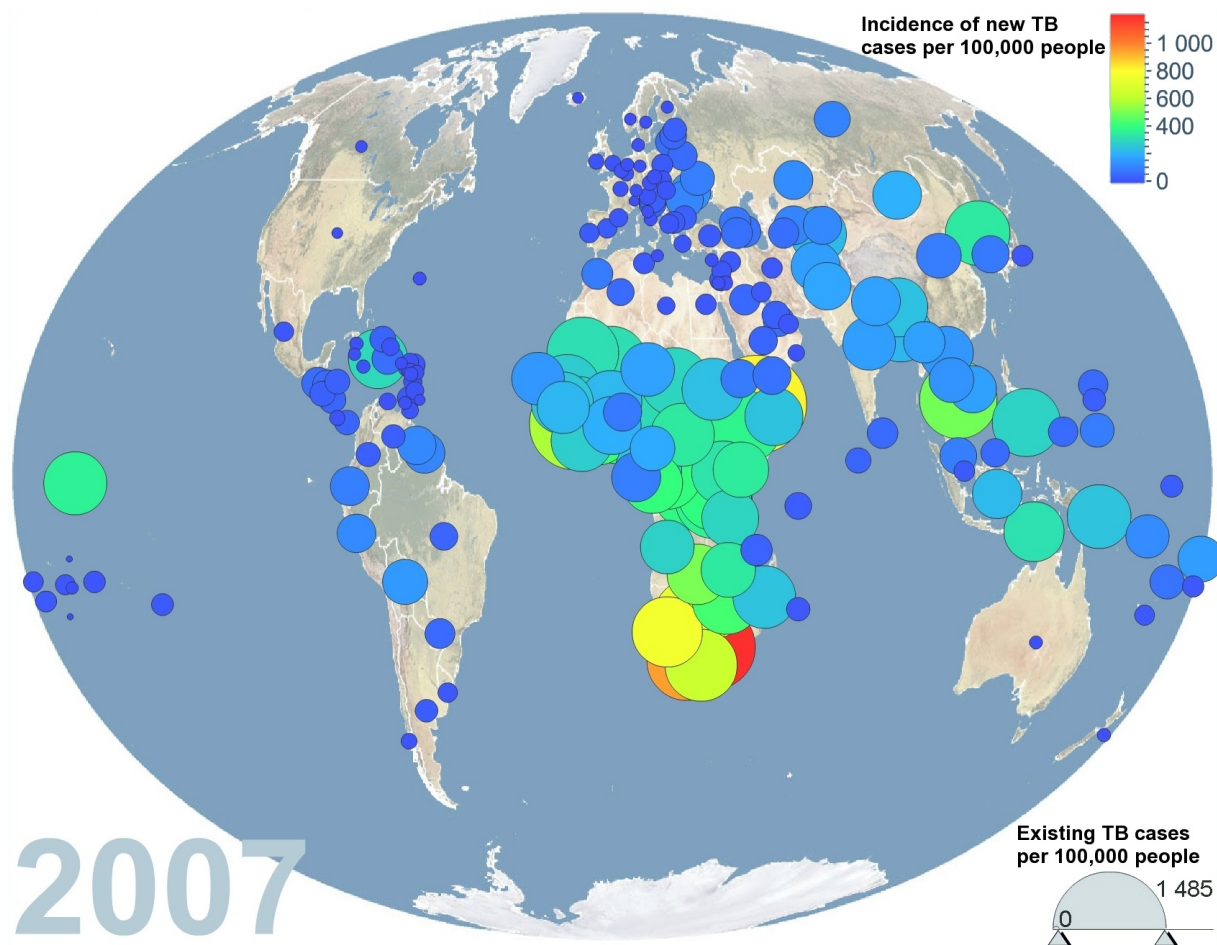


Figure 1: Global incidence (bubble temperature map) and prevalence (bubble size) of TB by country and population. Data from the World Health Organization (WHO, 2007) visualised by Gapminder World, powered by Trendalyzer from www.gapminder.org.

1.1.1 Anatomy of the Infection

TB is a lung disease spread by expulsion (often exacerbated by coughing) of fine droplets containing *Mtb* organisms, which can be inhaled by nearby individuals⁴. Typically TB is spread to other individuals who spend time in close proximity to the initially infected person. Once infection is established, it may either be cleared by the immune system, progress to active, clinically symptomatic TB, or remain asymptomatic as a so-called 'latent' infection⁵. It is estimated that there is a 10 percent chance of latent infection progressing to symptomatic TB over the course of a lifetime, with the risk decreasing with time after initial infection. However, weakening of the immune system, such as that which occurs during HIV progression, can lead to a greatly increased risk of the *Mtb* infection 'reactivating'⁵. This has led to a great number of clinical TB cases and deaths in populations that have high rates of *Mtb* and HIV coinfection and contributed to a global resurgence of TB³. Symptoms of TB include persistent cough, night sweats,

weight loss, and fever⁶. Progressive destruction of lung tissue can ultimately lead to death.

Mtb cells living within the lung are typically characterised as residing in alveolar macrophages, which as adaptive immunity develops, are surrounded by infiltrating inflammatory cells forming a granulomatous structure as the host immune system attempts to eliminate or wall off the infection. Recent advances in biomedicine have enabled a much greater understanding of the microenvironment of the host in which *Mtb* lives, and it is now thought that *Mtb* inhabits a variety of different microenvironments within the lung associated with different types of granulomatous tissue⁵. This also brings into question the dichotomy of 'latent' and 'active' clinical TB. In fact there is growing evidence that *Mtb* infecting the human lung creates a spectrum of disease from aggressively progressing clinical disease, through a slowly dividing community of organisms at the subclinical level, to an infection that has been completely cleared from a calcified lesion⁵.

The immunology of TB is complex. *Mtb* produces some of the most inflammatory compounds that are known; so powerful that they are often used as immunologic adjuvants for the administration of vaccines and other treatments⁷. There is mounting evidence that *Mtb* uses the host immune system to its advantage⁸ by using its own lipids and proteins to modulate the host immune response⁹. *Mtb* may seek to use the host response to wall itself off within granulomas where it can maintain a persistent population for long periods of time¹⁰. It is noteworthy that the immunological response to *Mtb* is almost exclusively cellular; few antibodies are raised against the bacterium, and when they are they tend to come in the later stages of infection against a heterogeneous range of antigens¹¹. This makes the development of antibody-based diagnostics difficult.

The mycobacterial cell wall of *Mtb* is particularly thick and waxy; having a thick layer of mycolic acids outside of the peptidoglycan and other polysaccharide layers¹² as illustrated in Figure 2. This formidable cell wall makes *Mtb* a hardy organism and prevents many drugs and other compounds from entering into the cytosol of the cell.

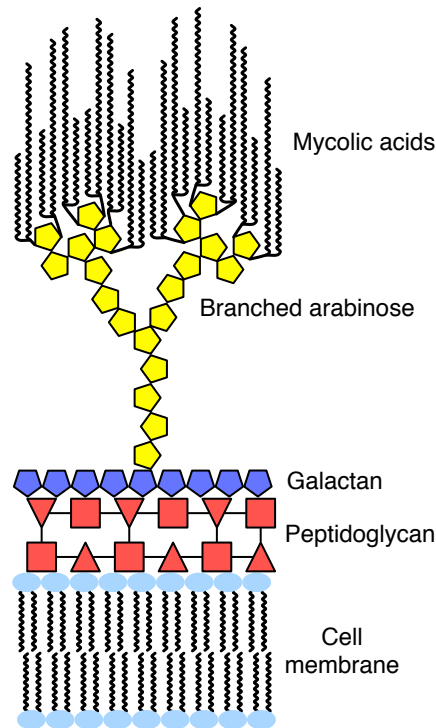


Figure 2: Schematic diagram of the mycobacterial cell wall.

1.1.2 Treatment

TB is usually treatable if properly diagnosed. The World Health Organization (WHO) directly observed treatment, short-course (DOTS) strategy for tuberculosis control calls for two months of combination chemotherapy with isoniazid, rifampicin, pyrazinamide, and ethambutol followed by continuation treatment for either four months with isoniazid and rifampicin or six months with isoniazid and ethambutol¹³. This prolonged treatment period combined with what can be a high and nausea-inducing pill burden, as well as the potential for drug supply interruptions over the extended time frame can often lead to inadequate or incomplete treatment. Initial treatment failure, in turn, gives rise to drug-resistant strains of *Mtb* that can be more difficult to treat¹³.

1.1.3 Diagnostics

1.1.3.1 Current Diagnostics

There is an urgent need for a low-cost sensor that is able to diagnose active TB in resource-poor settings. The WHO DOTS strategy relies heavily on sputum smear microscopy for diagnosis of TB¹⁴, and the technique is used extensively in resource-poor

settings because of its low cost¹⁵. However, smear microscopy is time and labour intensive and produces highly variable results with an estimated sensitivity of 31-80 percent¹⁶. The growing prevalence of smear-negative TB in HIV-positive patients and children also contribute to the poor performance and variability of this diagnostic method¹⁵.

The tuberculin skin test, another commonly used indicator of *Mtb* exposure, is complicated by various factors including Bacillus Calmette-Guérin (BCG) vaccine cross reactivity and failure to differentiate between latent and active TB¹⁷. It is vital to be able to make this differentiation in order to prioritise the treatment of clinically progressive TB¹³. More advanced tests include interferon- γ release assays, which require incubation of the patient's cells with *Mtb* components and measurement of any resulting interferon- γ release to gauge prior exposure¹⁸. These assays also do not differentiate active TB cases from 'latent' cases or other previous exposure¹⁹ and are too costly to be used in resource-poor settings, thus leaving these communities with no adequate means for TB diagnosis.

The recent WHO endorsement of nucleic acid amplification tests (NAATs) such as the Xpert MTB/RIF assay has signalled the biggest advance in TB diagnostics for many years, however the assay still fails to meet the requirements of point-of-care diagnostic for the developing world. It is still relatively expensive and requires sophisticated equipment and trained technical personnel to operate, thus it is not suitable for assay delivery at the community level²⁰.

1.1.3.2 Future Techniques and Potential Biomarkers

One of the most difficult obstacles to overcome is the unattractiveness of the market in the low-cost sector and the reluctance of private industry to expend significant resources in development and regulatory approval processes for a product aimed for delivery to impoverished settings²¹. This is in spite of the fact that the global market for TB diagnostics is estimated at \$1 billion, and \$326 million of that is spent outside of established market economies, where 73 percent of TB diagnostic testing currently takes place²².

Fluorescent reporters for β -lactamase detection have been used to visualise *Mtb* infections *in vivo* within living mice²³ and could hold promise for improving the sensitivity of fluorescent microscopy-based diagnoses. More interesting, is the potential

for this strategy to produce a point-of-care assay that does not require the use of expensive and bulky fluorescent technology in the field. This might be achieved through future development of new substrates for β -lactamase that utilise chemiluminescence rather than fluorescence detection.

Recently there has been a great deal of interest in detection of lipoarabinomannan (LAM) in the urine of TB patients for diagnostic use. LAM is a glycolipid antigen produced by *Mtb*²⁴ and exported into its environment within the host⁸ perhaps for the purpose of inhibiting macrophage activation and T cell proliferation²⁵. This would allow the bacterium to extend its inhabitation of the host cell. Recent studies of LAM detection by enzyme-linked immunosorbent assay (ELISA) showed promising results in the prediction of mortality in HIV-infected individuals with low CD4 cell counts²⁶. This could be useful in that these patients are difficult to diagnose by other methods, thus providing additive utility, however detection of LAM in patients with normal CD4 counts was less promising. LAM detection by other means remains a hopeful target for the development of TB diagnostics and there is work currently being done to develop a lateral flow point of care diagnostic based on direct detection of this lipidic *Mtb* antigen²⁷.

Siderophores are another class of lipidic *Mtb* products that have been heretofore unexplored as potential diagnostic biomarkers for TB. They are also produced specifically for excretion in that they must collect extracellular iron and return it to the bacterium²⁴. Because of their iron-binding ability and potential for redox chemistry, they provide an interesting and promising analyte to explore by electrochemical methods. An electrochemistry-based sensor for mycobactin would be well suited for deployment to the developing world due to its low cost and potential for point-of-care use by untrained operators and such an assay could open the door for an exciting new modality for TB diagnosis.

1.2 Siderophores and Mycobactin

Iron is a vital nutrient for the growth of mycobacteria, just as it is for other fungi and bacteria. It is necessary for the function of many essential enzymes and metabolic processes vital to the survival and growth of the organism. The advent of oxygen on our planet facilitated the easy oxidation of iron into its insoluble ferric form. This new state of insolubility turned iron into a rare and growth-limiting resource²⁸. To overcome this

deficiency, fungi and bacteria have evolved high-affinity iron-chelating molecules called siderophores to harvest the iron that they require from their environment²⁹.

The lipidic siderophores of the mycobacteria are known as mycobactins. Extensive research has been conducted on them since their initial discovery in 1912³⁰ and isolation in 1953³¹. Subsequent to their discovery it was postulated that mycobactin analogues could serve as vehicles for drug delivery to pathogenic mycobacteria. Mycobactins were among the first examples of microbial growth factors, allowing *in vitro* culture of *Mycobacterium avium* subsp. *paratuberculosis* for the first time. For 25 years scientists at Imperial Chemical Industries led by Alan Snow worked to elucidate the properties of these compounds. The culmination of this work was an exacting analysis of mycobactins from many different species of mycobacteria; the methods for their production and purification; and ascertainment of their physical and chemical properties³².

Interest in mycobactin and mycobactin biosynthesis intensified after mycobactin was determined to be essential for the pathogenicity of *Mtb*³³. Mycobactin biosynthesis is now one of the best-characterised nonribosomal polypeptide/polyketide syntheses in nature. A host of structurally related siderophores have since been discovered, as summarised in Table 1. This dissertation focuses the siderophores produced by *Mtb*, which are most closely related to those of other mycobacteria and nocardiae, both of the suborder corynebacterineae.

Table 1: Siderophore classes isolated from different organisms of the Actinobacteria and Proteobacteria phylums.

Organism	Siderophore Class
Mycobacteria	Mycobactin, carboxymycobactin (also called exomycobactin)
Mycobacteria (saprophytic sp.)	Exochelin ³⁴
Nocardiae	Nocobactin ³⁵ , nocardichelins ³⁶
<i>Pseudomonas aeruginosa</i>	Pyochelin ³⁷
<i>Agrobacterium tumefaciens</i>	Agrobactin ³⁸
<i>Vibrio cholerae</i>	Vibriobactin ³⁹
<i>Vibrio anguillarum</i>	Anguibactin ⁴⁰
Yersiniae	Yersiniabactin ⁴¹
Marinobacteria	Marinobactin ⁴²

1.2.1 Structure

The core structure of mycobactin is shown in Figure 3A. The core consists of salicylate linked to an oxazoline ring, followed by a linear lysine residue and a butyrate capped with a seven-membered ring formed out of a cyclised lysine. The linear lysine is acylated at R₁; this is the position of the long alkyl chain in most mycobactins. The butyrate subunit is the most diversely substituted and chirally variable section of the molecule and is the only subunit not derived directly from an amino acid. Both the cyclic and linear lysine residues are N⁶-hydroxylated to form the two hydroxamate metal coordination sites. These, together with an oxazoline-phenolate coordination site, serve to make mycobactin a hexadentate metal coordinator with an extremely high formation constant for complexation of Fe³⁺ ($4 \times 10^{26} \text{ M}^{-1}$)⁴³. Each species of mycobacteria has a defined set of R₂₋₆ substituents, while the alkyl chain at R₁ can vary in length (C₁₄₋₂₀) and degree of unsaturation. It is common for the alkyl chain to contain a *cis* double bond in the α - β position³². Figure 3B shows an example of a fully substituted molecule of mycobactin T from *Mtb*.

Mycobactin complexes are stable when bound to iron, but dissociate in acidic conditions⁴⁴. The desferri form of mycobactin is moderately stable to acid, but degrades easily when exposed to base³².

The configuration of the alkyl tail is critical for utilisation of mycobactins by mycobacteria⁴⁵. Carboxymycobactins have shorter alkyl chains at R₁ (C₂₋₁₃) that terminate in either a carboxylic acid⁴⁶ or a methyl ester⁴⁷. Carboxymycobactins are much more water-soluble than mycobactins, but the distinct functional role of these two forms is still unknown. Carboxymycobactins were once thought to occur only in pathogenic mycobacteria, but have since been isolated from the non-pathogenic *M. smegmatis*⁴⁸.

The siderophores of *M. marinum* and most nocardiae possess their major alkyl chain at R₅ instead of R₁, and those of nocardiae may have an additional double bond in the oxazoline ring between a and b. The stereochemistry of the chiral centres investigated thus far have conformed to the naturally occurring L-series of amino acids from which mycobactin is derived. The chiral centres d and e result from the action of a polyketide synthase, allowing their chiralities to fluctuate from species to species. Table 2 lists species of mycobacteria and nocardia that produce mycobactin-like siderophores and the details of their molecular substituents that have been reported in the literature.

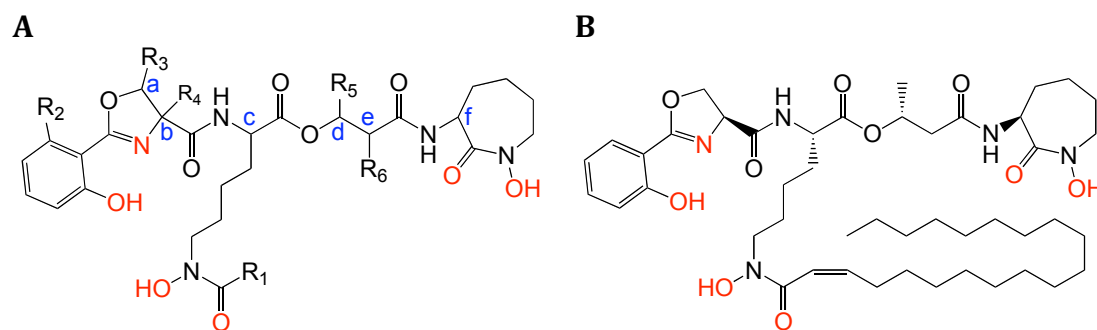


Figure 3A: Structure of mycobactin with coordination ligands shown in red⁴⁹, and chiral centres in blue. B: Mycobactin T from *M. tuberculosis*.

Table 2: Mycobactins and nocardial siderophores with similar known structures. The substituents are given, as well as the chirality of each stereo centre denoting either the D/L configuration of its parent amino acid, or the R/S absolute configuration where appropriate and known.

Species	Siderophore Name	R ₁	R ₁ Unsat.		R ₂	R ₃	R ₄	R ₅	R ₆	a	b	c	d	e	f
			Pos.												
<i>Mycobacterium africanum</i>	Mycobactin T ⁵⁰ (see below)														
<i>M. aurum</i>	Mycobactin A ⁴⁴	C ₁₄	2 ×		CH ₃	H		CH ₃	H	-					-
<i>M. avium</i> subsp. <i>avium</i>	Mycobactin Av ⁵¹ ,	C ₁₅ , C ₁₈ C ₁₄₋₁₇ (CH ₂) ₁₋₁₁	Sat α-β		H	CH ₃		C ₂ H ₅	CH ₃						
	Carboxymycobactin MA ^{46, 51}	COOH (CH ₂) ₂₋₆ COOCH ₃	Sat and unsat		H	CH ₃		C ₂ H ₅	CH ₃						
<i>M. avium</i> subsp. <i>paratuberculosis</i> *	Mycobactin J ⁵²⁻⁵⁴	C ₁₅	α-β		H	CH ₃		C ₂ H ₅	CH ₃	R	S	S	R	S	S
<i>M. bovis</i>	Mycobactin T ⁵⁰ (see below)														
	Carboxymycobactin ⁵⁵	(CH ₂) ₃₋₉ COOH (CH ₂) ₃₋₆ COOCH ₃	Sat and unsat		H	H, CH ₃		CH ₃	H						-
<i>M. farcinogenes</i>	Mycobactin F ^{44, 56}	C ₁₀₋₁₈	Unspecified		H	CH ₃		CH ₃	H				S	-	L
<i>M. fortuitum</i>	Mycobactin H ⁵⁷ (also produces mycobactin F, above ^{44, 56})	C ₁₈ , C ₂₀	Unspecified		CH ₃	CH ₃	H	CH ₃	H	R	L	L	S	-	L
<i>M. intracellulare</i>	Mycobactin ⁵³	Unsat alkyl	α-β		H	CH ₃	H	Sat. alkyl	CH ₃						
<i>M. kansasii</i>	Mycobactin K ⁴⁴	Not reported													

Species	Siderophore Name	R ₁ Unsat.		R ₂	R ₃	R ₄	R ₅	R ₆	a	b	c	d	e	f
		R ₁	Pos.											
<i>M. marinum</i>	Mycobactin M ⁴⁴	C ₂	None	H	CH ₃	H	C ₁₅₋₁₈	CH ₃						erythro
	Mycobactin N ⁴⁴	C ₃	None	H	CH ₃	H	C ₁₅₋₁₈	CH ₃						
<i>M. phlei</i>	Mycobactin P ⁵⁷	C ₁₄ , C ₁₆ , C ₁₈ , C ₂₀	2 × cis	CH ₃	H	H	C ₂ H ₅	CH ₃	-	L	L	S	R	L
<i>M. scrofulaceum</i>	Mycobactin ⁵³	Unsat alkyl	Unspecified	H	H	H	Sat. alkyl, CH ₃	CH ₃	-					
<i>M. senegalense</i>	Mycobactin F ^{44, 56} (see above)													
<i>M. smegmatis</i>	Mycobactin S ⁵⁷	C ₁₄ , C ₁₆ , C ₁₈ , C ₂₀	2 × cis	H	H	H	CH ₃	H	-	L	L	S	-	L
	Carboxymycobactin MS ⁴⁸	(CH ₂) ₅₋₁₂ COOH	None	H	H	H	CH ₃	H	-					-
<i>M. terrae</i>	Mycobactin R ⁴⁴	C ₂₀	2 ×	H	H	H	C ₂ H ₅	CH ₃	-	L	L	R	S	L
<i>M. thermoresistibile</i>	Mycobactin H ⁵⁷ (see above)													
<i>M. tuberculosis</i>	Mycobactin T ^{47, 57, 58}	C ₁₆₋₂₁	Sat and unsat	H	H	H, CH ₃	CH ₃	H	-			R	-	L
	Carboxymycobactin MT ⁴⁷	(CH ₂) ₁₋₇ COOCH ₃	Sat and unsat	H	H, CH ₃	H	CH ₃	H						-
<i>Nocardia asteroides</i>	Nocobactin NA ⁵⁹	CH ₃	None	CH ₃	H, oxazole	H	C ₉₋₁₁	CH ₃						
	Amamistatin B ^{60, 61}	H	None	CH ₃	CH ₃ , oxazole	H	C ₇	(CH ₃) ₂	-	-				-
	Asterobactin ⁶²	H	None	H	No oxazoline	H	C ₈	CH ₃						
<i>N. brasiliensis</i>	Nocobactin NB ⁶³	Alkyl	None	H	H	H	Alkyl	CH ₃						
	Brasilibactin A ^{64, 65}	H	None	H	H	H	C ₁₅	CH ₃	-					
<i>N. caviae</i> , <i>N. phenotolerans</i>	Nocobactin NC ⁶³	Alkyl	Sat and unsat	H	H, CH ₃	H	H, CH ₃	H						
<i>N. sp.</i> A32030	BE-32030 ⁶⁶	C ₁₂₋₁₆	Varies	H	H	CH ₃	CH ₃	H						-
<i>N. sp.</i> ND20	Formobactin ⁶⁷	H	None	H	CH ₃ , oxazole	H	C ₉	(CH ₃) ₂	-	-				-
<i>N. sp.</i> TP-A0674	Nocardimicin ⁶⁸	CH ₃	None	H	H, oxazole	H	C ₉₋₁₅	CH ₃	-	-				

*Mycobactin production by *M. avium* subsp. *paratuberculosis* is contingent upon selection for survival in iron-free media⁶⁹; thus several variations of mycobactin J have been observed.

It should be noted that mycobactin J is the only mycobactin that is currently available commercially. Mycobactin J is named as such because the originating organism was known as *M. johnei* (now known as *M. avium* subsp. *paratuberculosis*) at the time of its discovery³¹. It is a somewhat curious phenomenon in that *M. avium* subsp. *paratuberculosis* does not produce mycobactin *in vitro* and is dependent upon supplementation of the medium by mycobactin J. Mycobactin J was isolated from certain strains of *M. avium* subsp. *paratuberculosis* that were selected for survival in media⁶⁹ and its widespread use in culturing for the organism that causes Jöhne's disease is the reason why it is now produced on a commercial scale. This availability makes mycobactin J useful for mycobactin research.

Despite its long, lipophilic tail, mycobactin has a strong amphipathic character. All of the hydrophilic components of the molecule are concentrated in its peptidic head, while the alkyl tail provides the lipophilic counterpoint. Upon binding iron, many of the hydrophilic ligands are turned inward to coordinate the central iron atom⁴⁹. This causes the molecule to transition into a more compact, less flexible conformation and the external surface to become dominated by the lipophilic character of the alkyl chain. Figure 4 shows space-filling models of mycobactin T before and after binding Fe³⁺. Research on related siderophores, the marinobactins, has shown that the desferri form of the siderophore is capable of forming micelles⁴². The marinobactins have a more overall hydrophilic character than mycobactins, but share the attribute of a single C₁₂₋₁₆ alkyl chain, making them highly amphipathic. This gives rise to a conical molecular shape in which the hydrophilic iron-coordinating ligands are spread out on the surface of the micelle. Upon binding iron, marinobactins undergo a phase change to form bilayered vesicles⁴². These vesicles can form aggregates that traffic back to the organism. The length and degree of unsaturation of the lipophilic tail plays a major role in determining the lipophilicity and membrane permeability of the marinobactins, thereby affecting the critical concentration at which micelles of marinobactin spontaneously form and bud off from the membrane⁷⁰.

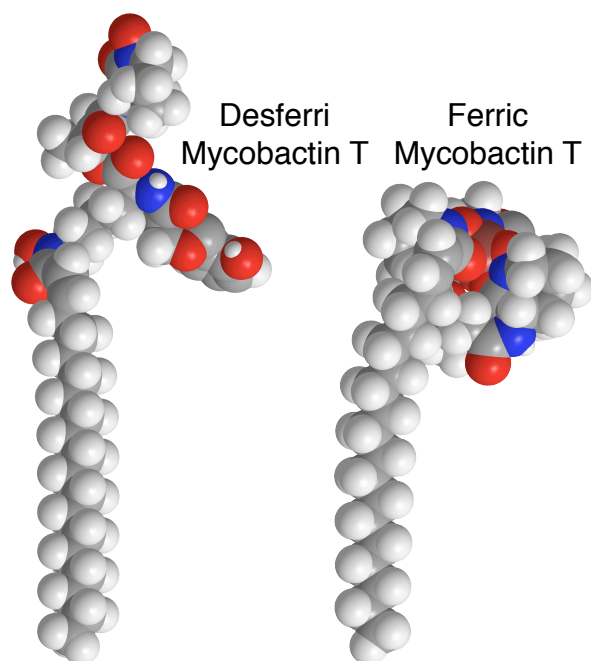


Figure 4: Mycobactin T before and after binding iron.

1.2.2 Biosynthesis

Mycobactin is synthesised via a complex hybrid nonribosomal polypeptide/polyketide biosynthetic process. This biosynthetic pathway was first delineated during analysis of the complete *Mtb* H37Rv genome based on homology with the yersiniabactin biosynthesis genes of *Yersinia pestis*. Cole et al. identified the *mbt* mycobactin biosynthesis operon⁷¹ simultaneously with Quadri and colleagues who also confirmed the first synthesis steps experimentally⁷² and later conducted a thorough mutational analysis of the cluster⁷³. The mycobactin core biosynthesis has been illustrated by De Voss et al.⁴³ The generation of an *mbtB* deletion mutant of *Mtb* demonstrated that this gene is necessary for mycobactin production, and definitively showed that mycobactin production is required for *Mtb* survival within macrophages³³. A second operon designated *mbt-2* was discovered several years later. This operon modifies and attaches the fatty acid that forms the alkyl chain at R₁⁷⁴. The *mbt* operon contains biosynthesis genes *mbtA-H*, while *mbt-2* contains genes *mbtK-N*. *mbtK-N* are also referred to as Rv1347c, Rv1344, fadD33, and fadE14 respectively in the literature⁷⁴. Figure 5 illustrates the role of each enzyme and the order of steps in mycobactin biosynthesis.

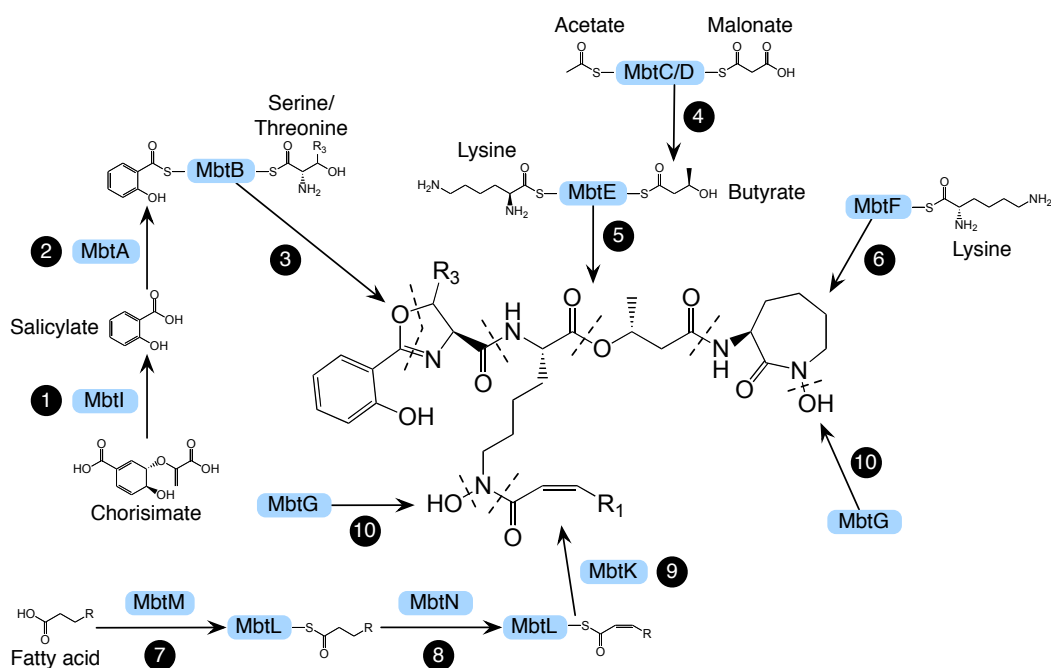


Figure 5: Schematic of mycobactin biosynthesis.

1. MbtI synthesises salicylate from chorismate, with an isochorismate intermediate. This process is dependent upon a Mg^{2+} cofactor^{75, 76}. There is also evidence that other proteins are able to accomplish this step⁷⁷. 6-Methylsalicylic acid is synthesised through an entirely different polyketide-based biosynthesis from acetate and malonate^{78, 79}, making the presence of both the methylated and unmethylated salicylate components in *M. fortuitum* mycobactins remarkable⁴⁴.
2. MbtA adenylates salicylic acid to create salicyl-AMP, which then forms a thioester with MbtB⁷².
3. MbtB catalyses formation of the peptide bond with either serine or threonine, followed by cyclisation of the peptide and final dehydration to form the oxazoline ring. The serine/threonine-activating domain of MbtB has shown preference for both serine and threonine⁸⁰.
4. The MbtC/D complex synthesises the butyrate subunit from acetate and malonate⁴³ or from propionate depending on the species⁸¹. The butyrate is then transferred to MbtE.
5. MbtE forms the peptide bond between the salicyl-oxazoline and linear lysine subunit, and the ester bond linking the butyrate subunit (the exact order of these steps is unknown)⁷².
6. MbtF attaches and cyclises the final lysine⁷².
7. MbtM activates a fatty acid by adenylation⁷⁴.

8. The fatty acid is transferred to MbtL and MbtN dehydrogenates the alkyl chain while it is bound to MbtL⁷⁴.
9. MbtK acylates the linear lysine residue, attaching the lipophilic alkyl chain⁸².
10. MbtG is thought to hydroxylate the lysine residues as the final step in mycobactin synthesis. This hypothesis is supported by evidence that N⁶-hydroxylysine is not incorporated into mycobactin⁸¹ nor is it a substrate for acylation by MbtK⁸². It is further supported by the discovery of dideoxymycobactin (DDM)^{83, 84}, which is presumed to be an intermediate in mycobactin synthesis. Study of a recombinant homologue of MbtG has also demonstrated its ability to hydroxylate lysine⁸⁵.

Note that MbtB, D, E, F and L must be activated with 4'-phosphopantetheinyl cofactors before they can participate in biosynthesis^{72, 74}. The precise functions of *mbtH* and *mbtJ* are still unknown, but *mbtH*-like genes in *Streptomyces coelicolor* have been found necessary for production of aminocoumarin⁸⁶. Furthermore, genetic analysis has revealed that MbtH-like proteins interact with nonribosomal peptide synthetases that contain adenylation domains⁸⁷. The branch point at which the biosynthetic pathways of mycobactin and carboxymycobactin bifurcate is also unknown.

Both *mbt* operons are regulated by IdeR, an essential iron regulator that suppresses mycobactin synthesis both in the presence of iron and upon exposure of cells to oxidative stress⁸⁸. During oxidative stress mycobactin synthesis is proposed to be downregulated to limit the iron-catalysed production of reactive oxygen species through the Fenton reaction. IdeR also regulates other genes involved in iron acquisition and storage^{89, 90}.

It has long been thought that the oxazoline ring is synthesised from serine or threonine. However, the antigen DDM from *Mtb* resembles mycobactin T, but lacks the N⁶-hydroxyl groups and incorporates a methyl group in the R₄ position^{58, 83}. This suggests the involvement of the uncommon amino acid α -methyl serine in mycobactin biosynthesis. Nuclear magnetic resonance spectroscopy (NMR) and tandem mass spectrometry (MS/MS) fragment analyses of DDM and synthetic analogues confirmed the presence of the methyl group at R₄. The only other report of a substituent at this position can be found in the siderophores isolated from *Nocardia* sp. A32030 that also exhibit a methyl group at R₄. It is possible that this methyl group is cleaved to form the finished mycobactin T structure, but this seems unlikely. Both of these structures were

elucidated using modern NMR technology not available during the initial determination of the mycobactin T structure⁹¹.

An *mbtM* orthologue deletion (*fadD33* in *M. smegmatis*) produced 90% less mycobactin than the wild type, and only produced mycobactins containing the saturated alkyl chain⁹². This suggests that MbtK is capable of attaching alternative substrates to mycobactin that do not result directly from the *mbt-2* pathway. However, it should be noted that complementation with the *mbtM* gene from *Mtb* failed to restore wild-type mycobactin production in *M. smegmatis*, so the two orthologues may have different functions⁹².

Para-aminosalicylic acid (PAS) was one of the standard drugs used to treat tuberculosis before the introduction of rifampicin and pyrazinamide⁹³. PAS is thought to act in part by inhibiting mycobactin synthesis^{94, 95}. While shown to decrease mycobactin production, PAS confoundingly increases production of carboxymycobactin in *M. smegmatis*⁹⁶. The mechanism through which this occurs is unknown and invites further investigation. PAS may interact with an enzyme involved with the differentiation between mycobactin and carboxymycobactin.

Wild type *M. avium* subsp. *paratuberculosis* is dependent on exogenous mycobactin for growth in the laboratory. Interestingly, when an *IS900* gene repeat was transformed into *M. smegmatis*, the property of mycobactin dependence was conferred unto the recombinant strain⁹⁷. *IS900* encodes p43, a protein of unknown function. The mechanism through which exogenous mycobactin dependence is conferred is unknown, but merits further investigation as a route toward mycobactin inhibition. p43 may be responsible for the mycobactin dependence and slow growth rate of *M. avium* subsp. *paratuberculosis*⁹⁷.

1.2.3 Function in Iron-acquisition by *Mtb*

Bacteria use siderophores to acquire iron when it is otherwise too scarce in the surrounding environment. In the case of pathogenic mycobacteria, the scarcity is compounded by two factors: first, that Fe^{3+} has very low solubility at physiological pH⁹⁸, and second, that the natural host response to infection includes sequestration of available iron. Sequestration is accomplished by upregulation of the iron-binding proteins transferrin, lactoferrin, and ferritin, as well as internalisation of iron by host cells⁹⁹.

Mycobactins can pilfer iron directly from all three of these proteins to overcome host sequestration¹⁰⁰. There is also evidence to suggest the pathogenic mycobacteria manipulate the host to traffic iron into infected cells^{101, 102}. Aside from being an essential cofactor in many metabolic processes, iron is especially important for production of many mycobacterial lipids. Testament to this is the requirement of iron supplementation for the formation of *M. smegmatis* biofilms¹⁰³. The aforementioned *mbtB* deletion mutant showed attenuated growth in low-iron conditions and in macrophages³³. Another mutant that constitutively expressed a homologue of the iron repressor IdeR also showed attenuated growth in BALB/C mice¹⁰⁴. Gene expression data has shown that mycobacteria are exposed to iron-restriction in human macrophages¹⁰⁵; similar data supporting this hypothesis have been reviewed by Waddell and Butcher¹⁰⁶. Furthermore, iron overload has long been associated with exacerbation of mycobacterial and other infections in both experimental models^{107, 108} and clinical practice¹⁰⁹⁻¹¹¹. A reanalysis of data from a pre-HIV 1929 study indicated that iron overload significantly increased the risk of death from tuberculosis¹¹². Most compelling was the discovery that transcripts of mycobactin biosynthesis gene *mbtB* were highly elevated in mice and to a more moderate extent in human clinical tissue samples¹¹³. Transcriptional analysis of human clinical samples has been highly variable^{113, 114}. All these data support that iron availability is a limiting factor for the progression of mycobacterial infections and the idea that *Mtb* actively produces mycobactin while inhabiting the infected lung.

Despite this compelling evidence for the importance of mycobactin, the *mbtB* mutant is still able to grow in culture medium supplemented with exogenous iron³³, suggesting the existence of an alternative iron acquisition pathway that has yet to be characterised. There is evidence that the xenosiderophore fericrocin and fungal siderophore rhizoferrin are internalised by *M. smegmatis*¹¹⁵. It is also possible that mycobacteria can take up iron from other common xenosiderophores and coordination compounds that might be found in their immediate environment, however this does not seem to be as effective as mycobactin-mediated iron acquisition in iron-restricted environments.

1.2.3.1 Current Model of Mycobacterial Iron Trafficking

Conventionally, mycobactins were thought to be associated with the cell wall and membrane of the mycobacteria. They have low solubility in water (5-10 µg/mL) and are typically extracted from the cell pellet, not from culture supernatants³². They have been reported to be entirely cell-associated when grown in the absence of the detergent Tween, but can be found in culture supernatants when Tween is added to the growth medium¹¹⁶. They have also been observed by electron microscopy to exist within the cell wall near the cytoplasmic membrane¹¹⁷. Accordingly, mycobactin was initially presumed to function simply as a means of ferrying iron across the thick mycobacterial cell wall and membrane¹¹⁸.

'Exochelins,'³⁴ were discovered in 1975. This group of water-soluble siderophores is now known to consist of two types: the true exochelins of the saprophytic mycobacteria, which are structurally unrelated to mycobactins, and the chloroform-extractable carboxymycobactins. The structures of the carboxymycobactins were elucidated in both *M. avium*⁴⁶ and *Mtb*⁴⁷ simultaneously and determined to be a variation of the mycobactins. To date, only *M. smegmatis* is known to produce both exochelins and carboxymycobactins¹¹⁹.

The discovery of extracellular siderophores brought into question the importance of lipophilic mycobactin¹¹⁶. Models began to emerge in which carboxymycobactins/exochelins scavenged iron in the extracellular milieu, then transferred it into the cell by means of a putative membrane-spanning reductase¹²⁰. In the case of excess iron and high concentrations of ferric carboxymycobactins/exochelins, the surplus iron may be donated to mycobactin residing in the cell membrane simply as a type of reservoir^{120, 121}. However, the growth promoting effect of mycobactin could not be ignored, and more recent studies have shown that mycobactins are more vital to iron acquisition than are exochelins. This was demonstrated by a mycobactin-deficient *M. smegmatis* mutant that was fivefold more susceptible to growth inhibition by the iron chelator ethylenediamine-N,N'-di(2-hydroxyphenylacetic acid) (EDDA) than either the wild type or exochelin-deficient mutant⁹².

Recently an ABC transporter system consisting of two proteins, IrtA and IrtB, was found to be required for effective utilisation of ferric carboxymycobactin but not for secretion¹²². The same study also found that mycobactin is not required for iron uptake

from ferric carboxymycobactin, but this was based on uptake from culture filtrates, not purified carboxymycobactin. Another study concluded that IrtA specifically exports siderophores and IrtB in conjunction with Rv2895c imports ferric siderophores¹²³, but more recent evidence has called the role of Rv2895c into question¹²⁴. It is unknown whether the IrtAB system transports lipophilic mycobactins in addition to carboxymycobactins. Likewise, the *esx-3* secretory system has recently been demonstrated to be essential for iron acquisition from exogenous mycobactin¹²⁵. Is not currently known whether *esx-3* interacts directly with mycobactin, or may export the machinery necessary for effective utilisation of the siderophore, such as a putative reductase or other iron-trafficking entity.

Figure 6 depicts a model of conventional carboxymycobactin-mediated iron acquisition. Carboxymycobactins are transported out of the bacterium by means of IrtAB and a putative porin-based mechanism¹²⁰ or other as-yet undefined method. The carboxymycobactins then scavenge iron from host iron-binding proteins, either within a macrophage or in the relatively aqueous extracellular milieu. Ferric carboxymycobactins are then either transported back into the cell through IrtAB, are relieved of iron by an undetermined reductive process in the periplasm, or hand excess iron off to mycobactin. Mycobactins in the cytoplasmic membrane creating a reservoir of readily accessible mycobactin-bound ferric iron¹¹⁷.

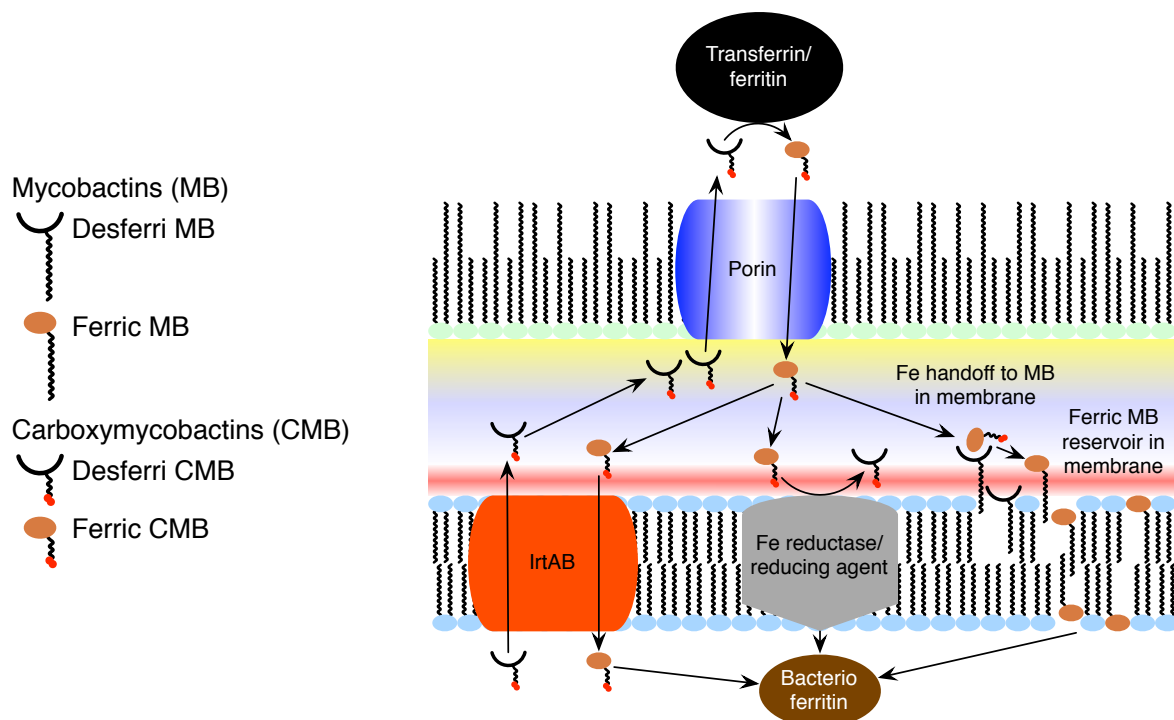


Figure 6: Model of mycobacterial iron acquisition; not drawn to scale.

1.2.3.2 Immunology of Mycobactin

It was not known whether mycobactins played a role in the adaptive immune response until the discovery of the antigen DDM, which is an incomplete form of mycobactin. Moody and colleagues showed that DDM is recognised by the CD1a antigen display protein and serves as a potent T cell activator^{58, 83}. Natural mycobactin did not activate T cells, and T cell activation seemed to be sensitive to the length of the alkyl chain at R₁. T cell activation by DDM may play an important role in the host immune response to *Mtb* and the formation of granulomas. CD1a has subsequently been co-crystallised with a synthetic DDM analogue¹²⁶. The crystal structure of this analogue in the binding pocket of CD1a is shown in Figure 7. The DDM analogue sits in a deep A' binding pocket that is connected to a shallower F' pocket near the surface of the CD1a protein and allows presentation of the peptidic portion of DDM to T cells. The binding pocket is quite rigid and the primary interactions with DDM are through van der Waals forces. Hydrogen bonding also occurs between arginine 73 and the oxazoline ring of the molecule, and between serine 77 in the F' pocket and the cyclised lysine moiety.

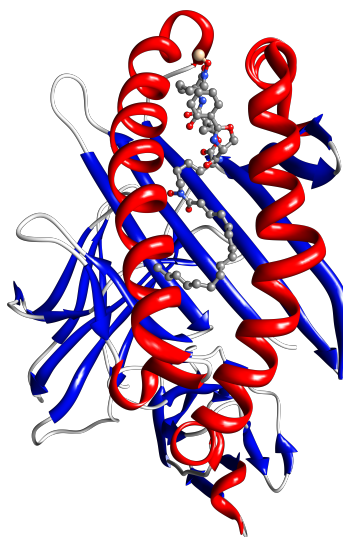


Figure 7: DDM analogue shown bound to the CD1a T cell antigen display protein.

Lipocalin 2 (Lcn2, also called siderocalin¹²⁷, neutrophil gelatinase-associated lipocalin¹²⁸, and other names^{129, 130}) is a secreted human neutrophil granule protein¹³¹. It is secreted during bacterial infection as part of innate immunity¹³² and binds several bacterial siderophores including the carboxymycobactins of *Mtb* and *M. smegmatis*¹²⁷, enterobactin from *Escherichia coli* (*E. coli*)¹³³, and parabactin from *Paracoccus*¹²⁷. In this

way, Lcn2 sequesters siderophore-bound iron to prevent harvest by the bacterium. Figure 8 shows the crystal structure of Lcn2 bound to ferric carboxymycobactin T.

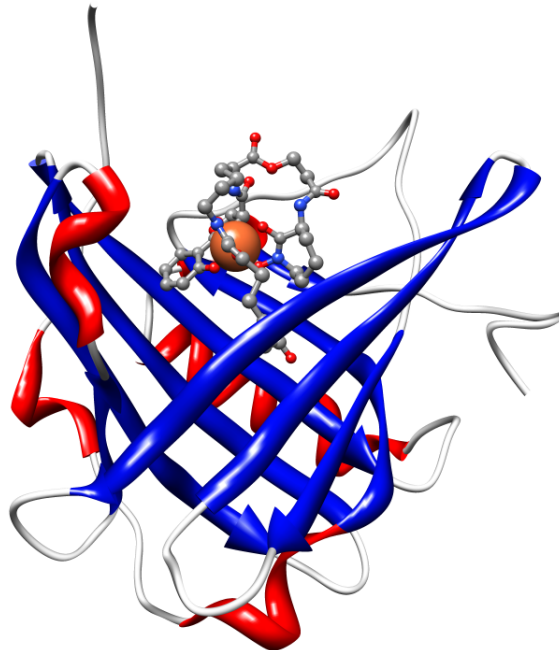


Figure 8: Lcn2 bound to ferric carboxymycobactin T; rendered from Protein Data Bank (PDB) accession code 1X8U¹²⁷ using Chimera¹³⁴.

Lcn2 is released from neutrophil granules as a monomer, a disulfide-linked homodimer, or a heterodimer with neutrophil gelatinase-B^{128, 135}. Neutrophil gelatinase-B is also known as matrix metalloproteinase-9 (MMP-9), which interestingly, has been shown to play a role in granuloma development to resist tuberculosis disease¹³⁶. Serum concentrations of Lcn2 have been recorded as high as 404 ng/mL during bacterial infection and can be used to differentiate between bacterial and viral infections¹³⁷.

Lcn2 binds the species of carboxymycobactin that contains eight methylene groups in its carboxylated alkyl chain at R₁. Lcn2 may also be able to bind carboxymycobactins of slightly differing chain lengths, but with reduced affinity¹²⁷. Previously, only chains containing up to seven methylene groups had been reported in carboxymycobactin⁴⁷. Lcn2 knockout mice have greater susceptibility to infection by *Escherichia coli*¹³² and *Mtb*.¹³⁸ Intratracheal infection with *Mtb* yielded significantly increased *Mtb* growth in alveolar epithelium, but not inside macrophages. The Lcn2 knockout mice also died more quickly than wild type mice.

It has been suggested that bacteria may modify their siderophores specifically to elude capture by Lcn2^{139, 140}. Although this has yet to be experimentally demonstrated, it could account for the diverse structural variability of mycobactins, even within a single

species. Enterobactin, another bacterial siderophore, undergoes a shift in coordination chemistry upon acidification that results in a conformational change of the molecules. This shift is sterically incompatible with the Lcn2 binding pocket, leading to release of the iron and degraded siderophore¹⁴¹. It has yet to be shown whether or not a similar release of iron occurs with carboxymycobactin. There is no evidence that carboxymycobactin undergoes a similar structural change, but carboxymycobactin does dissociate from iron at low pH⁴⁴. A recent study examined the role of electrostatics in siderophore capture by Lcn2. The authors concluded that electrostatic attraction between the siderophore and Lcn2 binding pocket is important for siderophore binding and that because of this, catecholate siderophores are the natural prey for Lcn2, while hydroxamate siderophores do not bind as well because the complex forms a neutral molecule¹⁴². Conversely, mycobactin utilises a primarily hydroxamate chelation modality and forms a neutral complex with Fe³⁺. Nevertheless, Lcn2 binds carboxymycobactins S and T with a high affinity, and the Lcn2 binding pocket is more completely filled by carboxymycobactin than by the catecholate enterobactin¹²⁷.

1.3 Therapeutic Applications of Mycobactins

Not only are mycobactins vitally important to the understanding of mycobacterial diseases, such as TB, but these unique natural products have also been investigated for a variety of therapeutic applications that span the gambit from chelation therapy agents and anti-cancer agents to antimicrobials.

1.3.1 Chelation Therapy

Chelation therapy is used to treat conditions that arise due to undesirable or excess quantities of metal within the body. These can include therapies for heavy metal toxicity¹⁴³ and the removal of internal radioactive contamination. Treatment for the removal of excess iron is the most common type of chelation therapy and is routinely carried out for the treatment of acute iron poisoning and chronic iron overload, such as hemochromatosis¹⁴⁴. Deferoxamine, deferasirox, and deferiprone are all pharmaceutical agents in use for iron-specific chelation therapy. The first of these agents, deferoxamine, was originally discovered as the siderophore of *Streptomyces pilosus*. Mycobactin is an excellent candidate as a potential chelation therapeutic because of its high association

constant for iron, allowing more efficient use of the agent at lower doses, coupled with its high degree of specificity for iron, which would prevent complications of undesirable chelation and excretion of other metals such as copper and zinc. The only other metals that mycobactin binds effectively are heavy metals and those not commonly found within the body, such as gallium. However there is one caveat: if the version of mycobactin that is used therapeutically is able to be taken up by mycobacteria, then care must be taken not to administer mycobactin to patients who may have a mycobacterial infection. This could risk exacerbating the infection.

1.3.2 Mycobactins as Anti-Cancer Agents

Iron-chelating compounds have also been investigated for their anti-cancer activities. Because iron plays a key role in the rate-limiting step of DNA synthesis performed by ribonucleotide reductase, cancer cells have an increased requirement for iron as they rapidly proliferate¹⁴⁴. Deferoxamine and other conventional pharmaceutical iron chelators have been investigated for cancer treatment¹⁴⁵, but attention has also been directed at mycobactins and related compounds for this purpose. The lipophilicity of mycobactin makes it a good candidate to enter cells and deplete the intracellular iron pools of cancerous cells¹⁴⁴. Additionally, the nature of mycobactin's lipophilic tail makes tailoring the lipophilic character of mycobactin a relatively simple alteration in the synthetic process, enabling the siderophore to be tuned to the optimal level of lipophilicity.

Carboxymycobactins^{146, 147} and their close cousins the nocardial siderophores^{66, 148} have been repeatedly examined for use as antitumor agents, chiefly because their strong iron-chelating activity is able to deprive cancer cells of iron. This inhibits DNA replication by limiting iron availability to ribonucleotide reductase¹⁴⁷. Carboxymycobactin T (referred to as exochelin in the study) was able to induce apoptosis of human breast cancer cells without harming normal breast tissue¹⁴⁶. Carboxymycobactin T outperformed desferoxamine as a ribonucleotide reductase inhibitor; the greater effect was attributed to the lipophilicity of carboxymycobactin enabling it to penetrate the cell membrane and scavenge intracellular iron, whereas desferoxamine was only able to chelate extracellular iron¹⁴⁷. Practically speaking, this would require local delivery of carboxymycobactin, since any carboxymycobactin

delivered systemically would almost certainly have chelated iron before reaching the target tumour cells.

The amamistatins of *N. asteroides* were also investigated for their antitumor activity^{60, 61}. Several analogues of these were subsequently synthesised and tested¹⁴⁹⁻¹⁵¹. Interestingly, the amamistatin fragment mentioned earlier also showed antitumor activity and histone deacetylase inhibition, which did not seem to be related to its iron chelation activity¹⁵⁰.

1.3.3 Antimicrobial Potential of Mycobactins and Their Analogues

Mycobactin analogues have been contemplated for use as either mycobactin synthesis inhibitors or vehicles for infiltrating the mycobacterial cell wall to deliver drugs since 1945³². Hu and collaborators synthesised mycobactin S and unexpectedly found that it inhibited *Mtb* growth with 99% growth inhibition (MIC₉₉) at 12.5 µg/mL¹⁵². This inhibition was not due simply to the chelation effect of the synthesised compound because medium iron concentrations were higher than those of the synthetic mycobactin S. The remarkable facet to this story is that mycobactin S is identical to mycobactin T except for the chiral centre at d (see Figure 3). It should be noted that this inhibitory activity has not been confirmed with naturally produced mycobactin S. Spurred on by this success, Marvin Miller's laboratory synthesised more mycobactin analogues, the most active of which included a boc-protected amino group at R₅ and demonstrated a MIC₉₉ of less than 0.2 µg/mL¹⁵³.

Transvalencin Z is a compound that was isolated from *Nocardia transvalensis*. It resembles the salicyl-oxazoline moiety of mycobactin up to the ester bond but lacks the long acyl chain. This compound was shown to have antimicrobial activity¹⁵⁴ and may act by interfering with the siderophore pathways on organisms with siderophores containing salicyl-oxazoline or salicyl-thiazoline moieties. Cross reactivity of this structural feature is tentatively supported by the finding that mycobactin S and carboxymycobactin S induce the expression of *Pseudomonas aeruginosa* extracytoplasmic function sigma factor PA1910¹⁵⁵. Although the function of PA1910 is not fully understood, the *Pseudomonas* siderophore pyochelin also contains a salicyl-thiazoline³⁷. This suggests the possibility of siderophore cross reactivity or inhibition.

The idea of a siderophore 'Trojan Horse' has also gained traction as a way to transport drugs that would otherwise fail to penetrate the mycobacterial cell wall. A

number of these compounds coupled to β -lactams have successfully been synthesised¹⁵⁶. Efforts to create therapeutic mycobactin analogues have also focused on creating competitive iron chelators to starve the bacteria of iron¹⁵⁷.

Elucidation of the mycobactin biosynthetic pathway kick-started the hunt for inhibitors against enzymes within this system. In the quest for an inhibitor of salicylate-activating enzymes (examples include MbtA in *Mtb* and YbtE in *Yersinia pestis*), two independent research groups generated the same bisubstrate inhibitor: salicyl-5'-O-(N-salicylsulfamoyl)adenosine (salicyl-AMS), as depicted in Figure 9B^{158, 159}. This inhibitor is a modification of activated salicyl-AMP, the natural product of MbtA (Figure 9A), and mimics both substrates while occupying both binding pockets of the enzyme. Salicyl-AMS showed inhibitory activity against both *Mtb* and *Y. pestis* under low-iron conditions, but only against *Mtb* under iron-supplemented conditions¹⁵⁸.

Following the design of salicyl-AMS, Courtney Aldrich and coworkers embarked on a systematic exploration of the salicyl-AMS structure-activity relationship. They synthesised a multitude of analogues with different modifications to the salicyl-glycosyl linker^{159, 160}, glycosyl subunit¹⁶¹, salicyl subunit¹⁶², and adenosine subunit^{163, 164} of salicyl-AMS. Luis Quadri and associates have also examined analogues of this compound^{158, 165}. The results suggested that the ribose subunit is critical for recognition by a putative transporter¹⁶¹. This could explain the ability of this compound to overcome the membrane permeability problem that has plagued other acyl adenylate-based inhibitors¹⁶⁶. Salicyl-AMS analogues were designed rationally with the help of a complete homology model of MbtA based on the crystal structure of DhbE from *Bacillus subtilis* in complex with an adenylated 2,3-dihydroxybenzoic acid. This epic conquest came to its dénouement in a compound exhibiting an MIC₉₉ of 0.39 μ M in iron-replete conditions and 0.049 μ M in iron-deficient conditions¹⁶³. This compound is depicted in Figure 9C. The potency of this compound and activity under both iron-replete and iron-deficient conditions suggests that it may be active in additional pathways beyond MbtA. Salicyl-AMS has also been tested for stability for up to 24 hours in human plasma and 1 hour in human liver microsomes¹⁶⁷.

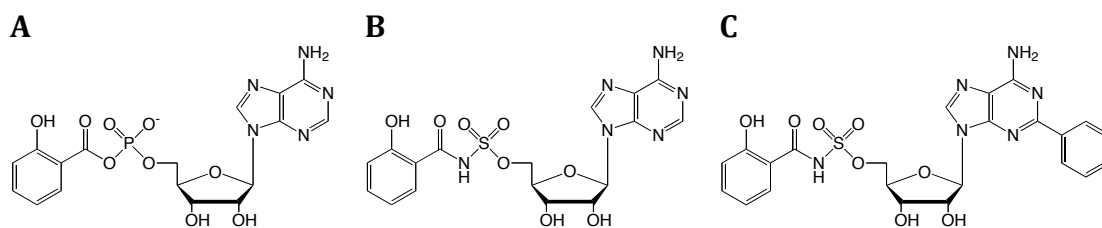


Figure 9A: Salicyl-AMP, the natural product of MbtA. B: Salicyl-AMS, the MbtA bisubstrate inhibitor. C: 2-Phenyl-salicyl-AMS, optimised inhibitor¹⁶³.

Some mycobactin analogues have also been found to have monoamine oxidase (MAO) inhibitory properties as well as some antitubercular activity¹⁶⁸. This was cited as a possible complicating factor for the development of antimicrobials based on these scaffolds. Siderophores from *Nocardia* sp. TP-A0674 showed inhibitory activity of muscarinic M3 receptor, an important neurotransmitter⁶⁸. The muscarinic M3 receptor is a potential target for treatment of a variety of disorders including respiratory, gastrointestinal, and urinary tract disorders⁶⁸.

1.4 Imaging Applications of Siderophores

Positron emission tomography (PET) is increasingly being used to visualise active TB infection within the lungs for research, treatment monitoring, and even potentially diagnostics¹⁶⁹. Most studies have used fludeoxyglucose (FDG) as the positron-emitting tracer, taking advantage of the inflammatory nature of TB disease to image regions of high metabolic activity within the lungs. However, the use of such a non-specific tracer is problematic in that there is significant background signal, especially from the heart and other organs with high metabolic activity. The use of siderophores as PET imaging tracers is intriguing both because of the ease and speed with which radioactive isotopes of iron, such as ⁵²Fe, or other trivalent metals, such as ⁶⁶Ga or ⁵⁵Co, can be added to complete siderophores and specific uptake of the siderophores by the target organism. Proof of principle studies have already shown great promise in using siderophores to image invasive pulmonary *Aspergillus fumigatus* infection¹⁷⁰.

Mycobactins and carboxymycobactins offer a promising new modality for PET imaging of TB. However, large quantities of purified mycobactin would be required in order for this application to be tested. Synthetic production of siderophores could provide this source of materials as well as serving as a mycobactin standard for a variety of research applications¹⁵².

1.5 Use of Mycobactin to Detect and Identify Mycobacteria

Given the quite specific structures of mycobactins from different species of mycobacteria, interrogation of their properties by thin layer chromatography (TLC) and NMR have been used to detect and differentiate mycobacterial species. Hall was able to use mycobactin as a specific chemotaxonomic marker to differentiate 17 closely related species of mycobacteria via TLC¹⁷¹. Similarly, Barclay and colleagues were able to use mycobactin TLC data to detect and identify organisms from the *M. avium*, *M. intracellulare*, and *M. scrofulaceum* (MAIS) group of pathogenic mycobacterial species⁶⁹, and Bosne and Lévy-Frédault achieved similar results using TLC analysis of mycobactin to identify subspecies of the clinically important organisms *M. fortuitum* and *M. chelonae* from patient isolates and environmental samples¹⁷². NMR has also been used to interrogate the properties of mycobactins from different species¹⁷³, but thus far no studies have addressed the potential to detect and identify mycobactin using relatively simple electrochemical techniques. Together, these studies demonstrate that mycobactins are useful as a unique marker for the organisms that produce them.

Methods for accurate detection of mycobactin have been developed, but thus far have been limited in their utility by either their lack of sensitivity or the requirement that they be carried out in an analytical laboratory environment. The ferric mycobactins of *Mtb* can be detected experimentally by their characteristic absorbance at 450 nm, due to the ligand-to-metal charge transfer indicative of iron-containing compounds; the desferri- forms lack the 450 nm absorbance peak⁴⁷. The mycobactins also have a major absorbance peak at 220 nm, indicative of amide and aromatic groups⁴⁷. This allows for simple differentiation between the ferric and desferri- forms. Gobin and coworkers used a combination of reverse-phase high-performance liquid chromatography (HPLC), simultaneous monitoring of absorbance at 220 nm and 450 nm, and mass spectrometry to purify and identify mycobactins¹⁰⁰.

A radiolabelling technique was first proposed by Snow¹⁷⁴ and later used by Ratledge & Marshall¹¹⁸, Barclay et al.⁶⁹, and Raghu & Sarma¹⁷⁵. Following growth of *Mtb* in iron-deficient medium, the siderophores are labelled using ⁵⁵Fe, extracted using chloroform, and analysed using a liquid scintillation counter. In an alternative radiolabelling strategy, when ¹⁴C-containing salicylic acid is added to *Mtb* culture, the salicylic acid is incorporated into siderophore biosynthesis. Siderophores may then be extracted with chloroform, and analysed using TLC and PhosphorImager for

quantification^{33, 72}. However, this technique would not be feasible for detecting siderophores produced *in vivo*.

A chrome azurol S-shuttle solution (CAS) is commonly used to detect the production of any iron-chelating siderophores¹⁷⁶. When the siderophores chelate iron, removing it from the dye complex, the dye changes from blue to orange. This can be observed as an absorbance extinction at 630 nm¹⁷⁶. Another dye-based method for catechol-based siderophores is to use the Arnow assay¹⁷⁷. Koedam et al. has suggested a method combining isoelectric focusing with CAS overlay for siderophore detection. These methods are useful for certain *in vitro* applications, however they lack the sensitivity and versatility required for many other uses.

Lastly, a proposed bioassay based upon the growth of mycobactin-dependent *M. avium* subspecies *paratuberculosis* was developed by Lambrecht and Collins¹⁷⁸. This assay failed to detect the presence of mycobactin in infected tissue samples with an estimated sensitivity of 6 nM and a readout time of 21 days. This is the only serious attempt that has ever been made to detect the presence of mycobactins *in vivo*.

1.6 Research Objectives

Mycobactins have been studied extensively over the course of the last 100 years, yet many mysteries still surround their exact role and function in mycobacterial biology and disease. The importance of mycobactin in pathogenic mycobacterial diseases is well established, and the evidence of an arms race between pathogen and host is fascinating. In spite of this, mycobactin remains an elusive entity that has never successfully been detected *in vivo*.

Given the necessity of mycobactin production and secretion for tuberculosis pathology, it bears investigation as to whether mycobactin might be used for a simple assay to detect and quantify the presence of mycobacterial species, particularly *M. tuberculosis*. Additionally, mycobactin is an important natural product that has potential pharmaceutical uses for chelation and anti-cancer therapy. As yet, there is no simple assay for the detection and quantification of mycobactin. Instead, most modern studies have relied on sophisticated and expensive HPLC techniques to detect mycobactin. An inexpensive sensor for mycobactin would open up exciting possibilities for a new TB diagnostic for the low-cost market. Additionally, such a sensor would help to finally

elucidate the role of mycobactin within an active *Mtb* infection by allowing *in vivo* detection for the first time.

The goal of this dissertation is to combine facets of analytical and clinical science to develop a new electrochemical assay for mycobactin and to test the relevance of that assay to the measurement of *Mtb* infection. This would serve as a potential new diagnostic modality for TB. Thus, the objectives of this dissertation include both the assay development and an evaluation of mycobactin as an analytical target through *in vitro* estimations of mycobactin production and testing clinical specimens for the presence of mycobactin. Ultimately, this dissertation aims to draw conclusions regarding diagnostic approaches to TB and to propose future strategies for assay development.

In line with the goals stated above, the research reported in this dissertation investigates:

1. The physiological level of mycobactin production in infected tissues to elucidate its role in *Mtb* infection based on *in vitro* data by:
 - a. Studying the production of mycobactin by *Mtb* under different conditions.
 - b. Developing a framework to understand how the conditions inside an actively infected lung will affect the expression of mycobactin and determine what levels of mycobactin might be expected within the local tissues.
2. The electrochemical properties of mycobactin to determine whether an assay based on electrochemical interrogation of the iron coordination complex can be created that is adaptable for use in a plurality of sampling media and methods of mycobactin extraction.
3. The utility of the assay for monitoring mycobactin levels within an example biological medium.
4. The presence of mycobactin and carboxymycobactin within clinical specimens of different biological media from TB patients and *Mtb* infected animal models in

order to draw conclusions regarding use of the assay as a measure of *Mtb* infection.

As a result of these studies, strategies are outlined for future investigation of mycobactin as a measure of *Mtb* infection and preliminary scoping research reported to:

1. Develop a method to improve the electrochemical assay through capture ligand modification of the electrode.
2. Develop synthetic mycobactin and carboxymycobactin standards and validate their function in Fe uptake by *Mtb*. Based on these data, the synthetic siderophores can be assessed as potential PET imaging probes and as antigens to which anti-mycobactin antibodies may be raised.

2 Production of Mycobactin *In Vitro*

An initial goal of this dissertation was to obtain preliminary estimates of the physiological level of mycobactin production in infected tissues and elucidate its role in *Mtb* infection based on *in vitro* data. In order to best inform the development of a simple mycobactin assay for TB diagnosis, it is important to understand the local environment of *Mtb* living within the lung and how this affects the production of mycobactin, particularly in regard to the availability of iron. A key component of this is the heterogeneous nature of the environments encountered by *Mtb*⁵, which make prediction difficult. However, as discussed in Section 1.2.3, it has been shown that *Mtb* increases the transcription of mycobactin biosynthesis genes both when infecting macrophages *in vitro* and within the human lung¹¹³. This, coupled with the established necessity of mycobactin production for the pathogenicity of *Mtb* makes it clear that some level of mycobactin production must take place within the infected lung, but how much?

Detection of mycobactin produced by *Mtb in vivo* has thus far eluded researchers¹⁷⁸, partly due to the lack of an effective and sensitive assay for the siderophore. However, this information is important in order to ascertain the sensitivity requirements for a perspective diagnostic sensor. Chapter 1 discussed the environment of the infected human lung. Clearly the multiple local microenvironments inhabited by any of the infecting bacteria present a complex array of conditions in which the organism must live⁵. In that context, focus shall be maintained upon investigating a few key points that are most likely to affect the production of mycobactin:

1. The iron-restricted environment of the bacteria
2. Their inhabitation and ability to thrive in lipid-rich environments, such as those induced within foamy macrophages
3. The metabolic need for iron is highest when the organism is dividing rapidly in the exponential phase of growth, as is analogous to a rapidly-dividing active infection

2.1 Materials and Methods

2.1.1 Culture of *Mycobacterium tuberculosis*

The laboratory strain *M. tuberculosis* H37Rv (ATCC 27294) from the stocks of the Tuberculosis Research Section, NIAID was used for all experiments unless otherwise noted. An *mbtB* mycobactin deletion mutant ($\Delta mbtB$) of the *Mtb* H37Rv was also used in this dissertation³³. *Mtb* stocks were grown in liquid Middlebrook 7H9 medium in roller bottles (Nalgene) at 37°C with constant rolling. All culturing of *Mtb* organisms took place in the BSL3 biocontainment facility of NIAID.

2.1.1.1 Low-Iron Media

The production of mycobactin is regulated by the availability of iron to the organism via the iron-responsive IdeR regulatory pathway⁸⁸. Because iron is a micronutrient, even trace quantities of iron can dramatically affect mycobactin production. *Mtb* exists in an iron-restricted state *in vivo*. For the *in vitro* model it is imperative to precisely control the iron levels not only in the culture medium, but also the internal iron stores within the bacteria.

Because *Mtb* reside in a lipid-rich environment within the host, it was hypothesised that it would be necessary to take steps to maintain the mobility of the lipophilic mycobactin. To maintain this mobility in the relatively aqueous culture medium, the detergent Tween 80 was included in the medium to facilitate lipophilic mycobactin mobility. This can have the effect of dissociating lipophilic mycobactin from the cell wall, as may also be the case inside of infected foamy macrophages¹⁷⁹.

Low-iron glycerol alanine salts Tween (GAST) medium consisted of the following (per litre): 0.3 g of Bacto Casitone (pancreatic digest of casein, BD), 4.0 g of dibasic potassium phosphate, 2.0 g of citric acid, 1.0 g of L-alanine, 1.2 g of magnesium chloride hexahydrate, 0.6 g of potassium sulfate, 2.0 g of ammonium chloride, 1.80 mL of 10 M sodium hydroxide, 10.0 mL of glycerol, and 0.5 mL of Tween 80³³. Note that 50 mg of ferric ammonium citrate was excluded from the original glycerol alanine salts medium recipe except where indicated as 'iron replete' GAST. All ingredients were purchased as metals-basis pure except for Casitone. Where indicated, hygromycin was added at

50 µg/mL. Growth was regularly measured by the 650 nm absorbance of the culture after subtracting a blank media baseline.

It should be noted that citrate has demonstrated a low to moderate promotion of mycobacterial growth under low iron conditions, compared with a high growth promotion effect from mycobactin¹¹⁵. However, it was postulated that the citrate effect is merely due to citrate transferring iron to mycobactin.

2.1.1.1.1 Effects of Different Media Preparations

In order to establish reproducible methods of strict iron limitation in the media, the effect of different methods of media preparation and the use of the polyvalent metal ion chelator resin Chelex 100 (Sigma) on the rate of *Mtb* growth were measured. Where indicated, the water or water-Casitone solution used to make the GAST was treated by shaking with Chelex 100 and allowing to stand for 15 min before filtering. Except where indicated, GAST was made in plastic bottles, avoiding contact with glassware and metal spatulas.

2.1.1.2 *Siderophore Production*

Two different batches of iron-restricted *Mtb* cultures were grown for comparison. Batch A (4.4 L) was growth from *Mtb* H37Rv that had been iron-restricted for two subculture periods, while batch B (6 L) was growth from cells that had been iron-restricted for seven subculture periods, thereby having a greater level of iron starvation. The growth rates were monitored by their optical density at 650 nm (OD₆₅₀). Batch A was harvested after 19 days of growth at which point the culture had reached stationary phase. Batch B was harvested after 12 days of growth while still in the exponential phase.

2.1.1.3 *Correlation of Optical Density and Cell Mass*

Figure 10 illustrates the correlation between OD₆₅₀ and the wet cell mass. Wet cell mass measurements are subject to a high degree of variability due to both compositional variation^{180, 181} and experimental error due to loss of cell mass and reproducibility of dryness associated with centrifugation and decanting the supernatant.

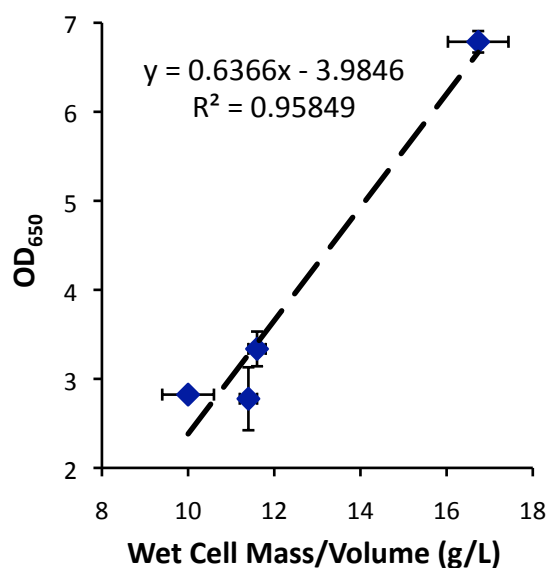


Figure 10: Correlation of wet cell mass per volume with 650 nm absorbance values, n = 3.

2.1.1.4 Extraction of Mycobactin from Culture

The mycobactin extraction protocol was adapted from De Voss³³ and Gobin et al.⁴⁷. Liquid cultures were centrifuged at 5000 g (3500 rpm) for 10 min in tared 250 mL conical tubes. The supernatant was decanted and filtered through 0.2 µm surfactant-free cellulose acetate filters (Nalgene). 1 M hydrochloric acid was slowly added to 2% by volume, then the supernatant was saturated to 555 µM ferric chloride from a 20 g/L (74 mM) stock of ferric chloride hexahydrate in water.

The cell pellet was weighed, then resuspended in 6 mL of ethanol per gram of cells and shaken for 24 hours at 37°C. The suspension was centrifuged again and the ethanol was decanted and filtered through a 0.2 µm filter. This pellet extract was then saturated to 2.2 mM ferric chloride from a 20 g/L (74 mM) stock of ferric chloride hexahydrate in ethanol.

Both the supernatant and pellet extract were then allowed to equilibrate overnight at 4°C. Following equilibration, the pellet extract was diluted 1:1 with water. The solutions were each extracted thrice into chloroform by shaking 1 volume with 0.75 volumes chloroform. The organic layer was separated and washed once with saturated sodium chloride solution. The organic layer was then dehydrated with anhydrous magnesium sulfate, filtered through a Whatman filter, and the solvent was removed under rotary evaporation.

As a control, an extract was also attempted from the $\Delta mbtB$ mycobactin deletion strain of *Mtb*³³. No mycobactin was detected in this extract.

2.1.2 HPLC Analysis

2.1.2.1 HPLC/DAD/MSD Instrumentation

High performance liquid chromatography/mass spectrometry (HPLC/MS) analysis was performed using an Agilent 1100 HPLC/electrospray quadrupole mass detector (MSD) with a diode array detector (DAD) for measurement of UV-visible absorbance. The column used was a 2.1 mm x 50 mm Phenomenex Luna(2) C₁₈ column with 3 µm particles and 100 Å pore size. A 0.3 mL/min flow rate was used and the column temperature was set at 60°C. The MSD was used in scanning mode 300-750 m/z at 400 V fragment voltage and 751-1500 m/z at 100V fragment voltage. Capillary voltage was set to 3000 V, the gain was set to 0.10, the step to 0.25, and the drying gas flow rate to 12 L/min. An injection volume of 10 µL was used. Several different elution protocols were used for mycobactin detection via HPLC/MS.

2.1.2.2 Techniques Used for Mtb Culture Extracts

The buffers and gradients are given in the tables below. Ferric mycobactin J (FeM_J, Allied Monitor) was used as a quantitative standard.

Table 3: Isocratic 70% acetonitrile method (ISOYJ70F).

Buffer A:	Aqueous with 0.1% formic acid	
Buffer B:	Acetonitrile with 0.1% formic acid	
Time (min)	0	60
% B	70	70

Table 4: MYCEX method.

Buffer A:	Aqueous with 0.1% formic acid							
Buffer B:	Acetonitrile with 0.1% formic acid							
Time (min)	0	20	50	120	140	170	175	180
% B	30	30	70	70	98	98	30	30

Table 5: NM_MYCO3 method.

Buffer A:	Aqueous with 0.05% trifluoroacetic acid						
Buffer B:	Acetonitrile with 0.035% trifluoroacetic acid						
Time (min)	0	75	130	135	150	152	160
% B	15	70	70	98	98	15	15

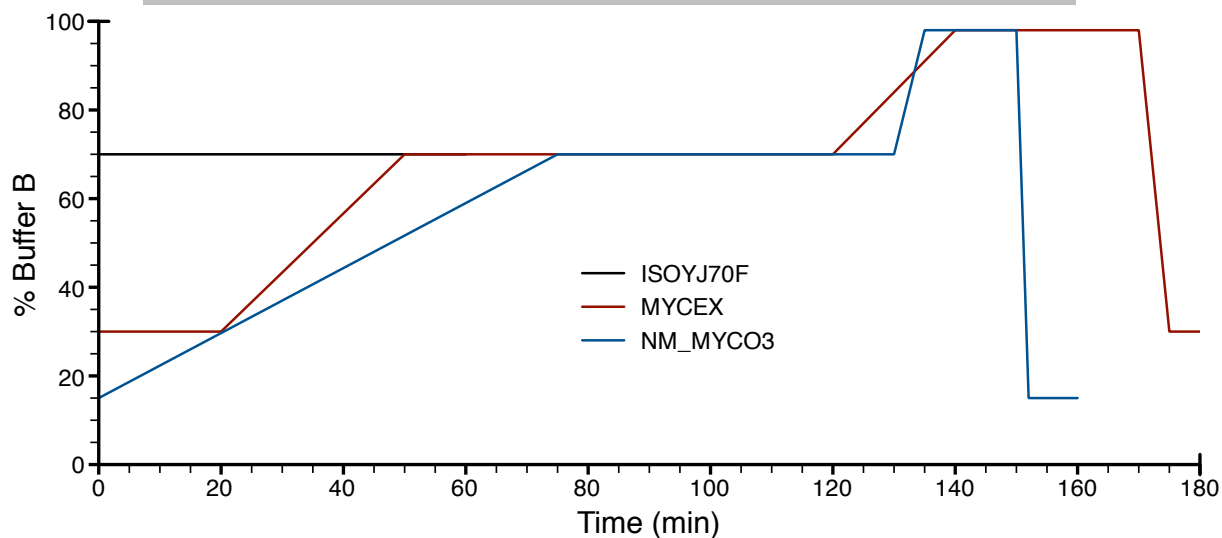


Figure 11: Graphical representation of the solvent gradients that were used for HPLC/MS analysis.

2.1.2.3 HPLC/DAD Quantification of Mycobactin

For quantification of extracted ferric mycobactin T (FeMT) compounds by HPLC/DAD, a standard curve was created by measuring the integrated area under the 450 nm absorbance signals of both the unsaturated and saturated peaks of known concentrations of FeMJ. This curve is given in Figure 12.

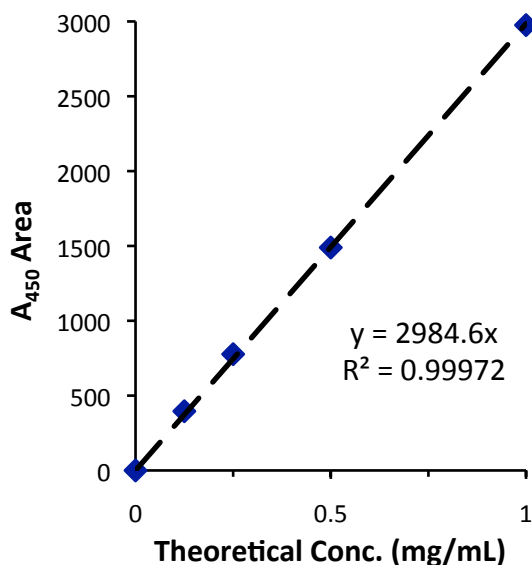


Figure 12: Standard curve of A₄₅₀ peak area vs. FeMJ concentration.

2.2 Results

2.2.1 Comparison of Media Preparation Methods

The results from the 650 nm absorbance (OD_{650}) growth curves shown in Figure 13A indicate that GAST that had been prepared in glass bottles produced a markedly higher growth rate compared with media prepared in plastic bottles. This difference had a dominant effect on the growth. The wet cell mass measurements yielded similar evidence, as shown in Figure 13B. The glass bottles that were used are reusable bottles, used frequently for making iron-replete medium, cleaned and autoclaved for reuse. This finding aroused concern that this cleaning process did not fully remove the media nutrients (iron specifically, however potentially other unknown compounds could be present as well), some of which may have remained adsorbed to the inside of the bottle and leached into new media preparations. This is in contrast to the plastic bottles, which were factory sterilised and not reused. The findings could also be explained by leaching of components from the plastic that cause growth inhibition¹⁸², however to ensure consistency between preparations, all cultures were grown in the same plastic roller bottles, since preparation of media in these bottles is unlikely to have an additional variable effect. Previously researchers have gone to great lengths to ensure that their glassware is free from trace metal contamination including overnight treatment with ethanolic potassium hydroxide and nitric acid¹⁸³⁻¹⁸⁵.

The OD_{650} data (Figure 13A) also indicate that Chelex 100 treatment of the Casitone may limit the nutrients in such a way as to slow growth. Given that this is intended to be an iron-limiting medium and that the other essential metals were added after treatment with Chelex, iron deprivation is assumed to be the cause of the lower growth rate. However, this contrasts with the wet cell mass data, which indicated that Chelex 100 treatment did not have a significant effect on the wet cell mass (Figure 13B). Chelex 100 treatment of the already purified water made no difference in growth rate. The wet cell mass measurements were prone to greater experimental error than the absorbance measurements as described in Section 2.1.1.3, therefore in order to avoid any possibility of iron contamination in further experiments relied on GAST made in plastic bottles with the Casitone fraction of the medium treated by Chelex 100. This was intended to achieve the most reproducible results by avoiding any trace iron contamination or the contribution of any potential unknown nutrients due to unclean

glass bottles as well as limiting the iron content of the only undefined medium ingredient, Casitone.

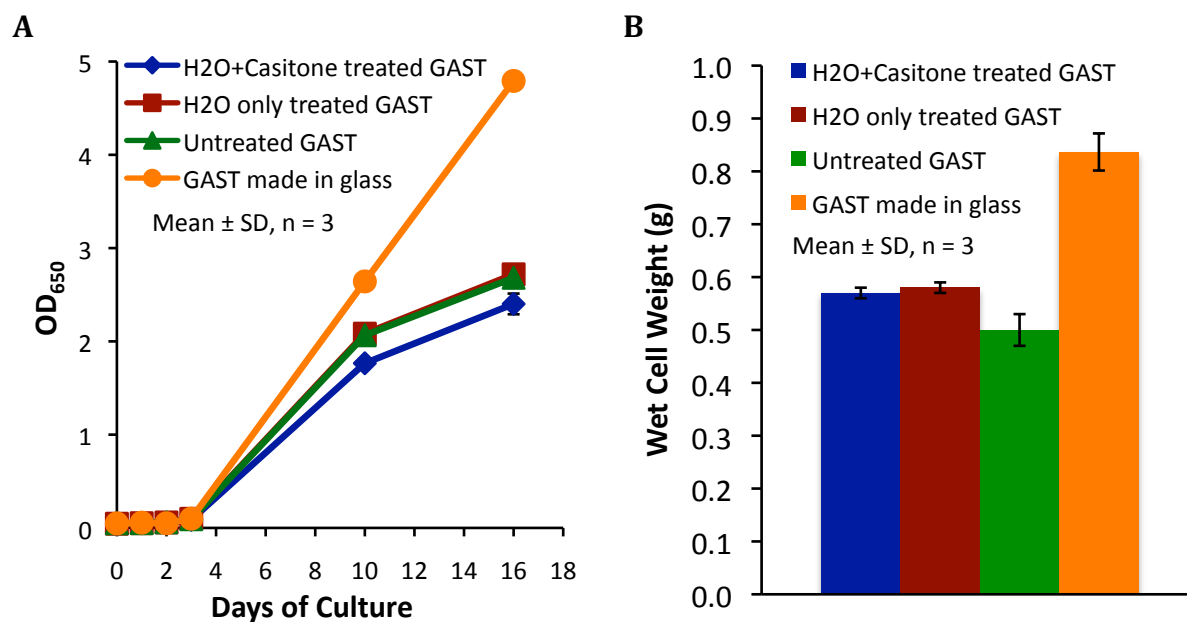


Figure 13A: Growth curves of *Mtb* H37Rv in differently prepared GAST media; blue indicates that both the water and the Casitone solution were Chelex 100 treated and media was mixed in plastic bottles, red indicates that only the water was Chelex 100 treated and media was mixed in plastic bottles, green indicates no Chelex 100 treatment with media mixed in plastic bottles, and yellow indicates no Chelex 100 treatment with media mixed in glass bottles. B: Total wet cell masses from each culture condition at day 16.

2.2.2 Absorbance and Mass Spectrum Identification of Mycobactins

Chromatograms of the FeMJ standard show a small secondary peak with a greater retention time than the primary peak (Figure 14). This is assigned to the presence of a small quantity of the form of FeMJ that has a fully saturated fatty acyl moiety. The spectrum of each peak is shown in Figure 15A. The unsaturated spectrum exhibits an increased absorbance in the 250-340 nm range. The characteristic spectra from the extracted FeMT are shown in Figure 15B. The FeMT spectra match well with the spectra of the FeMJ standard, as well as reference spectra from literature⁹¹.

The mass spectrum data corroborated the unsaturated/saturated structure hypothesis in that HPLC elution peaks that exhibit the unsaturated spectrum produce a mass signal at $M - 2H$ relative to adjacent peaks that exhibit the saturated spectrum. The mass spectra of FeMT and FeMJ in Figure 16 also corroborated well with the predicted isotopic distribution pattern, demonstrated in Table 6 for FeMJ. The peak at $M - 2$ is

indicative of a ferric compound containing the ^{54}Fe isotope in the naturally occurring abundance of 5.8 percent.

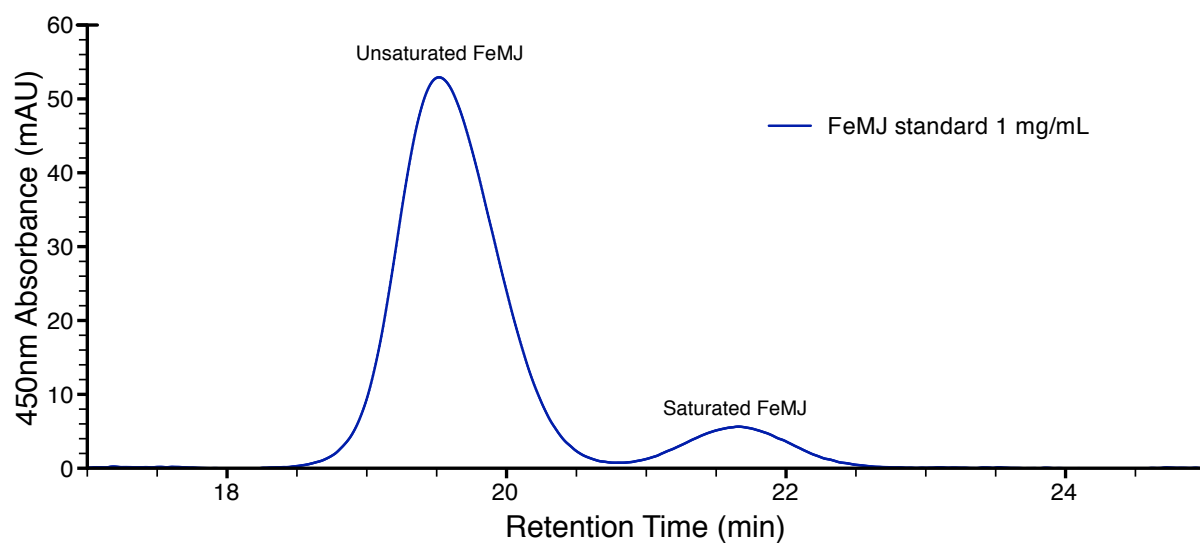


Figure 14: FeMJ standard eluting under the ISOYJ70 method.

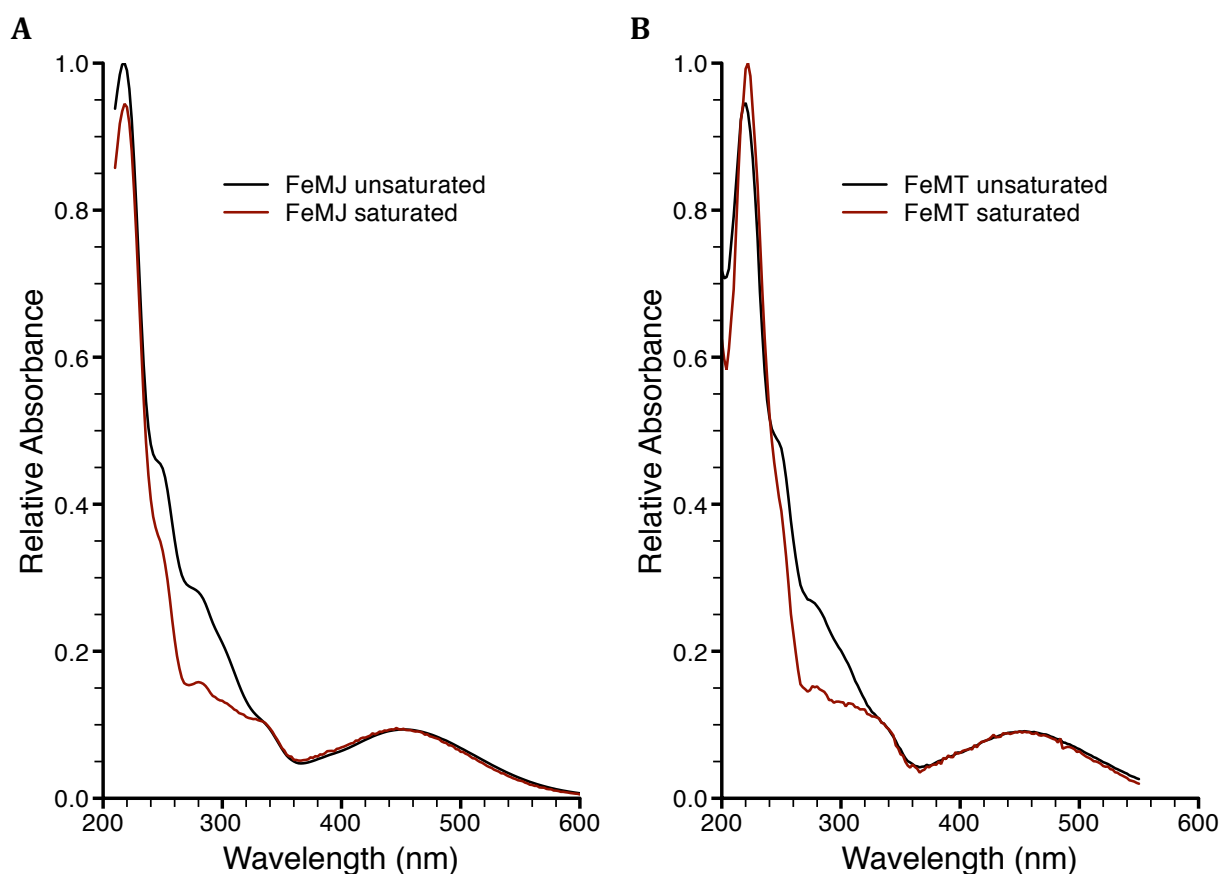


Figure 15A: Absorbance spectrums of mycobactin J (FeMJ) containing either unsaturated or saturated acyl moieties. B: comparable absorbance spectrums captured from HPLC elution of mycobactin T extracted from *Mtb* culture (FeMT). Spectrums were normalised at 450 nm, then plotted with a maximum absorbance of unity.

Table 6: Predicted mass spectrum of the protonated ion of FeMJ containing an unsaturated acyl chain (ChemDraw).

m/z	Relative Abundance
895.4	100.0 %
896.4	54.0 %
897.4	16.7 %
893.4	6.4 %
898.4	3.5 %
894.4	3.2 %

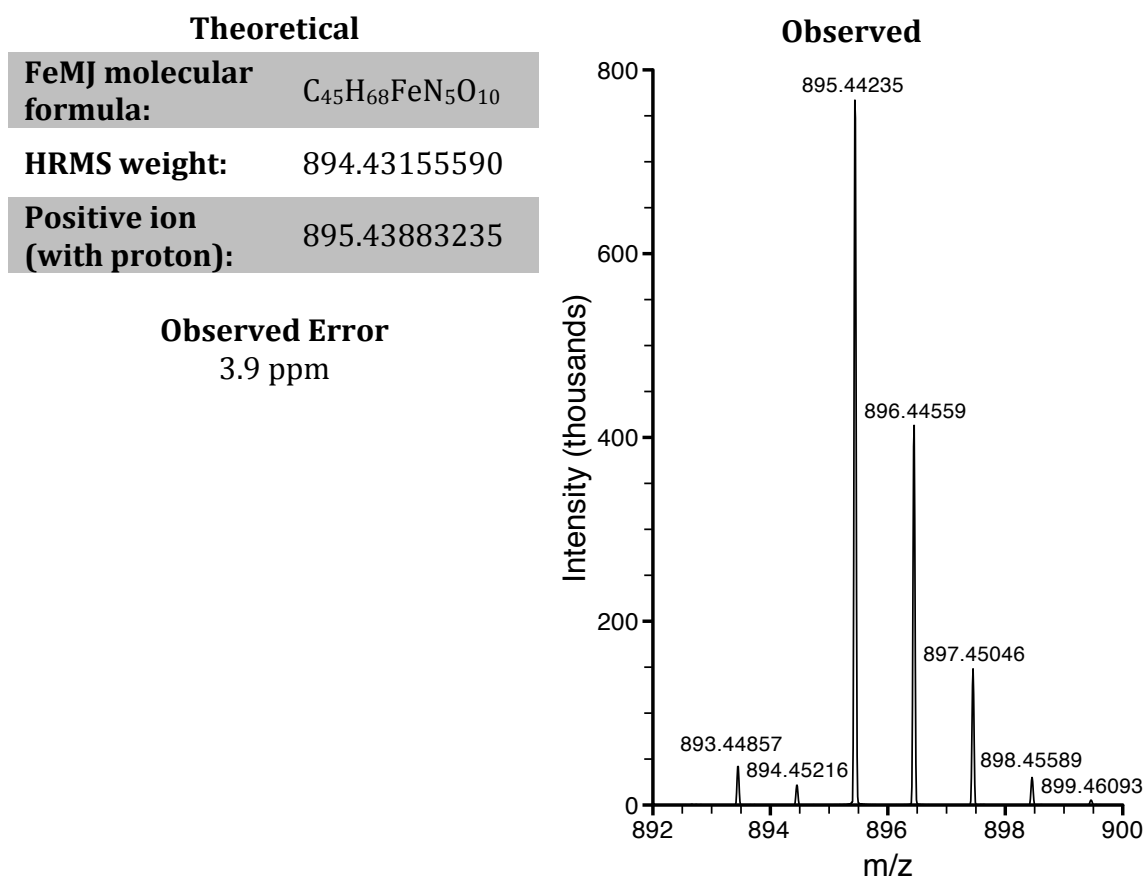


Figure 16: Mass spectrum of FeMJ; note the M - 2 peak indicating the presence of ⁵⁴Fe at the natural isotopic composition of 5.8 percent.

2.2.3 Siderophore Production Growth Curves

The growth curves for two different batches of *Mtb* grown for siderophore extraction are shown in Figure 17. Batch A was grown from *Mtb* that had a lower degree of iron depletion through division in low-iron GAST, while batch B was grown from *Mtb* that had a higher degree of iron depletion. This resulted in the higher initial growth rate exhibited by batch A. Growth of batch A also plateaued into stationary phase growth at

an earlier time point (7 days) versus batch B, which had not reached stationary phase at the time of harvest (12 days).

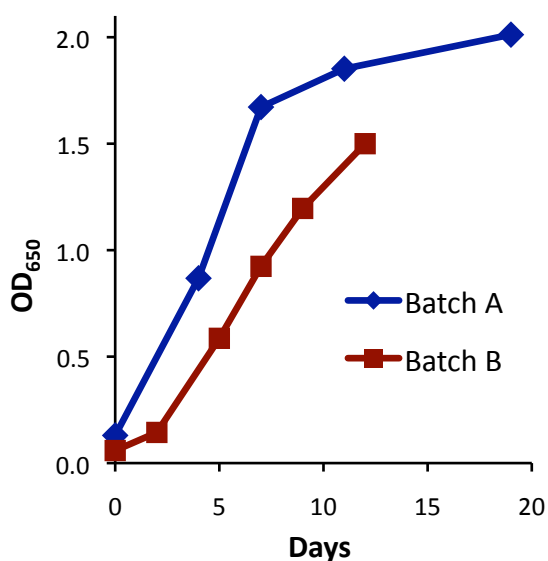


Figure 17: Batch A was inoculated with *Mtb* that had been subcultured twice in low-iron GAST; batch B was inoculated with *Mtb* that had been subcultured seven times in low-iron GAST.

2.2.4 Identification and Quantification of Siderophore Species

Following extraction of the siderophores from the *Mtb* cell pellet, eight HPLC elution peaks were initially identified as mycobactins based upon their absorbance and mass spectra. The overall yield of mycobactins and the relative abundance of each species were calculated based on the standard curve in Figure 12. These quantitative results are shown in Figure 18 and summarised in Table 7. The supernatant extract contained considerably more siderophores than the cell pellet extracts of either batch A or B.

The chromatographic data coupled with the mass spectrometry data allowed the structure of the mycobactin in each peak to be deduced based on previously reported findings (see Table 2); the structures are shown in Table 8. The M + H signal of the ferric compound ($M - 2H + Fe^{3+}$ relative to the desferri compound) that was observed via mass spectrometry matched the pattern reported by Gobin et al.⁴⁷ and the pattern that was observed for the FeMJ standard using the known structure of FeMJ⁵⁴.

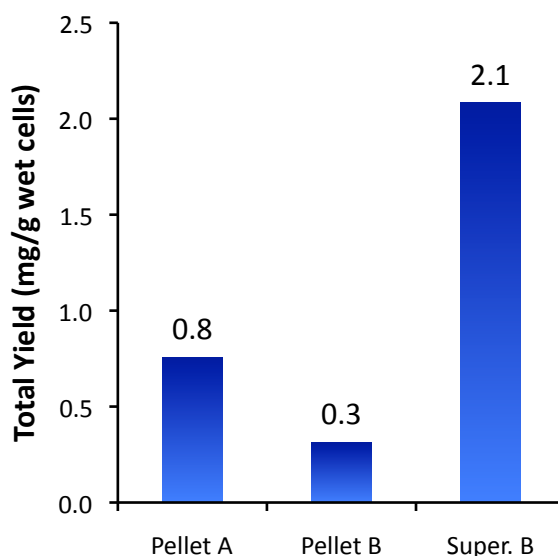
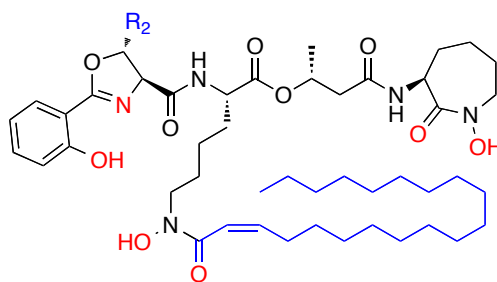


Figure 18: Mycobactin yield from culture extracts.

Table 7: Total mycobactin yields from extractions A and B.

Extraction	Yield/culture volume	Yield/g wet cells	Purity
Batch A pellet	3.4 mg/L	0.8 mg/g	4.9%
Batch B pellet	1.2 mg/L	0.3 mg/g	3.3%
Batch B supernatant	7.8 mg/L	2.1 mg/g	2.2%

Table 8: Detailed mycobactin yield information for each chromatographic peak; yields are given as percentage of total mycobactin detected. The general structure of mycobactin T is given for reference with the substituents of structural variation highlighted in blue and iron coordination ligands in red; a $\Delta 20$ fatty acyl moiety is shown for example.



Peak	Experimental m/z*	Carbons in Fatty Acyl Moiety**	R ₂	Pellet A	Pellet B	Supernatant B
1	827.5	$\Delta 18$	H	4.10%	1.90%	1.84%
2	829.6	18	H	2.54%	11.02%	10.89%
3	841.4	$\Delta 18$	CH ₃	8.23%	1.49%	1.71%
4	843.6	18	CH ₃	3.10%	2.76%	2.21%
5	855.6	$\Delta 20$	H	20.48%	13.78%	6.52%
6	857.5	20	H	10.95%	46.52%	47.95%
7	869.5	$\Delta 20$	CH ₃	38.43%	5.32%	11.89%
8	871.6	20	CH ₃	12.17%	15.17%	14.81%

*Represents exact mass of major isotope signal, $M + H^+$ of the ferric compound.

**Including the carbonyl carbon; Δ indicates an unsaturation in the fatty acyl moiety.

Comparison of the total mycobactin yield from the two batches shows that the batch A pellet (harvested at 19 days) had a higher yield per unit of wet cell mass than that of the batch B pellet (harvested at 12 days). Literature values indicate that yields up to 98 mg/g (dry cell mass) are achievable under conditions optimised for mycobactin production¹¹⁸. The difference between batch yields can be attributed to the fact that batch A had grown for a longer period of time and achieved stationary phase growth, while batch B was harvested earlier while still in logarithmic growth phase. This shows that mycobactins are able to accumulate over time and continue to build up as the organism remains in an iron-restricted state over a long period of time. This is further supported by a subsequent experiment in which two different cultures were grown under iron-depleted conditions. One was harvested and the mycobactins extracted after 15 days of growth, the other after 32 days of growth (both of which had reached stationary phase). Significant quantities of mycobactin were detected in the 32-day extract, but only traces were found in the 15-day extract (data not shown). These data also serve to indicate that *Mtb* continues to produce mycobactin even as it is exiting the logarithmic growth phase and beginning to enter stationary phase. This is perhaps due to consumption of all available internal iron stores coinciding with the inability to sustain further bacterial division within the culture.

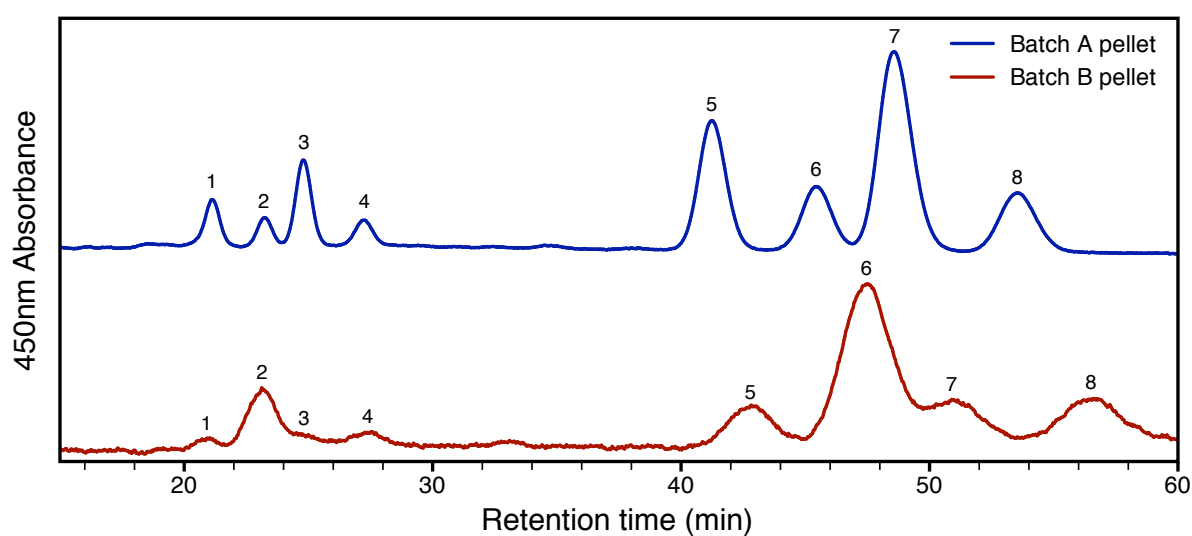
2.2.5 Abundance of Different Mycobactin Species

The chromatograms from cell pellet extracts of siderophore production batches A and B are compared in Figure 19A. The sequentially eluting peaks exhibit alternating absorbance spectra characteristic of unsaturated followed by saturated structures eluting shortly thereafter, similar to the results from FeMJ (see Figure 14 and Figure 15). The slight shift to later elution times for batch B can be explained by the aging of a heavily used column becoming slightly slower (the samples were analysed 38 days apart).

The same pattern of eight compounds is apparent in both batches, however their abundance ratios vary considerably (Figure 19B). The unsaturated mycobactins are dominant in batch A, whereas the saturated mycobactins were dominant in batch B. During mycobactin biosynthesis the acyl chain of mycobactin is dehydrogenated by the protein MbtN, which is part of the *mbt-2* mycobactin biosynthetic gene locus first characterised by Krithika et al.⁷⁴ (see Figure 5 for a complete overview of mycobactin

biosynthesis). Its activity was confirmed by preliminary studies of a recombinant version of the protein⁷⁴. Mycobactin most often carries its unsaturation in a *cis* conformation at the α - β position³². This is in contrast with the more typical activity of acyl-CoA dehydrogenases⁷⁴ and may indicate an unusual conformation created by the combination of MbtN and the acyl-carrier protein MbtL. It is possible that a *cis* bond at the α - β position, in close proximity to one of the iron-coordinating hydroxamates, allows for a slightly better complexation of iron either sterically or through acting to some extent as an electron donor.

A



B

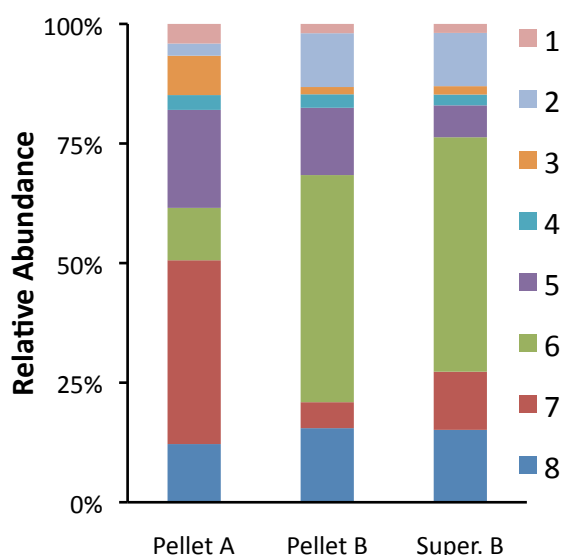


Figure 19A: Chromatogram of mycobactins comparing the pellet extracts from batches A and B using the ISOYJ70 HPLC method. B: Relative abundance of each species of detected mycobactin.

This would be difficult to test directly given that both compounds would possess extremely high affinities for ferric iron³³. However, it is supported by recent findings from a large lipidomic study that showed unsaturated monodeoxymycobactin was still able to bind iron to some degree, while saturated monodeoxymycobactin was only detected in its desferri form⁸⁴. Therefore the unsaturation would provide an advantage to the iron-chelation ability of mycobactin, but not a critical one.

As such, the process by which a particular mycobactin-bound acyl chain is dehydrogenated may be stochastic and governed by the relative turnover rates of MbtN and the 'competing' protein that performs the final acylation of mycobactin, MbtK. Kinetics have been reported for MbtK^{74, 82} but not MbtN. As a culture enters stationary phase, by definition the rate of division and many metabolic processes slow, which could lead to depleted levels of acylated MbtL within the cell. If it were assumed that the turnover rate of MbtK is higher than that of MbtN (to account for the general production of saturated mycobactins), such a scenario would result in a higher proportion of acyl-MbtL being dehydrogenated before attachment to the mycobactin core structure by MbtK. This could account for the greater ratio of unsaturated to saturated mycobactins extracted from batch A.

Another explanation could be that this ratio is influenced by the relative abundance of the fatty acids that are already available within the cell, which can include fatty acids that have already been dehydrogenated. Mechanistic studies of recombinant MbtK have revealed a clear preference for longer acyl chains, however only fatty acids up to 16 carbons were tested due to complications arising from micelle formation for longer chain lengths⁸². Unfortunately preference for α - β unsaturated fatty acids was not tested. Enzymatic promiscuity of MtbL and MbtK is likely advantageous to *Mtb*. The composition of this acyl moiety shows greater variability than are able to be bound by Lcn2¹²⁷ or antigen display protein CD1a^{58, 83, 126}, components of the human immune system that have evolved to recognise them. Binding of incomplete mycobactins and carboxymycobactins of relatively short acyl chain length has been observed with these proteins and variation in the acyl moiety would be an effective means to avoid recognition through these sterically constrained binding events. This points toward a strategy for avoiding immune recognition of one particular mycobactin structure in favour of presenting a variable and rotating series of compounds to the host immune system through enzymatic promiscuity. This is, of course, assuming that the bacterium is

not gaining an advantage in being recognised¹⁰. A late-stage culture may simply have more dehydrogenated fatty acids present due to degradatory processes⁷⁴, which are then opportunistically incorporated into mycobactin by MtbL and MbtK. An important note in regard to this is that the cultures grown in this study used only glycerol and alanine as their carbon source with no supplementation fatty acids such as oleic acid. Therefore all of the longer fatty acids that are present are the products of *Mtb* biosynthesis from these rudimentary building blocks. This underscores the idea that the observed change is due to differences in the growth phases of the culture. There is likely to be a much wider array of lipids available to the bacterium within the host environment, especially within foamy macrophages¹⁷⁹.

Similar ratios and patterns of mycobactins were found to be present in extracts from the cell pellet and the supernatant of batch B. The supernatant of batch A was not extracted because at the time of its growth it was not realized that the supernatant would yield such large quantities of mycobactin. These two extracts are compared in Figure 20. No carboxymycobactins were detected using this extraction technique. The extraction method was adapted from that employed by Gobin et al.⁴⁷, which was designed to extract carboxymycobactins as well as mycobactin and included an acidification step intended to protonate the free acids of carboxymycobactins and allow them to better partition into chloroform. Further experiments showed that carboxymycobactin partitioned into chloroform with greater efficiency than mycobactin even without this protonation step (see Figure 43).

The inability to detect carboxymycobactin is consistent with literature reports that lipophilic mycobactins are produced in much greater quantities than carboxymycobactins, which comprise only 0.2-3.1 percent of total mycobactin production by mass¹¹⁹. This means that carboxymycobactin levels in the *in vitro* cultures would have been below the limit of detection of the instruments used.

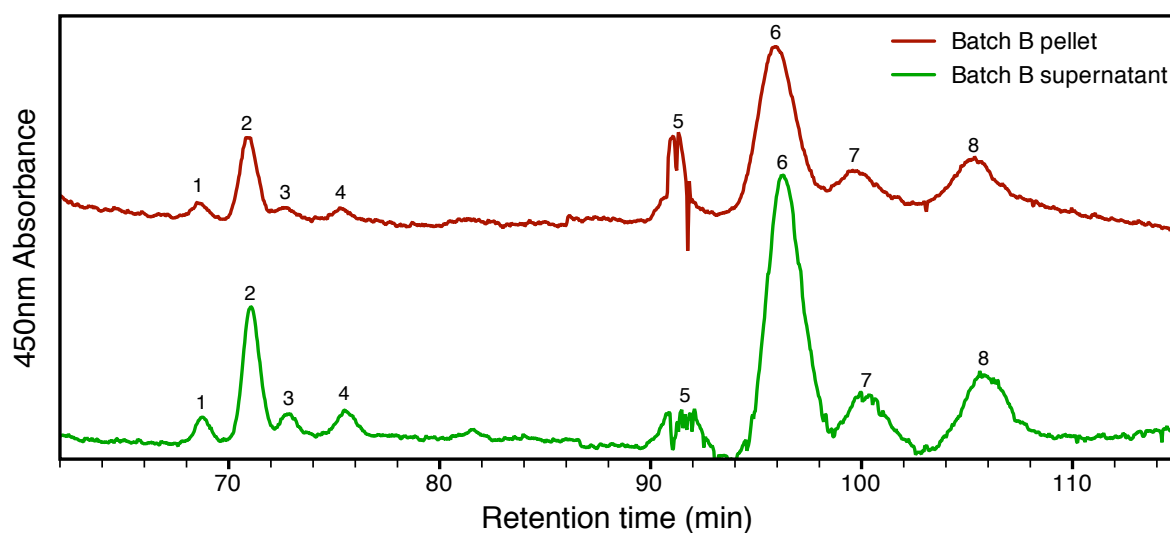


Figure 20: Chromatogram of mycobactins comparing the pellet and supernatant of extract B using the MYCEX HPLC method.

2.3 Conclusion

2.3.1 The Role of Mycobactin in *Mtb* Pathogenesis

This study found substantial production and secretion of lipophilic mycobactins under the given experimental conditions. Carboxymycobactin was not detected in either the cell pellet extract or the culture filtrate. Such a high lipophilic mycobactin to carboxymycobactin production ratio challenges the model of carboxymycobactin-mediated iron trafficking set forth in Section 1.2.3.1 and instead supports a model in which lipophilic mycobactin acts as the primary extracellular siderophore.

Further supporting this new model, Luo et al. recently showed that the lipophilic mycobactins were able to diffuse freely in and around macrophages when added exogenously, and that gallium-loaded mycobactins were found preferentially in lipid bodies in direct contact with phagosomes¹⁸⁶. Interestingly, other studies have shown that the oxygenated mycolic acids produced by *Mtb* and *M. avium* induce the formation of ‘foamy’ macrophages that are filled with many lipid bodies. *Mtb* living within the phagosomes of foamy macrophages colocalise with, and subsequently engulf these lipid bodies¹⁷⁹. Not only does this provide the bacteria with a lipid-rich environment in which to persist¹⁷⁹, but it may represent a new route for trafficking iron that involves subverting host lipid bodies to serve as reservoirs of nutrients and ferrimycobactins, a veritable smörgåsbord on which to grow fat and lazy¹⁸⁷.

These findings also complement research discussed earlier in Section 1.2.1 on the formation of marinobactin micelles^{42, 70} and the finding that mycobacterial lipids in *Mtb*- and *M. avium*-infected macrophages are capable of trafficking out of the mycobacterial vacuole⁸. The new model for mycobacterial iron acquisition begins to emerge, in which lipophilic mycobactins act as extracellular siderophores, and iron is trafficked through intracellular lipid bodies back to phagosomes infected by *Mtb*¹⁸⁸. It should be noted that in contrast to the findings reported here, in the absence of Tween lipophilic mycobactin is more likely to stay associated with the cell wall¹¹⁶. However, the lipid-rich environment of the foamy macrophage likely lends greater mobility to the lipophilic mycobactins than does the aqueous environment of liquid culture media.

Figure 21 depicts a model of mycobactin-mediated iron acquisition within macrophages that takes advantage of lipid body trafficking¹⁸⁶. This can be contrasted with the classical model for mycobacterial iron acquisition, depicted in Figure 6. Mycobactins leave the bacterium either by trafficking out of the phagosome with other mycobacterial lipids⁸ or by forming micelles⁷⁰. It might be necessary for mycobactins to use a specific mechanism that has yet to be discovered in order to cross the thick cell wall. The micelles diffuse throughout the macrophage and bind iron from the macrophage iron pool, including iron plundered from ferritin and imported transferrin¹⁰⁰. Ferric mycobactins then traffic preferentially to macrophage lipid bodies¹⁸⁶ that are engulfed by infected phagosomes¹⁷⁹. The ferric mycobactins translocate through the cell wall once again and may exchange iron with carboxymycobactin on an equilibration basis¹⁰⁰. This iron can then be imported through the IrtAB system. Alternatively, the mycobactins may diffuse across the membrane or handoff their iron payload to other mycobactins within the cell membrane. Because membrane affinity is modulated by the length and degree of unsaturation of the alkyl chain⁷⁰, these recipient mycobactins in the membrane could form a gradient of mycobactins with differential membrane affinities. In this way they could assemble a 'bucket brigade' to transport the iron into the bacterium¹⁸⁹.

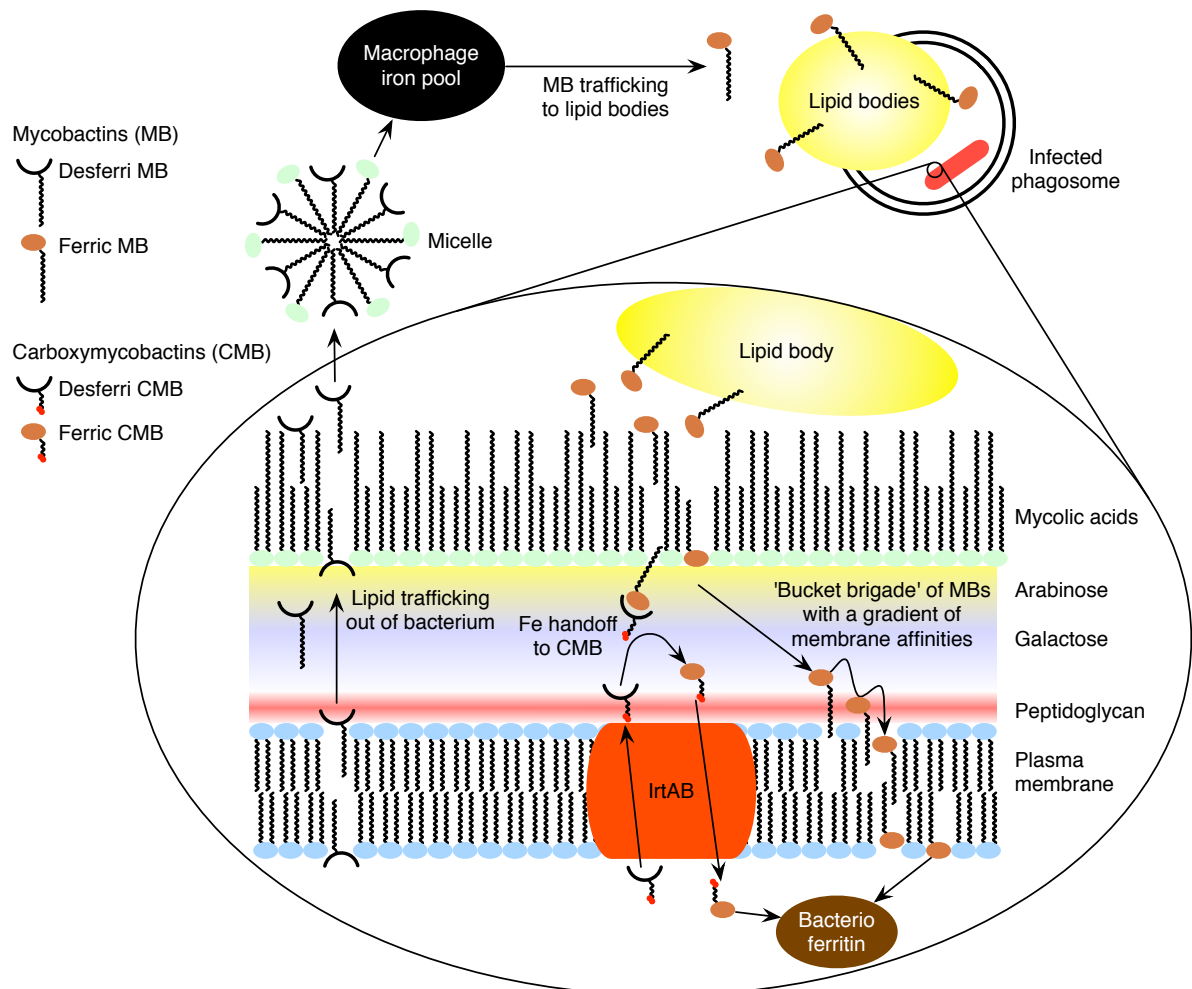


Figure 21: New model of mycobacterial iron acquisition; not drawn to scale.

The lipid-rich environment within a foamy macrophage is more conducive to diffusion of lipophilic mycobactins. Mycobacteria residing outside of such a lipid-rich environment may require a more aqueous-friendly method of iron acquisition. It can be hypothesised that lipophilic mycobactin is the principal iron scavenger within the lipid-rich environment of the macrophage, while carboxymycobactin serves as the principal scavenger for bacteria living in the relatively aqueous extracellular milieu. The reality is likely to be a hybrid of these mechanisms, adapted by the bacterium to its particular condition and environment. Many components of this model are still speculative; it does not account for normal secretion of carboxymycobactins in the IrtAB deletion mutant¹²², nor for the translocation of mycobactin across the formidable mycobacterial cell wall. Likewise, further elucidation of the role of *esx-3* will require future research. The trafficking of mycobactins, carboxymycobactins, and iron within mycobacteria will likely prove to be a much more complex system pending the discovery of other siderophore transport mechanisms.

2.3.2 Species of Mycobactins Produced

Eight specific mycobactin structures were identified in *Mtb* culture extracts (Table 8). These structures corroborate well with the structures detected in other studies⁸⁴. There are three points of variation between the structures:

1. Length of the fatty acid component: here the inclusion of stearic acid and arachidic acid have been detected, although other studies have also reported smaller quantities of palmitic acid incorporation⁸⁴.
2. The presence or absence of an unsaturation in the fatty acid component: saturated acyl chains were dominant in logarithmically growing culture, while unsaturated acyl chains were dominant in stationary phase culture.
3. The inclusion of either serine or threonine (or potentially α -methyl serine, as discussed in Section 1.2.2, see Figure 5 for details of the biosynthesis) in the oxazoline ring: the results presented here indicate either component is incorporated indiscriminately.

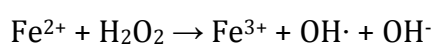
The length of the fatty acyl chain and the addition of a methyl group may affect the biodistribution of the different species of mycobactin as depicted in Figure 21 however it is unlikely to effect the metal coordination in any way. It is difficult to predict whether this differentiation in hydrophobicity would have a major influence on which mycobactin species being more likely to be found in the blood or preferentially distributed in other bodily fluids of a TB patient. If the unsaturation does affect the affinity of mycobactin for iron, then this could potentially affect the reduction potential of the complex, as will be discussed further in Chapter 3. However, this will once again be difficult to test experimentally in that it is very difficult to obtain usable quantities of sufficiently purified FeMT, especially without contamination from other, closely eluting structures.

2.3.3 Physiological Range of Mycobactin Production

These studies have shown that lipophilic mycobactins can be produced in the filtrate of liquid cultures at concentrations up to 7.8 mg/L or 8.6 μ M. Any mycobactins available to a prospective biosensor would likely be equivalent to quantities recovered

from the supernatant (Section 2.2.4) rather than the cell pellet. Bearing this in mind, the supernatant extract B yield of 2.1 mg/g cells can be taken as a conservative value to use in the calculation of mycobactin production in the iron-restricted, lipid-rich host environment. Assuming a rod shape, the average volume of a bacterium is calculated to be $3.46 \times 10^{-19} \text{ m}^3$ ⁽¹⁹⁰⁾, which gives a mass of $3.71 \times 10^{-13} \text{ g}$ per cell assuming an average density of 1.08 g/cm^3 ⁽¹⁹¹⁾. Mycobactin production per bacterium is therefore $7.80 \times 10^{-16} \text{ g}$, or $8.64 \times 10^{-19} \text{ mol}$ using the averaged molecular weight of the mycobactin compounds extracted from *Mtb* culture (902 g/mol). Information on the number of bacteria that might be found in infected lung tissue is difficult to obtain, however a good estimation for bacteria within the granuloma of an early-stage primate infection is 10^6 colony-forming units (CFU)/g⁽¹⁹²⁾. This yields an estimated mycobactin concentration of 864 pM within the granuloma. If the highest reported production level of mycobactin (98 mg/g dry cell mass¹¹⁸) is used, and adjusting for an estimated mycobacterial water content of 83 percent¹⁹³, the estimated mycobactin concentration rises to circa 250 nM.

It should be noted that these *in vitro* estimations are limited in their ability to simulate the complexity of the host environment that *Mtb* inhabits *in vivo*. Add to that the complexity of the many different microenvironments that define specific regions of the lung and granuloma and at different stages within the spectrum of infection⁵. For example *Mtb* organisms in close proximity to neutrophils, as they are within caseous granulomas⁵, may have more exposure to siderophore-sequestering Lcn2, thus necessitating increased production of siderophores. Varying levels of hypoxia are also likely to effect siderophore production as it is intimately linked with the iron trafficking pathway⁸⁸. The expression of mycobactin biosynthesis genes is downregulated under conditions of oxidative stress to the organism. This is due the risk that excess iron poses under oxidative conditions in which highly reactive hydroxyl radicals are produced through the Fenton reaction¹⁹⁴:



The Fenton reaction

thus more siderophores may be produced under hypoxic conditions, such as within some, if not all, granulomas^{5, 195}.

2.3.4 Implications for Development of an Assay for Mycobactin

These results affirm the production of mycobactin and thus form the basis for development of a simple mycobactin assay with the potential to serve as a measure of *Mtb* infection within the lung. Such an assay should have sensitivity in the range of 0.85-250 nM in order to enable detection mycobactin at the physiological levels of production projected from this *in vitro* study. This would of course have to be adjusted depending on the still-unknown biodistribution profile of mycobactin and whether the compound may be widely distributed within the body or whether it might become concentrated in specific bodily fluids that would be conducive to sampling. Given the evidence that lipophilic mycobactin is more prevalent than carboxymycobactin, the assay and any optimisation or accompanying sample processing techniques must have the ability to handle this lipidic analyte. This could present challenges, but also opportunities for ways to tailor sample preparation through established organic extraction techniques and the specificity of the assay by taking advantage of the unique molecular properties of mycobactin.

3 A Simple Electrochemical Assay for Mycobactin

One example of a very successful assay for medical purposes is the electrochemical glucose oxidase-based blood glucose meter¹⁹⁶. This type of sensor is currently in use for monitoring and control of diabetes symptoms worldwide, including deployment in impoverished and developing markets similar to those most afflicted by TB. This technology offers a suitable low-cost sensing platform for point-of-care TB diagnostic applications. Thus, the goal of this chapter is to explore the electrochemical properties of mycobactin and determine whether an assay based on electrochemical interrogation of the iron coordination complex can be created that is adaptable for use in a plurality of sampling media. In particular, electrochemical sensing appears well suited for measurement of mycobactin because of the following factors:

1. Ferric mycobactin contains one ferric iron atom, which may be interrogated via electrochemical redox processes to yield information about the complex.
2. The unique chelation chemistry of different siderophores shifts the ferric/ferrous redox couple to a potential that is specific to that particular siderophore complex¹⁹⁷, thus allowing assay specificity.
3. Reduction of ferric to ferrous mycobactin greatly decreases the affinity of the siderophore for the iron, which may also be exploited to gain information about the complex. There is speculation that this is how the bacterium frees the iron from mycobactin for its own use by means of a putative reductase¹²⁰.

Ferric mycobactin J (FeMJ) was chosen as the model mycobactin for these experiments due to its ready availability in a relatively pure form and similarity to mycobactin T in its core structure and iron-coordination ligands (see Table 2).

3.1 Methods

3.1.1 Instrumentation

Cyclic voltammetry and potentiostatic measurements were performed on a Princeton Applied Research 263A potentiostat and a PC running CorrWare software. For high-speed cyclic voltammetry a Solartron 1286 potentiostat was used in analogue mode to drive the potential, while a PicoScope 4224 was used for data acquisition. A custom Matlab program was written to process the high-speed cyclic voltammetry data, which can be found in Appendix 1.

A 3 mm diameter glassy carbon electrode (GCE) was purchased from Bioanalytical Systems, Inc. (BASi) The electrode surface was prepared by polishing successively with 1.0 μm and 0.05 μm alumina powder using MicroCloth polishing cloths (Buehler) affixed to a glass base. A 1.6 mm diameter gold electrode (AuE) was also used for one experiment. An Ag/AgCl matrix pellet electrode was used as a reference electrode in aqueous media, while a silver wire Ag/Ag⁺ pseudo reference electrode was created for non-aqueous electrochemistry. A coiled platinum wire was used as a counter electrode.

3.1.2 Electrode Pretreatment

For all electrochemical experiments alumina residue was removed by oxidative cleaning at 0.8 V vs. Ag/AgCl in aqueous 1 M sodium hydroxide and 1 M potassium chloride using the method of Kiema et al.¹⁹⁸ This is a procedure seeks to firstly remove the layer of aluminium oxide residue left over from the electrode polishing process and secondly creating a chemically reproducible surface by oxidising off a layer of carbon. This is done with a minimal increase in glassy carbon surface oxidation, increasing the X-ray photoelectron spectroscopy (XPS) band area attributable to oxygen species on the surface from approximately 9 percent to 13 percent¹⁹⁸.

3.1.3 Electrochemical Techniques

3.1.3.1 Cyclic Voltammetry

Aqueous electrochemistry was carried out in a 1:1 water:ethanol solution containing 0.1 M potassium chloride. FeMJ was dissolved in this solution at a stock concentration and diluted with the same solvent when necessary. Nonaqueous electrochemistry was performed in dimethyl sulfoxide (DMSO) containing 0.1 M lithium chloride supporting electrolyte except for square-wave voltammetry, which was done using 0.5 M lithium chloride. Oxygen was removed from the electrochemical cell by bubbling nitrogen gas for at least 10 min and maintaining a unidirectional gas-flow environment; longer times were required to adequately deoxygenate desferri mycobactin solutions.

Care had to be taken to deoxygenate the solution thoroughly in order to avoid the oxygen reduction wave in the potential window of interest. This was accomplished by bubbling nitrogen gas through the electrochemical cell for at least 10 min.

3.1.3.2 Amperometric Titration

A GC working electrode was maintained at -0.6 V versus Ag/Ag⁺. A magnetic stirrer was placed in the bottom of the electrochemical cell and FeMJ was titrated into the cell with stirring. After each addition of FeMJ, stirring was stopped and the solution was allowed to settle.

3.1.4 Deferration and Referration of Mycobactin

Because of its extremely high affinity for iron ($k_a \approx 4 \times 10^{26} \text{ M}^{-1}$)⁴³, mycobactin is almost always encountered in its ferric form. This is attributable to the fact that during isolation, synthesis, or purification it is difficult to maintain an environment so completely free from trace iron that mycobactin will not acquire any. The commercially available mycobactin J is obtained in its ferric form. Thus, to investigate the properties of desferri mycobactin the iron had to be removed. The iron removal was done as a simplified technique first pioneered by Snow⁹¹. Under low-pH conditions the hydroxamic acid and phenolic ligands of mycobactin are protonated, allowing the

chelated ferric ion to escape. Figure 22 shows presumptive pK_a values for the iron-chelating ligands of mycobactin.

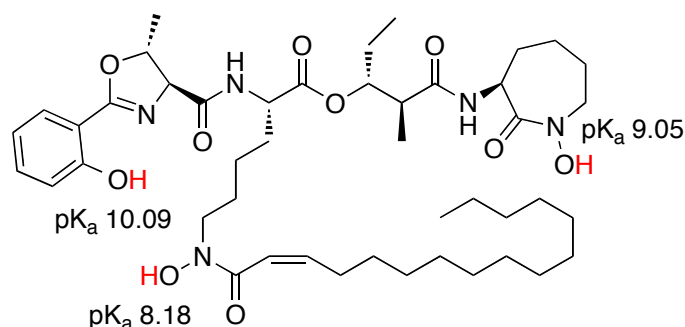


Figure 22: Mycobactin J shown with pK_a values for its iron-chelating ligands based upon measurements of a similarly-structured water-soluble analogue¹⁹⁹.

Deferration of FeMJ was accomplished by dissolving 2 mg of mycobactin in 10 mL of chloroform and shaking with 10 mL of 5 M hydrochloric acid. The aqueous phase was extracted twice more with 10 mL of chloroform and the organic phases were combined and the solvent was removed under vacuum to give desferri mycobactin J (DFMJ).

Ferric chloride was used for referration of DFMJ in spectrophotometric experiments due to its low absorbance at 450 nm, whereas ferric acetylacetonate ($Fe(acac)_3$) was used in electrochemical experiments in order to maintain a more stable pH, which is strongly influenced by the addition of ferric chloride.

The absorbance spectrum of DFMJ matched that published by Snow for desferri mycobactin T with its characteristic double peak at 240-250 nm⁹¹ (Figure 23). Spectrophotometric titration of ferric chloride was used to quantify the yield for the procedure. With the addition of ferric chloride the absorbance spectrum shown in Figure 23 changed from that characteristic of DFMJ to FeMJ in accordance with spectra previously reported in the literature³². Based on a stoichiometric binding of one ferric ion per molecule of mycobactin⁹¹, it was possible to determine the concentration of mycobactin in solution. As shown in Figure 23, the peak at 450 nm becomes saturated at 40 μ M ferric chloride, and further addition of ferric chloride only elevates the region in which ferric chloride itself absorbs. Thus, the concentration of DFMJ was determined to be 40 μ M.

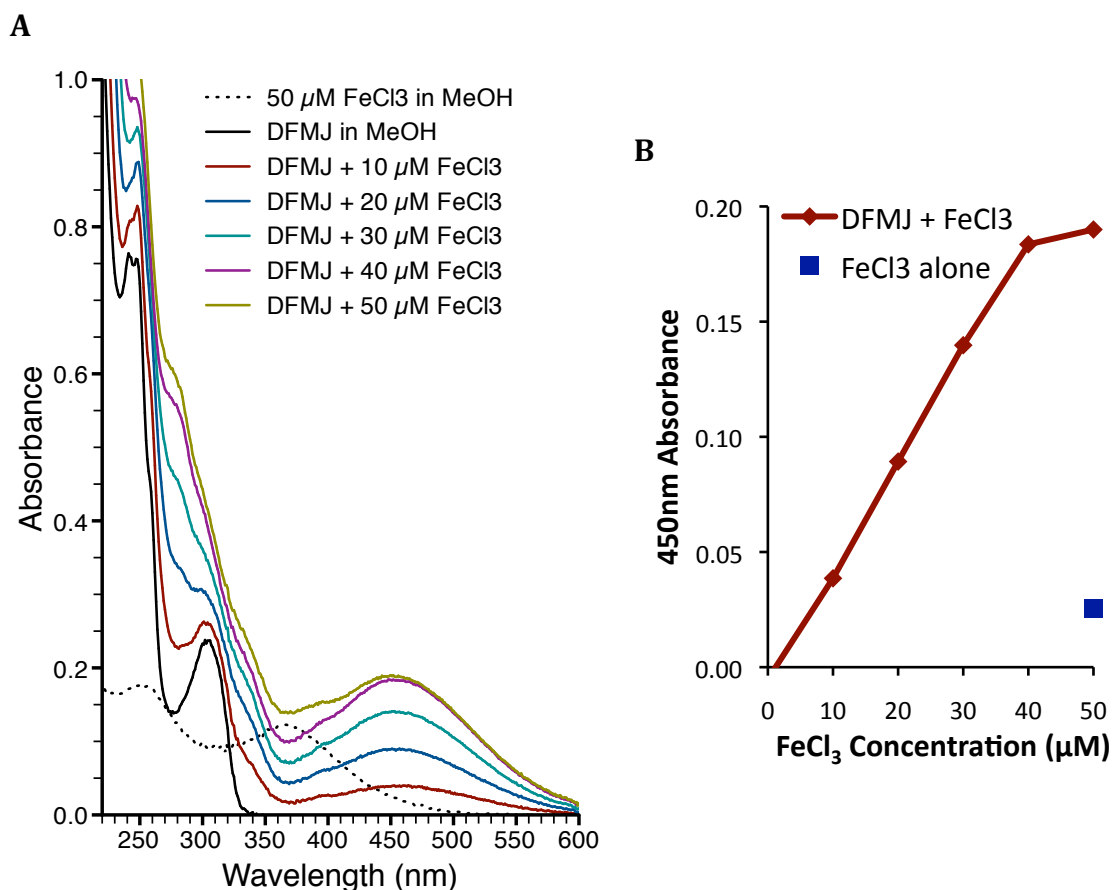


Figure 23A: Spectrophotometric titration for ferric chloride into deferrated MJ (DFMJ) in methanol. B: Plot of 450 nm absorbance versus ferric chloride concentration for both addition of ferric chloride to DFMJ and ferric chloride alone.

3.2 Results and Discussion

3.2.1 Cyclic Voltammetry of Mycobactin

3.2.1.1 Aqueous Cyclic Voltammetry

Cyclic voltammograms (CVs) of FeMJ showed a distinctive redox couple for the ferric complex centred at -0.600 V versus Ag/AgCl as shown in Figure 24. Since CVs of desferri mycobactin J (DFMJ) show no peaks, it can be deduced that this couple corresponds to the redox activity associated with the chelated iron bound by FeMJ rather than structural components of the siderophore itself. The clearly discernible oxidation peak is in contrast to recent reports of FeMJ exhibiting irreversible electrochemistry in 95 percent ethanol with a cathodic peak at -0.856 V versus the standard hydrogen electrode (equivalent to -1.144 V versus Ag/AgCl)²⁰⁰. The CVs shown by Miller et al. in this report were done at much more negative potentials and could

correspond to a further reduction of the mycobactin complex that does not correspond to the $\text{Fe}^{3+}/\text{Fe}^{2+}$ couple observed here. However, as shown in Figure 24, CVs down to -1.25 V versus Ag/AgCl failed to produce an additional cathodic peak. However, since Miller's experiments were performed in 95% ethanol with NaClO_4 , the protonation equilibria will be different. This can have a significant effect on the reduction potential, as discussed below.

In order to discover whether the redox couple could be restored to DFMJ by referration to form the ferric complex, ferric iron was titrated into the electrochemical solution. The addition of ferric chloride to DFMJ under unbuffered aqueous conditions led to a significant drop in pH and subsequent loss of reversibility as indicated both by an increase in redox peak separation and a decrease in the ratio of the anodic peak current to the cathodic peak current (i_{pa}/i_{pc}) (data not shown). When the solution was buffered using phosphate buffered saline (PBS) at pH 7.4, DFMJ was successfully referrated to recover the characteristic redox couple as shown in Figure 25. Note that in this instance the DFMJ CV shows a residual peak due to incomplete deferration, however the amplitude of this peak is increased significantly upon addition of ferric chloride.

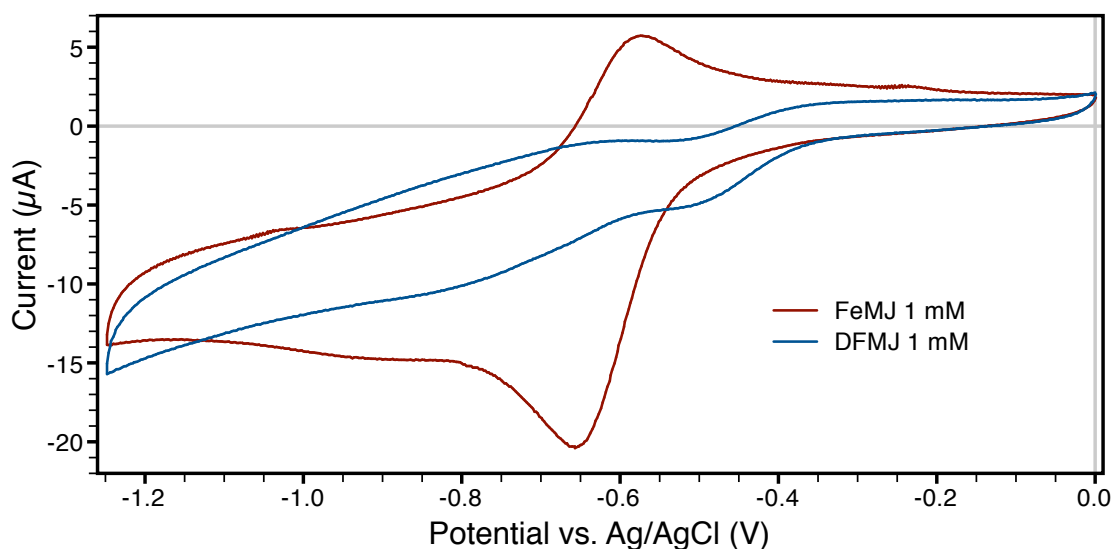


Figure 24: Cyclic voltammograms of FeMJ and DFMJ in 50 percent ethanol, 0.1 M potassium chloride, 0.2 V/s scan rate.

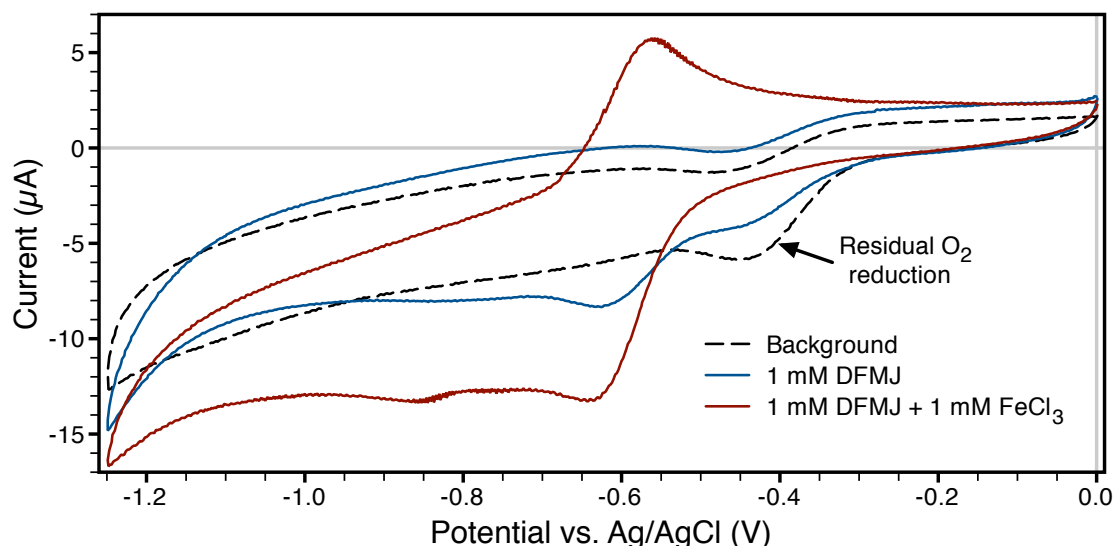


Figure 25: Cyclic voltammograms of DFMJ and referrated DFMJ in PBS buffered 50 percent ethanol, 0.1 M potassium chloride, 0.2 V/s scan rate.

A rearrangement of the Nernst equation, as shown by Harrington et al.¹⁹⁹, provides the relationship between the reduction potential of the siderophore complex and of ratio of formation constants between the two oxidation states of iron:

$$E_{complex}^0 - E_{aq} = -59.16mV \log\left(\frac{\beta^{III}}{\beta^{II}}\right) \quad \text{Equation 1}$$

where $E_{complex}^0$ is the standard potential for reduction of the complex, E_{aq} is standard potential for reduction of Fe^{3+} in solution, and β^{III} and β^{II} are the formation constants for the complex with Fe^{3+} and Fe^{2+} respectively. Using the redox midpoint from the aqueous experiment (Figure 24), this yields a β^{III}/β^{II} ratio of 1.9×10^{18} . This signifies a difference in the affinity of mycobactin for the different oxidation states of iron, preferring Fe^{3+} to Fe^{2+} by 18 orders of magnitude. This finding is in agreement with previously published estimations for a water-soluble analogue of mycobactin¹⁹⁹.

The underlying mechanism behind this difference in affinity is due not only to the resulting coordination mismatch within the structurally-constrained hexadentate siderophore but also because the ‘hard’ Lewis acid Fe^{3+} has a preference for hard electron donor groups (e.g. the oxygen-containing anionic ligands found in hydroxamic acids). It is typical for this to result in Fe^{3+} equilibrium constants that differ from those of the ‘soft’ Lewis acid Fe^{2+} by 13 orders of magnitude, as measured for other hydroxamate siderophores^{201, 202}.

Cyclic voltammetry of FeMJ was also tested using a gold electrode (AuE) with similar results. A comparison of CVs of FeMJ using Au and GC working electrodes is given in Figure 26. The residual oxygen reduction peak was more pronounced on gold, merging with the reduction peak of the FeMJ complex. Notwithstanding this confounding factor, i_{pa}/i_{pc} was increased slightly using AuE in contrast to GCE.

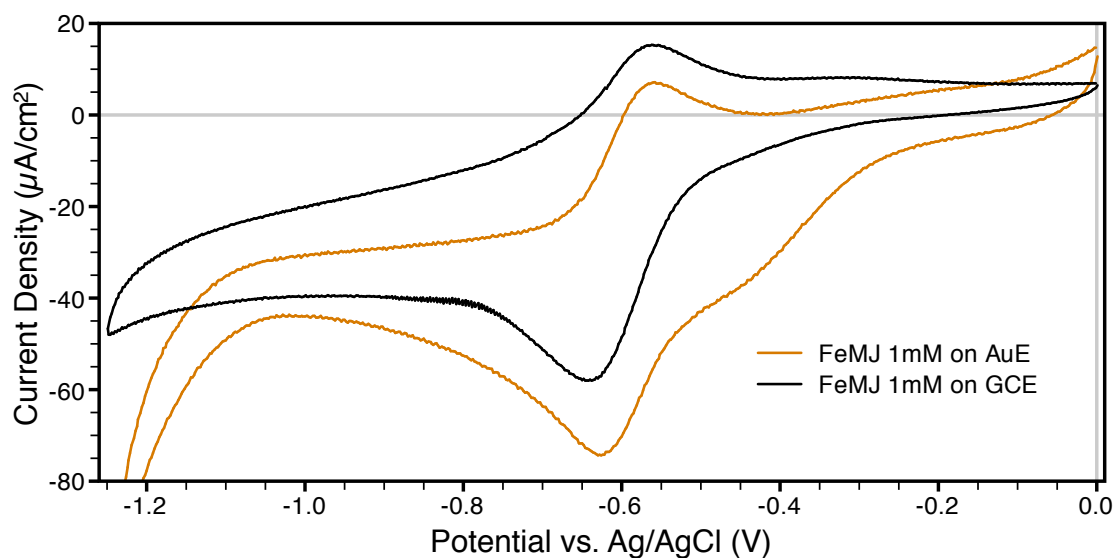


Figure 26: Cyclic voltammograms of FeMJ on either AuE or GCE in 50 percent ethanol, 0.1 M potassium chloride, 0.2 V/s scan rate.

3.2.1.2 Nonaqueous Cyclic Voltammetry

The solubility of the mycobactins is a limitation in the study of their electrochemistry. The relatively hydrophobic nature of mycobactin lends itself to solvation in organic solvents. Furthermore, it may be desirable to utilise this property of mycobactin for pre-analysis sample processing, which may include elution of mycobactin into the test cell by an organic solvent, as discussed in Chapter 2. In this context, DMSO was chosen for its useful electrochemical window, universal solvation properties, and low volatility, which allowed facile deoxygenation of the solvent by bubbling nitrogen gas through the cell. Under this nonaqueous solvent system, more detailed and quantitative information was gained about the redox couple attributed to the FeMJ complex.

Under this nonaqueous solvent system typical CVs of FeMJ (Figure 27A) show a redox couple assigned to Fe^{3+}/Fe^{2+} with midpoint -0.409 V versus Ag/Ag^+ (at 25 mV/s, 0.64 mM). The effective elimination of interfering oxygen reduction allowed for a

subtraction of the background current to be performed and superior quantitative information to be measured regarding the peaks attributable to the $\text{Fe}^{3+}/\text{Fe}^{2+}$ couple (Figure 27B). The quasi-reversible behaviour exhibited by this couple is consistent with both slow electron transfer and a coupled chemical reaction that limits the chemical reversibility of the couple.

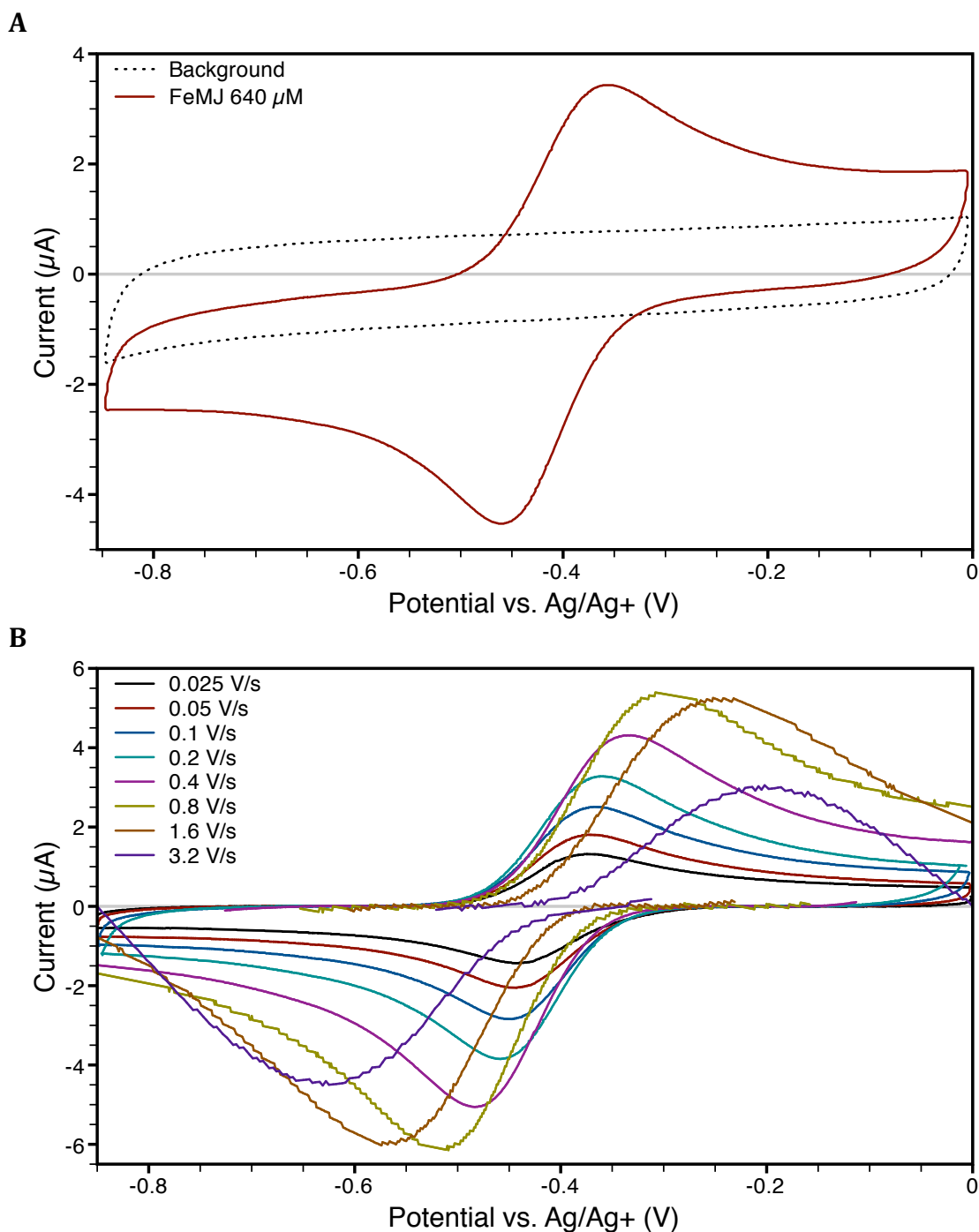


Figure 27A: Cyclic voltammogram of FeMJ (640 μM); 0.2 V/s in DMSO with 0.1 M LiCl. **B:** Background-corrected CVs of FeMJ at varying scan rates showing oxidation and reduction peaks.

3.2.1.2.1 Coupled Chemical Reaction After Reduction to Ferrous Mycobactin

For a simple electron transfer that is limited by diffusion, $i_p/v^{1/2}$ is independent of scan rate (v), as given by a rearrangement of the Randles-Sevcik equation^{203, 204}:

$$\frac{i_p}{\sqrt{v}} = 0.4463 nFAC\sqrt{\frac{nFD}{RT}} \quad \text{Equation 2}$$

where n is the number of electrons transferred, F is the Faraday constant, D is the diffusion coefficient, R is the universal gas constant, and T is the absolute temperature. However, diagnostic plots of $i_p/v^{1/2}$ versus $v^{1/2}$ decreased with scan rate (Figure 28) with a slope that increased with FeMJ concentration. This points toward a more complex process characterised by a coupled electrochemical-chemical pathway.

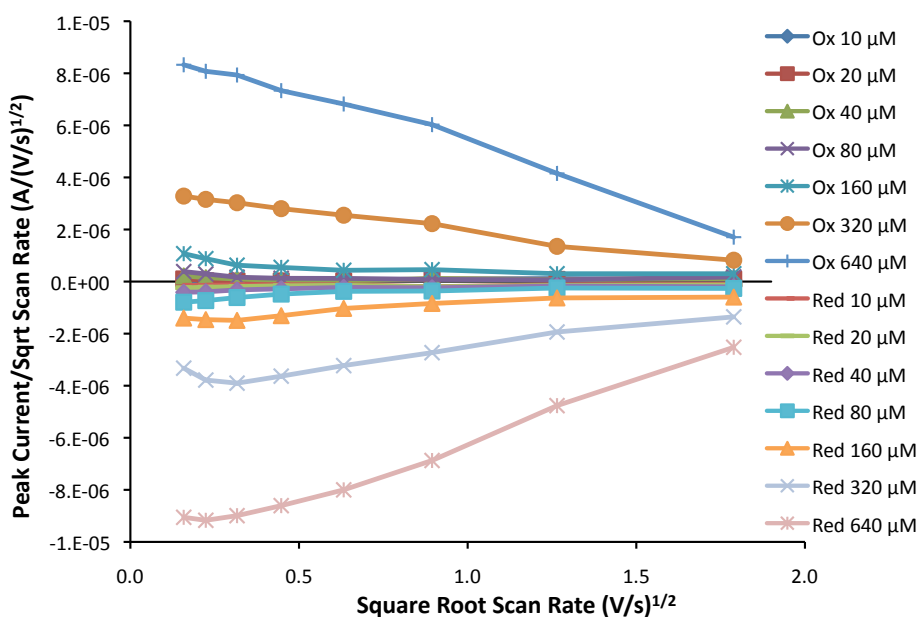


Figure 28: Plot of $i_p/v^{1/2}$ versus $v^{1/2}$ shown for both the reduction and oxidation peaks of FeMJ.

The anodic (oxidation) peak is typically small compared with the cathodic (reduction) peak, with i_{pa}/i_{pc} less than 1 for all scan rates and concentrations, as shown in Table 9 and Figure 29. This is also consistent with the presence of a competing chemical reaction following reduction. For FeMJ this could be due to the partial or complete dissociation of reduced Fe^{2+} from the MJ complex (k_2 in Scheme 1).

Table 9: FeMJ i_a/i_c ratios on GCE in DMSO with 0.1 M LiCl.

FeMJ Concentration	Scan Rate (V/s)							
	0.025	0.05	0.1	0.2	0.4	0.8	1.6	3.2
10 μM	0.25	0.23	0.17	0.33	0.30	0.46	0.94	0.73
20 μM	0.42	0.14	0.10	0.15	0.14	0.50	0.57	0.70
40 μM	0.53	0.38	0.31	0.14	0.11	0.49	0.42	0.59
80 μM	0.48	0.40	0.27	0.26	0.32	0.23	0.27	0.66
160 μM	0.76	0.60	0.42	0.41	0.42	0.54	0.48	0.50
320 μM	0.99	0.83	0.78	0.77	0.79	0.82	0.70	0.61
640 μM	0.92	0.88	0.88	0.85	0.85	0.88	0.87	0.68

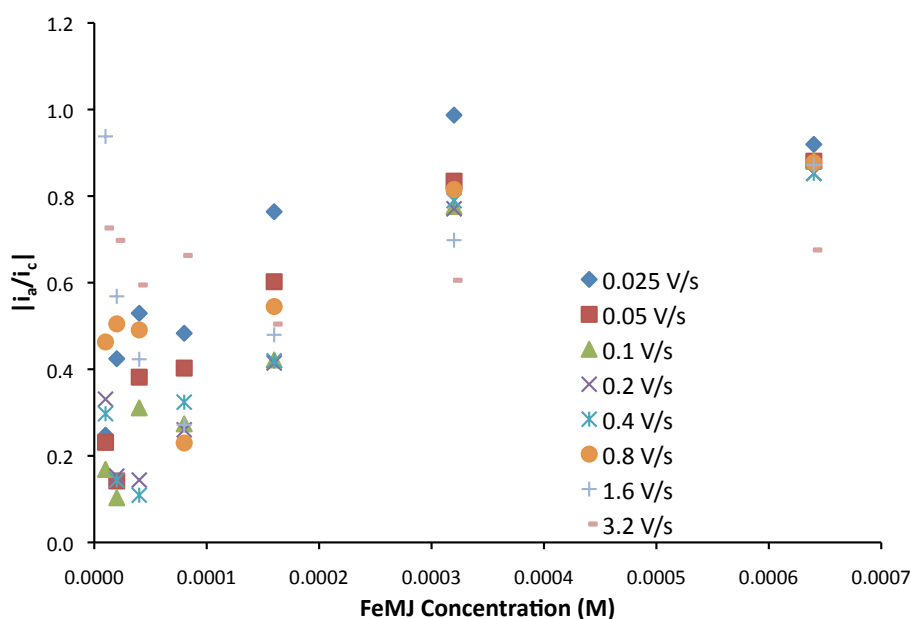
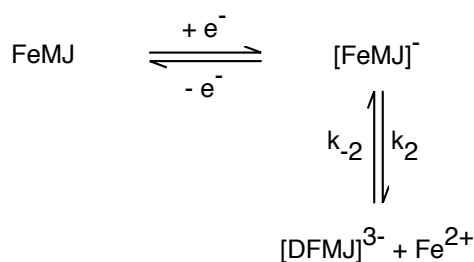


Figure 29: FeMJ i_a/i_c ratios on GCE in DMSO with 0.1 M LiCl.



Scheme 1

Consistent with this, i_{pa}/i_{pc} increases from ~ 0.3 to ~ 0.8 with increasing scan rate at low FeMJ concentrations. At high scan rates the oxidation competes with the rate of the dissociation and the oxidation peak is recovered. For a given scan rate, i_{pa}/i_{pc} mostly increases with concentration, suggesting that Fe^{2+} dissociation is influenced by the overall concentration of siderophore, which could suggest intermolecular exchange of Fe^{2+} .

However, at high concentrations of FeMJ (greater than 150 μM) $i_{\text{pa}}/i_{\text{pc}}$ appeared to decrease (from ~ 0.9 to ~ 0.8), or remain constant with increasing scan rate (see CVs in Figure 27B). This also supports a scheme whereby Fe^{2+} dissociation competes with the electrochemical oxidation of FeMJ. Upon addition of exogenous Fe^{3+} in the form of $\text{Fe}(\text{acac})_3$, $i_{\text{pa}}/i_{\text{pc}}$ continues to increase to near unity for low scan rates, possibly due to high Fe^{2+} concentrations near the electrode (from exogenous Fe^{3+} being reduced at a potential cathodic of the $\text{Fe}(\text{acac})_3$ redox potential) driving the k_2/k_{-2} equilibrium away from dissociation.

3.2.1.2.2 Referration of DFMJ in Nonaqueous Solvent

CVs of DFMJ in nonaqueous solvent lacked the peaks characteristic of FeMJ but these peaks returned upon titration with $\text{Fe}(\text{acac})_3$, as shown in Figure 30. The 1:1 iron-binding ratio of DFMJ to Fe^{3+} is evident and in the presence of excess $\text{Fe}(\text{acac})_3$, with the reduction peak of this compound appearing at -0.28 V versus Ag/Ag^+ . This also creates a background current due to $\text{Fe}(\text{acac})_3$ reduction, resulting in excess Fe^{2+} near the electrode surface and pushing the k_2/k_{-2} equilibrium toward stability of the Fe^{2+} complex, as discussed above. In accordance with this, reversibility appears to increase with increasing Fe^{3+} :DFMJ ratio as well as with increasing overall siderophore concentration, suggesting that higher concentrations of the ferric complex inhibit Fe^{2+} dissociation.

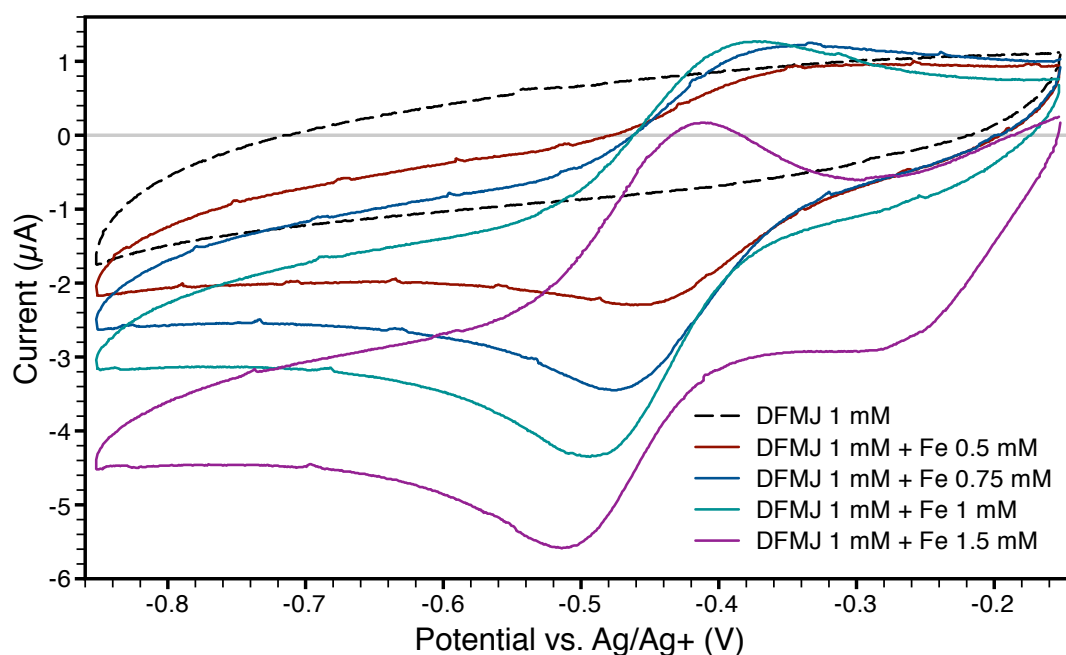


Figure 30: Referration of DFMJ by titration with $\text{Fe}(\text{acac})_3$ at 0.2 V/s in DMSO, 0.1 M LiCl.

The chelated ferric iron in Fe(acac)₃ and FeMJ, exhibit distinctly different reduction potentials. This is due to the greater stabilisation effect of the high-affinity iron-chelating ligand of mycobactin, which shifts the reduction potential in the negative direction¹⁹⁷, requiring more energy to achieve reduction than the relatively unstable Fe(acac)₃ iron ion. CVs of Fe(acac)₃ alone are shown in Figure 31 for reference.

These data allow us to expand upon Scheme 1 to include the initial ferration of DFMJ as given in Scheme 2 below. The depiction of Fe(acac)₃ in Scheme 2 is an oversimplification, as the relatively labile complex²⁰⁵ most likely dissociates to different degrees in the DMSO solvent. This is readily observed in the CVs of Fe(acac)₃ in Figure 31 where the complex gives rise to several different redox couples, which likely correspond to different species of metal-ligand coordination and solvation by DMSO (such as [Fe(acac)₂(DMSO)₂]⁺). However, in the interest of maintaining focus on the electrochemistry of mycobactin, it has been simplified as Fe(acac)₃ in Scheme 2.

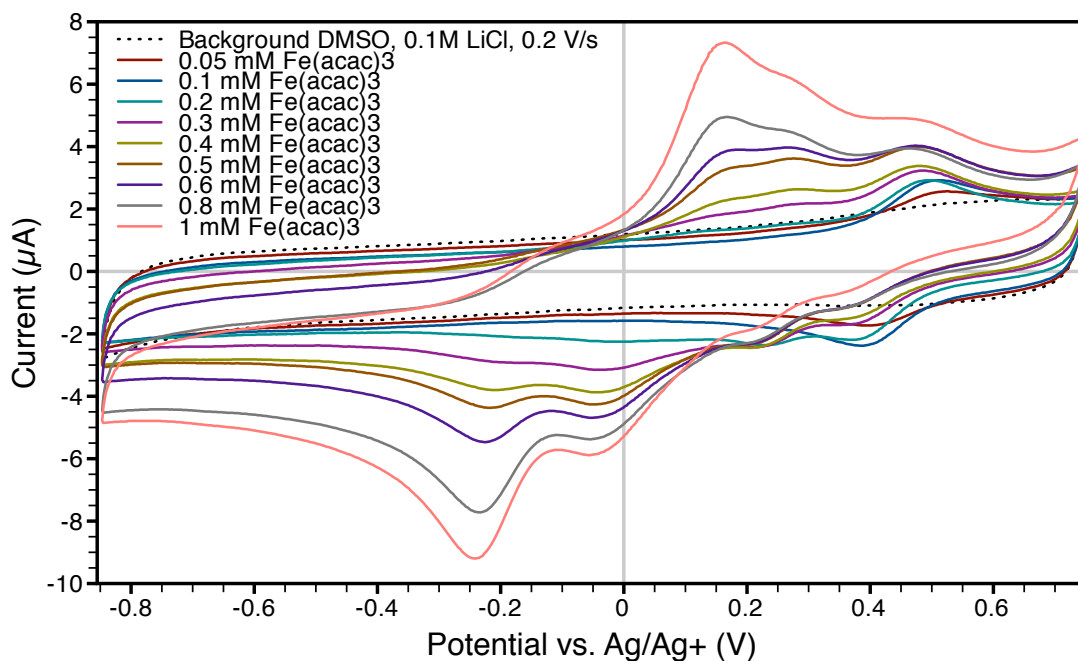
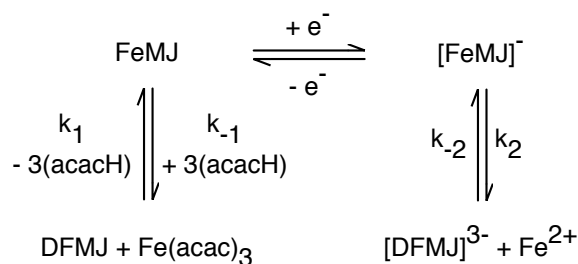


Figure 31: Cyclic voltammetry of Fe(acac)₃ at 0.2 V/s in DMSO, 0.1 M LiCl.



Scheme 2

3.2.1.2.3 Thermodynamic Stability of the Complex

Analysis of plots of the peak potential (E_p) versus $\ln v$ (Figure 32A) reveals that the peak potential tends toward more negative potentials with increase in FeMJ concentration, specifically at low scan rates. The same phenomenon is observed when the concentration of DFMJ is held constant and $\text{Fe}(\text{acac})_3$ is titrated into the cell, as in Figure 30 and Figure 32B, but not when $\text{Fe}(\text{acac})_3$ is titrated into solution containing already ferrated FeMJ as shown in Figure 32C. This indicates that the shift is specific to concentration of the complex and not to excess DFMJ or $\text{Fe}(\text{acac})_3$ that might be present. This is comparable to the increase in reversibility that is also observed with increasing complex concentration. A negative shift in the position of the redox couple indicates a further stabilisation of the ferric siderophore complex taking place¹⁹⁷.

Pursuant to Equation 1, any increase in the ratio of the affinity constants for $\text{Fe}^{3+}/\text{Fe}^{2+}$ will result in a negative potential shift for the complex redox couple. This could be either due to increased stability of the Fe^{3+} complex, or decreased stability of the Fe^{2+} complex. The reversibility data indicate that stability of the Fe^{2+} complex mostly increases with siderophore concentration, which would indicate that stability of the Fe^{3+} complex must be increasing in order to exhibit this negative peak potential shift. A possible explanation for this is that at relatively high concentrations of mycobactin, some self-assembly into micelles takes place, leading to a higher degree of structural stability, and thus stability of the complex. Measurements of related siderophores in aqueous media have yielded critical micelle concentrations in the range of 25-150 μM ⁴², however this would likely be much higher in organic solvents such as DMSO.

Additionally, the transition from quasi-reversible character to irreversible character, as indicated by spreading peak separation, shifts from relatively high scan rates at low FeMJ concentrations to lower scan rates at high concentrations. This is especially evident in the oxidation peak. Peak separation at low scan rates also decreases with increase in concentration, lending further support to the idea that Fe^{2+} dissociation is reversed in the presence of higher concentrations of FeMJ.

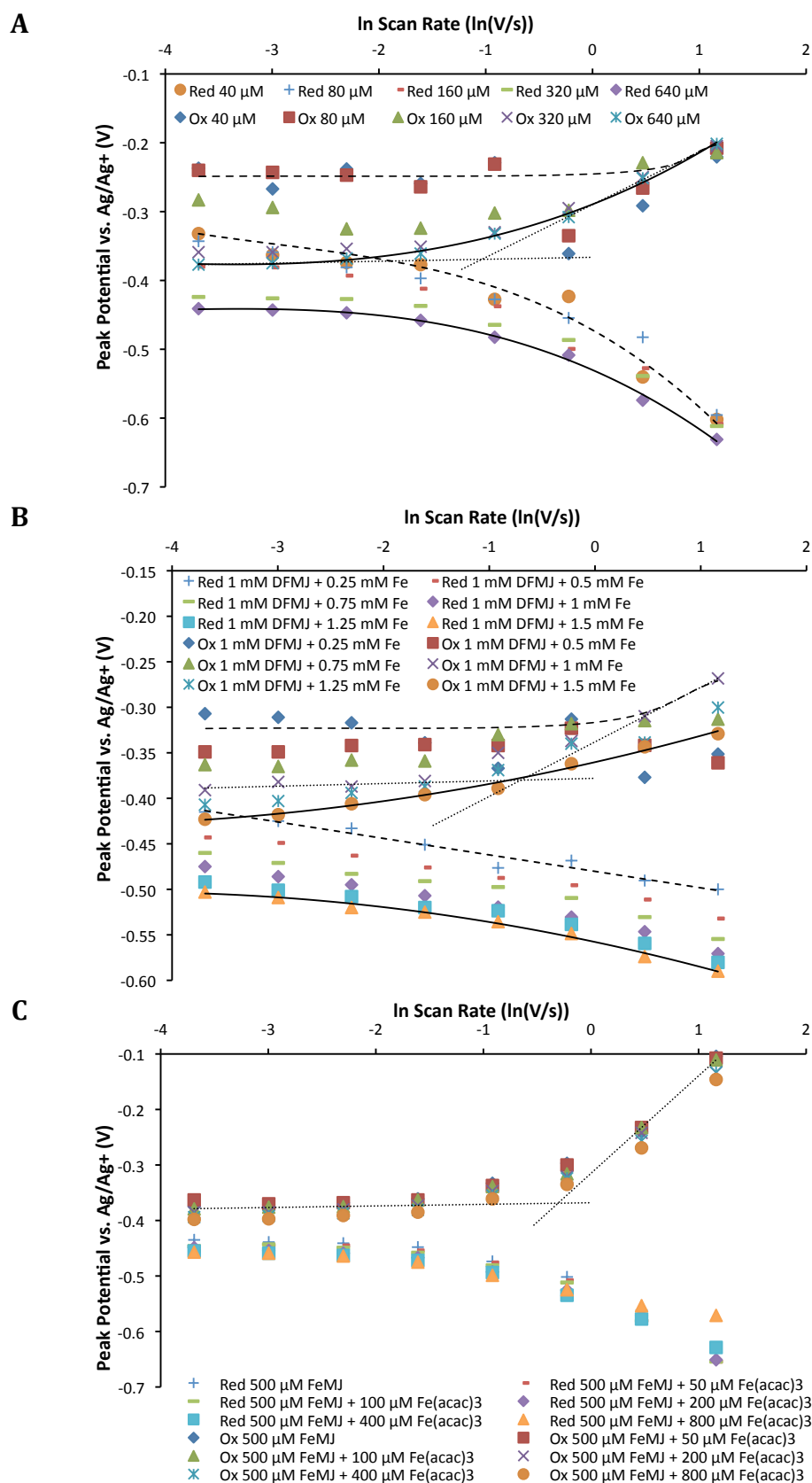


Figure 32A: E_p versus $\ln v$; dashed lines indicate bounds of the lower concentration data, while solid lines indicate bounds of the higher concentration data for either the reduction or oxidation peak; light dotted lines are linear trend lines for the low and high scan rate oxidation data, the intersection of which indicates the critical scan rate (v_c). **B:** The same plot, but for a constant concentration of DFMJ referred to by a titration of $\text{Fe}(\text{acac})_3$. **C:** The same plot, but for a constant 0.5 mM concentration of FeMJ and addition of excess $\text{Fe}(\text{acac})_3$.

3.2.1.2.4 Calculation of the Heterogeneous Electron Transfer Rate Constant

Plots of the cathodic peak potential (E_{pc}) for FeMJ, versus $\log_{10} v$ yielded slopes greater than 30 mV per decade for scan rates greater than 0.2 V/s at all concentrations (Figure 32A shows E_{pc} versus $\ln v$). The same is true for the anodic peak potential (E_{pa}) at high FeMJ concentrations. This indicates an adequate degree of irreversibility of the reaction²⁰⁶ at scan speeds greater than 0.2 V/s to allow use of a theory first developed by Nicholson and Shain²⁰⁷, followed by Klingler and Kochi²⁰⁶. This theory is applicable to organometallic complexes such as mycobactin and allows calculation of the apparent transfer coefficients β_v and β_w from kinetic data at E_p . Ultimately this allows calculation of the heterogeneous electron transfer rate constant (k_s). According to this method β_v and β_w are given by:

$$\beta_v = \frac{2.3RT}{2nF} \left[\frac{dE_p}{d\log v} \right]^{-1} \quad \text{Equation 3}$$

$$\beta_w = \frac{1.857RT}{nF} [E_p - E_{p/2}]^{-1} \quad \text{Equation 4}$$

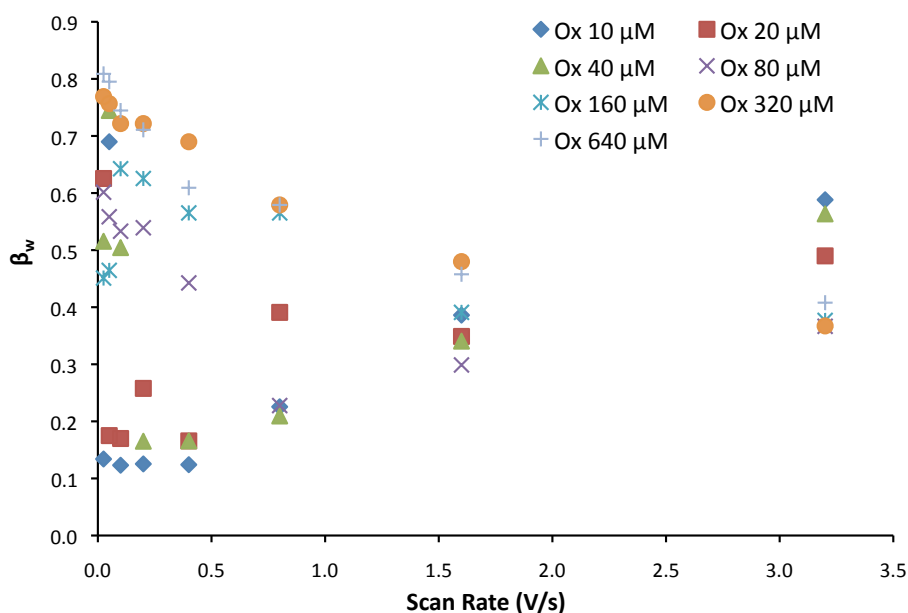


Figure 33: β_w vs. scan rate for different concentrations of FeMJ.

Using these solutions β_v can be extracted from the data plotted in Figure 32A. This analysis shows that β_v reduces from ~ 0.86 at low scan rates to ~ 0.36 for scan rates of 0.2 V/s and higher (when the reaction has irreversible character). This agrees well

with β_w obtained from Equation 4 (shown in Figure 33), which tends toward ~ 0.4 at high scan rates and concentrations. According to Klingler and Kochi, good agreement between β_w and β_v (correlated with a reversibility factor less than 0.5) allows the electron transfer rate constant at the CV peak potential $k(E_p)$ to be obtained and thence k_s according to:

$$k_s = 2.18 \left(\frac{D\beta n F v}{RT} \right)^{1/2} \exp \left[-\frac{\beta^2 n F}{RT} (E_{pa} - E_{pc}) \right] \quad \text{Equation 5}$$

Assuming a diffusion coefficient (D) of $1.7 \times 10^{-5} \text{ cm}^2/\text{s}$ yields $k_s \approx 5 \times 10^{-3} \text{ cm/s}$. These data further support the proposed quasi-reversible chemically coupled reaction scheme as summarised in Scheme 2 above.

3.2.2 Chronoamperometry

In principle an amperometric titration should produce a concentration-dependent response. This is the method of choice in most electrochemical test-strips such as those used for glucose, although chronocoulometry is seen as an alternative and potentially more sensitive technique when the precise sample size can be controlled. If it is assumed that the FeMJ is present in the Fe^{3+} form then electrochemical reduction (-0.6 V versus Ag/Ag^+) at a potential negative of the redox midpoint (-0.409 V versus Ag/Ag^+) should produce a steady-state, diffusion-limited reduction current proportional to FeMJ concentration.

However, in an amperometric titration of FeMJ no step-change in current was observed at FeMJ concentrations up to $100 \mu\text{M}$, as shown in Figure 34. This is disappointing, but referencing the CV data shows that the steady state current (estimated from the CV from the exponential current decay after the reduction peak at -0.8 V) does not rise above the noise of the background signal until FeMJ concentration is greater than $160 \mu\text{M}$ (Figure 35). Even at $640 \mu\text{M}$ it is less than twice the background current. This low signal to background ratio would have to be improved in order to take advantage of this technique for the present assay.

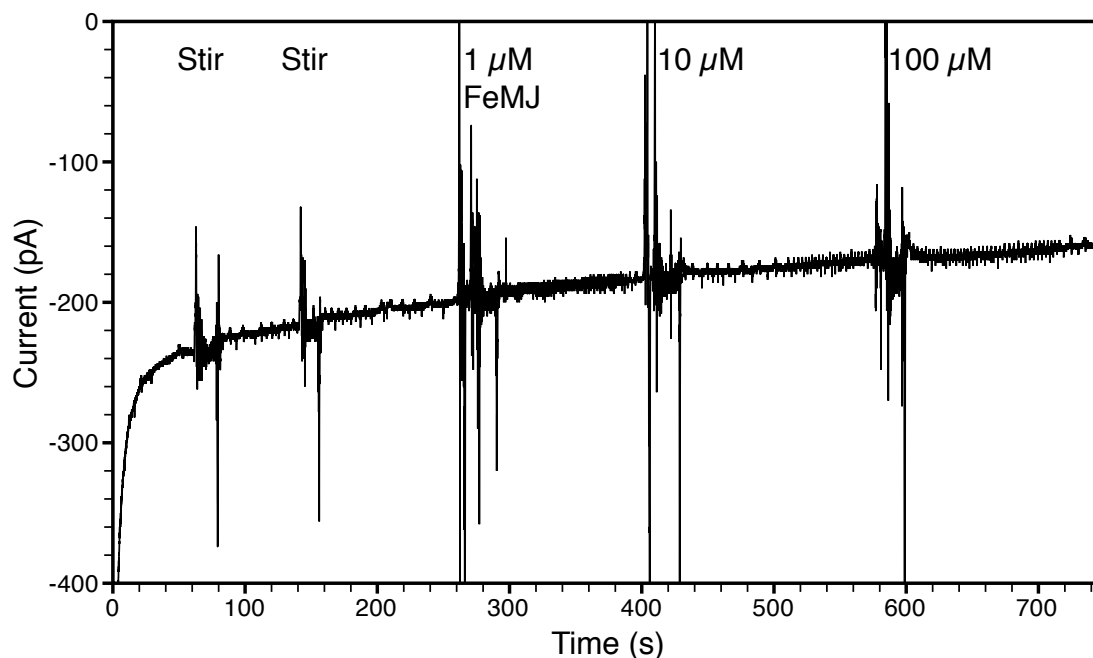


Figure 34: Amperometric titration of FeMJ at -0.6 V versus Ag/Ag⁺. The areas with spikes of noise correspond to periods of stirring with a magnetic stir bar following addition of FeMJ. No FeMJ was added to the cell during the first two stirring events to serve as controls.

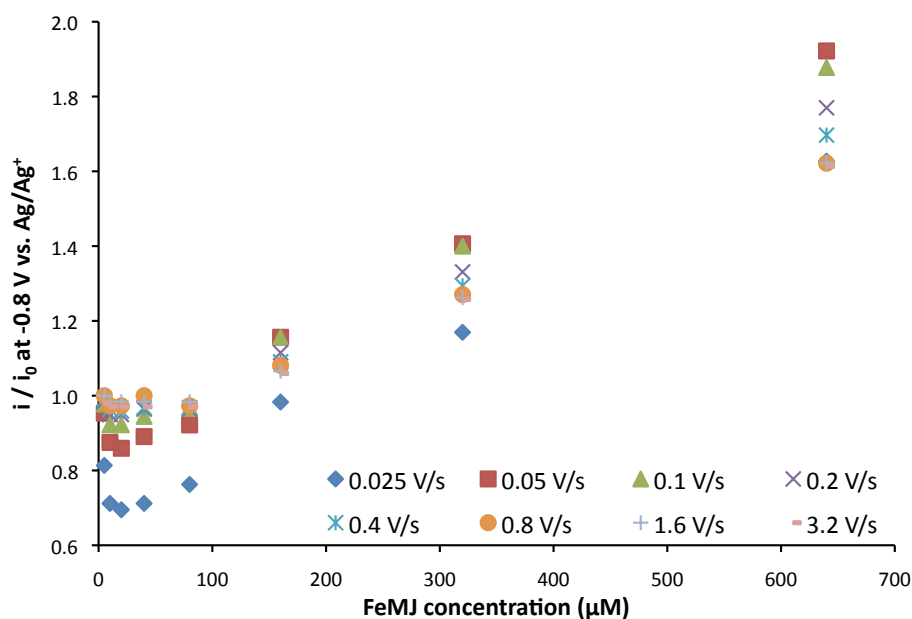


Figure 35: Ratio of the measured current (i) over background current (i_0) at -0.8 V from CV data to approximate steady-state values.

In most electrochemical test strips an immobilisation system is employed to either capture the analyte or catalyse an electrochemical reaction to enhance the measured charge transfer at the electrode surface. In the former case this enhancement occurs because analyte is concentrated near the electrode surface for immediate reduction. Such a capture and concentration scheme is especially useful when trying to detect low analyte concentrations. In contrast to the test strips, the measurand of this

assay is not being generated or captured at the electrode surface and this low, bulk solution response is typical for some redox systems with slow kinetics. If this type of technique were to be used it would require a mycobactin binding ligand on the electrode to capture and concentrate mycobactin from the sample. This possibility is discussed further in Chapter 6.

Another way of potentially improving upon this response is by improving the specific surface binding properties between the electrode and FeMJ itself. This can be done through surface engineering of the electrode, which will also be discussed further in Chapter 7. Since the target mycobactin concentration proposed in Chapter 1 is less than 250 nM, potentiostatic methods were not pursued any further at this stage.

3.2.3 Electrochemical Limit of Detection

Using cyclic voltammetry, peak height/non-faradaic current ratios can be manipulated through scan speed. High scan speeds yield a greater current peak at high FeMJ concentrations, as would be expected. However, this advantage is lost at lower concentration due to peak broadening at high scan rates inhibiting accurate quantification. The result is that low scan rates (25 mV/s) produced the best sensitivity and a linear relationship between i_p and concentration at FeMJ concentrations in the 10-160 μM range (Figure 36). As predicted from the mechanistic analysis in section, 3.2.1.2, the electron transfer exhibits a more irreversible character at low concentrations and the oxidation signal does not begin to appear until FeMJ concentrations have reached 20 μM . At 1 mM, FeMJ redox peaks were observed up to 20 V/s scan rate; however, quantitative analysis was only possible up to 5 V/s due to excessive broadening of the peaks. A standard curve was created based on these measurements to enable electrochemical quantification of mycobactin.

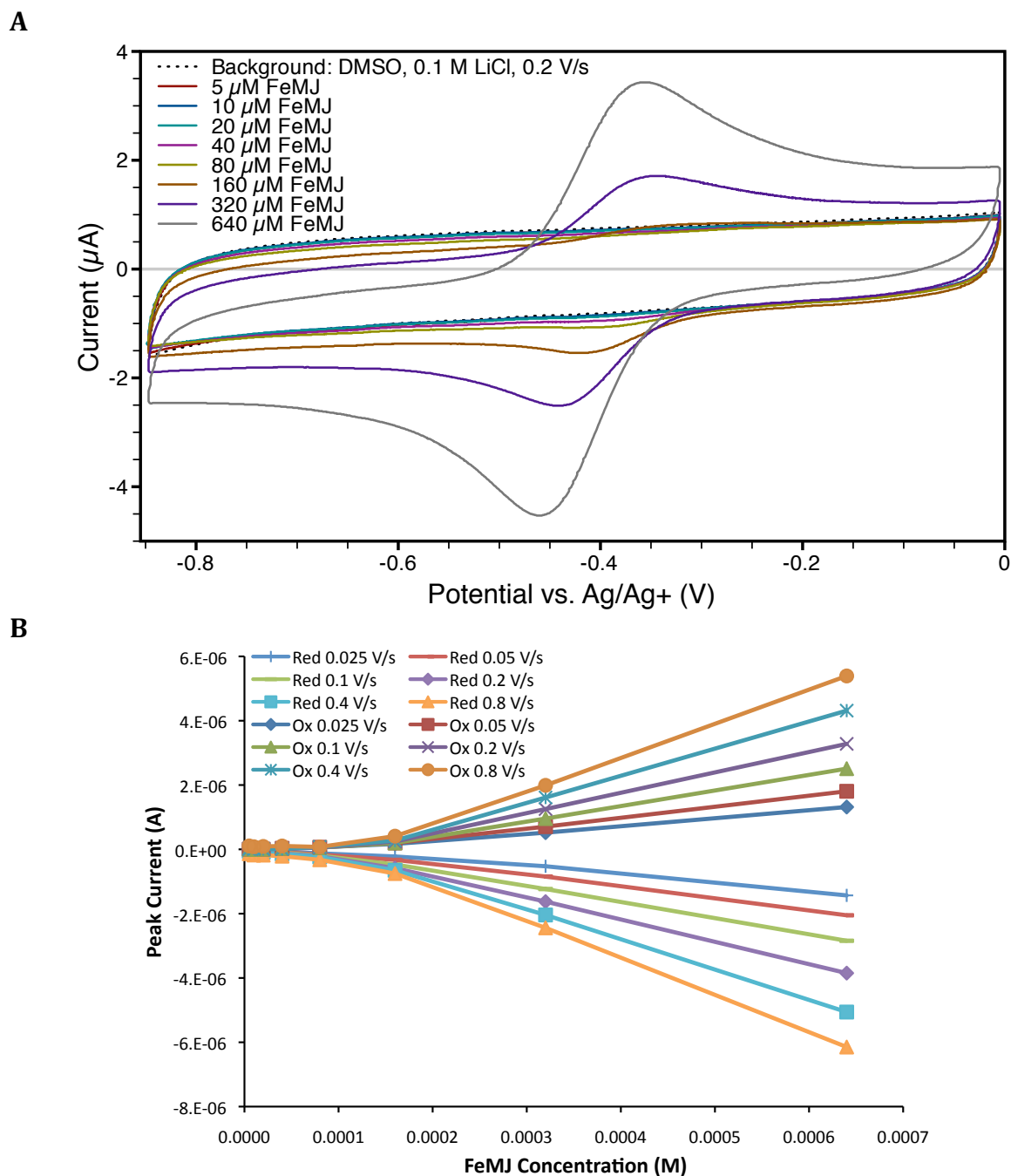


Figure 36A: Titration of FeMJ by cyclic voltammogram at 0.2 V/s in DMSO, 0.1 M LiCl. B: CV peak current versus FeMJ concentration.

In section, 3.2.1.2, it was shown that addition of $\text{Fe}(\text{acac})_3$ to the FeMJ solution increased the reversibility. The relationship between the electrochemistry of FeMJ and $\text{Fe}(\text{acac})_3$ may also offer another way of increasing the sensitivity of mycobactin detection. When DFMJ was titrated into a solution of $\text{Fe}(\text{acac})_3$ the decrease in the concentration of $\text{Fe}(\text{acac})_3$ upon the iron being competitively chelated by DFMJ to form FeMJ was observable with higher sensitivity than the signal due to the increase of $[\text{FeMJ}]$ alone. This suggested a potential use in which the concentration of DFMJ may be

indirectly measured through ratiometric measurement of $\text{Fe}(\text{acac})_3$ redox peaks. This is demonstrated in Figure 37. The best sensitivity could be achieved by taking the ratio of the current at 0.38 V to the current at -0.02 V, taking advantage of the changes in the electrochemical signal from $\text{Fe}(\text{acac})_3$ with addition of DFMJ. However, in order for this method to be used, we encounter the limitation of having to deferrate the mycobactin prior to conducting the detection assay, which is an unrealistic requirement. However, changes are observable for DFMJ concentrations at least as low as 10 μM .

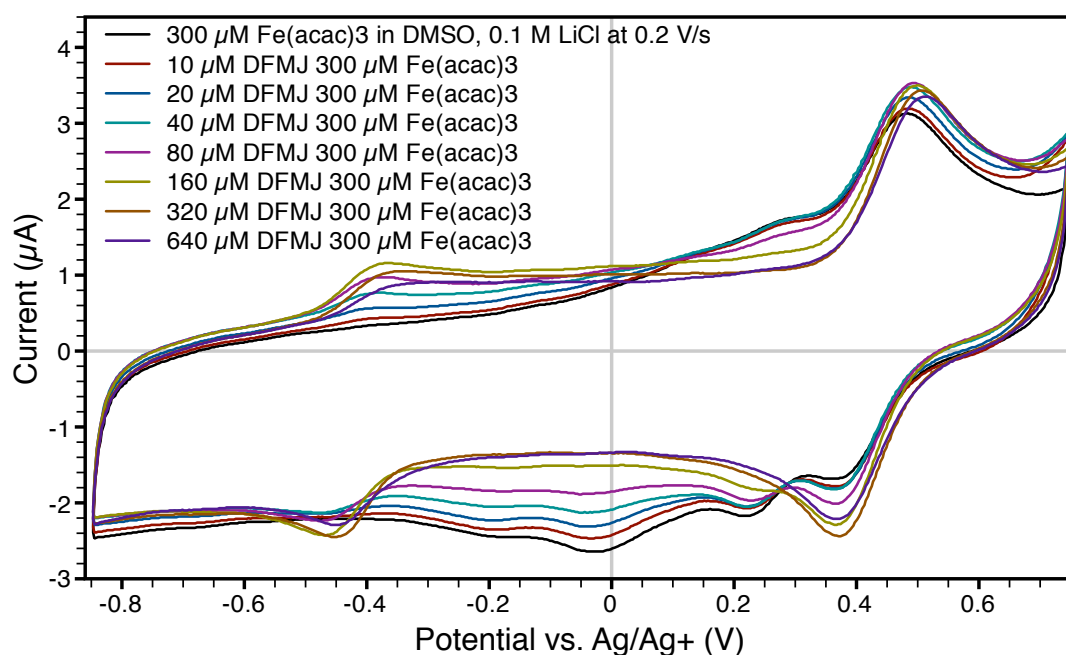


Figure 37: Titration of DFMJ into a 300 μM solution of $\text{Fe}(\text{acac})_3$ at 0.2 V/s in DMSO, 0.1 M LiCl.

3.3 Conclusions

The redox electrochemistry for FeMJ shows slow quasi-reversible kinetics. The chemically coupled electron transfer mechanism for FeMJ is influenced by the presence of Fe^{2+} and Fe^{3+} in solution, despite the affinity for Fe^{3+} being 18 orders of magnitude greater than for Fe^{2+} . At the redox potential for FeMJ, Fe^{3+} (typically complexed with acetylacetonate under the conditions used here) is reduced to Fe^{2+} at the electrode and thus $[\text{Fe}^{2+}]$ is always elevated, pushing the FeMJ^- dissociation equilibrium towards the complex (Scheme 2).

In a simple voltammetric experiment the limit of detection for mycobactin by CV was found to be in the order of 10 μM and allowed quantitative analysis of the mycobactin content of an electrochemical test solution. This compares with a

preliminary target of less than 250 nM as suggested in Chapter 2. Unfortunately it was not possible to improve upon this limit of detection through the use of other electrochemical techniques including chronoamperometry, square-wave voltammetry (data not shown), and dual-circuit four-electrode gap electrochemistry utilising feedback diffusion (data not shown).

Addition of excess Fe^{2+} into the sample can improve the chemical reversibility, but did not improve sensitivity of the assay. Sensitivity of the sensor is core to its usefulness as the quantity of mycobactin to be found circulating within TB patients is likely to be minute. The level of mycobactin production in an infection and the level at which it may be present is crucial to whether an effective TB diagnostic can be developed.

Clearly, based on the Chapter 2 estimate of physiological mycobactin production further work on either the electrochemical method or sample preparation is required to further reduce the detection limit. As seen here, solubility of the mycobactin in typical biological aqueous based media is poor (hence its association with lipids) so that DMSO has been employed as the assay solvent. This preparation step also offers the possibility of linking sample concentration into the protocol thereby improving on the detection limit. Therefore this electrochemical assay is, in principle, applicable for use with material from a variety of biological sampling media depending on sample processing. This is further explored in Chapter 4 with a proof of concept detection and quantification of mycobactin from urine as an example sampling medium.

4 Proof-of-Concept Application of the Assay

The research reported in this chapter demonstrates the utility of the simple electroanalytical mycobactin assay, described in Chapter 3, for monitoring mycobactin levels within an example biological medium. This included a determination as to whether there is any significant background interference when using the example medium.

The primary motivation for this investigation was the need for a biosensor for use as a TB diagnostic. However, since mycobactin trafficking within the body of the host is still under investigation, concentration of mycobactins in different bodily fluids or tissues is not yet well enough defined to allow an assay to be directed toward one specific sampling medium to the exclusion of others. Thus, an example biological sampling medium had to be selected for proof-of-concept testing of the assay.

Collection and handling of the sample material, particularly when it is of biological origin is integral to the ultimate safety, utility, and sensitivity of the assay. Relatively simple analyte concentration methods can be applied to the sample prior to analysis, thus greatly increasing the sensitivity, and also removing a great deal of background interference. Thus, a further goal in this chapter is to define and evaluate the processing steps to collect the mycobactin that might be present in a complex biological matrix while simultaneously removing bulk contaminants that could physically impede the analysis. It is also necessary to ascertain whether any conflicting signals might be observed from compounds commonly found in the sampling medium. An example of this would be a hypothetical compound that exhibits a similar redox potential to ferric mycobactin, thereby interfering with the electrochemical assay.

The biological sampling media of potential interest for consideration in mycobactin detection include blood, urine, hair, and stool as well as homogenised lung tissue, sputum, and saliva. The collection and handling of blood samples poses a significant risk of infection to the clinician obtaining the sample, as well as anyone who must process it thereafter. This is especially risky in areas with high rates of HIV/AIDS co-infection with TB, which is a growing problem in many populations. This, as well as the invasiveness of sample collection makes blood a less desirable diagnostic sampling medium. Urine would be the ideal sampling medium due to its relatively low

infectiousness and ease of collection. For comparison, of the clinically useful siderophores, deferoxamine and deferiprone are excreted primarily in the urine, whereas deferasirox is excreted faecally. However, the biodistribution and pharmacokinetics of mycobactin and carboxymycobactin are still unknown. It remains to be seen as to whether these compounds would be found in the urine due to filtration in the kidneys and partitioning of the significantly hydrophobic mycobactins into cell membranes. Saliva would be a secondary choice, as a relatively non-invasive sampling medium. It is considered more infectious and may harbour live mycobacteria.

In contrast, homogenised lung tissue, while being the most probable to contain high concentrations of mycobactin produced by the infecting organism, is both difficult to obtain and unsuitable for ongoing monitoring of patients. Routine harvesting of lung tissue is only an option in the case of animal models during necropsy. Sputum samples are also difficult to obtain and to ship due to their potential to be highly infectious, thereby requiring measures to avoid infection at all times during sample handling. Additionally, sputum samples have a high degree of variability and inconsistency.

Taking all of these considerations into account urine was chosen as the example biological medium on which to test the assay.

4.1 Materials and Methods

4.1.1 Bovine Urine Samples

Bovine urine donated anonymously by cattle from the University of Cambridge dairy herd was made available through collaboration with Duncan Maskell of the Department of Veterinary Medicine. The herd is tested every four years for bovine tuberculosis via intradermal skin test with the last test having taken place in August of 2009. Routine testing for Jöhne's disease is not done, however there had been no suspected clinical cases within the past six years at the time of writing. Urine sample collection was carried out by Nicholas McBride on the 27th of September and 22nd of October, 2010. Urination was induced in female cattle by rubbing the perineum. In the capacity that this sampling medium may also serve for future TB diagnostic testing there is relevance in the prevalence of the spread of bovine tuberculosis in the United Kingdom. The urine was spiked with FeMJ to test both the effectiveness of the

electrochemical detection method and to develop a chromatographic mycobactin concentration step that is effective for an actual biological matrix.

4.1.2 Preparatory Chromatographic Concentration of Mycobactin

Due to the relatively hydrophobic nature of mycobactin, and even carboxymycobactin, chromatographic concentration was performed using reverse-phase Waters Sep-Pak tC₁₈ cartridges containing 50 mg of sorbent and having a bead size of 37-55 μm , pore size of 125 \AA , and bed volume of 0.13 mL. The sample was eluted in 3 \times 0.5 mL of diethyl ether and the eluate solvent was subsequently removed under vacuum. Spectrophotometric analysis was done after dissolving the residue in 0.75 mL methanol. Alternatively, electrochemical analysis was performed after dissolving the residue in 0.1 mL DMSO containing 0.1 M lithium chloride. In the case that both analyses were performed, the dry eluates were first analysed spectrophotometrically, the methanol was removed, then the samples were analysed electrochemically.

4.1.3 Spiking of Samples

Initial testing of the chromatographic method was done using water in place of urine. 25 mL of purified, deionised water was spiked with a stock solution of 5 mM FeMJ in either DMSO or methanol to give final concentrations of 5 μM FeMJ and 0.1 percent of the respective solvent.

For the triplicate bovine urine experiment, urine was collected from three female cows and divided into 25 mL aliquots. These samples were then either spiked with 2 μM FeMJ and 0.1% DMSO (final concentration), or left unspiked and frozen at -80°C until chromatography was performed. They were not filtered prior to analysis.

4.1.4 Effects of Sample Processing

The urine processing was tested using urine collected from one healthy female cow and split into 25 mL aliquots. Each aliquot (designated NEG1, NEG2, POS1, POS2, and POS3) was then treated as defined in Table 10. When indicated, spiking of the samples by FeMJ was done as above using a DMSO stock of FeMJ.

Table 10: Bovine urine processing method validation; addition of FeMJ gave a final concentration of 5 μ M FeMJ. The steps highlighted in red were performed at the University of Cambridge Department of Veterinary Medicine due to biosafety category 2 requirements, whereas steps highlighted in green were performed and the Department of Chemical Engineering and Biotechnology.

	Treatment	NEG1	NEG2	POS1	POS2	POS3
Process Steps →	Add FeMJ before filtration	-	-	+	+	-
	0.22 μ m filtration	-	+	-	+	+
	Add FeMJ after filtration	-	-	-	-	+
	Frozen at -80°C	+	+	+	+	+
	Sep-Pak tC ₁₈ chromatography	+	+	+	+	+
	Analysis (spectrophotometric and electrochemical)	+	+	+	+	+

4.2 Results and Discussion

4.2.1 Chromatographic Collection and Elution of Mycobactin

Spectrophotometric analysis of the eluates and flow-throughs from initial C₁₈ chromatography of spiked water reveal that when FeMJ is initially solubilised in DMSO, it is retained on the C₁₈ column, whereas when it is initially solubilised in methanol, the vast majority of FeMJ passes through the column with only a small quantity retained on the stationary phase. This is demonstrated by the difference in absorption at 450 nm, as shown in Figure 38. A potential explanation for this phenomenon is that the DMSO remains associated with the mycobactin even upon dilution in water. This is consistent with studies of DMSO solvation of lipid membranes that show strong associations between DMSO and the lipids, thus creating a disordered solvation environment between the hydrophobic tails and increasing permeability of the membrane to water²⁰⁸. In contrast, methanol has been shown to induce aggregate transition of chlorophyll at relatively low water content (32%)²⁰⁹. This is due to the relatively high charge density of the small, polar methanol molecule acting to dissociate it from mycobactin and in preference to contributing the structure and stability of water-water interactions^{209, 210}. Hydrophobic aggregation of the lipid tails of mycobactin would sequester them from interacting with the stationary phase of the column. Further supporting this is the observation that methanol-solvated mycobactin tended to form a precipitate at the bottom of its vial after several days on the bench, whereas DMSO-solvated mycobactin did not form a precipitate. Based on these data, DMSO solubilisation of FeMJ was used for all further experiments.

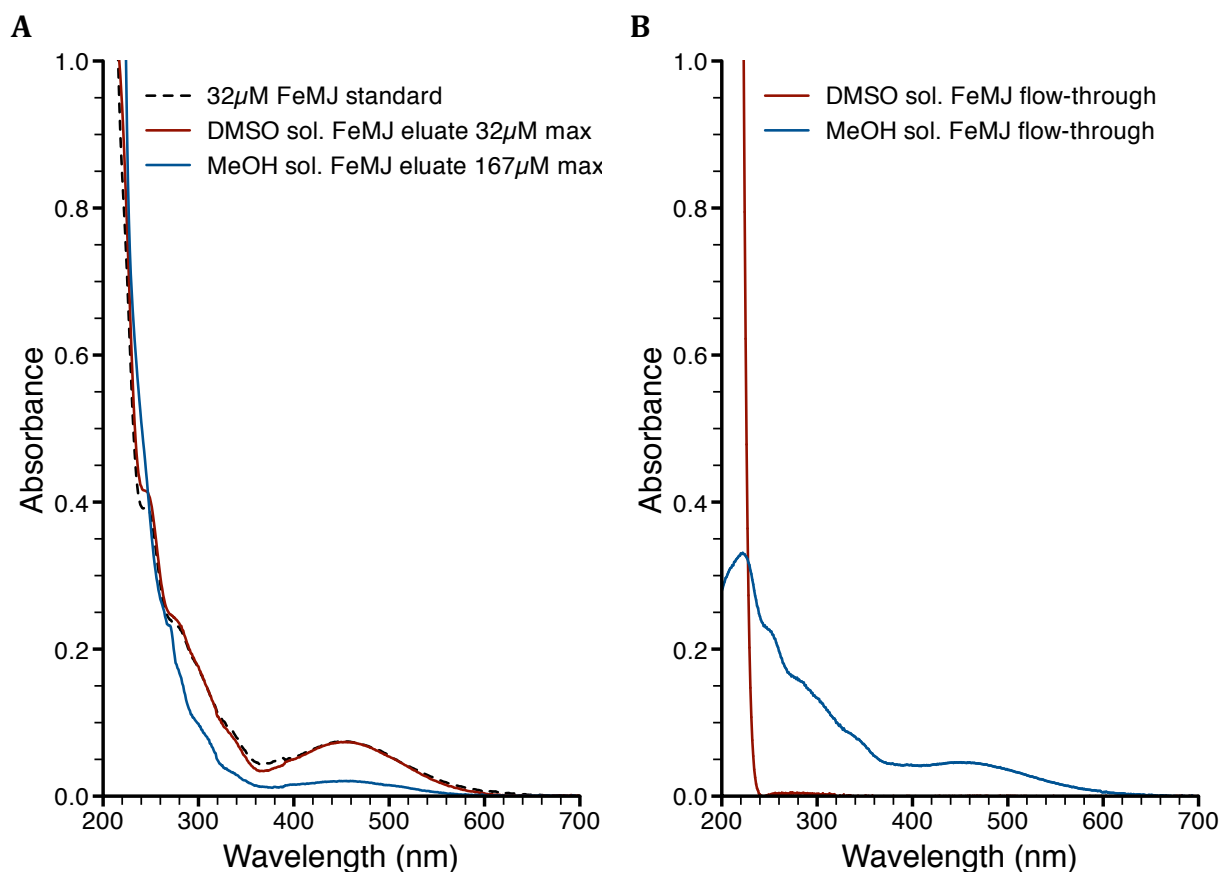


Figure 38: Effectiveness of Sep-Pak tC₁₈ separation of FeMJ from water when FeMJ is initially solubilised in either DMSO or methanol (MeOH). A: spectrophotometric absorbance after elution in diethyl ether, drying, and dissolution in methanol; solutions were diluted to give the stated concentrations given 100 percent theoretical retention. B: absorbance of the undiluted flow-through of the initial 25 mL sample.

4.2.2 Effects of Sample Processing

This simple procedure formed a basis for developing an assay protocol. However, other practicalities in the procedure also needed to be accommodated. In order to mitigate risk of infection from the sample, passage through a 0.22 μ m filter to remove any infectious bacteria is desirable. For experimental purposes, this would also allow easier handling of samples under less stringent biosafety precautions. However, the possibility that mycobactin may be retained on the filter would negate the utility of the assay for filtered samples.

The samples used to test the impact of filtration were aliquots from a single pool of urine from one female cow and designated NEG1, NEG2, POS1, POS2, and POS3, as defined in Table 10. Their absorbance spectra are shown in Figure 39A. Unfiltered samples (NEG1 and POS1) exhibited high background absorbance in the 450 nm region, making spectrophotometric detection of mycobactin impossible. In the filtered samples,

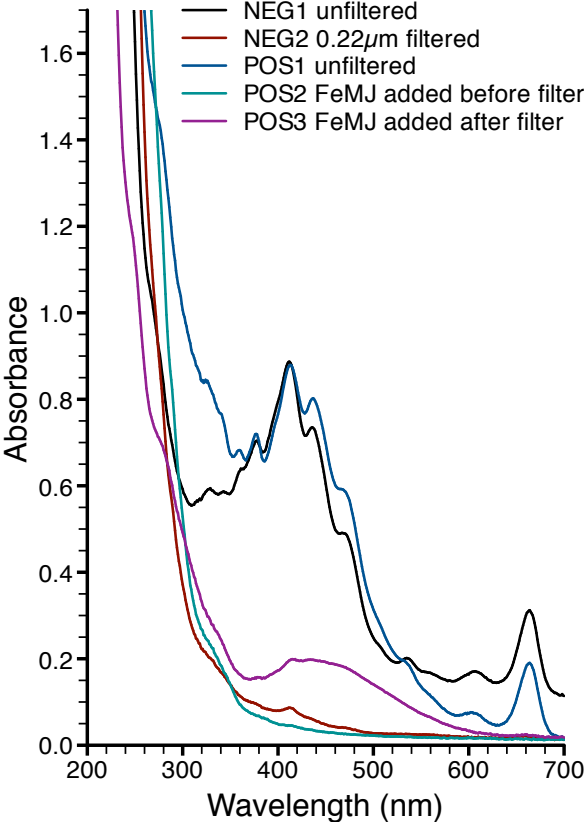
the presence of a significant 450 nm peak attributed to FeMJ is observable when FeMJ is added after filtration of the sample (POS3), but not when added before filtration (POS2). This suggests that mycobactin may aggregate or otherwise adsorb to particulates in the urine that are unable to pass through the 0.22 μm filter, or that it is adsorbed on the filter itself. This also has implications for the chromatographic separation, as the pores in the reverse-phase cartridges are smaller than 0.22 μm , FeMJ may remain on top of the sorbent column, then elute off and simultaneously through the column, rather than eluting off the column itself. It should be noted that in contrast to the urine samples, which showed visible concentration on top of the reverse-phase cartridge, when mycobactin was dissolved in water alone (Section 4.2.1) the FeMJ colouration was observed to adsorb throughout the length of the reverse-phase cartridge. This supported the idea that it is a specific property of the urine that causes the aggregation or adsorption to particulates of mycobactin.

The electrochemical analyses of these samples, shown in Figure 39B, are also broadly consistent with the above interpretation. However, in contrast to the spectrophotometric assay, the CVs demonstrate an eloquent and clean signal, free from interference except for a small peak in the unfiltered NEG1 sample. This sample was repeated using the same source urine with similar results, but the same peak did not reappear in any subsequent samples from other cows (see Figure 41). This is interesting because of the possibility that the cow in question may have contracted an as-yet undetected infection by a mycobacterium or other siderophore-producing bacterium. The peak is more negative than the results for the reduction potential of FeMJ, but its reproducibility indicates a redox active species that is appearing in the potential range for Fe-complexed siderophores (and other compounds). It may serve as an interesting target for future analysis, if it can be correlated with other routine diagnostic measurements amongst the herd. Unfortunately we were unable to revalidate the health status of the specific cow in question because the samples were donated anonymously.

It is clear from these data that identification of mycobactin is limited as much by the extraction method as by the electrochemical detection. The signal is completely lost by filtration, indicating a loss of greater than 99% of the material. Therefore it was determined that filtration was not suitable for processing of the urine samples and testing proceeded on the basis of using unfiltered urine. The variability between POS1

and POS3 likely also reflects variability in the extraction process and is similar to the range of variability observed in subsequent experiments.

A



B

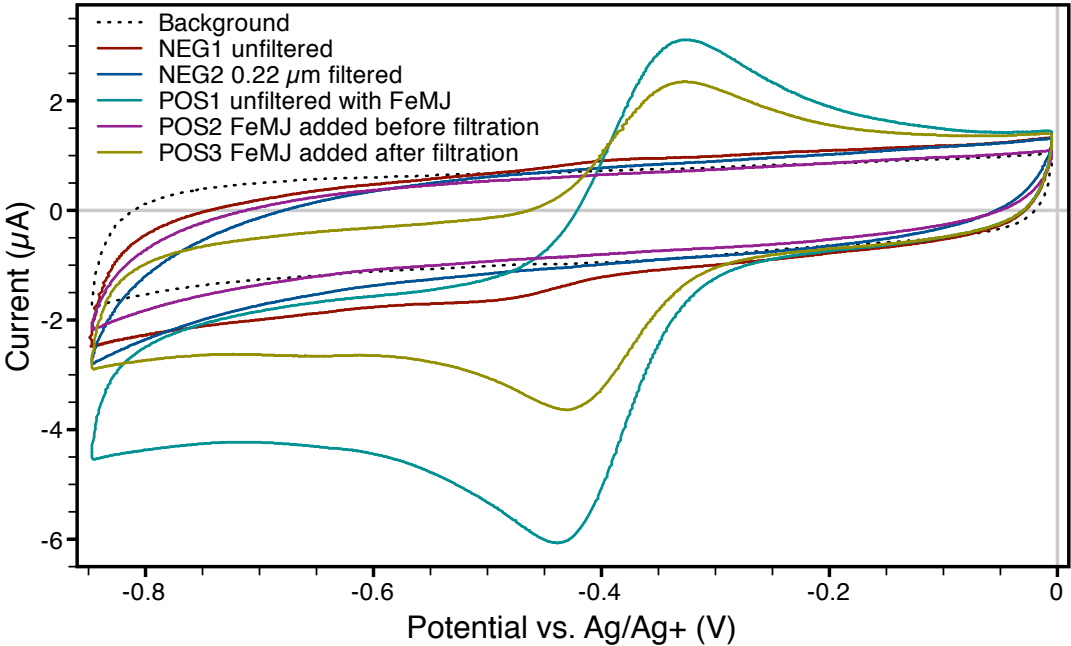


Figure 39: Analysis of Sep-Pak tC_{18} eluates from the bovine urine samples from a single urine pool and treated as defined in Table 10; spectrophotometric absorbance in 0.75 mL methanol (A) and CV analysis in 0.1 mL DMSO, 0.1 M LiCl at 0.2 V/s scan rate (B) are shown.

4.2.3 Application of the Assay for Monitoring Mycobactin in Urine

Following initial testing of the urine sample processing and analysis protocol, the investigation was expanded to gather data from a larger set of cattle. Samples from three cows were each subjected to chromatographic concentration and electrochemical analysis. The samples were unfiltered, making the processing of the negative controls equivalent to NEG1, and the positives equivalent to POS1.

Although it was possible to discern the addition of FeMJ spectrophotometrically by comparison with the unspiked control samples, variability between the spectra of different samples precluded the usefulness of this technique to detect mycobactin from a complex biological matrix in the absence of a negative control, as shown in Figure 40.

CV analysis of the samples (Figure 41) revealed a recovery yield of mycobactin in spiked bovine urine samples of $40 \pm 10\%$ (standard deviation) based upon the standard curve for the peak current developed in Chapter 3. This was done using a starting concentration of $2 \mu\text{M}$ FeMJ. Based on these results it can be seen that the opportunity to detect mycobactin is limited by poor extraction and that recovery yields are clearly influenced by the sample matrix as discussed above.

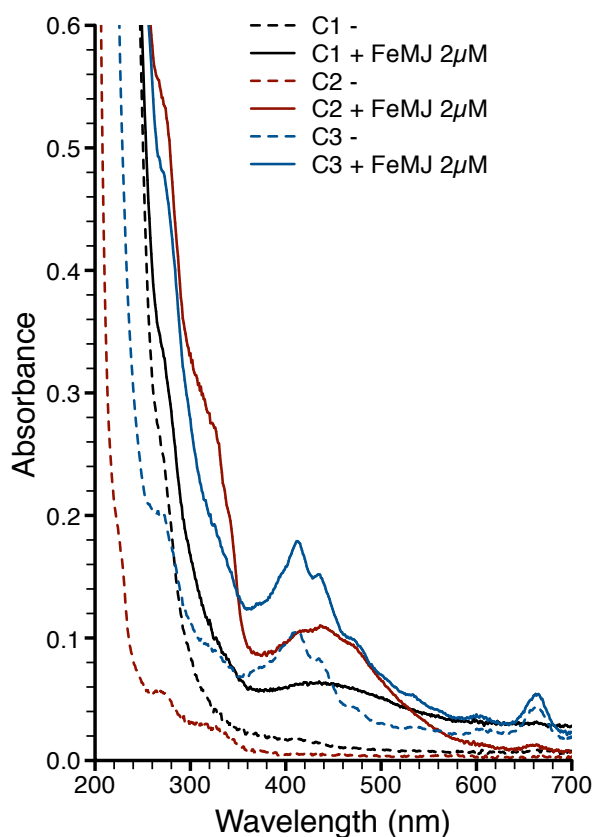


Figure 40: Spectrophotometric absorbance of bovine urine Sep-Pak tC₁₈ eluates in 0.75 mL methanol; C1-C3 refer to samples take from three individual cows with and without the addition of $2 \mu\text{M}$ FeMJ.

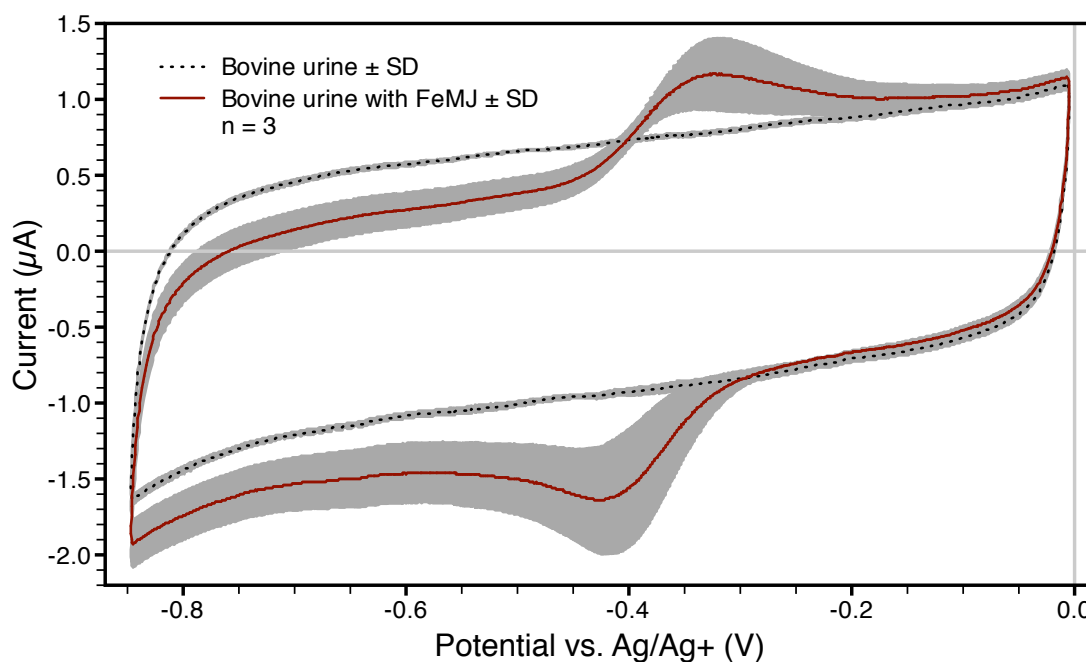


Figure 41: Mean cyclic voltammogram of standardised bovine urine eluates; the grey area indicates the range of standard deviation.

4.3 Conclusions

These proof-of-concept testing results in bovine urine demonstrated the ability of this simple assay system to detect and quantify mycobactin present within one example of a complex biological medium. Using the simple electrochemical method, a clean background signal could be obtained even using raw sample urine. It is highly encouraging that this approach yielded such low levels of background interference, even within the complex biological matrix of a urine sample. This is an important finding and suggests that the assay could easily be adapted to use other sampling media.

The quantitative limit of detection by CV of 10 μM , as discussed in Chapter 3, could be reduced to 300 pM for an original sample size of 25 mL through sample concentration using C_{18} separatory columns, thereby placing the assay within reach of the preliminary target of 0.85-250 nM (Chapter 2). This could be achieved assuming a 0.3 μL assay volume, which is common for handheld electrochemical diagnostic products, and extrapolating the recovery yield of 40 percent. Thus, in the design of a stand-alone single use test-strip, the inclusion of a lateral flow chromatography support for sample concentration must be envisaged. From spiked samples, it could be seen that filtration to remove incidental bacteria also removed greater than 99 percent of the mycobactin, which would have the effect of rendering false negatives were filtration to

be applied in the use of this assay. Therefore it can be concluded that such filtration should be avoided during sample processing, or that filtration could potentially be used as a simple method for sample concentration, eliminating the need for a reverse-phase column.

The simple electroanalytical assay developed in Chapter 3, was robust in its applicability to the example sampling medium of urine. This gives considerable scope to improve the detection limit through further sample capture or concentration methods. The ability to use this simple assay to detect and quantify mycobactins could provide a low-cost sensor to effectively diagnose active TB in resource-poor settings if the actual concentrations of mycobactin within samples from infected patients can be determined and found to be within the range of sensitivity determined here.

5 Evaluation of Siderophore Contents of Different Biological Media

Leading on from the improved detection levels for mycobactin estimated in Chapter 4 following sample concentration, the goal of the work reported in this chapter, was to explore the presence of mycobactin and carboxymycobactin within clinical specimens of different biological media, from TB patients and *Mtb* infected animal models and to draw conclusions regarding use of the electrochemical assay as a measure of *Mtb* infection. Although the *in vitro* modelling in Chapter 2 is useful to give a rough idea of mycobactin production levels by *Mtb* in an infection scenario, the only way to determine the true mycobactin levels within TB patients is to analyse clinical samples directly. Availability and access to such samples is costly in terms of both time and resources. For the purposes of this research, clinical specimens of both urine and blood plasma were obtained from Korean TB patients as part of an ongoing clinical protocol. Sputum samples were unobtainable due to the regulatory complexity of securing their international shipment and containment. Specimens of urine, stool, and hair from infected animal models were obtained for this study. The rationale behind the use of these sampling media has already been explored in the introduction to Chapter 4. The rationale for also examining hair and stool was that the relatively lipophilic mycobactin might be excreted through these pathways. Hair would only be useful as a marker for long-term infection unless recent-growth root samples are used.

As a gold standard of mycobactin detection to be compared with the electrochemical assay, high performance liquid chromatography/high resolution mass spectrometry (HPLC/HRMS) was adopted as the most sensitive laboratory-based detection of mycobactin to reveal information about the distribution of mycobacterial siderophores within the different tissues of infected individuals.

5.1 Materials and Methods

5.1.1 Samples

All work involving potentially infectious *Mtb* including handling of infected animals and clinical samples was performed in the BSL3 biocontainment facility of NIAID.

5.1.1.1 Infected Animal Samples

Infected animal samples were obtained from the NIAID Tuberculosis Research Section facility in Bethesda, Maryland, United States. The protocol governing animal handling, infection, sample collection, and euthanasia procedures was approved by the NIAID Animal Care and Use Committee (ACUC) prior to commencement of the study. The ACUC is responsible for applying U.S. Government Principle IV. Animal infections and sample collections were carried out by facility staff including Jacqueline Gonzales, Laura Via, Danielle Weiner, and Emmanuel Dayao.

Animals were placed into tubular polycarbonate exposure chambers for nose only exposure using the CH Technologies inhalation exposure system. Aerosol inocula were delivered via a dynamic aerosol chamber modified to allow nose-only exposure. Animals were acclimated to the aerosol chamber by allowing them to breathe filtered air, provided to the chamber at 25 L/min, prior to the initiation of *Mtb* aerosol delivery. The aerosol was generated using a BioAerosol Nebulising Generator (BANG) using 20 lb/in² (psi) of filtered air at a flow rate of 6.5 L/min. Mice and rabbits do not require sedation as they readily enter the holding tubes.

Mouse²¹¹ and rabbit¹⁹⁵ infections were carried out as described previously. Virulent *Mtb* reference strains and *M. bovis* were used in this study. Animals were monitored visually during the exposure period. An all-glass impinger was used to sample bacilli in the aerosol generated by the nebuliser at each concentration of bacteria used.

Before infection, *Mtb* cultures were adjusted to OD₆₅₀ of 0.5 and stored at -70 °C as 20% glycerol stocks. Inocula were prepared by diluting these stocks to 4×10⁶ CFU/mL in PBS/Tween 80 (0.05%). Six-week-old B6D2 F1 (C57BL/6×DBA/2; F1 progeny) mice (Taconic) were loaded into nose-only aerosol-exposure tubes without

sedation, exposed to the BANG generated aerosol for 10 minutes and clean air for 5 minutes, and then removed from the tubes and replaced in their cages. In this manner, approximately 50–100 CFU per lung were implanted as confirmed by homogenising sample lungs in M7H9/ADC at 3 h after infection and plating for CFU determination.

For rabbit infection the aerosol inocula were prepared by diluting the frozen stocks to $1\text{--}1.5 \times 10^5$ CFU/mL in phosphate-buffered saline PBS/Tween 80 (0.05%). Rabbits were placed (without sedation) in cat-restraint bags with hoods and then loaded into the rabbit nose-only aerosol exposure tubes. They were exposed to the bacteria-laden aerosol for 10 minutes and clean air for 5 minutes, and then removed from the tubes and the bags (cat restrainers) and replaced in their cages. The solution delivered approximately 200 CFU/L of infectious aerosol and generated 50 to 100 granulomas per rabbit lung. Animals used to determine bacterial deposition were harvested 2 h postinfection.

Animals used in this study had been infected for a period of 90-120 days before sample collection.

5.1.1.2 Clinical Samples

Control human urine and plasma was obtained from healthy volunteers and human clinical samples were obtained from the International Tuberculosis Research Center facility in the Republic of Korea under ongoing clinical protocol NCT00341601 (clinicaltrials.gov). The study population consisted of subjects with pulmonary tuberculosis receiving treatment at the National Masan Tuberculosis Hospital, the largest tertiary referral centre for patients with previously treated and drug-resistant tuberculosis in the Republic of Korea. The hospital also serves as a site where the local population (~1,000,000) is treated as inpatients for new cases of tuberculosis. In all cases informed written consent was obtained prior to sample collection.

Regulatory compliance for this study was monitored by the Regulatory Compliance and Human Subjects Protection Branch of the NIAID. Sample collection was conducted in compliance with International Conference on Harmonisation Good Clinical Practices and all applicable regulatory requirements. The sample collection protocol was approved by all local Institutional Review Boards before commencement of sample collection.

5.1.2 HPLC/HRMS Instrumentation

The HPLC/HRMS instrument used was a Thermo Electron Corporation system consisting of a Finnigan LTQ ion trap coupled to an LTQ FT Ultra time-of-flight (TOF) mass spectrometer. The analytical column was a monolithic 0.1×150 mm Phenomenex high-density C₁₈ column, while the trap was as monolithic 0.2×24.25 mm Phenomenex high-density C₁₈ column. Solvent flow was controlled by a Waters nanoACQUITY HPLC system. HRMS data were acquired using Xcaliber software. Column temperature was maintained at 60°C unless otherwise noted. The HPLC/HRMS injection setup is shown in Figure 42. The trap was taken out of line for sample loading and the samples were injected backward onto the trap. The trap was then reconnected to the solvent pumps and allowed to equilibrate for 5 min before connecting it to the analytical column.

HPLC elution protocols were developed on an in-house Agilent liquid chromatography (LC) system with a diode array detector (DAD) for UV-visible absorbance detection, electrospray ionisation and an Agilent G1946D quadrupole mass selective detector (MSD). Column temperature was maintained at 60°C.

An 5 mM equimolar mixture of ferric synthetic carboxymycobactin (FeSCM), ferric synthetic mycobactin T (FeSMT), and FeMJ in DMSO was used as a positive control for all HPLC/MS experiments and was added to the sample to achieve the desired concentration. Synthesis of FeSCM and FeSMT is described in Section 6.1.3.2.

The HPLC methods that were optimised in the in-house LC system were translated for use on the HPLC/HRMS instrument located at the National Institute of Diabetes and Digestive and Kidney Diseases facility in Bethesda, Maryland, United States by Nicholas McBride with the support of John Lloyd. Of the experimental setup depicted in Figure 42, the instrument with nanospray needle, housing, pressure tubing, valve, and pumps was already in place while the choice of analytical column and trap system, as well as the solvent control protocol were developed and used by Nicholas McBride.

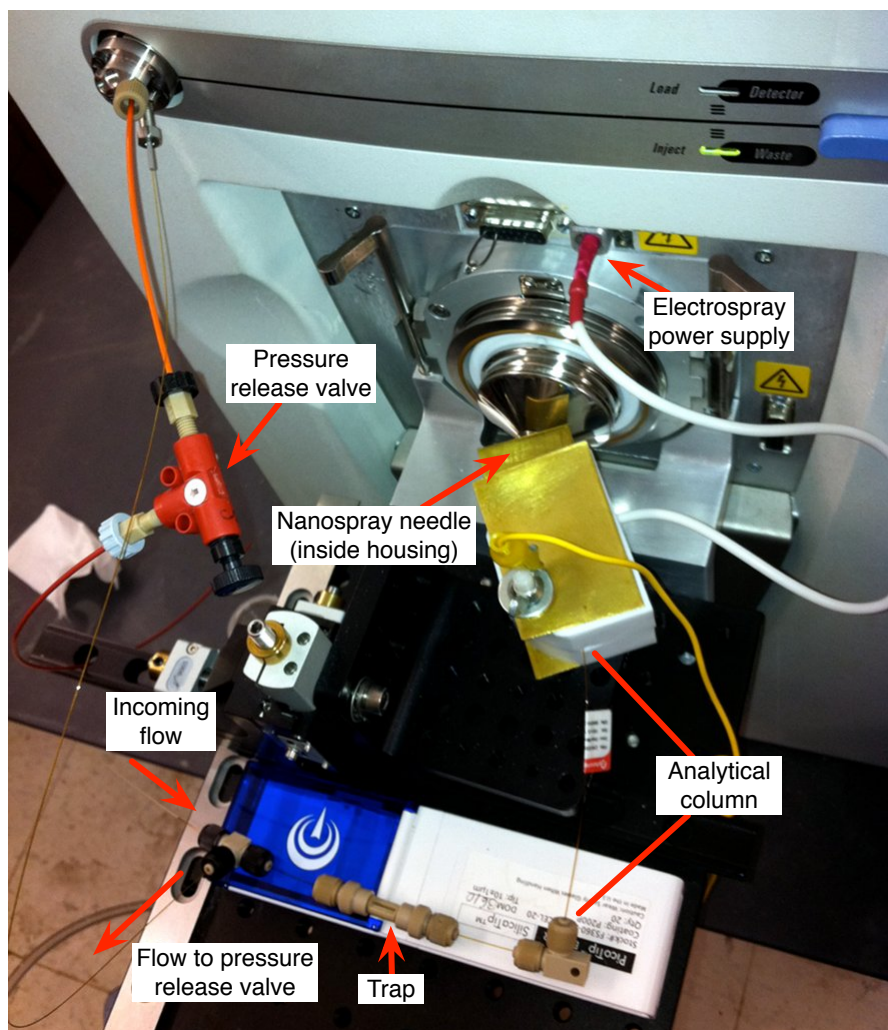


Figure 42: HPLC/HRMS injection configuration.

5.1.3 Extraction of Mycobactins from Biological Media for HPLC/HRMS Analysis

Mycobactins and carboxymycobactins were extracted from urine by shaking thrice with a 1:1 volume of chloroform. The organic layer was separated and filtered through Whatman #3 filter paper. It might be noted that filtration of mycobactins in organic solvents such as chloroform, ethyl acetate, and diethyl ether does not result in the same loss of material the as filtration of FeMJ dissolved in aqueous urine described in Section 4.2.2. Filtration of mycobactin dissolved in organic solvents has been used in many extraction protocols^{32, 53, 84, 100} including in Section 2.1.1.4, and in Section 4.2.2 it can be seen that even FeMJ collected on top of a reverse-phase column was successfully eluted with diethyl ether.

The majority of the solvent was removed under rotary evaporation and the sample was transferred to a small polytetrafluoroethylene (PTFE)-coated glass vial to dry under ambient conditions. This ensured that residue was collected in the conical

base of the vial. The residue was then taken up in methanol (5 μ L) and injected into water (45 μ L). The vial was then centrifuged at 4750 rpm for 10 min at 4°C to avoid injection of any precipitate into the instrument. The sample (25 μ L) was taken up into a syringe and injected onto the trap for HPLC/HRMS analysis as described above. Single ion chromatograms were obtained using a mass range of 10.0 ppm. A list of the mycobactin and carboxymycobactin ion masses that were screened is given in Appendix 2.

Mycobactins and carboxymycobactins were extracted from plasma by initially diluting the plasma sample 1:10 in water before shaking with a 1:1 volume of chloroform. Centrifugation was used to separate the organic phase, and it was filtered through Whatman #3 filter paper and processed as above.

Rabbit hair and stool samples underwent Soxhlet extraction. The samples were placed in a fiberglass thimble inside a Soxhlet extractor apparatus. Chloroform was refluxed through the apparatus for 48 hours, after which the solvent was removed under rotary evaporation and processed as above.

5.1.4 HPLC Method Development

5.1.4.1 Optimisation of HPLC Conditions

HPLC analysis of mycobactin was optimised on an in-house LC system. High-sensitivity HPLC/HRMS detection of mycobactins required the development of an extraction technique that would produce samples suitable for HPLC injection from biological specimens that range from quite small (600 μ L) to large (80 mL). The variability in specimen size stems from the desire to use as large a sample as possible to maximise the chances of mycobactin detection combined with the practical availability of difficult-to-obtain clinical materials. As such, conventional organic extraction techniques were used. In comparative extractions using chloroform and ethyl acetate it was found that FeSCM was extracted into chloroform with 34 fold better efficiency than into ethyl acetate. FeMJ and FeSMT were extracted into ethyl acetate with 6.4 fold better efficiency than into chloroform for a single extraction. This is demonstrated in Figure 43. Ethyl acetate extraction also led to co-extraction of significantly more unwanted material, which would limit the quantity of sample that could be injected into the

HPLC/HRMS system. Bearing both of these factors in mind, the triple chloroform extraction described above was selected.

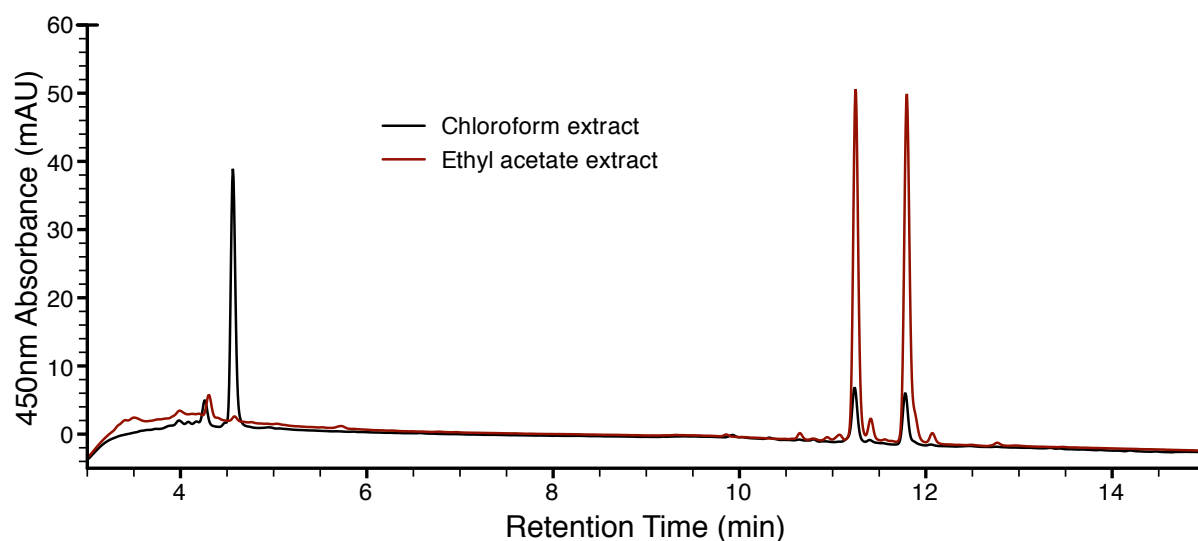


Figure 43: Comparison of chloroform versus ethyl acetate extraction of mycobactins from human urine via in-house LC/DAD; the three prominent absorbance peaks indicate the elution of FeSCM, FeMJ, and FeSMT respectively.

In order to select an appropriate column formulation for use with mycobactin and carboxymycobactin, several different stationary phases were tested to ascertain the degree of chromatographic separation that they would yield between different species of mycobactin. Figure 44 shows the difference in elution time (Δt) of different mycobactin compounds within the same chromatographic run. C_{18} and C_{18} -pentafluorophenyl (PFP) phases gave the highest resolution between different mycobactin compounds.

The results of a systematic optimisation of the MSD ionisation parameters are summarised in Figure 45. The best ionisation efficiency for a bolus injection of FeMJ was achieved using a fragmentation voltage of 160 V, drying gas flow rate of 9 L/min, and capillary voltage of 4 kV. Capillary voltages higher than 4 kV run the risk of arcing through the spray, which not only destroys the ionisation efficiency, but can also be damaging to the instrument.

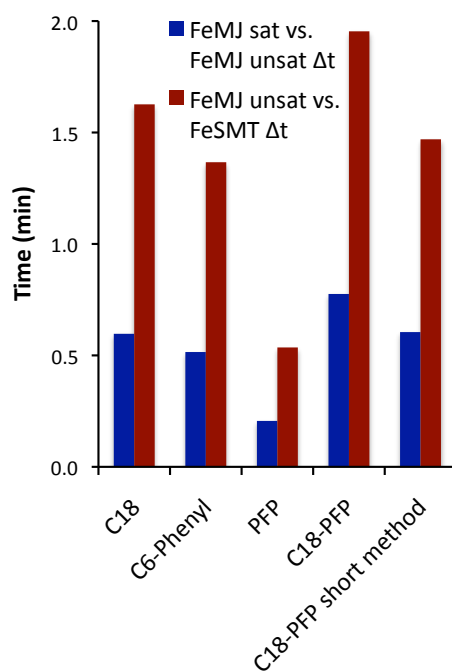


Figure 44: Comparison of different stationary phases for LC elution resolution. The y-axis measures the time between the elution of the mycobactin compounds indicated in the legend as a measure of resolution.

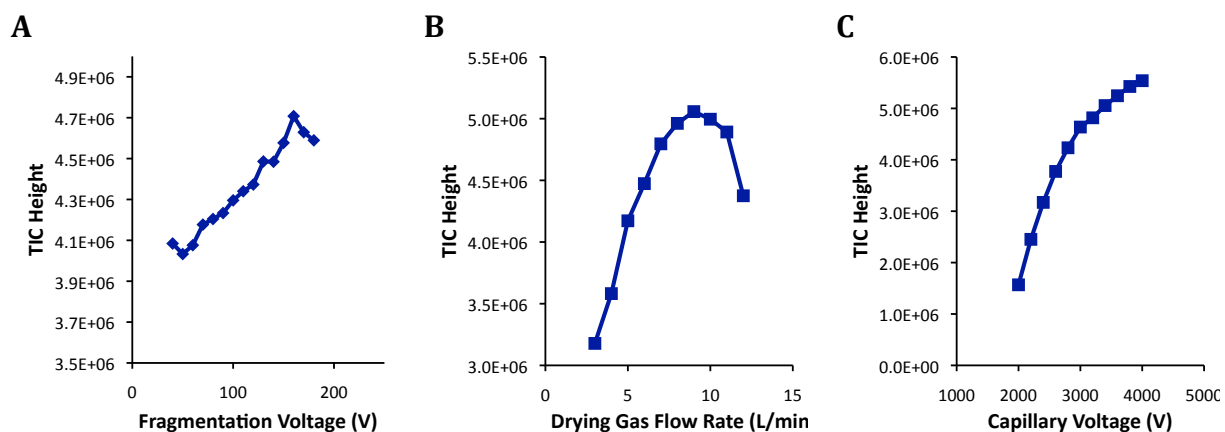


Figure 45: Optimisation of three mass spectrometry parameters; A: fragmentation voltage, B: drying gas flow rate, and C: capillary voltage. Signal was optimised to give the greatest total ion current (TIC) for a bolus injection of FeMJ.

The most important parameter that affects the sensitivity of an HPLC method is the solvent mixture gradient used for eluting the compound of interest. This was investigated utilising the in-house LC system with several different solvent profiles detailed in Figure 46. Figure 47 shows the peak 450 nm absorbance for each corresponding solvent profile. The following attributes were found to be important to maximise mycobactin sensitivity:

1. The initial equilibration concentration of mobile phase must be kept very low (2%), followed by stepping up to near the elution concentration for carboxymycobactin. This allowed the sample to adsorb to the column in a unified bolus before elution. This element is incorporated in the solvent profiles displayed as solid lines in Figure 46.
2. Because of the relatively disparate hydrophobic character of the carboxymycobactins and the lipophilic mycobactins, a step-up in mobile phase concentration was done between the elution of the carboxymycobactins and that of the lipophilic mycobactins. This helped to narrow the elution peaks of the lipophilic mycobactins while maintaining sensitivity for carboxymycobactins in the same chromatographic run and simultaneously shortening the run time.
3. The steepness of the gradient was adjusted to optimise peak sensitivity while minimising co-elution of interfering compounds.

The final method (NMC18PF9, see Figure 46) gathered all of these elements for optimal HPLC performance in detecting both carboxymycobactins and mycobactins.

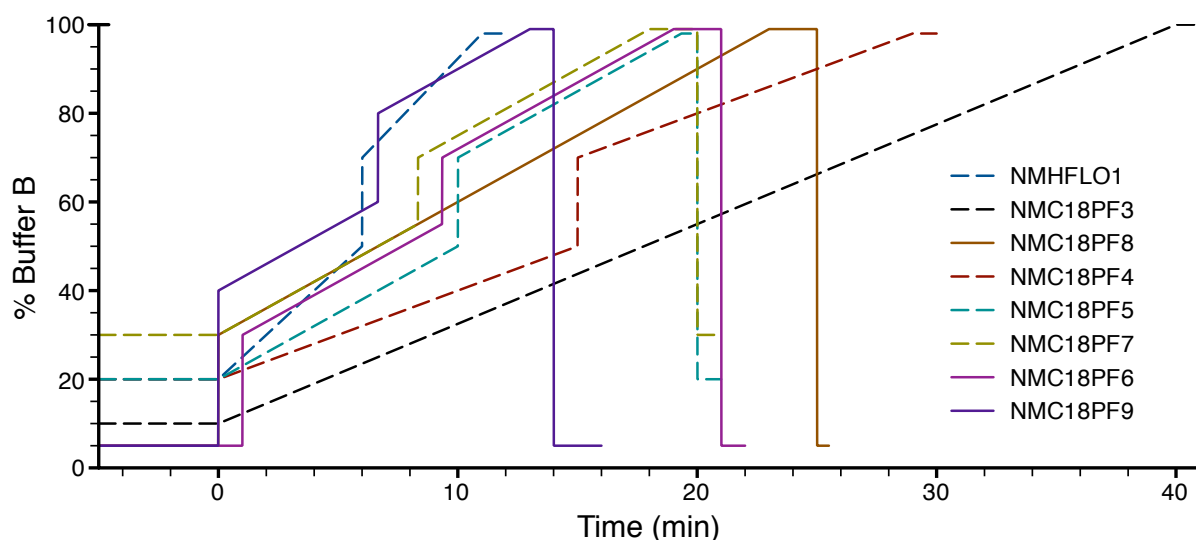


Figure 46: Solvent gradient profiles that were tested to optimise sensitivity for carboxymycobactins and mycobactins. Buffer A consisted of aqueous 0.1 percent formic acid, while buffer B consisted of acetonitrile with 0.1 percent formic acid.

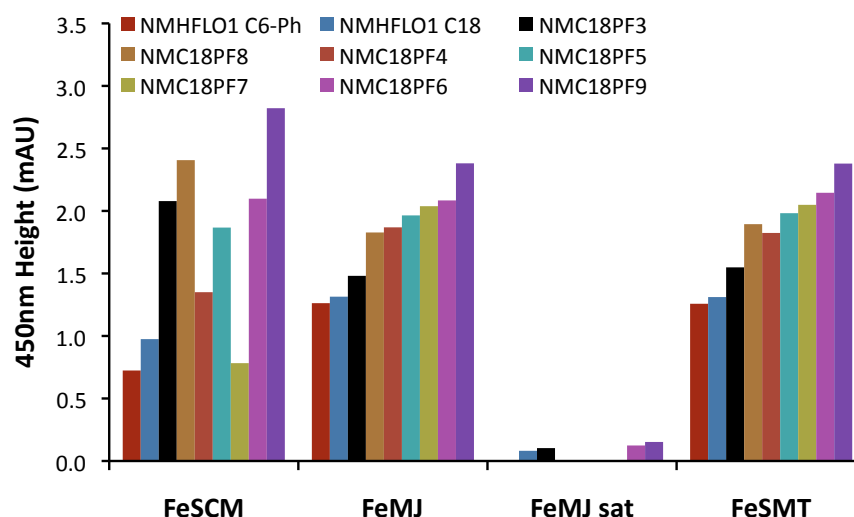


Figure 47: Results from elution of the test compounds using the solvent gradients displayed above. All elutions were done on a C₁₈-PFP column except for the NMHFLO1 method, which was tested on C₆-phenyl and C₁₈ core-shell columns as indicated. Note that the saturated form of FeMJ is only present in trace quantities in the control samples, whereas FeSCM, FeMJ, and FeSMT are present in equimolar quantities.

The optimised protocol was used to establish the lower limit of detection for a positive control sample comprised of equimolar FeSCM, FeMJ, and FeSMT. Figure 48 shows a chromatogram of extracted ions within 0.05 units of each compound's expected m/z ratio. An injection containing 50 fmol of each standard compound in 2% acetonitrile achieved a signal to noise ratio (S/N) of 3.3 and 3.7 for FeMJ and FeSMT respectively, however FeSCM only achieved a S/N of 0.5, suggesting that 300 fmol of FeSCM is required to achieve detectability with a S/N greater than 3. A standard consisting of 50 pmol of each compound is used to reference the expected elution times of each compound.

For comparison with the elution of naturally extracted mycobactins, a sample of mycobactin extract from the batch B supernatant (see Chapter 2) was run using this optimised LC/MSD method. The elution of these natural mycobactin compounds is shown in Figure 49. Note that the peaks are close together and there is overlap in some instances, however these are easily resolved by the differing m/z ratios of each compound, as described in Table 8 of Chapter 2. It should be noted that ferric siderophores can be identified by their M - 2 signal due to the ⁵⁴Fe isotope found in the natural abundance of 5.82 percent (thus producing an ⁵⁶Fe/⁵⁴Fe ratio of 15.7). This experiment verifies that natural mycobactins can be effectively detected using this method and to differentiate the various species by their mass signatures.

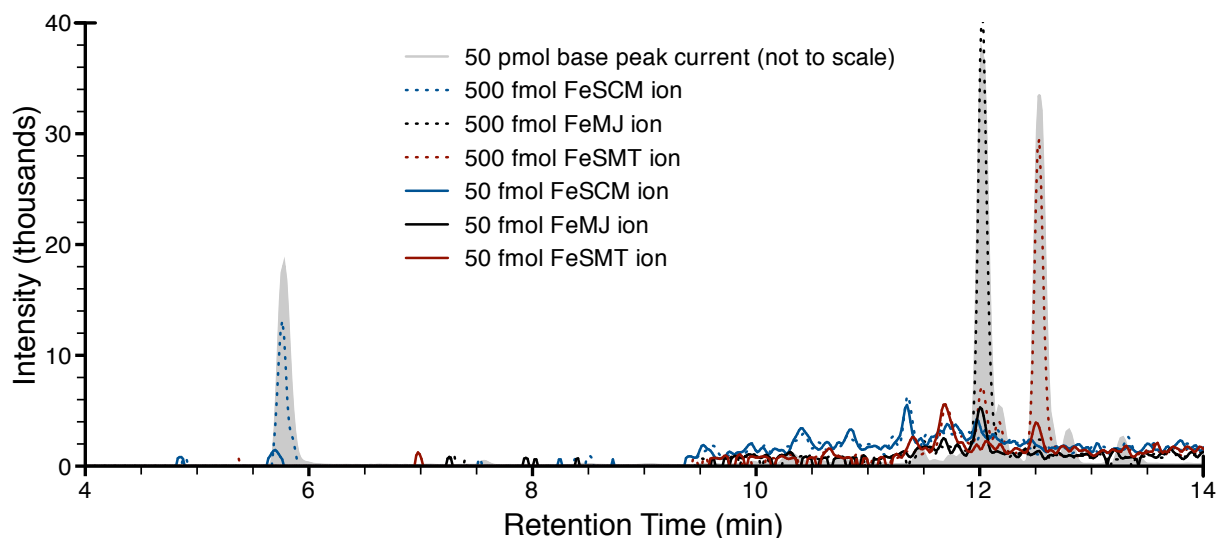


Figure 48: The limit of detection for the test compound is shown to be in the range of 50-500 fmol using the NMC18PF9 solvent profile; the 50 pmol standard (not to scale) is shown in gray to indicate the expected elution times of the standard compounds FeSCM, FeMJ, and FeSMT.

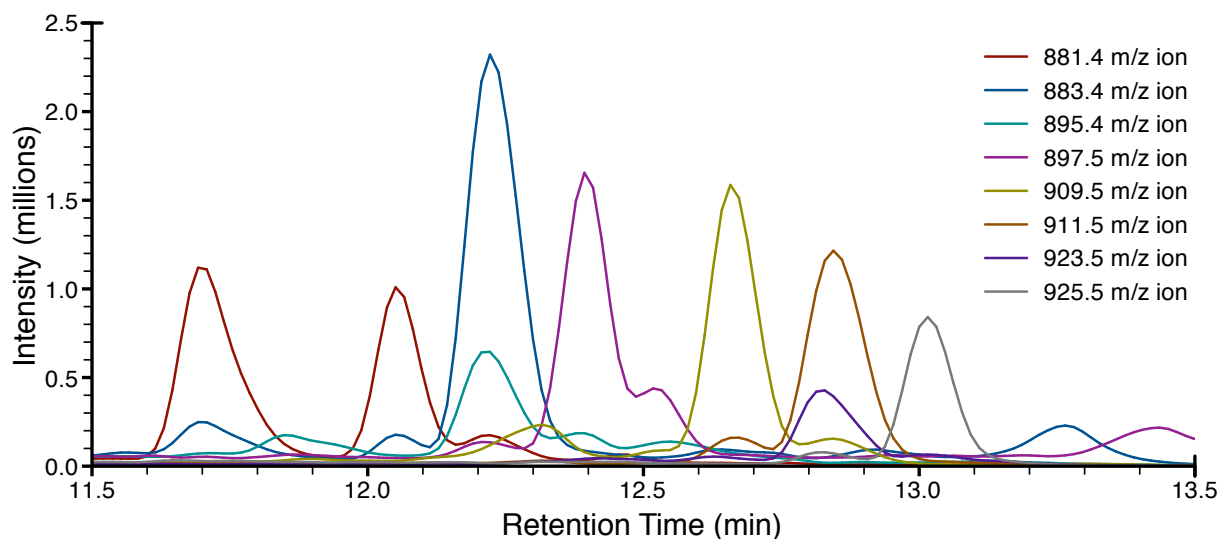


Figure 49: Elution of mycobactins extracted from *Mtb* culture using the optimised NMC18PF9 LC/MSD method.

5.1.4.2 Adaptation to High-Sensitivity HPLC/HRMS System

It was expected that the HPLC/HRMS system would greatly improve upon the limit of detection that was established using the LC/MSD due to both the ion trap TOF mass detection setup versus the MSD and the increased mass resolution, which would result in an improved S/N.

As the HPLC/HRMS instrument uses very low flow rates to achieve superior nanospray efficiency, there were a few parameters that had to be adjusted. The capillary column that was required for using the C₁₈-PFP stationary phase was found to cause precipitation of the sample at the end caps and was thus abandoned in favour of a

monolithic C₁₈ capillary column. Elution at 60°C improved the amplitude of the ion signal over elution at 20°C by a factor of 2.9 for FeSCM, 11.9 for FeMJ, and 19.8 for FeSMT, as can be seen in Figure 50.

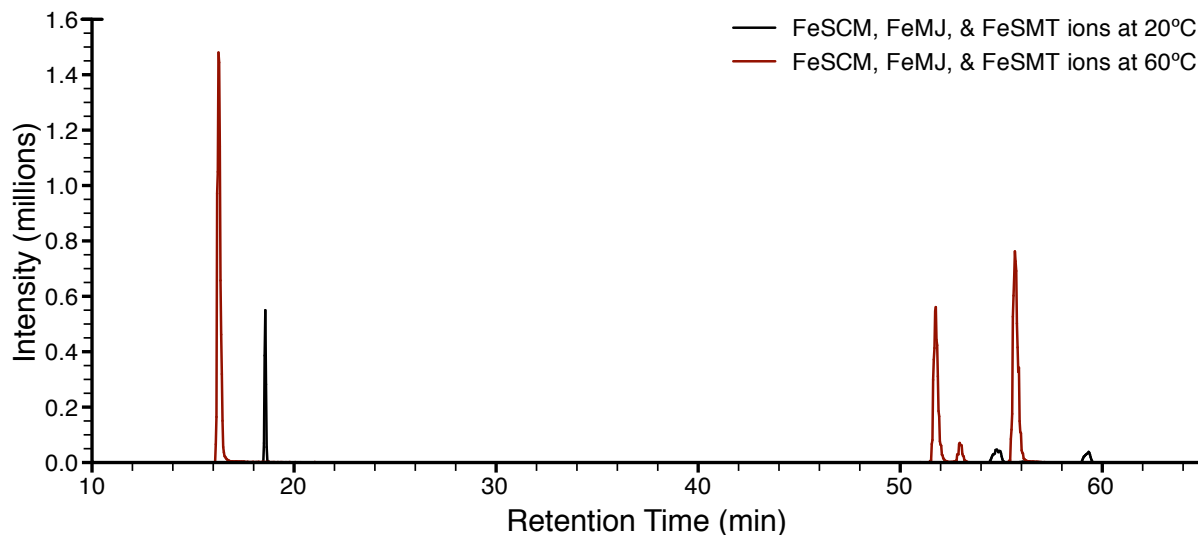


Figure 50: Combined ion chromatograms of FeSCM, FeMJ, and FeSMT (2.5 pmol) eluting at 20°C and 60°C.

5.2 Results and Discussion

5.2.1 Limit of Detection in Urine and Plasma

In order to test the limit of detection for mycobactins in urine through the entire sample extraction and analysis process, healthy human urine was spiked with the mycobactin positive control compound mixture. This was intended to be representative of mycobactin compounds in the urine of infected TB patients. Using the chloroform extraction process described in the methods section and analysis by HPLC/HRMS, a urine sample that was spiked with 50 fmol of the standards yielded a satisfactory S/N of 6.0 for FeMJ and 2.8 for FeSMT, as shown in Figure 51A. The amplitude of the FeSCM signal was much lower, perhaps due to poorer ionisation than the lipophilic compounds, however the noise level in the FeSCM ion range was also lower (Figure 51B), allowing a S/N of 1.2 to be achieved at 50 fmol of spiked compound. From this it was calculated that 150 fmol of FeSCM in the original urine sample would be required in order to achieve a satisfactory S/N for detection.

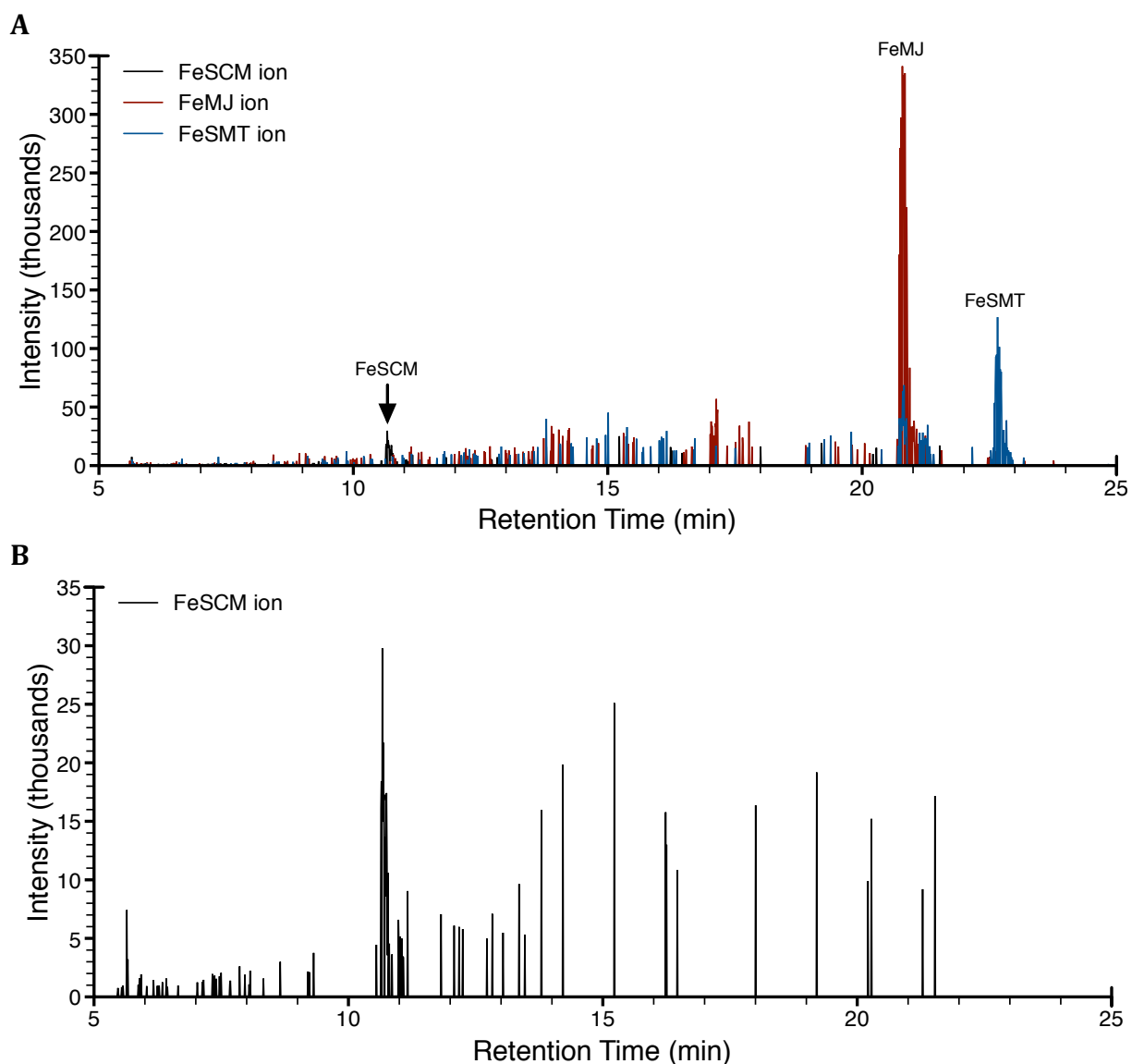


Figure 51A: HPLC/HRMS chromatogram of extract from human urine spiked with 50 fmol of FeSCM, FeMJ, and FeSMT. **B:** An enlarged plot of the FeSCM ion signal alone to give detail.

Extraction of mycobactins from plasma was more difficult than urine because of the high content of proteins and other organic-soluble compounds. The extraction method had to be adjusted to include the dilution step described in the methods. This improved the yield of the extraction, but the achievable limit of detection was still higher than for urine. This result is probably due to poorer extraction of these compounds from the more complex biological matrix and highlights the potential problems in identifying the presence of mycobactins in any sample of biological origin. Interestingly, in plasma FeSCM was easier to detect than the lipophilic mycobactins. The limit of detection for FeSCM was 350 fmol versus at least 1 pmol for the lipophilic mycobactins. Figure 52 shows HPLC/HRMS analysis of 2 pmol of standard compounds spiked into 6 mL of plasma, which yielded a S/N of 16.1, 8.6, and 3.6 for FeSCM, FeMJ, and FeSMT

respectively. The HPLC/HRMS limit of detection from spiked samples is summarised in Table 11.

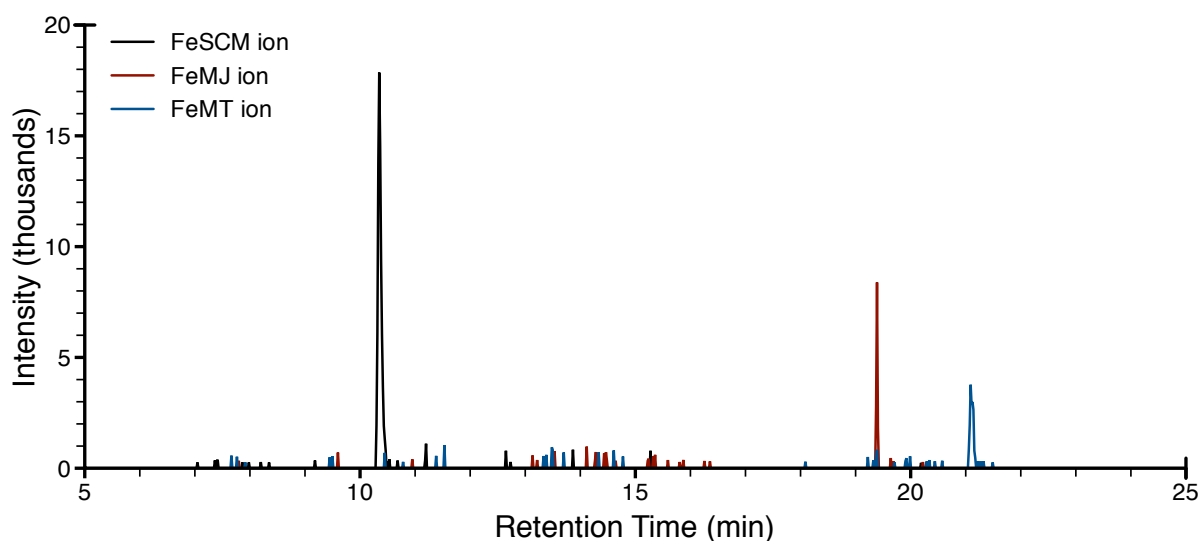


Figure 52: HPLC/HRMS chromatogram of extract from human plasma spiked with 2 pmol of FeSCM, FeMJ, and FeSMT.

Table 11: HPLC/HRMS limit of detection for siderophores spiked into either urine of plasma.

	Limit of Detection	
	Carboxymycobactin	Mycobactin
In spiked urine	150 fmol	50 fmol
In spiked plasma	350 fmol	1000 fmol

The raised limit of detection for lipophilic mycobactins is consistent with the idea that they associate strongly with plasma components, making their extraction with organic solvents more difficult. The lipophilic compounds may be binding irreversibly to lipoprotein, cholesterol, and triglyceride components of plasma, or to albumin and other proteinaceous components. The same phenomenon would contribute to the poorer detection of FeSCM in plasma as compared with urine, but would not affect FeSCM as strongly as with the lipophilic mycobactins. The prospect that this occurs so readily calls into question the likelihood of these compounds traversing the body from their source in the lungs to be detectable in significant quantities in the urine or any other sample.

5.2.2 Analysis of Clinical Tuberculosis Samples

Using these methods, Table 12 summarises the various samples from infected animal models and TB patients that were extracted and analysed via HPLC/HRMS. No mycobactins were detected in any of the samples tested. The final two columns list the limit of detection back calculated to account for the sample size and injection volume for each sample to estimate the effective limit of detection for ferric carboxymycobactin (FeCM) and ferric mycobactin T (FeMT) within each original sample. The limits of detection reflect both the efficiency of the extractions from either urine or plasma and the limitations of the instrument, thereby taking into account any irreversible adsorption and retention on the sample matrix. These results are disappointing, particularly in view of the identification of other lipid antigens such as LAM in urine of infected patients. However, they highlight the ambiguity associated with correlating mycobactin excretion with TB infection.

Table 12: List of animal and human clinical samples analysed by HPLC/HRMS.

Subject	Species	Study Enrolment Week	Sample	Sample Size	Extraction	Material Extracted	Mycobactins Detected	FeCM Effective Limit of Detection	FeMT Effective Limit of Detection
R1	Rabbit		Urine	12 mL	3X CHCl ₃ , 1X EtAc	2.97 mg (CHCl ₃)	0	41.7 pM	13.9 pM
R2	Rabbit		Urine	2 mL	1X CHCl ₃		0	107.1 pM	35.7 pM
R3	Rabbit		Urine	0.5 mL	1X CHCl ₃		0	428.6 pM	142.9 pM
R4	Rabbit		Urine	5 mL	3X CHCl ₃ , 1X EtAc		0	60.0 pM	20.0 pM
R5	Rabbit		Hair		CHCl ₃ 48 hrs Soxhlet	0.75 mg	0		
			Stool		CHCl ₃ 48 hrs Soxhlet	60.81 mg	0		
R6	Rabbit		Hair	300 mg	CHCl ₃ 48 hrs Soxhlet	5.73 mg	0		
			Stool	2.1 g	CHCl ₃ 48 hrs Soxhlet	79.25 mg	0		
R3	Rabbit		Hair	339 mg	CHCl ₃ 48 hrs Soxhlet		0		
			Stool	1.98 g	CHCl ₃ 48 hrs Soxhlet		0		
R1	Rabbit		Urine	12 mL	3X CHCl ₃	~0.2 g	0	41.7 pM	13.9 pM
R7	Rabbit		Urine	70 mL	3X CHCl ₃	6.22 mg	0	4.3 pM	1.4 pM
R8	Rabbit		Urine	80 mL	3X CHCl ₃	5.52 mg	0	3.8 pM	1.3 pM
H1	Human	0	Urine	6 mL	3X CHCl ₃	1.03 mg	0	50.0 pM	16.7 pM
H2	Human	0	Urine	6 mL	3X CHCl ₃	0.92 mg	0	50.0 pM	16.7 pM
H3	Human	0	Urine	6 mL	3X CHCl ₃	9.00 mg	0	50.0 pM	16.7 pM
H4	Human	0	Urine	10 mL	3X CHCl ₃	2.62 mg	0	30.0 pM	10.0 pM
H5	Human	0	Urine	10 mL	3X CHCl ₃	1.28 mg	0	62.5 pM	20.8 pM
H6	Human	6	Urine	40 mL	3X CHCl ₃	19.51 mg	0	7.5 pM	2.5 pM
H7	Human	8	Urine	40 mL	3X CHCl ₃	8.79 mg	0	7.5 pM	2.5 pM
H6	Human	4	Urine	40 mL	3X CHCl ₃	14.33 mg	0	7.5 pM	2.5 pM
H5	Human	0	Plasma	0.6 mL	H ₂ O dilution, CHCl ₃	0.37 mg	0	729.2 pM	2083.3 pM
H6	Human	0	Plasma	0.6 mL	H ₂ O dilution, CHCl ₃	0.67 mg	0	1166.7 pM	3333.3 pM
H7	Human	0	Plasma	0.6 mL	H ₂ O dilution, CHCl ₃	0.44 mg	0	729.2 pM	2083.3 pM

5.3 Conclusions

HPLC/HRMS analysis was able to achieve an effective lower limit of detection for mycobactin that is below or within the physiological levels of mycobactin production that were calculated in Chapter 2. Notwithstanding this, neither carboxymycobactin nor mycobactin were detected in any of the infected animal models or clinical patient samples.

A higher degree of sensitivity was not possible due to the limited efficiency of extracting the siderophores from the samples, which had to contend with irreversible adsorption of the siderophores to the sample matrix proteins and other components, particularly in the case of plasma samples. If these compounds are present within the plasma or urine of infected individuals, they either fail to be extracted with a high-enough degree of efficiency in the protocol developed here, or are only to be found at very low concentrations below the current detection threshold. On the other hand, it is certain that *Mtb* produces mycobactin *in vivo*, but many questions remain regarding the trafficking of this siderophore. The use of direct sputum and saliva samples was not investigated in this study, and sputum, while not ideal, may still provide a superior sample matrix for diagnosing TB through siderophore detection.

As first discussed in Section 1.1.3.2, *Mtb* glycolipid lipoarabinomannan (LAM) has been detected in the urine as a potential diagnostic biomarker²¹² despite the strong lipophilic character of its structure, complemented by hydrophilic head groups, much like mycobactin²⁴. This provided part of the rationale that mycobactin may also be detectable in urine. However, it now seems evident that mycobactin is not present in the urine at levels that would warrant its usefulness as a diagnostic biomarker. This may be due to the fact that relatively little mycobactin is produced in comparison to LAM, which composes a significant portion of the mycobacterial cell wall where they are anchored to the cell surface by their lipid components¹². LAM is also shed and trafficked outside of the bacterium⁸, possibly as a means of causing inflammation advantageous to *Mtb*¹⁰. While there is a strong case for the extracellular trafficking of mycobactin¹⁸⁶, it is still unclear whether mycobactin behaves in a similar fashion or in comparable quantities within the immediate environment of the bacterium.

There is still considerable scope to improve the detection limit through the use of sample capture and concentration methods, alternative detection methods, or by

utilising other sampling media, such as saliva or sputum, which may prove more fruitful in the search for mycobactin and carboxymycobactin *in vivo*.

6 Further Development of Mycobactin Assays

As an outcome of this thesis, the electrochemical properties of mycobactin have been elucidated and a protocol has been outlined for a mycobactin assay. However, while culture studies place the likely mycobactin levels in the range of 0.85-250 nM (Chapter 2), which is achievable for the electrochemical assay including a preconcentration step (Chapter 4), no mycobactin could be detected in clinical samples of urine and plasma from infected patients (Chapter 5). Yet it remains tantalising that the culture studies suggest mycobactin could become a useful analytical target. Thus, preliminary work was undertaken to:

1. Develop a method to improve the electrochemical assay through capture ligand modification of the electrode.
2. Develop synthetic mycobactin and carboxymycobactin standards and validate their function in Fe uptake by *Mtb*. Based on these data, the synthetic siderophores can be assessed as potential PET imaging probes and as antigens to which anti-mycobactin antibodies may be raised.

The ability to specifically bind mycobactin and thereby concentrate it close to the electrode surface has the potential to greatly increase the sensitivity of the assay as well as provide greater signal stability. The carboxymycobactin-binding capabilities of Lcn2 were reviewed in Section 1.2.3.2. This human protein may hold the key to enabling specific binding of mycobactins close to the surface of the electrode for electrochemical interrogation. Design elements for a prospective biosensor device and receptor immobilisation strategy are shown in Figure 53. In Figure 53B a protein receptor, such as Lcn2, that specifically binds ferric mycobactin is immobilised to the electrode via a hexahistidine tag. In the presence of ferric siderophore, cyclic voltammetry or other electroanalytical methods can be used to interrogate the iron centre, producing a signal with superior sensitivity than for the siderophore in bulk solution.

In making the first steps toward creating a Lcn2-based biosensor the initial cloning of Lcn2 is reported in this chapter together with preliminary synthesis and electrodeposition of an immobilisation ligand onto the surface of a GCE.

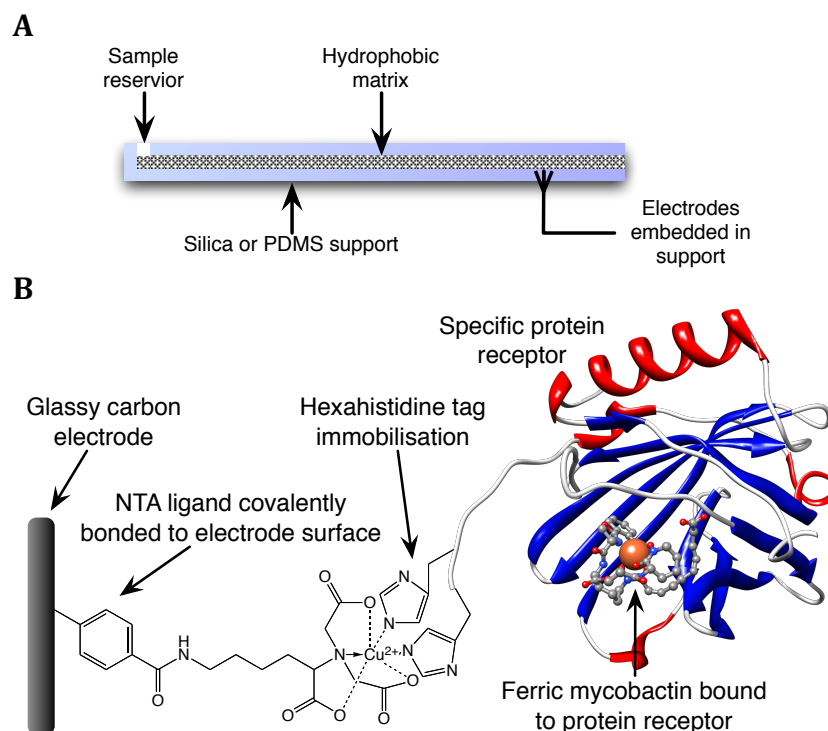


Figure 53A: Lateral flow device design that could be used for concentrating mycobactin from a sample into a small volume for electrochemical analysis. B: Example of a specific receptor (Lcn2) for mycobactin bound to the electrode surface.

An alternative strategy in capture ligand development would be to use antibodies against mycobactin. The development of the synthetic mycobactin compounds would allow the first antibodies against mycobactin and carboxymycobactin to be raised. Synthetic mycobactins and carboxymycobactin would also provide structurally authentic and pure materials to be used as standards for assay development. As seen in Chapter 5, mycobactin and carboxymycobactin differ significantly in their extraction and detection properties. FeMJ is limited in its capacity as an analytical standard because, as an extract of biological origin, it is composed of multiple siderophore structures (see Section 2.2.3) and contains other impurities as well. Furthermore, the development of synthetic mycobactin is useful for research on the use of siderophores as PET imaging agents, as discussed in Section 1.4.

As such, suitable, purified synthetic materials were created for both mycobactin and carboxymycobactin. The target synthetic compounds are shown in Figure 54. This was desirable since it is still unconfirmed which siderophore would be more prevalent within the tissues of infected individuals.

This synthetic standard also allowed studies to be carried out that elucidate the mechanism of *Mtb* iron acquisition and the question of whether lipophilic mycobactin or

water-soluble carboxymycobactin acts as the primary extracellular siderophore. This question, extends the work in Chapter 2, and is important in order to ascertain which siderophore must be targeted as a marker for TB.

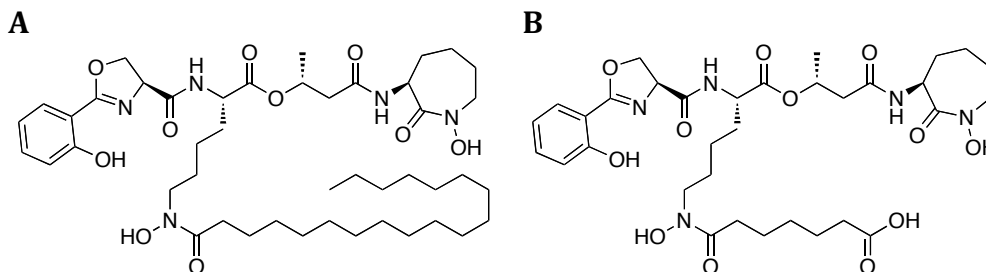


Figure 54: Structure of synthetic mycobactins. A: Synthetic mycobactin T (SMT). B: Synthetic carboxymycobactin (SCM).

6.1 Materials and Methods

6.1.1 Cloning of Lcn2

Lcn2 was cloned from the human cDNA (accession NM_005564, purchased from OriGene) and ligated into the pET28b expression vector for expression with an amino-terminal hexahistidine tag in BL21 *E. coli*. After induction of expression using isopropyl- β -D-thio-galactoside (IPTG), Lcn2 was purified by nickel-affinity chromatography. Sodium dodecyl sulfate polyacrylamide gel electrophoresis (SDS-PAGE)²¹³ was performed using a 4-12% polyacrylamide gradient gel (Novex).

6.1.2 NTA Immobilisation Ligand

6.1.2.1 Synthesis of NTA Immobilisation Ligand

In order to functionalise a GCE with nitrilotriacetic acid (NTA), 4-aminophenyl-NTA was first synthesised using the synthetic scheme shown in Figure 55 and described previously²¹⁴. The synthesis was carried out with three times the original quantities of reagents and the final recrystallisation from heptane-toluene was omitted.

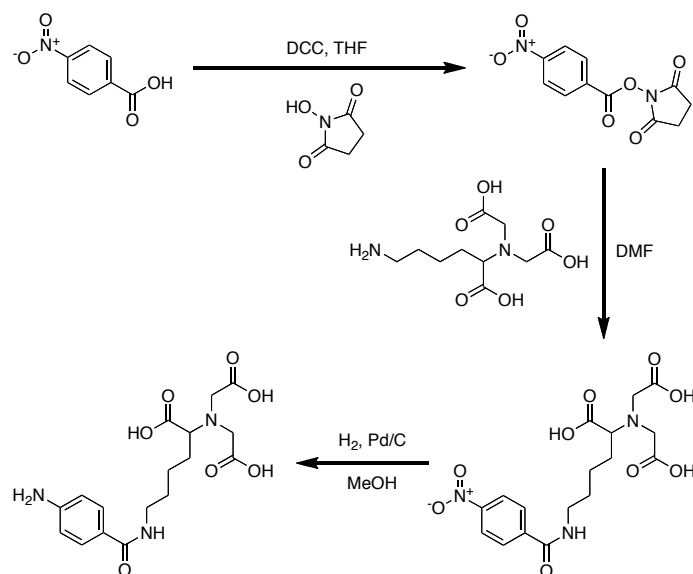


Figure 55: Synthesis of 4-aminophenyl-NTA.

6.1.2.2 Deposition of NTA onto the Electrode Surface

Deposition of 4-aminophenyl-NTA onto the electrode surface was performed as described previously²¹⁴ and follow-up electrochemistry was carried out in aqueous 1 mM ferricyanide ($\text{Fe}(\text{CN})_6$), 0.1 M potassium chloride, and in the presence of either phosphate buffer (pH 7.5) or HCl (pH 1.0).

6.1.3 Synthesis of Mycobactins

Synthesis of mycobactins was carried out by Tobin J. Dickerson and Petr Čápek at Scripps Research Institute and the products of this effort are evaluated in this chapter. This synthesis and accompanying evaluation form the basis of one manuscript that has been submitted for publication²¹⁵.

6.1.3.1 Synthesis of Mycobactin T Using the Reported “Minimal Protecting Group Strategy”

Oxazoline fragment **4** was prepared in 50% overall yield from commercially available material as described previously (Figure 57)¹⁵². Briefly, methyl salicylate **2** was protected with benzyl bromide followed by saponification of the methyl ester to give the benzyl ether of salicylic acid. This molecule was then coupled with L-serine benzyl ester and the resulting amide **3** cyclised to the corresponding oxazoline with

Burgess's reagent. Finally, both benzyl protecting groups were cleaved by catalytic hydrogenolysis leading to oxazoline fragment **4**.

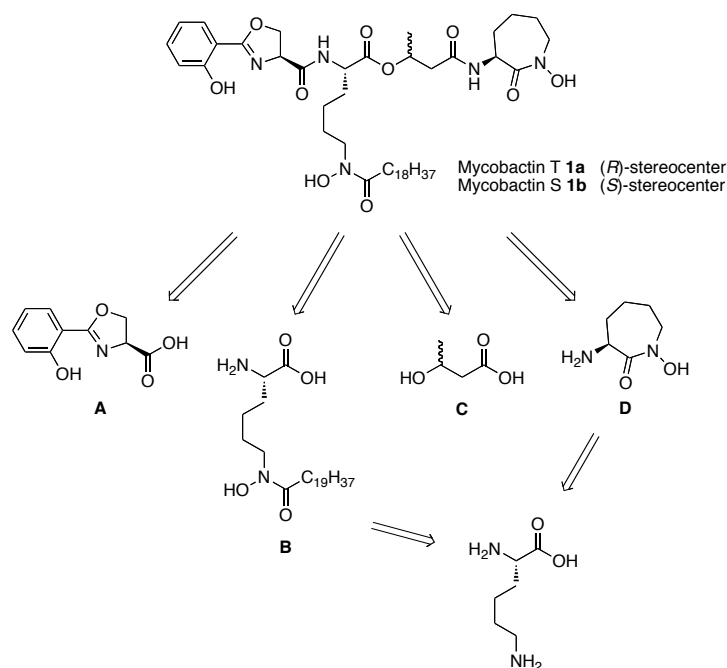


Figure 56: Retrosynthetic analysis of mycobactin T **1a and mycobactin S **1b**. In mycobactin T, the stereocentre is of the *R* configuration and in mycobactin S, this stereocentre is of the *S* configuration.**

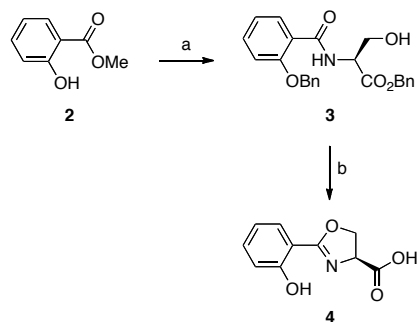


Figure 57: Synthesis of oxazoline fragment **4. Reagents and conditions: (a) (i) BnBr, K₂CO₃, MeOH/DCM 1:1, reflux, overnight, 88%; (ii) NaOH, dioxane/water, reflux, 2 h, 93%; (iii) L-serine-OBn, EDC, DCM, RT, overnight, 89%; (b) (i) Burgess's reagent, THF, reflux, 30 min, 66%; (ii) H₂, 10% Pd/C, MeOH, 2 h, 99%.**

Using commercially available α -Cbz-L-lysine as a starting material, both linear hydroxamic acid fragment **11**, which possesses a nonadecanoyl fatty tail representative of mycobactin T and S, and caprolactam hydroxamic acid **8** were synthesised from a common precursor (Figure 58)²¹⁶. Condensation of Cbz-L-lysine with benzaldehyde was followed by oxidation with *meta*-Chloroperoxybenzoic acid (*m*-CPBA) to form the corresponding oxaziridine intermediate, which was then isomerised under acidic conditions to nitron **6**. Heating of **6** with NH₂OH·HCl in methanol gave hydroxylamine

7, which was used as a common intermediate leading to both hydroxamic acid building blocks. In one route, hydroxylamine **7** was treated with thionyl chloride in methanol and the resulting methyl ester **9** was acylated with an excess (4 equivalents) of nonadecanoyl chloride to give a bis-acylated hydroxyl-amine. The undesired *O*-nonadecanoyl group was then removed by treatment with 6% *N,N*-Diisopropylethylamine (DIPEA) in methanol to form **10** in 36% overall yield from α -Cbz-L-lysine. Quantitative deprotection by hydrogenolysis of the Cbz group then afforded the desired building block **11**. In order to make fragment **8**, hydroxylamine **7** was cyclised using ethyl(dimethylaminopropyl) carbodiimide (EDC)/1-hydroxy-7-azabenzotriazole (HOAt) to generate the desired caprolactam hydroxamic acid²¹⁶.

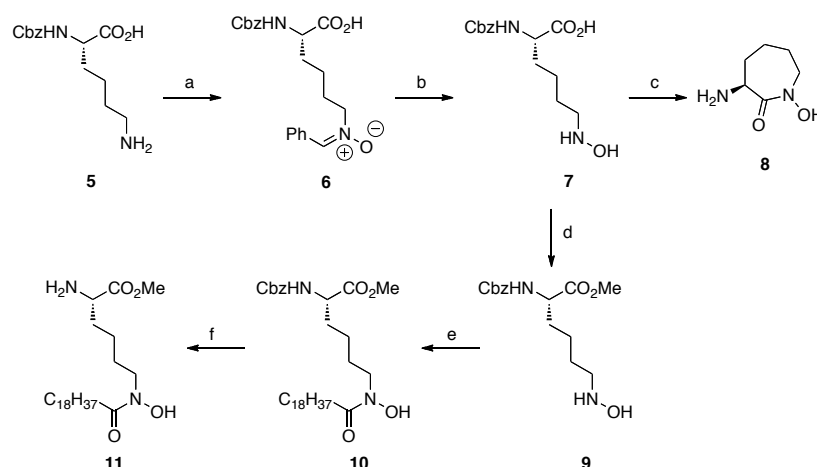


Figure 58: Synthesis of unprotected hydroxamic acid fragments. Reagents and conditions: (a) (i) PhCHO, KOH, MS, MeOH, overnight, RT; (ii) m-CPBA, MeOH, 0 °C to RT, 5 h; (iii) TFA/DCM, 1:1, RT, 1 h; (iv) PhCHO, EtOAc, 0 °C to RT, 2 days, 66% over 4 steps; (b) NH₂OH·HCl, MeOH, 65 °C, 20 min, 87%; (c) (i) EDC/HOAt, NaHCO₃, CH₃CN, DMF, RT, 48 h, 50%; (ii) H₂, Pd/C, MeOH, 2 h, 97%; (d) SOCl₂, MeOH, 0 °C to RT, 12 h, 83%; (e) (i) nonadecanoyl chloride, NaHCO₃, DCM, RT, overnight; (ii) 6% DIPEA in MeOH, RT, 2 days, 76% over 2 steps; (f) H₂, Pd/C, MeOH, RT, 2 h, 95%.

Final assembly of four fragments was done in convergent fashion following the strategy highlighted above (Figure 59)^{153, 216}. First, linear hydroxamic acid **11** was coupled to oxazoline fragment **4** in a EDC/HOAt-mediated amide bond forming reaction to provide methyl protected mycobactic acid **13a**. Free mycobactic acid **13b** was prepared by saponification of the methyl ester with 3 eq. of LiOH^{153, 216} or alternatively, using the milder reagent Ba(OH)₂. Cobactin **14** was prepared by EDC/HOAt/4-dimethylaminopyridine (DMAP) mediated coupling of caprolactam hydroxamic acid **8** and commercially available (*R*)- β -hydroxybutyric acid **12a**. As previously observed, the product of this reaction was extremely difficult to isolate²¹⁶ and as such the coupling of mycobactic acid **13b** and cobactin **14** was performed in a one-pot reaction in the same

flask, as previously described. The final coupling of the sequence was initiated by addition of **13b** and an equivalent of EDC·HCl directly to the cobactin reaction mixture after consumption of all hydroxamic acid **8** (less than 4 h). The reaction was then stirred at room temperature overnight to produce coupling product **15**, which could be isolated by chromatography. The final product was characterised using standard methods and was consistent with previous literature data.

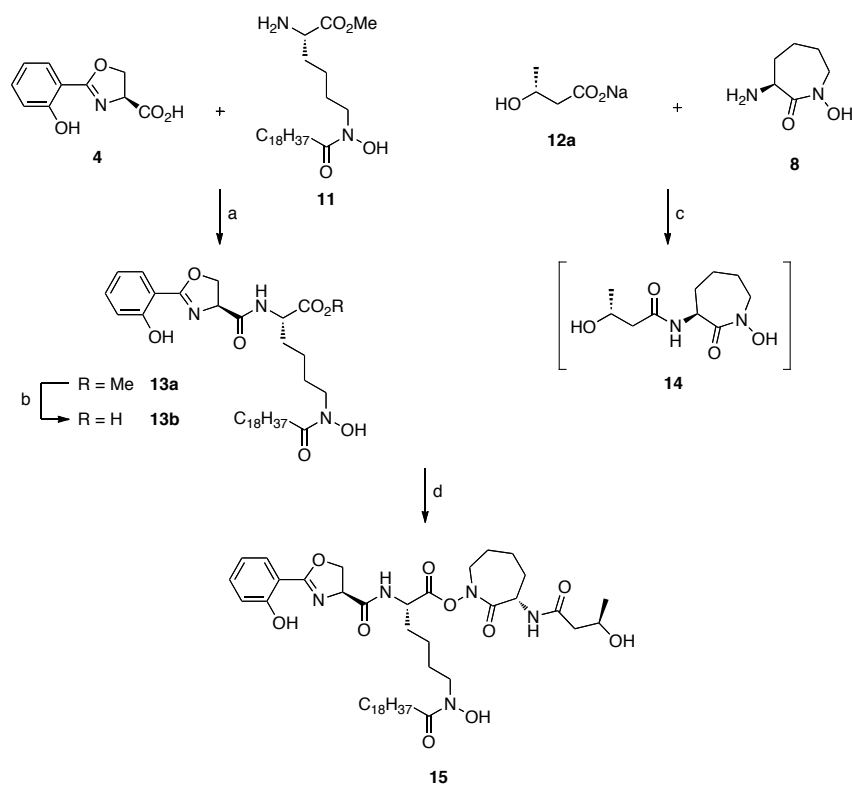


Figure 59: Assembly of fragments using the reported “minimal protecting group” strategy. Reagents and conditions: (a) EDC/HOAt, DCM, RT, 6 h, 49%; (b) Ba(OH)₂, THF/water, RT, 1 h, 95%; (c) EDC·HCl/HOAt and catalytic DMAP, DMF, RT, 4 h; (d) EDC/HOAt, DMAP (cat.), DMF, RT, 16 h, 55% over 2 steps.

This miscoupled product **15** would form during the final coupling that was intended to result in the desired internal ester present in the natural product. To test this hypothesis, the hydroxamate moiety of the caprolactam hydroxamic acid fragment was protected and the coupling of protected cobactin fragment **16a** attempted (Figure 60). This reaction was performed under identical conditions as the reaction of unprotected cobactin with mycobactinic acid using EDC/HOAt and catalytic DMAP in DMF (Figure 59)^{153, 216} however, the desired coupling product was not detected by LCMS after overnight incubation. Instead, under these conditions mycobactinic acid **13b** cyclised to form cyclic product **17** which was isolated together with unreacted starting material.

Cyclised product **17** was highly unstable in solution. Attempts to generate the desired product, including increased reaction temperature (up to 60°C), reaction time and/or additional DMAP catalyst, did not result in the desired coupling, suggesting that the β -hydroxyacid fragment is not reactive enough under these conditions to form an ester with mycobactinic acid.

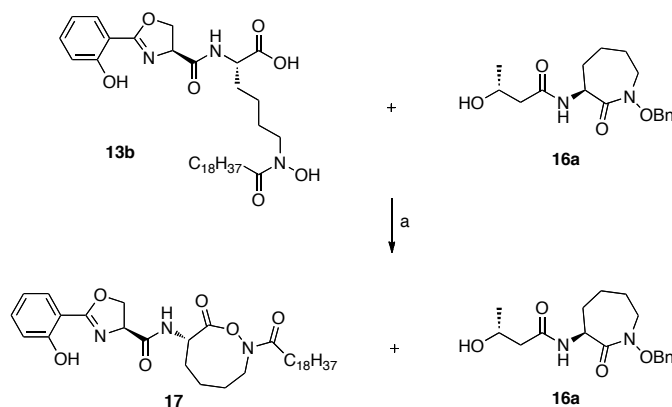


Figure 60: Assembly of benzyl protected fragments. Reagents and conditions: (a) EDC/HOAt, catalytic DMAP, DMF, RT, 16 h.

6.1.3.2 Revised Synthesis of Mycobactins

Benzyl protected caprolactam hydroxamic acid was synthesised by a published procedure¹⁵¹ with several modifications (Figure 61). α -Cbz-L-lysine was treated with sodium nitroprusside in basic aqueous solution to form Cbz-hydroxynorleucine intermediate **18**¹⁵¹, that was converted without purification to benzyl hydroxamate **19** by EDC-mediated coupling with *O*-benzyl hydroxylamine. This product was then iodinated and cyclised in the presence of base to provide benzyl-protected cyclic hydroxamic acid fragment **20a**. Cyclisation of **19** in dimethylformamide (DMF) with Cs₂CO₃ was performed instead of the previously reported cyclisation with mesyl hydroxamate performed in refluxing acetone in the presence of K₂CO₃¹⁵¹. This synthetic route gave cyclic benzyl hydroxamate in 4 steps with a yield of 32% (Figure 58). The Cbz protecting group of **20a** was selectively cleaved in the presence of the benzyl protected hydroxamate using 33% HBr in acetic acid (AcOH) to quantitatively yield amine intermediate **20b**, which could be subsequently coupled with the sodium salt of (*R*)- or (*S*)- β -hydroxybutyric acid to give benzyl-protected cobactins **16a** and **16b**.

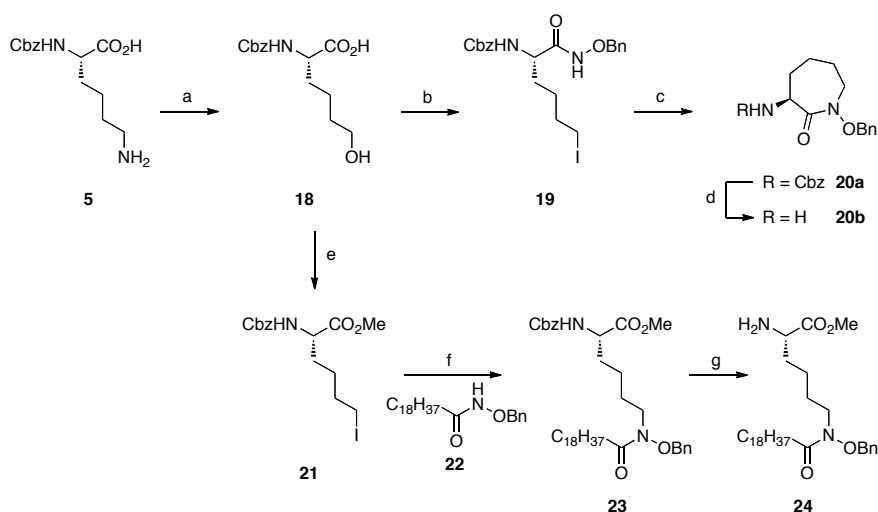


Figure 61: Synthesis of cyclic and linear benzyl hydroxamate fragments. Reagents and conditions:
 (a) $\text{Na}_2[\text{Fe}(\text{CN})_5\text{NO}]$, water, pH 9.5, 60 °C, 6 h, 86% (crude); (b) (i) $\text{NH}_2\text{OBn}\cdot\text{HCl}$, EDC, THF/water, pH 4, 2 h, 45%; (ii) I_2 , PPh_3 , imidazole, THF, RT, 1 h, 80%; (c) Cs_2CO_3 , DMF, 70 °C, 2 h, 74%; (d) 33% HBr in AcOH, DCM, rt, 30 min, 86%; (e) (i) CH_2N_2 in Et_2O , MeOH, rt, 30 min; (ii) I_2 , PPh_3 , imidazole, THF, RT, 1 h, 50% over 2 steps; (f) **2** or **3**, K_2CO_3 , acetone, 70 °C, 2 h, 79%; (g) 33% HBr in AcOH, DCM, RT, 30 min, 98%.

Nucleophilic substitution of linear iodo norleucine **21** was performed with benzyl protected hydroxamates in a similar fashion as to the preparation of caprolactam hydroxamate **20a**. This route allows the introduction of various fatty acid tails, expediting the synthesis of mycobactin derivatives. For this purpose, unpurified hydroxynorleucine intermediate **18** was treated with diazomethane to give the corresponding methyl ester, which was purified and subsequently converted into iodonorleucine **21** in quantitative yield. The hydroxamate needed for alkylation was prepared by amide coupling of *O*-benzylhydroxy amine with nonadecanoic acid. Alkylation of the hydroxamate with iodo derivative **21** was then performed in refluxing acetone in the presence of K_2CO_3 to give the desired protected fragment **22**. Assembly of the protected mycobactin acid fragment was then performed in a similar fashion as before (Figure 59). Briefly, the Cbz protecting group of linear hydroxamate **23** was selectively cleaved with 33% HBr in AcOH (Figure 61) and the intermediate amine **24** coupled to oxazoline **4** in a EDC/HOAt mediated coupling to give protected mycobactin acid **24a** in 71% yield. Orthogonal hydrolysis of the methyl ester by aqueous $\text{Ba}(\text{OH})_2$ gave free mycobactin acid **24b** (Figure 62).

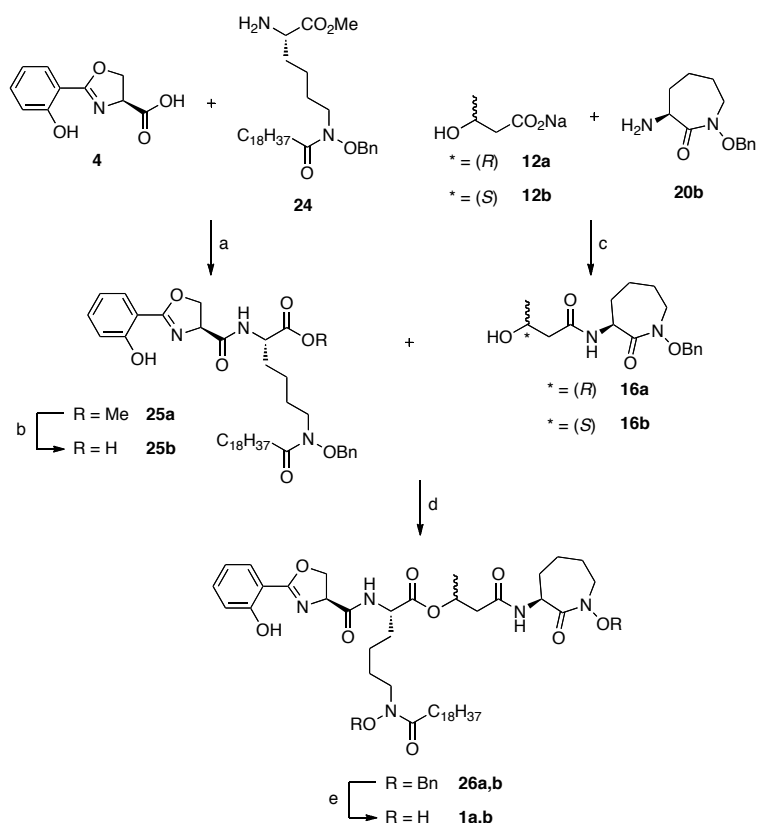


Figure 62: Assembly of benzyl protected fragments. Reagents and conditions: (a) EDC/HOAt, DCM, RT, 5 h, 71%; (b) Ba(OH)₂, THF/water, RT, 1 h, 90%; (c) EDC/HOAt, DMF, RT, 4 h, 63%; (d) PPh₃, DIAD, THF, RT, 16 h, 45%; (e) H₂, Pd/C, MeOH or EtOH/EtOAc, 40 psi, 16 h; for **26a and mycobactin **S 1b**, * = (S), for **26b** and mycobactin **T 1a**, * = (R), 95%.**

In order to form the final internal ester linkage cobactin (**16a** or **16b**) and mycobactinic acid (**25b**) fragments were coupled using triphenylphosphine (PPh₃) and diisopropyl azodicarboxylate (DIAD) in tetrahydrofuran (THF), with the inversion of configuration on the β-hydroxy group of the cobactin fragment to form benzyl-mycobactin S **26a** and benzyl-mycobactin T **26b** in 55% and 45% yield, respectively (Figure 62). Palladium-catalysed hydrogenolysis of **26a** and **26b** at 40 psi overnight in a mixture of methanol and ethyl acetate gave unprotected mycobactins **1a** and **1b** after the filtration of the catalyst and solvent evaporation (greater than 95% purity as measured by HPLC/MS). This material was not further purified as attempts to use chromatography on silica gel using freshly distilled solvents resulted in contamination of the sample with Fe³⁺.

Henceforth, the products of the minimal protecting group synthesis are labelled as mpSMT (for the mycobactin T version) and mpSCM (for the carboxymycobactin version), whereas the products of the revised synthesis are labelled as SMT and SCM. Synthetic mycobactin S (SMS) was also produced using the revised synthetic method.

6.1.4 Evaluation of Synthetic Mycobactins

Absorbance spectra were acquired using either a PerkinElmer Lambda 16 spectrophotometer in methanol, or by an HPLC/DAD in 70 percent acetonitrile. HPLC was performed using the NM_MYCO3 protocol described in Section 2.1.2.2.

SCM, SMT, and SMS were also tested for biological activity. Valentina Dona of the NIAID Tuberculosis Research Section generously carried out these experiments for analysis in this work.

6.1.4.1 Radiolabelling of Mycobactins

Radiolabelling of mycobactins was performed by Valentina Dona. FeSMT and FeSMS were diluted in chloroform and the bound iron was removed as described previously and the desferri-mycobactins were diluted to the desired concentration in methanol. $^{55}\text{FeCl}_3$ (American Radiolabeled Chemicals) was then mixed with the desferri-mycobactins in 1:1 molar ratio. After an incubation of 5 minutes at room temperature, two volumes of chloroform were added. The samples were vortexed briefly and then centrifuged at 15,000 g for 10 minutes. After centrifugation, the chloroform layer was removed and washed once with $\frac{1}{4}$ volumes of water in order to remove unbound iron. The samples were then left to evaporate at 80°C in a heat-block and were finally resuspended in methanol. Quantification of the radiolabelled mycobactins was achieved through liquid scintillation counting on a liquid scintillation counter (LSC, Beckman Coulter) and autoradiography.

6.1.4.2 Uptake by *Mtb* in Liquid Culture

Mycobacterial cells were grown in iron-replete GAST to an OD_{650} 0.5-0.6. The cultures were washed once with low iron GAST and diluted in low iron GAST to an OD_{650} 0.1. After 48 hours the cultures were washed once with RPMI 1640 (Life Technologies) and diluted in RPMI 1640 containing 0.05% Tween 80 to a final concentration of 2×10^6 CFU/mL. After the addition of 80 nM of radiolabelled FeSMT, FeSMS, or FeSCM the cultures were plated in 24-well plates (1 mL/well) and the plates were incubated at 37°C for 24 hours.

The cells were then transferred to 1.5 mL tubes and centrifuged for 3 minutes at 15,000 g. The pellet was then washed three times with PBS + 0.05% Tween 80. Finally,

the pellet was resuspended in 200 μ L of PBS + 0.05% Tween 80 and the amount of radioactivity quantified with a LSC. Three wells were used for each time point. Wells containing medium alone were used as negative controls.

6.1.4.3 Growth Rescue Assay

Mtb H37Rv or the Δ *mbtB* mutant strain were grown in iron-replete GAST medium to mid-exponential phase (OD₆₅₀ 0.4-0.6), washed once with 1 volume of low iron GAST and diluted in low iron GAST to OD₆₅₀ 0.05. The strains were then plated in 24 well plates (1 mL/well) in absence or in presence of 0.1 μ M, 0.01 μ M, or 0.001 μ M of FeSMT, FeSMS, or FeSCM. The plates were incubated at 37°C, and 3 wells for each concentration of mycobactin for each strain were used daily to determine the OD₆₅₀ at the spectrophotometer (Thermo-Spectronic).

6.1.4.4 Uptake by *Mtb* Within Infected Macrophages

To model the mycobactin-mediated iron uptake in an actual infection model, uptake ⁵⁵Fe labelled siderophores by *Mtb* living within infected of macrophages was measured. *Mtb* cells were grown in GAST to an OD₆₅₀ of 0.5-0.6. The cultures were then washed once and resuspended in low iron GAST to an OD₆₅₀ 0.1. After 24 hours the cultures were washed once with RPMI + foetal bovine serum (FBS) and diluted to 8 \times 10⁷ CFU/mL.

THP-1 macrophages seeded in 24 well plates (1 mL/well, 10⁶ cells/mL), that had been activated 48 hours prior infection with PMA (50 ng/ml), were infected with a multiplicity of infection (MOI) of 20 (250 μ L bacteria/well). The plates were incubated for 2 hours at 37°C and then each well was washed three times with RPMI. Finally the cells were fed 1 mL of fresh RPMI + FBS and incubated again at 37°C. 24 hours after the infection ⁵⁵Fe-leaded siderophores (at a concentration of 0.08 μ M) were added to each well.

At 2, 7, and 24 hours the medium was removed, the supernatant collected and added to liquid scintillation vials for counting with a LSC (supernatant fraction). The wells of the 24-well plates were then washed 2 times with PBS and 0.25 mL PBS + 1% Triton X-100 were added to each well to lyse the macrophages. The lysate was centrifuged for 5 min at 14,000 rpm and the supernatant was collected and added to

scintillation tubes for counting (lysate fraction). The remaining pellet is washed 3 times with PBS + 0.05% Tween 80, resuspended into 0.2 mL of PBS and added to scintillation fluid for counting (pellet fraction).

6.1.5 Production of Anti-Mycobactin Antibodies and Determination of Binding Constants

Mice were used to raise antibodies against SCM conjugated to the carrier protein bovine serum albumin (BSA) by linkage of the free acid. Monoclonal antibodies were isolated and their binding constants determined by Petr Čapek of Scripps Research Institute.

Determination of the binding constants was done by competitive ELISA. The SCM-BSA conjugate was used as the coating protein and the competing antigen was either SCM, SMT, a form of synthetic mycobactin T with a C₆ alkyl tail (SMT-C₆), or SMS in milk blocking buffer with 1% DMSO.

6.2 Results and Discussion

6.2.1 Capture Ligand Development

6.2.1.1 Deposition of NTA onto the Electrode Surface

The receptor immobilisation strategy depicted in Figure 53B calls for the receptor protein to be anchored by means of an NTA-functionalised electrode surface. The synthesis and diazonium salt deposition of an NTA ligand has been elucidated by Blankespoor et al.²¹⁴ NMR spectra of 4-aminophenyl-NTA matched values given in the literature. After formation of the diazonium ion, it undergoes a two-electron reduction to evolve gaseous N₂ and form a highly reactive aryl radical (Figure 63). This radical rapidly forms a covalent bond with the nearby electrode surface to form a functional layer. Deposition of the diazonium salt of 4-aminophenyl-NTA is shown in Figure 64A. The deposition was quantified by integrating the charge transferred, assuming a two-electron reduction. In this manner, the NTA surface coverage on the electrode was calculated to be 5.2 nmol/cm². Attachment of the NTA ligand to the electrode surface was verified by monitoring the change in ferricyanide redox couple with pH as shown in Figure 64B. At low pH (1.0) the three carboxylated arms of NTA become protonated, and

the ferricyanide couple is observed normally. At neutral pH (7.5) NTA becomes deprotonated, thus creating a layer of negative charge on the surface of the electrode. This layer of negative charge inhibits the negatively charged ferricyanide ions from reaching the electrode surface, decreasing the amplitude of the observed redox peaks. This ligand is now ready for Lcn2 attachment as proposed in Figure 53B.

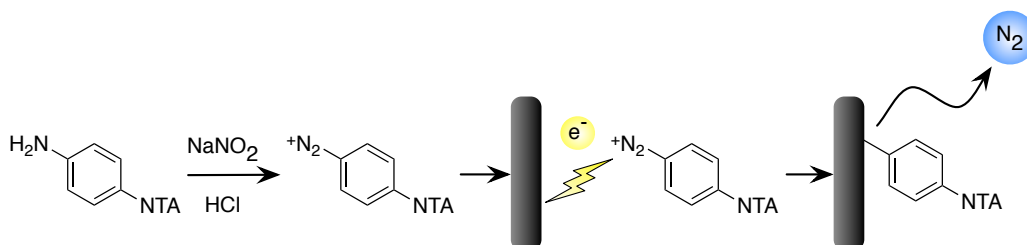


Figure 63: Diazonium electrodeposition mechanism for 4-aminophenyl-NTA.

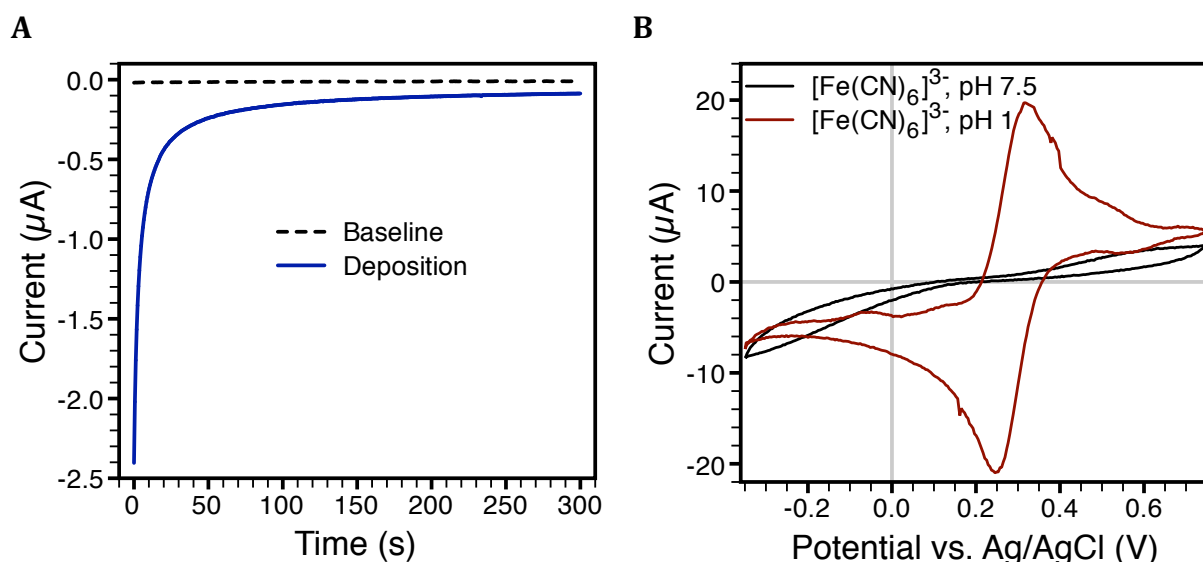


Figure 64A: Deposition of the diazonium ion onto a GCE surface at -0.4 V versus Ag/AgCl. B: CVs of potassium ferricyanide at pH 7.5 and 1.0 indicate the successful functionalisation of the electrode surface by slowing of the electrochemical process at pH 7.5; 0.1 M potassium chloride, 0.2 V/s scan rate.

6.2.1.2 Cloning of Lcn2

Cloning of Lcn2 was undertaken producing the Lcn2-pET28b plasmid, which contained the expected sequence encoding Lcn2 with the addition of a hexahistidine tag. SDS-PAGE showed that the majority of Lcn2 produced was found in the soluble fraction of the cell lysate (Figure 65A). Preliminary isolation and purification, produced a distinct band observed at 22 kDa, the expected molecular weight for the recombinant Lcn2 (Figure 65B). The purified protein yield was 8.5 mg/L as measured by Bradford assay.

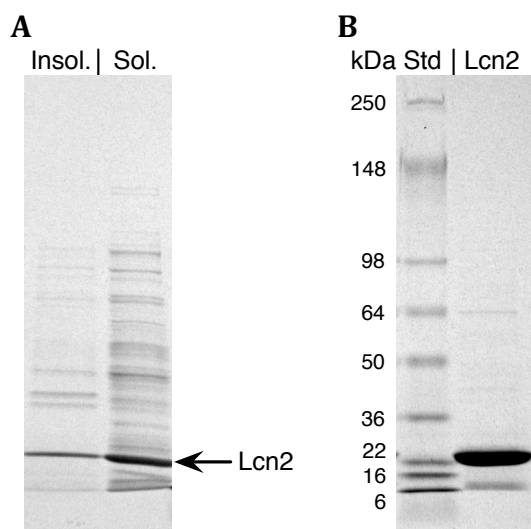


Figure 65A: SDS-PAGE of insoluble and soluble fractions of Lcn2-pET28b BL21 *E. coli* cell lysate after induction with IPTG. B: SDS-PAGE of the Lcn2 purification shows Lcn2 with the expected molecular weight of 22.8 kDa.

6.2.2 Synthetic Mycobactins

Initially, synthesis of mycobactins was done following a minimal protecting group strategy developed by Hu and Miller¹⁵². Figure 54 shows the structures for the synthetic target compounds carboxymycobactin (SCM) and mycobactin T (SMT). To compare these with the natural structures described in Table 8 of Chapter 2, SCM contains 7 carbons in its fatty acyl moiety, while the SMT fatty acyl contains 19 carbons. In addition to SCM and SMT, a synthetic version of mycobactin S (SMS) was made, which differs from SMT by only one chiral centre (see Table 2).

For clarification, the products of the minimal protecting group synthesis are labelled as mpSMT (for the mycobactin T version) and mpSCM (for the carboxymycobactin version).

6.2.2.1 Minimal Protecting Group Product

The absorbance spectra of the ferric compounds synthesised through the minimal protecting group strategy had an absorbance maxima shifted from the normal 450 nm position to 500 nm at neutral pH. Figure 66A shows these contrasting spectra. Note that the natural FeMT shown here possesses a fully saturated acyl moiety, as do the synthetic target structures, however the natural FeMJ possesses an unsaturated acyl moiety, giving rise to the absorbance difference in the 250 nm to 340 nm range, as discussed in Section 2.2.2.

Further to this, it was noted that the ferric peak shifts to a longer wavelength upon addition of ferric chloride, as shown for mpSCM in Figure 66B. The ferric peak is located at 480 nm in the presence of 10 μM ferric chloride, but shifts to 510 nm upon saturation with 80 μM ferric chloride. Addition of sodium hydroxide to the solution shifted the absorbance maxima back toward shorter wavelengths, followed by loss of the ferric peak, presumably due to degradation of the compound. This absorbance shift is consistent with the pH change accompanying ferric chloride addition and a reversal upon the addition of sodium hydroxide to again raise the pH. In contrast, authentic DFMJ does not exhibit any shift in position of the major absorbance peak with addition of ferric chloride.

These data call into question the veracity of the products of the minimal protecting group synthesis. The shift in this peak, which corresponds to a chelated iron centre, indicates that iron coordination undergoes a gradual change with pH, which does not occur with the authentic mycobactin siderophores. Furthermore, aqueous cyclic voltammetry of the minimal protecting group products failed to produce the characteristic redox couple present in FeMJ as shown in Figure 67 (compare with the redox couple of authentic mycobactin reported in Figure 24). Instead, mpSMT and mpSCM exhibit a single, irreversible reduction at -0.85 V in both the presence and absence of iron. Given, that this reduction wave is not dependent on the presence of iron, it must be a reduction of the compound itself and suggests that these minimal protecting group products have a reducible ligand, which is absent from the authentic siderophore.

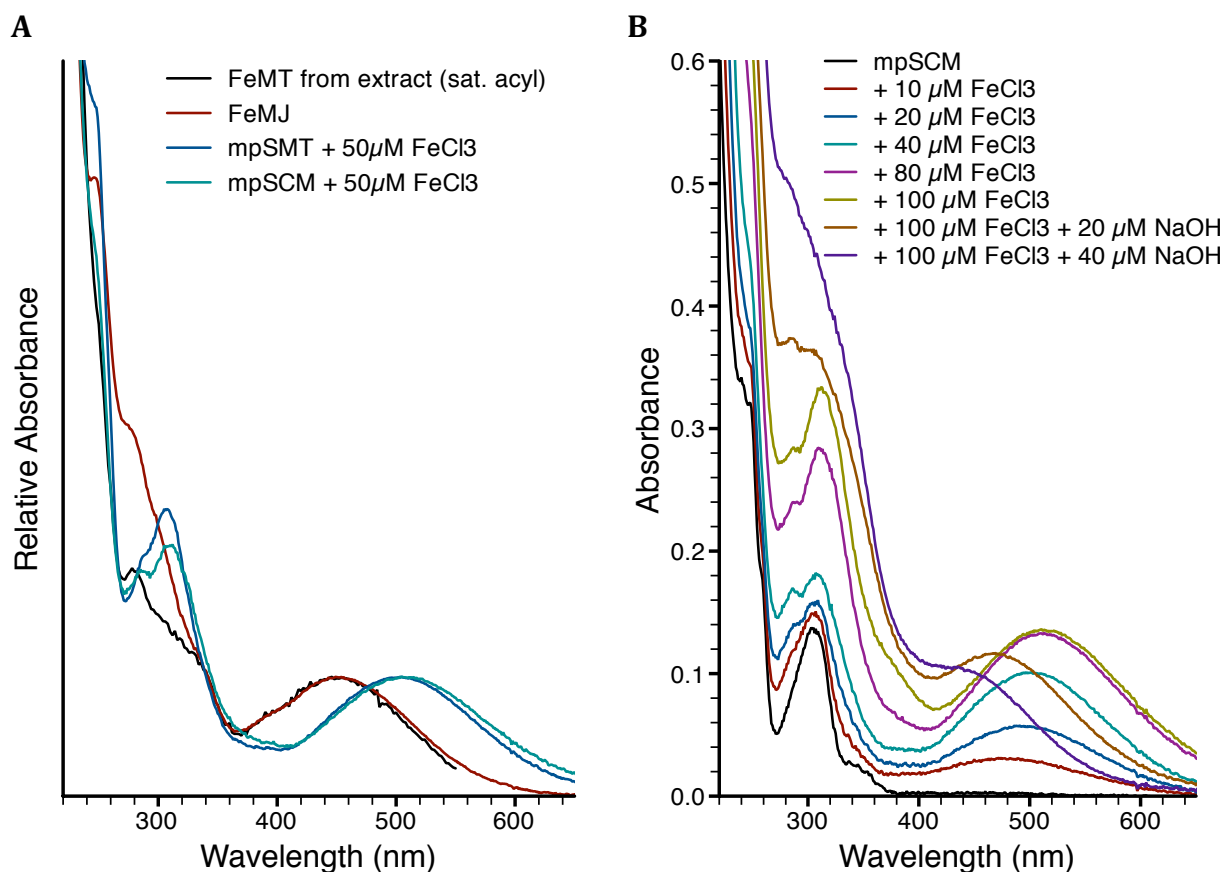


Figure 66A: Contrasting absorbance spectra of the minimal protecting group products, and authentic FeMJ and FeMT. Spectra were normalised to their respective maxima at either 450 nm or 500 nm. B: Desferri mpSCM was ferrated using ferric chloride, then sodium hydroxide was titrated into the solution to observe the peak shift under re-alkalinisation.

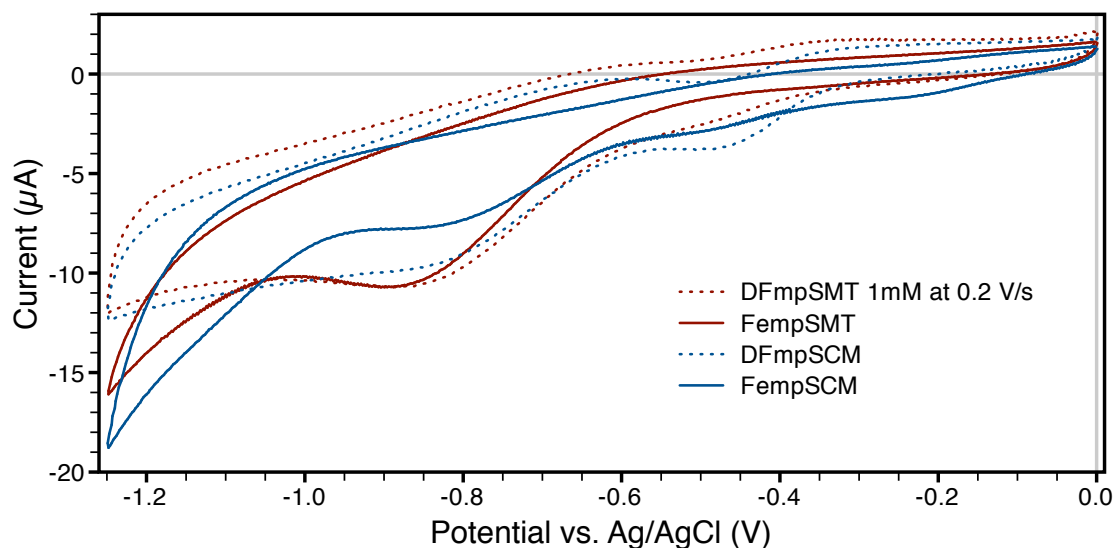


Figure 67: Cyclic voltammetric analysis of minimal protecting strategy products. All analytes at 1 mM concentration, 0.1 M potassium chloride in 50 percent aqueous ethanol, 0.2 V/s scan rate.

Due to the presence of trace amounts of iron in the synthetic process, the products were initially partially ferrated; the anticipated ionic mass of the SMT product is 844.5 amu without iron and 897.5 amu with iron bound. The addition of ferric

chloride to the product unexpectedly produced a double elution peak of the ferric compound, as shown in Figure 68. The doubling of the peak suggested that racemisation of a chiral centre was occurring at some point of the synthesis after the compound had already been exposed to, and chelated, trace amounts of iron.

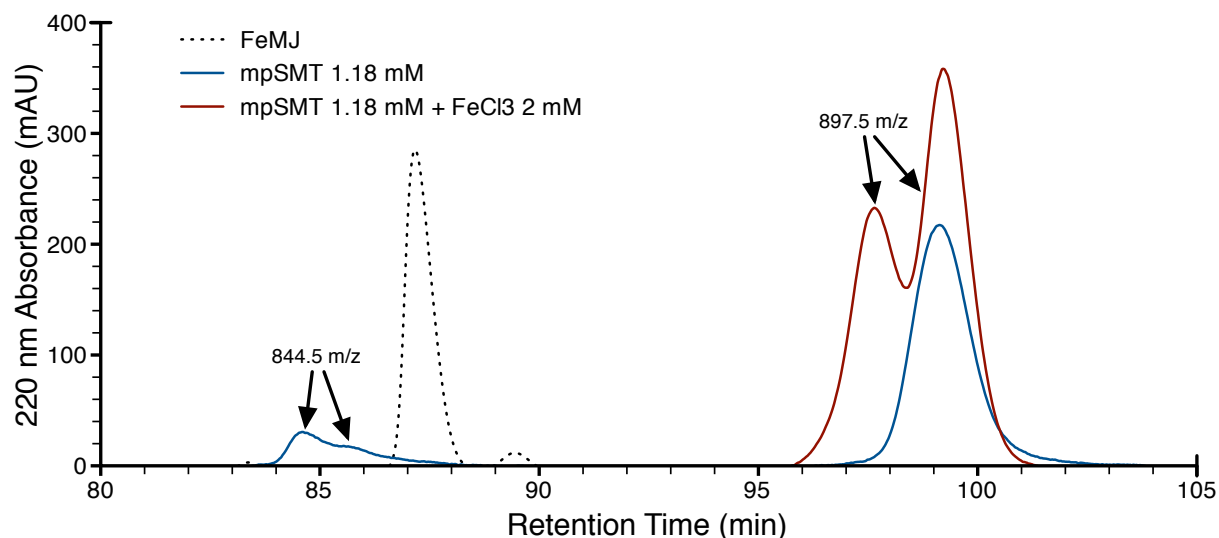


Figure 68: HPLC chromatogram of mpSMT elution under the NM_MYCO3 protocol (see Section 2.1.2.2). Addition of ferric chloride to mpSMT gave rise to a doubled elution peak; the elution of authentic FeMJ is shown for comparison of elution times.

Based upon these data, as well as additional NMR analysis performed at Scripps Institute, it was concluded that Miller's minimal protecting group strategy was not producing the desired mycobactin target compound. Instead, these further investigations suggested the isomer shown in Figure 69 as the product of an alternate coupling between cobactin and mycobactin acid under the conditions described by Hu and Miller. This compound exhibited different iron-binding properties from mycobactin, and hence was not suitable as a mycobactin standard. Additionally, this calls into question previously published findings that mycobactin S (MS) is a potent growth inhibitor of *Mtb*¹⁵², but rather, may indicate that mpSMT is the growth inhibitor. Although the compound did not exhibit a particularly potent effect, with 99% growth inhibition at a concentration of 12.5 $\mu\text{g}/\text{mL}$ ¹⁵², the surprising element of the previously published data was the impression that such a nearly identical siderophore, differing by only one chiral centre, could be a growth inhibitor. Thus the finding that a different structure was responsible for growth inhibition regrettably lessens the impact of this discovery.

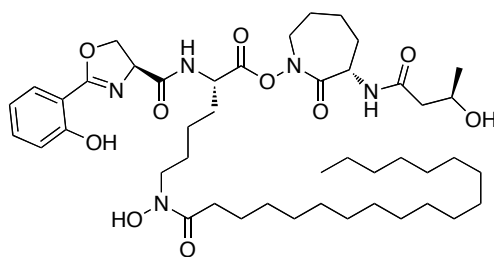


Figure 69: Structure of the minimal protecting group product mpSMT; not mycobactin.

6.2.2.2 Revised Synthetic Product

A revised coupling strategy was able to produce a compound exhibiting the correct spectrophotometric properties as shown in Figure 70 and in contrast to Figure 66A. The HPLC elution of this compound is shown in Figure 71. Addition of ferric ion in the form of ferric acetylacetonate resulted in a single peak, indicating that no racemisation had taken place under the revised synthesis. Figure 72 shows FeSMT coeluting with natural FeMT compounds extracted from *Mtb* culture. The elution pattern is exactly as expected given the length of the hydrophobic tail. With a fatty acyl moiety containing 19 carbons, FeSMT eluted between the two major groups of natural mycobactins that contain 18 and 20 carbons in their fatty acyl moieties respectively.

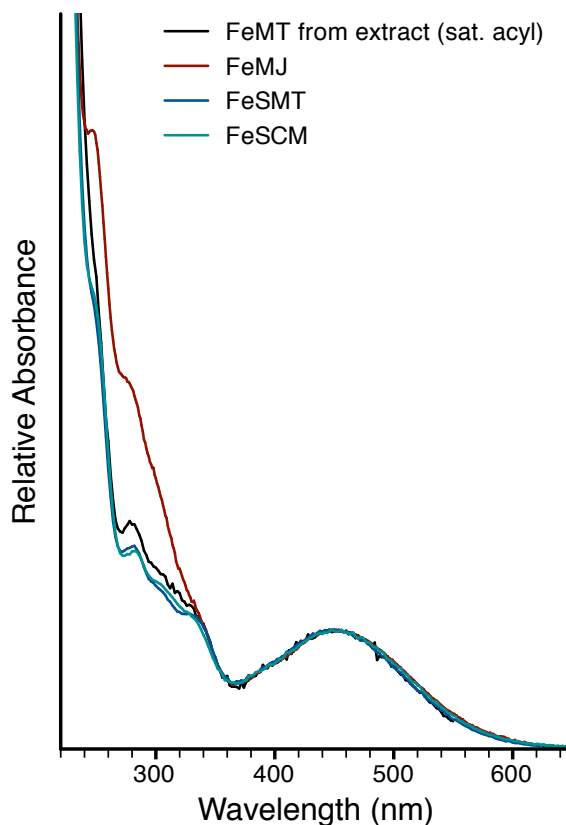


Figure 70: UV-visible spectra of FeSMT and FeSCM exhibited the same absorbance profile as natural FeMT and FeMJ.

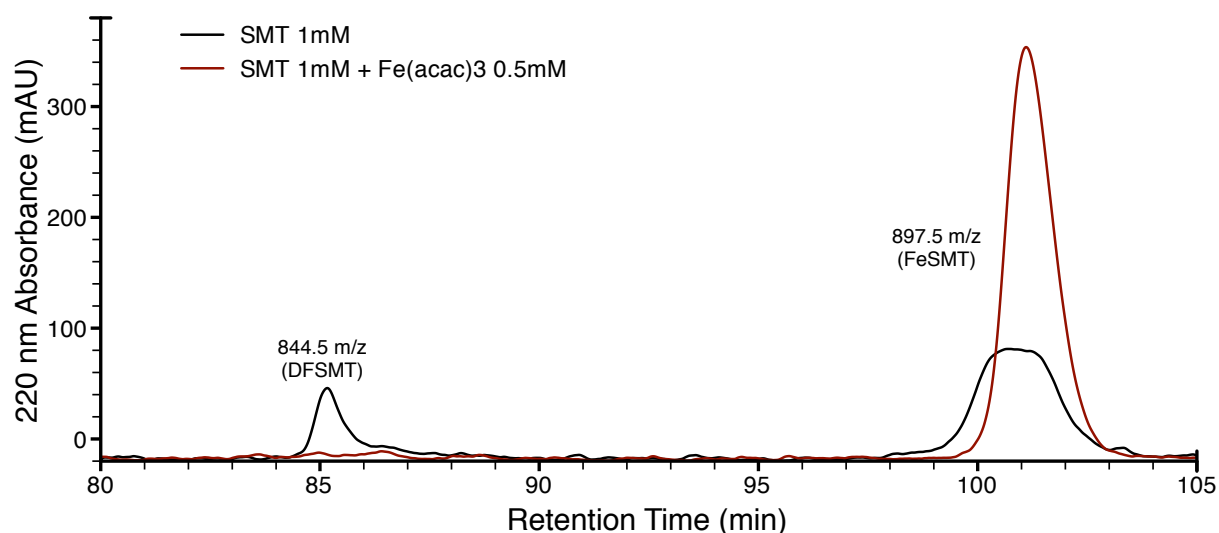


Figure 71: HPLC chromatogram of SMT elution under the NM_MYCO3 protocol (see Section 2.1.2.2). Addition of ferric acetylacetonate ($\text{Fe}(\text{acac})_3$) produces only a single peak.

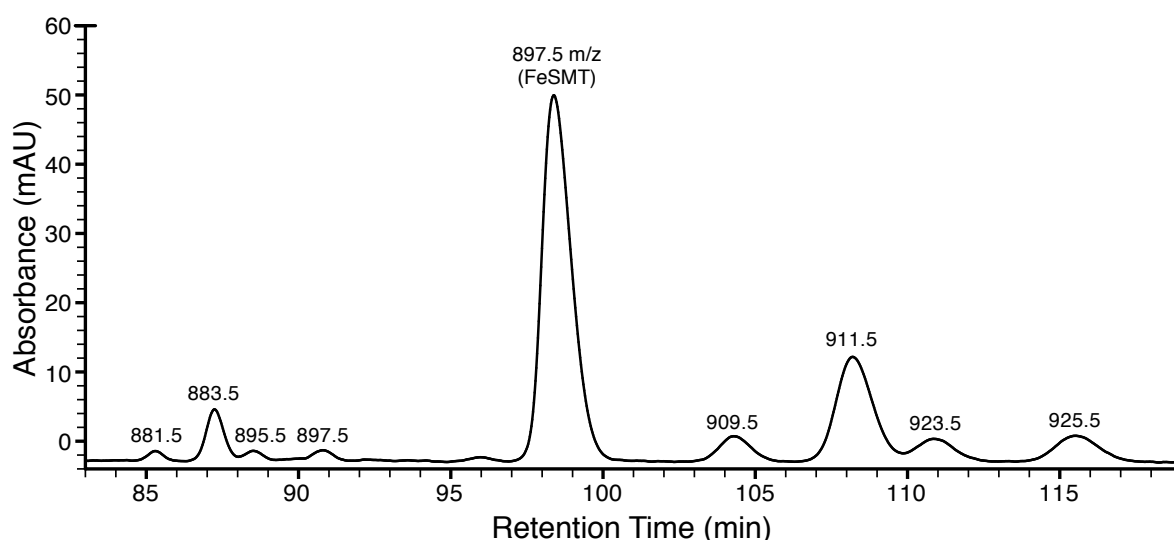


Figure 72: HPLC chromatogram of FeSMT eluting alongside mycobactins extracted from *Mtb* culture (NM_MYCO3 protocol, see Section 2.1.2.2).

Both the minimal protecting strategy product mpSMT and the revised synthesis product SMT were analysed via tandem mass spectrometry (MS/MS). The presence of a peak at 758.5092 m/z in the MS/MS spectra of the undesired product was particularly diagnostic (Figure 73); this peak corresponds to the cleavage of the amide bond between the β -hydroxy acid and azepinone fragments ($\text{C}_{41}\text{H}_{68}\text{N}_5\text{O}_8^+$) and provides unequivocal evidence for the proposed connectivity of the minimal protecting strategy product shown in Figure 69. In contrast to the product of the minimal protecting group strategy, fragmentation between building blocks **C** and **D** (Figure 56) produced a species with 717.4797 m/z, corresponding to fragment **A-B-C** of the correctly coupled mycobactin, with no peak corresponding to the miscoupled product at 758.5092 m/z.

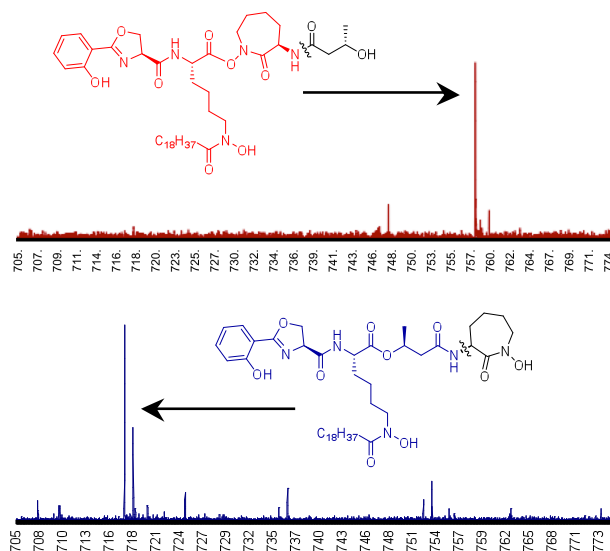


Figure 73: MS/MS spectra of the miscoupled product (mpSMT) (red, arrow points to $m/z = 758.5092$) and authentic mycobactin T (SMT) (blue, arrow points to $m/z = 717.4797$). In both cases, the parent peak has $m/z = 844.5432$. Figure provided by Tobin J. Dickerson and Petr Čapek.

6.2.2.3 Biological Activity of Synthetic Mycobactins

Biological activity analysis and evaluation were largely based upon raw data collected by Valentina Dona.

6.2.2.3.1 Uptake by *Mtb* in Liquid Culture and Growth Rescue Assay

The mechanism of mycobactin-mediated iron uptake remains shrouded in mystery. In order to gain some insight into this process and to test the biological effectiveness of the revised synthetic products, uptake of radioactive ^{55}Fe labelled mycobactins was measured both on the wild type *Mtb* strain H37Rv and the mycobactin deletion mutant $\Delta mbtB$. The revised synthetic compounds FeSMT and FeSMS both show successful incorporation of their iron payloads into the mycobacterial cell pellet of both strains, as shown in Figure 74. Again, note that FeSMT and FeSMS differ in structure only at one chiral centre. However, the FeSCM compound fails to efficiently incorporate its iron payload within the organism. It is evident that the organism does not need to produce endogenous mycobactin in order to utilise the exogenously added compound, however the presence of endogenously produced mycobactins or carboxymycobactins may aid in the transport and internalisation of iron and could explain why incorporation of iron is greater in the wild type strain than in the $\Delta mbtB$ strain that is unable to biosynthesise mycobactin.

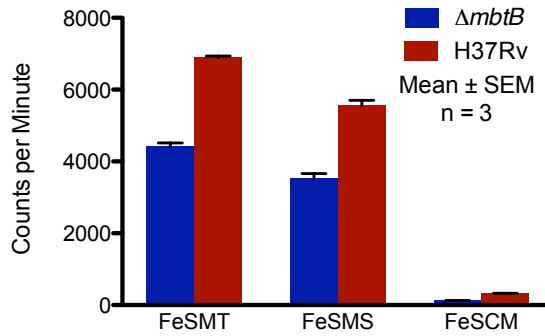


Figure 74: Comparison of *Mtb* H37Rv and $\Delta mbtB$ uptake of 80 nM Fe⁵⁵ labelled FeSMT. Based on data collected by Valentina Dona.

As expected, the $\Delta mbtB$ mutant exhibited depressed growth compared with the wild type H37Rv (Figure 75A-C). $\Delta mbtB$ cultures that were supplemented with FeSMT and FeSMS exhibited a dose-dependent recovery to near wild type growth rates, whereas FeSCM failed to restore wild type growth rates.

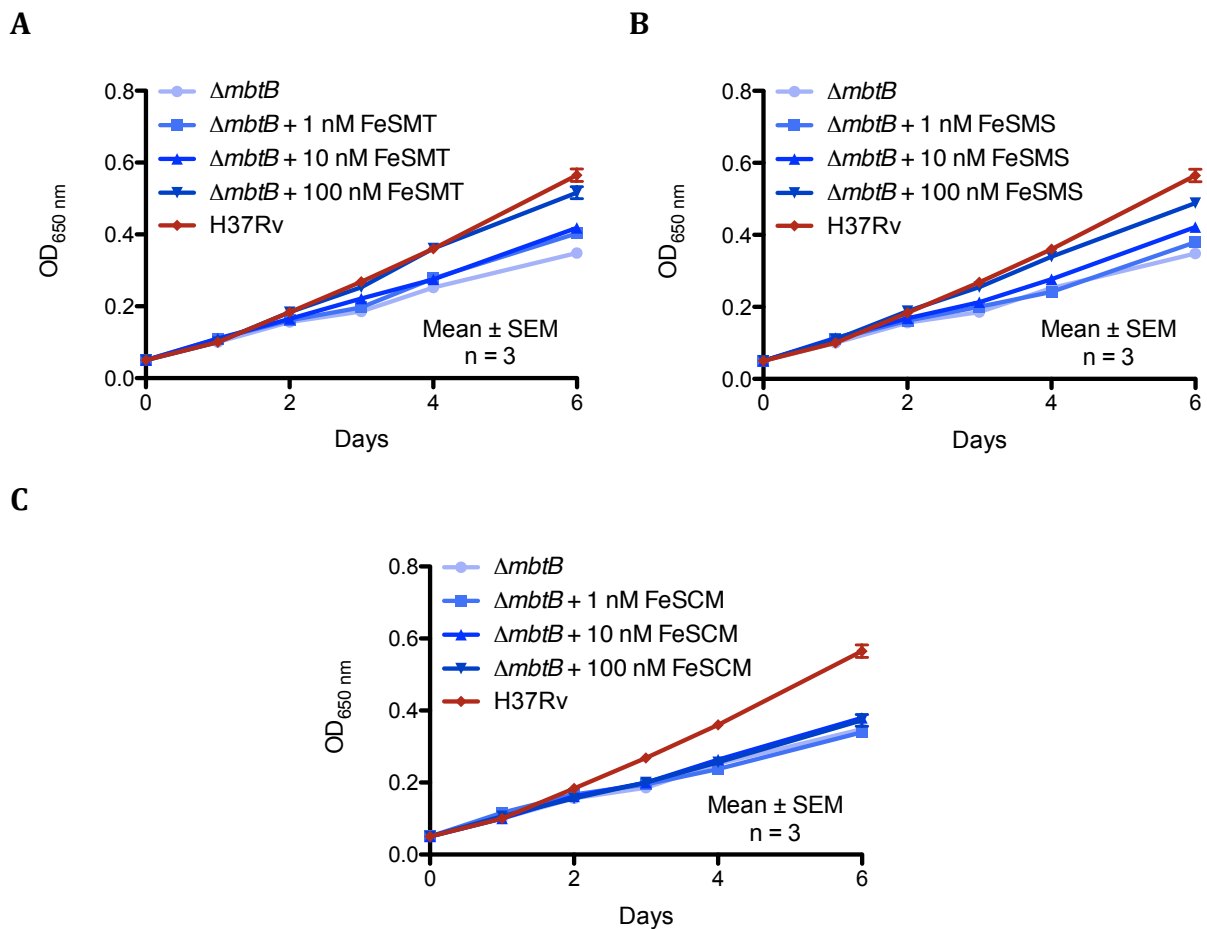


Figure 75: Growth rescue of $\Delta mbtB$ by FeSMT (A), FeSMS (B), or FeSCM (C). Based on data collected by Valentina Dona.

The failure of FeSCM to either incorporate iron into *Mtb* cultures or rescue growth of the $\Delta mbtB$ mutant could be explained in several different ways. First is the possibility that the biologically active compound is in fact the methyl ester rather than the carboxylic acid form of mycobactin. There has been debate regarding this proposition in the literature and it remains somewhat inconclusive as to which is the naturally produced compound^{46, 47, 119}. In particular, Wong et al. have argued that the free-acid form of mycobactin is likely just a degradation product, particularly as it is most readily obtained under acidic conditions, and that the methyl ester acts as the true siderophore⁵¹. A second intriguing possibility is that *Mtb* does not use carboxymycobactin as a means of extracellular iron acquisition. This would support the model proposed in Section 2.3.1 in which carboxymycobactin serves a role in iron trafficking primarily within the confines of the mycobacterial cell wall, and therefore there is no mechanism to facilitate transport of exogenous FeSCM into the cell. However, this interpretation would contradict results published elsewhere demonstrating uptake of exogenous carboxymycobactin-bound iron^{122, 125, 217, 218}.

6.2.2.3.2 Uptake by *Mtb* Within Infected Macrophages

In the macrophage infection model, it was observed that uptake was significantly higher for the $\Delta mbtB$ mutant at 80 nM ($p < 0.0001$ by two-way ANOVA), however the difference was insignificant at 400 nM ($p = 0.26$) (Figure 76). This could be due to saturation of the uptake mechanism at the higher concentration. The reversal of relative uptake may indicate the more stringent iron-restricted environment within the macrophage. Under these conditions, the $\Delta mbtB$ mutant is deprived of even trace quantities of iron that may be present in the culture medium, having to rely exclusively on the exogenously added mycobactin, while in the case of the wild type H37Rv strain, the exogenous mycobactin is competing with endogenously produced mycobactin. This effect could be compounded by the fact that exogenous mycobactin must first penetrate the macrophage, and thus is unable to fulfil the iron acquisition needs of the wild type strain as well as its own endogenously produced siderophores.

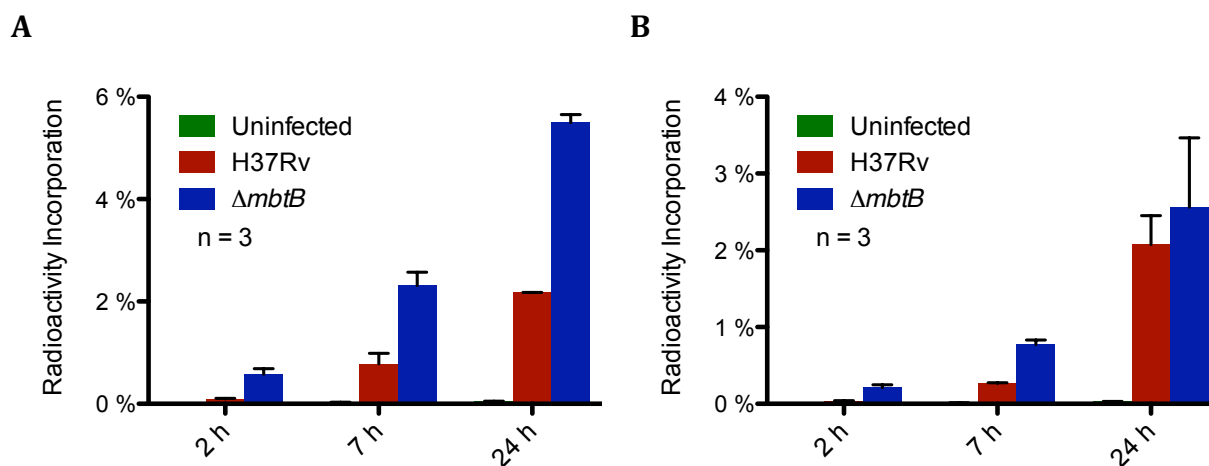


Figure 76: 80 nM (A) or 400 nM (B) ^{55}Fe labelled FeSMT uptake into *Mtb* within macrophages infected with strain H37Rv or $\Delta mbtB$. Based on data collected by Valentina Dona.

6.2.3 Evaluation of Anti-Mycobactin Antibodies

Two monoclonal antibodies were successfully raised to a SCM-BSA conjugate. The rationale for conjugating SCM by its free acid tail was to raise an antibody that would be specific to the iron-chelating core of mycobactin T, rather than one that has specificity to a particular length of the fatty acyl tail. The binding constants for the two antibodies against various synthetic siderophores including a version of mycobactin T with a shortened C_6 acyl tail are reported in Table 13.

Antibody **1** exhibits a particularly high affinity for SCM and the shortened SMT- C_6 over the lipophilic mycobactins with longer acyl chains. This preference is less pronounced with antibody **2**, however its overall weaker affinities for three out of the four siderophores indicate that antibody **1** is the more promising option. Although the specific epitopic regions of binding have not been determined, given the small size of mycobactin it is highly likely that the epitopes overlap each other to an extent that simultaneous binding by both antibodies would be sterically inhibited.

Table 13: Binding constants for two monoclonal antibodies for different species of synthetic mycobactin as measured by competitive ELISA. Data provided by Petr Čapek (personal communication).

Antibody	Type	Binding Constant			
		SCM	SMT	SMT- C_6	SMS
1	Mouse IgG ₁	1.3 nM	1190 nM	2.6 nM	2400 nM
2	Mouse IgG _{2a}	43 nM	1090 nM	222 nM	3400 nM

6.3 Conclusions

In summary, the minimal protecting group strategy for mycobactin synthesis published by Hu and Miller¹⁵² failed to produce the correct target compound. The revised synthetic method yielded a mycobactin representative of the natural compound in spectrophotometric absorbance, liquid chromatographic elution properties, and biological activity.

The revised synthetic products FeSMT and FeSMS are biologically active and are able to transfer iron to *Mtb* without the need for direct mycobactin production by the organism, however endogenous mycobactin may aid in the process, at least *in vitro*. Furthermore, it has here been demonstrated that exogenous mycobactin T can be taken up by *Mtb* both in culture growth conditions and when infecting a macrophage. Both mycobactin T and mycobactin S, but not carboxymycobactin were able to promote growth of the $\Delta mbtB$ mutant.

This revised synthetic product was used as a standard in the previous chapter investigating clinical samples for mycobactins and carboxymycobactins. However, these products now offer starting blocks for antibody production and alternative biorecognition and capture ligands to the Lcn2 ligand proposed in Figure 53. The development of these synthetic mycobactin compounds has allowed the first antibodies against mycobactin and carboxymycobactin to be raised. These antibodies could also serve the role as specific mycobactin binding agents, replacing Lcn2 in a design. Alternatively, if it is possible to bind mycobactin simultaneously with two binding agents it would be possible to amplify the signal through the generation of enzymatically-generated measurand by and enzyme conjugated to one binding agent, as in a traditional sandwich assay. Because of the deep binding pocket of Lcn2¹²⁷ and the small size of mycobactin, as discussed in Section 6.2.3, this would be difficult to achieve.

With the electrode now modified to accept either of these biorecognition ligands via a hexahistidine tag (Section 6.1.2.2) further work can establish the best strategy for optimising such a 'capture and report' electrode. Traditionally, protein-modified electrodes have relied on the generation of a reporter molecule²¹⁹ or electron transfer through an intermediate to the electrode²²⁰. However more recent designs of 'third generation' biosensors take advantage of direct electron transfer from the redox reaction of interest (usually catalysed within an enzyme) to the electrode²²¹⁻²²³. Improvements in the applicability of direct electron transfer to a wider variety of

proteins have included the modification of the electrode surface with carbon nanotubes^{224, 225} or molecular wires²²³ in order to reduce the distance of electron transfer from the catalytic pocket. In the case of mycobactin the reaction is not catalysed enzymatically, but is initiated directly by the potential drop near the electrode surface, so the specific catalytic activity of the enzyme is not important. This gives more scope for manipulation of the binding orientation to maintain mycobactin near the electrode surface for direct electron transfer. Direct electrochemistry has long been used for sensitive detection of non-proteinaceous biomolecules, such as DNA²²⁶.

Mycobactins and carboxymycobactins also offer a promising new modality for PET imaging of TB. The synthetic siderophores that have been developed in conjunction with this project have now been scaled up in production and offer the best option for testing the PET probe potential of siderophores for the visualisation of TB. The results from the mycobactin and carboxymycobactin uptake experiments indicate that mycobactin would offer superior labelling of *Mtb* cells themselves, however the divergent biodistribution profiles of carboxymycobactins and mycobactins will need further investigation to ascertain which one offers the best PET labelling strategy. The use of mycobactin as a PET probe, if it becomes a widespread technique, may also require the use of a companion diagnostic for safety purposes.

7 Future Implications

Here the implications of this work for future research and the understanding of siderophores as potential diagnostic markers for TB are addressed. Other potential applications of the assay are explored, such as a biosensor for companion diagnostics and other industrial uses. Finally, some future possibilities for increasing the sensitivity of the assay are set forth.

7.1 Tuberculosis Diagnostic Potential of Mycobactin and Carboxymycobactin

There are two questions to be addressed regarding the possible use of mycobactins as diagnostic biomarkers for TB. One is a question of instrumentation and the creation of a biosensor for mycobactin/carboxymycobactin detection. The other is the question of the presence of these siderophores in significant enough quantities and with a biodistribution profile that is conducive to detection with such a biosensor. This work has sought to tackle the first question by developing a simple assay that could serve in the capacity of a diagnostic biosensor. Furthermore this study has established a low level of background signal interference when the assay is used to analyse urine samples. Unfortunately, the results are disappointing thus far in regard to the second question of siderophore biodistribution and empirical measurement of siderophores within the body tissues that have been tested here. If mycobactins are present, they are at very low levels within plasma and urine, but other tissues may hold better prospects for use with this assay. Further high-sensitivity laboratory-based testing of alternative tissues more proximal to the *Mtb* infection itself would provide the next step to establish the presence and levels of mycobactin in clinical samples. Only then will be possible to use this mycobactin assay as a novel TB diagnostic biosensor.

7.1.1 Bovine Tuberculosis

Bovine TB, defined as infection of cattle by *M. bovis* rather than *Mtb*, is a major concern for cattle ranchers and is particularly widespread in the United Kingdom. *M. bovis* is the only other mycobacterium to produce a siderophore structurally identical to

that of *Mtb*⁵⁰. As such, the simple assay could serve as a new diagnostic for this veterinary disease in addition to human TB. Diagnostics for animal and livestock use face fewer regulatory hurdles, reducing time-to-market, and, as the technology would be largely similar, could also serve as a way to gather more data for ongoing development of a human diagnostic.

7.2 Other Applications of the Mycobactin Assay

7.2.1 Companion Diagnostic for Therapeutic Administration of Mycobactins

Mycobactin is an important natural product that has potential pharmaceutical uses for chelation and anti-cancer therapy, as well as the basis for antimicrobial analogues, as discussed in Chapter 1. The simple electrochemical assay for mycobactin could serve as a companion diagnostic for these therapeutic administrations of mycobactins and their analogues. Anti-cancer applications of mycobactin in particular could benefit from a simple assay to serve as a companion diagnostic. Pharmaceutical companies have been increasingly turning to companion diagnostics as a means to improve safety and efficacy of new prospective pharmaceuticals, including cancer treatments²²⁷. Because of the disruption that aggressive iron chelation would have on iron homeostasis in the normal tissues of cancer patients, it would be desirable to closely monitor concentrations of the therapeutic mycobactin and its chelated iron content upon excretion.

This dissertation has shown that a simple assay for mycobactin is able to detect and quantify mycobactin directly at concentrations of 10 μM and above. A streamlined concentration method that could potentially reduce the limit of detection to 300 pM has also been demonstrated. This limit of detection is well within the required sensitivity range for a sensor targeted as a companion diagnostic for mycobactin used as a chelation or anti-cancer therapies. Typical therapeutic plasma concentrations for iron chelators are in the range of 5-450 μM ²²⁸⁻²³¹. Therefore it may be possible to directly use the assay without extensive sample processing and concentration. This depends on the levels of mycobactin that ultimately prove to be effective for therapeutic administration versus toxicity and on the rate of mycobactin filtration by the kidneys.

In order to answer the next series of questions in regard to the applicability of the assay, the biodistribution and pharmacokinetic of mycobactin and its therapeutic

analogues of interest must be investigated. The assay that has been developed here will serve as a useful tool that may undergo co-development along with animal and clinical trials of mycobactin-based therapeutics.

7.2.2 Biosensor for Industrial Siderophore Production

In this study, *Mtb* grown in liquid culture produced siderophores at a concentration of 8.6 μM that would be accessible to a sensor exposed the culture medium, however much higher levels of production have been achieved under different conditions¹⁸⁴. The CV limit of detection for the assay was in this same range at 10 μM . Strategies to concentrate the sample at the electrode surface, such as those set forth in Chapter 6, would be necessary in order to allow real-time monitoring of early-stage siderophore production and accumulation.

Such a real-time sensor could have applications in monitoring commercial siderophore production. Mycobactin J is one industrially significant siderophore that is required for culturing *M. avium* subspecies *paratuberculosis*, which is routinely done to monitor cattle for Jöhne's disease. Another application would be the ability of the assay to inexpensively identify an unknown organism as one that produces mycobactin. Monitoring of siderophore production within chemostats could provide information about the organisms' metabolic state, their need for iron, and could even reveal details about oxidative stress that the organism is experiencing. These are added to the usefulness of such a sensor in ongoing mycobacterial siderophore research.

7.3 The Role of *In Vivo* Mycobactin Reduction in Iron Trafficking

It has long been thought that a putative reductase plays a role in the biological mechanism of iron dissociation from mycobactins or carboxymycobactins¹²⁰. There are three different mechanisms that have been suggested by which bacteria may dissociate iron from their high-affinity siderophores: reduction of Fe^{3+} to Fe^{2+} , cleavage of the siderophore, and protonation of the siderophore ligands¹⁹⁷. While the cleavage mechanism has been observed in the case of catecholate siderophores with relatively simple structures²³², it has been postulated that the chelation properties of hydroxamate siderophores are more conducive to dissociation by reduction of the ferric centre. This would also allow reuse of the siderophore, which in the case of mycobactin is quite

complex and metabolically costly to produce. Recently Ryndak and colleagues found evidence of a flavin adenine dinucleotide (FAD) binding domain in the transmembrane IrtA transporter protein, which is necessary for iron uptake from carboxymycobactin. The presence of this FAD binding domain suggests that IrtA may serve not only as part of an ABC transported system together with IrtB, but also possesses FAD reductase functionality. In fact, mutations in the domain that prevented FAD binding reduced the organism's ability to grow in conditions where iron is supplied solely chelated by carboxymycobactin²¹⁸. This domain is thought to be on the cytoplasmic side of the cell membrane. This suggests an intimately linked siderophore import and reduction system for the utilisation of chelated ferric iron.

This work has revealed the mechanism of mycobactin reduction (Chapter 3), which likely has implications for how *Mtb* internalises and utilises iron from mycobactin *in situ*. Protonation of siderophore ligands has generally been dismissed as requiring pH values too low to be physiologically practical. However, protonation of the enzyme-siderophore complex may not require such a low pH. As the proposed mechanism suggests, protonation of one or more of mycobactin's chelation ligands can occur following reduction of the Fe³⁺ centre under non-acidic conditions. Facilitation of this protonation by an enzymatic process may help to thermodynamically favour the reduction, allowing both the low reduction potential and the low pH requirement to be overcome. Protonation of one or more of the chelation ligands could also prevent re-oxidation of Fe²⁺ while in the stabilising confines of the siderophore and facilitate dissociation of the Fe²⁺ ion from the complex.

7.4 Electrode Surface Engineering

The development of a novel biosensor is a long process that can take years, especially for medical diagnostic devices. The simple assay developed in this dissertation provides a foundation for such a biosensor. Here we look to the future to suggest some potential developments to further improve the sensor sensitivity.

Mycobactin concentration at the electrode surface can be improved through modification of the surface itself to enhance the specific surface binding properties between the electrode and mycobactin through physical modification and patterning of the electrode surface. This is an alternative binding strategy that typically leads to less specific binding than the methods explored in Chapter 6. There is a large and active

body of research on the binding of analytes based upon molecular imprinting^{233, 234}, which can be applied to the surface of electrodes. The idea of molecular imprinting is that the analyte of interest is bound solely on the basis of its physical interactions with the substrate. Glassy carbon can also be imprinted with microstructures via mechanical machining, focused ion beam, and laser techniques²³⁵. The combination of these approaches would entail micropatterning of physical features on the electrode surface that could interact with and preferentially adsorb mycobactin. Plasma etching can also be used to create patterned regions with differing hydrophilic/hydrophobic properties in order to give a combined physical/chemical approach to homing in on analyte-specific binding morphologies²³⁶. This could be especially interesting to apply to the problem of mycobactin surface adsorption.

Figure 77 shows a hypothetical molecular model of this scenario in which a hydrophobic groove has been etched in the surface of a graphite electrode with conformation designed to preferentially bind mycobactin. This hydrophobic groove is modelled after the hydrophobic pocket used to bind carboxymycobactin by Lcn2¹²⁷. The groove shown in Figure 77 is 6 Å wide and the length of the groove that is occupied by mycobactin is 42 Å. Assuming equidistant groove spacing of 6 Å between grooves, the area occupied by one molecule of mycobactin is therefore approximately 42×12 Å. Such a sensor would have a maximum total surface binding capacity of 66 pmol/cm² for mycobactin T, which would result in a charge transfer density of 6.4 μC/cm² for the one-electron reduction of mycobactin.

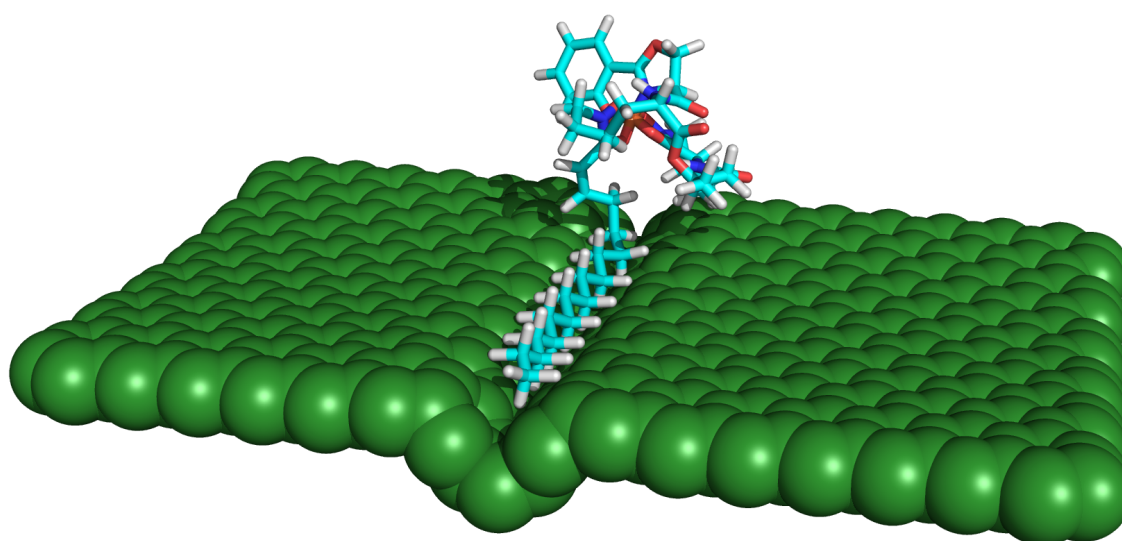


Figure 77: Hypothetical molecular model of mycobactin T bound to a hydrophobic groove etched in the surface of a graphite electrode. Molecular modelling and image were generously contributed by Craig Saperstein using PyMOL version 1.5.0.1²³⁷ and Avogadro version 1.0.3 (avogadro.openmolecules.net).

7.5 Conclusions

In this chapter the prospects of using the simple mycobactin assay developed in this dissertation for diagnosis of TB has been addressed, as well as a number of potential applications for the assay. The assay system has potential uses that run the gambit from TB and companion diagnostics to research utilisation and monitoring the industrial production of siderophores. These preliminary data also help to identify the direction of future research that may be done to further improve the sensitivity of the assay system for mycobactin. Furthermore, this dissertation has sought to elucidate what role the reduction of ferric mycobactin might play in the complex iron-trafficking machinery of one of the world's most deadly pathogens, *Mycobacterium tuberculosis* through the proposal of a novel, lipophilic mycobactin-mediated iron acquisition pathway. Although mycobactin and carboxymycobactin were not detected in the clinical samples of urine and plasma tested here, future investigations into the biodistribution of mycobactin in other tissues of infected individuals may show that the goal of a low-cost TB diagnostic device is still within reach. Ultimately, through the diligence of future endeavours, the simple assay for mycobacterial siderophores will serve to benefit science and the greater good of global health.

References

1. Kappelman, J.; Alçiçek, M. C.; Kazancı, N.; Schultz, M.; Ozkul, M.; Sen, S., First Homo erectus from Turkey and implications for migrations into temperate Eurasia. *Am J Phys Anthropol* **2008**, *135* (1), 110-6.
2. Hershkovitz, I.; Donoghue, H. D.; Minnikin, D. E.; Besra, G. S.; Lee, O. Y.-C.; Gernaey, A. M.; Galili, E.; Eshed, V.; Greenblatt, C. L.; Lemma, E.; Bar-Gal, G. K.; Spigelman, M., Detection and Molecular Characterization of 9000-Year-Old Mycobacterium tuberculosis from a Neolithic Settlement in the Eastern Mediterranean. *PLoS ONE* **2008**, *3* (10), e3426.
3. WHO, *Global tuberculosis control*. WHO: 2009.
4. Schluger, N. W.; Rom, W. N., The Host Immune Response to Tuberculosis. *Am. J. Respir. Crit. Care Med.* **1998**, *157* (3), 679-691.
5. Barry, C. E., 3rd; Boshoff, H. I.; Dartois, V.; Dick, T.; Ehrt, S.; Flynn, J.; Schnappinger, D.; Wilkinson, R. J.; Young, D., The spectrum of latent tuberculosis: rethinking the biology and intervention strategies. *Nat Rev Microbiol* **2009**, *7* (12), 845-55.
6. Reid, M. J. A.; Shah, N. S., Approaches to tuberculosis screening and diagnosis in people with HIV in resource-limited settings. *Lancet Infect Dis* **2009**, *9* (3), 173-184.
7. Billiau, A.; Matthys, P., Modes of action of Freund's adjuvants in experimental models of autoimmune diseases. *J Leukoc Biol* **2001**, *70* (6), 849-60.
8. Xu, S.; Cooper, A.; Sturgill-Koszycki, S.; van Heyningen, T.; Chatterjee, D.; Orme, I.; Allen, P.; Russell, D., Intracellular trafficking in Mycobacterium tuberculosis and Mycobacterium avium-infected macrophages. *The Journal of Immunology* **1994**, *153* (6), 2568-2578.
9. Beatty, W. L.; Rhoades, E. R.; Ullrich, H. J.; Chatterjee, D.; Heuser, J. E.; Russell, D. G., Trafficking and release of mycobacterial lipids from infected macrophages. *Traffic* **2000**, *1* (3), 235-47.
10. Russell, D. G.; Barry, Clifton E., 3rd; Flynn, J. L., Tuberculosis: what we don't know can, and does, hurt us. *Science* **2010**, *328* (5980), 852-6.
11. Lyashchenko, K. P.; Pollock, J. M.; Colangeli, R.; Gennaro, M. L., Diversity of antigen recognition by serum antibodies in experimental bovine tuberculosis. *Infect Immun* **1998**, *66* (11), 5344-9.
12. Alsteens, D.; Verbelen, C.; Dague, E.; Raze, D.; Baulard, A.; Dufrière, Y., Organization of the mycobacterial cell wall: a nanoscale view. *Pflügers Archiv European Journal of Physiology* **2007**.
13. WHO, *Treatment of Tuberculosis: guidelines for national programmes*. 3rd ed.; WHO: 2003.
14. WHO, *Improving the diagnosis and treatment of smear-negative pulmonary and extrapulmonary tuberculosis among adults and adolescents*. WHO: 2007.
15. Getahun, H.; Harrington, M.; O'Brien, R.; Nunn, P., Diagnosis of smear-negative pulmonary tuberculosis in people with HIV infection or AIDS in resource-constrained settings: informing urgent policy changes. *The Lancet* **2007**, *369* (9578), 2042-2049.
16. Steingart, K. R.; Ng, V.; Henry, M.; Hopewell, P. C.; Ramsay, A.; Cunningham, J.; Urbanczik, R.; Perkins, M. D.; Aziz, M. A.; Pai, M., Sputum processing methods to improve the sensitivity of smear microscopy for tuberculosis: a systematic review. *Lancet Infect Dis* **2006**, *6* (10), 664-74.
17. Brodie, D.; Schluger, N. W., The Diagnosis of Tuberculosis. *Clinics in Chest Medicine* **2005**, *26* (2), 247-271.
18. Pai, M.; Zwerling, A.; Menzies, D., Systematic review: T-cell-based assays for the diagnosis of latent tuberculosis infection: an update. *Ann Intern Med* **2008**, *149* (3), 177-84.
19. Menzies, D.; Pai, M.; Comstock, G., Meta-analysis: new tests for the diagnosis of latent tuberculosis infection: areas of uncertainty and recommendations for research. *Ann Intern Med* **2007**, *146* (5), 340-54.
20. Denlinger, C. M.; Pai, M., Point-of-care tuberculosis diagnosis: are we there yet? *Lancet Infect Dis* **2012**, *12* (3), 169-70.
21. Mabey, D.; Peeling, R. W.; Ustianowski, A.; Perkins, M. D., Diagnostics for the developing world. *Nature Reviews Microbiology* **2004**, *2* (3), 231-240.
22. WHO, *Diagnostics for tuberculosis: Global demand and market potential*. **2006**.
23. Kong, Y.; Yao, H.; Ren, H.; Subbian, S.; Cirillo, S. L. G.; Sacchetti, J. C.; Rao, J.; Cirillo, J. D., Imaging tuberculosis with endogenous beta-lactamase reporter enzyme fluorescence in live mice. *Proc Natl Acad Sci U S A* **2010**, *107* (27), 12239-44.

24. Kastrinsky, D. B.; McBride, N. S.; Backus, K. M.; LeBlanc, J. J.; Barry, C. E., 3rd, Comprehensive Natural Products II: Chemistry and Biology. Mander, L.; Liu, H.-W., Eds. Elsevier: 2010; Vol. 1, pp 65-145.
25. Hunter, S. W.; Brennan, P. J., Evidence for the presence of a phosphatidylinositol anchor on the lipoarabinomannan and lipomannan of *Mycobacterium tuberculosis*. *J Biol Chem* **1990**, *265* (16), 9272-9.
26. Talbot, E.; Munseri, P.; Teixeira, P.; Matee, M.; Bakari, M.; Lahey, T.; von Reyn, F., Test Characteristics of Urinary Lipoarabinomannan and Predictors of Mortality among Hospitalized HIV-Infected Tuberculosis Suspects in Tanzania. *PLoS One* **2012**, *7* (3), e32876.
27. Lawn, S. D.; Kerkhoff, A. D.; Vogt, M.; Wood, R., Diagnostic accuracy of a low-cost, urine antigen, point-of-care screening assay for HIV-associated pulmonary tuberculosis before antiretroviral therapy: a descriptive study. *Lancet Infect Dis* **2012**, *12* (3), 201-9.
28. Crichton, R. R.; Pierre, J.-L., Old Iron, Young Copper: from Mars to Venus. *BioMetals* **2001**, *14* (2), 99-112.
29. Neilands, J. B., Siderophores: Structure and Function of Microbial Iron Transport Compounds. *Journal of Biological Chemistry* **1995**, *270* (45), 26723-26726.
30. Twort, F. W.; Ingram, G. L. Y., A Method for Isolating and Cultivating the *Mycobacterium enteritidis chronicae pseudotuberculosis bovis*, Johnes, and some Experiments on the Preparation of a Diagnostic Vaccine for Pseudo-tuberculous Enteritis of Bovines. *Proceedings of the Royal Society of London B* **1912**, *84* (575), 517-542.
31. Francis, J.; Macturk, H. M.; Madinaveitia, J.; Snow, G. A., Mycobactin, a growth factor for *Mycobacterium johnnei*. I. Isolation from *Mycobacterium phlei*. *Biochem J* **1953**, *55* (4), 596-607.
32. Snow, G. A., Mycobactins: iron-chelating growth factors from mycobacteria. *Bacteriol Rev* **1970**, *34* (2), 99-125.
33. De Voss, J. J.; Rutter, K.; Schroeder, B. G.; Su, H.; Zhu, Y.; Barry, C. E., 3rd, The salicylate-derived mycobactin siderophores of *Mycobacterium tuberculosis* are essential for growth in macrophages. *Proc Natl Acad Sci U S A* **2000**, *97* (3), 1252-1257.
34. Macham, L. P.; Ratledge, C., A new group of water soluble iron binding compounds from mycobacteria: the exochelins. *Journal of General Microbiology* **1975**, *89* (2), 379-382.
35. Ratledge, C.; Patel, P. V., Isolation, properties and taxonomic relevance of lipid-soluble, iron-binding compounds (the nocobactins) from *Nocardia*. *J Gen Microbiol* **1976**, *93* (1), 141-152.
36. Schneider, K.; Rose, I.; Vikineswary, S.; Jones, A. L.; Goodfellow, M.; Nicholson, G.; Beil, W.; Sussmuth, R. D.; Fiedler, H.-P., Nocardichelins A and B, Siderophores from *Nocardia* Strain Acta 3026#. *Journal of Natural Products* **2007**, *70* (6), 932-935.
37. Cox, C. D.; Rinehart, K. L.; Moore, M. L.; Cook, J. C., Pyochelin: novel structure of an iron-chelating growth promoter for *Pseudomonas aeruginosa*. *Proceedings of the National Academy of Sciences of the United States of America* **1981**, *78* (7), 4256-4260.
38. Ong, S. A.; Peterson, T.; Neilands, J. B., Agrobactin, a siderophore from *Agrobacterium tumefaciens*. *J. Biol. Chem.* **1979**, *254* (6), 1860-1865.
39. Griffiths, G.; Sigel, S.; Payne, S.; Neilands, J., Vibriobactin, a siderophore from *Vibrio cholerae*. *Journal of Biological Chemistry* **1984**, *259* (1), 383-385.
40. Jalal, M. A. F.; Hossain, M. B.; Van der Helm, D.; Sanders-Loehr, J.; Actis, L. A.; Crosa, J. H., Structure of anguibactin, a unique plasmid-related bacterial siderophore from the fish pathogen *Vibrio anguillarum*. *Journal of the American Chemical Society* **1989**, *111* (1), 292-296.
41. Drechsel, H.; Stephan, H.; Lotz, R.; Haag, H.; Zähler, H.; Hantke, K.; Jung, G., Structure elucidation of yersiniabactin, a siderophore from highly virulent *Yersinia* strains. *Liebigs Annalen* **1995**, *1995* (10), 1727-1733.
42. Martinez, J. S.; Zhang, G. P.; Holt, P. D.; Jung, H.-T.; Carrano, C. J.; Haygood, M. G.; Butler, A., Self-Assembling Amphiphilic Siderophores from Marine Bacteria. *Science* **2000**, *287* (5456), 1245-1247.
43. De Voss, J. J.; Rutter, K.; Schroeder, B. G.; Barry, C. E., 3rd, Iron acquisition and metabolism by mycobacteria. *J Bacteriol* **1999**, *181* (15), 4443-4451.
44. Snow, G. A.; White, A. J., Chemical and biological properties of mycobactins isolated from various mycobacteria. *Biochem J* **1969**, *115* (5), 1031-1050.
45. Lin, Y. M.; Miller, M. J.; Mollmann, U., The remarkable hydrophobic effect of a fatty acid side chain on the microbial growth promoting activity of a synthetic siderophore. *Biometals* **2001**, *14* (2), 153-157.
46. Lane, S. J.; Marshall, P. S.; Upton, R. J.; Ratledge, C.; Ewing, M., Novel extracellular mycobactins, the carboxymycobactins from *Mycobacterium avium*. *Tetrahedron Letters* **1995**, *36* (23), 4129-4132.

47. Gobin, J.; Moore, C.; Reeve, J., Jr.; Wong, D.; Gibson, B.; Horwitz, M., Iron Acquisition by Mycobacterium Tuberculosis: Isolation and Characterization of a Family of Iron-Binding Exochelins. *PNAS* **1995**, *92* (11), 5189-5193.
48. Lane, S. J.; Marshall, P. S.; Upton, R. J.; Ratledge, C., Isolation and characterization of carboxymycobactins as the second extracellular siderophores in Mycobacterium smegmatis. *BioMetals* **1998**, *11* (1), 13-20.
49. Hough, E.; Rogers, D., The crystal structure of ferrimycobactin P, a growth factor for the mycobacteria. *Biochemical and Biophysical Research Communications* **1974**, *57* (1), 73-77.
50. Barclay, R.; Ratledge, C., Mycobactins and exochelins of Mycobacterium tuberculosis, M. bovis, M. africanum and other related species. *J Gen Microbiol* **1988**, *134* (3), 771-776.
51. Wong, D.; Gobin, J.; Horwitz, M.; Gibson, B., Characterization of exochelins of Mycobacterium avium: evidence for saturated and unsaturated and for acid and ester forms. *J. Bacteriol.* **1996**, *178* (21), 6394-6398.
52. McCullough, W. G.; Merkal, R. S., Structure of mycobactin J. *Current Microbiology* **1982**, *7* (6), 337-341.
53. Barclay, R.; Ewing, D. F.; Ratledge, C., Isolation, identification, and structural analysis of the mycobactins of Mycobacterium avium, Mycobacterium intracellulare, Mycobacterium scrofulaceum, and Mycobacterium paratuberculosis. *J. Bacteriol.* **1985**, *164* (2), 896-903.
54. Schwartz, B. D.; De Voss, J. J., Structure and absolute configuration of mycobactin J. *Tetrahedron Letters* **2001**, *42* (21), 3653-3655.
55. Gobin, J.; Wong, D. K.; Gibson, B. W.; Horwitz, M. A., Characterization of Exochelins of the Mycobacterium bovis Type Strain and BCG Substrains. *Infection and Immunity* **1999**, *67* (4), 2035-2039.
56. Hall, R. M.; Ratledge, C., Equivalence of mycobactins from Mycobacterium senegalense, Mycobacterium farcinogenes and Mycobacterium fortuitum. *J Gen Microbiol* **1985**, *131* (7), 1691-1696.
57. White, A. J.; Snow, G. A., Isolation of mycobactins from various mycobacteria. The properties of mycobactin S and H. *Biochem J* **1969**, *111* (5), 785-792.
58. Young, D. C.; Kasmar, A.; Moraski, G.; Cheng, T.-Y.; Walz, A. J.; Hu, J.; Xu, Y.; Endres, G. W.; Uzieblo, A.; Zajonc, D.; Costello, C. E.; Miller, M. J.; Moody, D. B., Synthesis of dideoxymycobactin antigens presented by CD1a reveals T cell fine specificity for natural lipopeptide structures. *J Biol Chem* **2009**, *284* (37), 25087-96.
59. Ratledge, C.; Snow, G. A., Isolation and structure of nocobactin NA, a lipid-soluble iron-binding compound from Nocardia asteroides. *Biochem J* **1974**, *139* (2), 407-413.
60. Suenaga, K.; Kokubo, S.; Shinohara, C.; Tsuji, T.; Uemura, D., Structures of amamistatins A and B, novel growth inhibitors of human tumor cell lines from an actinomycete. *Tetrahedron Letters* **1999**, *40* (10), 1945-1948.
61. Kokubo, S.; Suenaga, K.; Shinohara, C.; Tsuji, T.; Uemura, D., Structures of Amamistatins A and B, Novel Growth Inhibitors of Human Tumor Cell Lines from Nocardia asteroides. *Tetrahedron* **2000**, *56* (35), 6435-6440.
62. Nemoto, A.; Hoshino, Y.; Yazawa, K.; Ando, A.; Mikami, Y.; Komaki, H.; Tanaka, Y.; Grafe, U., Asterobactin, a new siderophore group antibiotic from Nocardia asteroides. *J Antibiot (Tokyo)* **2002**, *55* (6), 593-597.
63. Ratledge, C., Mycobactins and nocobactins. 2nd ed.; Laskin, A. I.; Lechevalier, H. A., Eds. CRC Press: 1982; Vol. IV, pp 575-580.
64. Tsuda, M.; Yamakawa, M.; Oka, S.; Tanaka, Y.; Hoshino, Y.; Mikami, Y.; Sato, A.; Fujiwara, H.; Ohizumi, Y.; Kobayashi, J. i., Brasilibactin A, a Cytotoxic Compound from Actinomycete Nocardia brasiliensis. *Journal of Natural Products* **2005**, *68* (3), 462-464.
65. Mitchell, J. M.; Shaw, J. T., Synthesis and Stereochemical Assignment of Brasilibactin A. *Organic Letters* **2007**, *9* (9), 1679-1681.
66. Tsukamoto, M.; Murooka, K.; Nakajima, S.; Abe, S.; Suzuki, H.; Hirano, K.; Kondo, H.; Kojiri, K.; Suda, H., BE-32030 A, B, C, D and E, new antitumor substances produced by Nocardia sp. A32030. *J Antibiot (Tokyo)* **1997**, *50* (10), 815-821.
67. Murakami, Y.; Kato, S.; Nakajima, M.; Matsuoka, M.; Kawai, H.; Shin-Ya, K.; Seto, H., Formobactin, a novel free radical scavenging and neuronal cell protecting substance from Nocardia sp. *J Antibiot (Tokyo)* **1996**, *49* (9), 839-845.
68. Ikeda, Y.; Nonaka, H.; Furumai, T.; Onaka, H.; Igarashi, Y., Nocardimicins A, B, C, D, E, and F, Siderophores with Muscarinic M3 Receptor Inhibiting Activity from Nocardia sp. TP-A0674. *Journal of Natural Products* **2005**, *68* (7), 1061-1065.

69. Barclay, R.; Furst, V.; Smith, I., A simple and rapid method for the detection and identification of mycobacteria using mycobactin. *J Med Microbiol* **1992**, *37* (4), 286-290.
70. Xu, G.; Martinez, J. S.; Groves, J. T.; Butler, A., Membrane Affinity of the Amphiphilic Marinobactin Siderophores. *Journal of the American Chemical Society* **2002**, *124* (45), 13408-13415.
71. Cole, S. T.; Brosch, R.; Parkhill, J.; Garnier, T.; Churcher, C.; Harris, D.; Gordon, S. V.; Eiglmeier, K.; Gas, S.; Barry, C. E., 3rd; Tekaia, F.; Badcock, K.; Basham, D.; Brown, D.; Chillingworth, T.; Connor, R.; Davies, R.; Devlin, K.; Feltwell, T.; Gentles, S.; Hamlin, N.; Holroyd, S.; Hornsby, T.; Jagels, K.; Krogh, A.; McLean, J.; Moule, S.; Murphy, L.; Oliver, K.; Osborne, J.; Quail, M. A.; Rajandream, M.-A.; Rogers, J.; Rutter, S.; Seeger, K.; Skelton, J.; Squares, R.; Squares, S.; Sulston, J. E.; Taylor, K.; Whitehead, S.; Barrell, B. G., Deciphering the biology of *Mycobacterium tuberculosis* from the complete genome sequence. *Nature* **1998**, *393* (6685), 537-544.
72. Quadri, L. E. N.; Sello, J.; Keating, T. A.; Weinreb, P. H.; Walsh, C. T., Identification of a *Mycobacterium tuberculosis* gene cluster encoding the biosynthetic enzymes for assembly of the virulence-conferring siderophore mycobactin. *Chemistry & Biology* **1998**, *5* (11), 631-645.
73. Chavadi, S. S.; Stirrett, K. L.; Edupuganti, U. R.; Vergnolle, O.; Sadhanandan, G.; Marchiano, E.; Martin, C.; Qiu, W.-G.; Soll, C. E.; Quadri, L. E. N., Mutational and phylogenetic analyses of the mycobacterial mbt gene cluster. *J Bacteriol* **2011**, *193* (21), 5905-13.
74. Krithika, R.; Marathe, U.; Saxena, P.; Ansari, M. Z.; Mohanty, D.; Gokhale, R. S., A genetic locus required for iron acquisition in *Mycobacterium tuberculosis*. *Proc Natl Acad Sci U S A* **2006**, *103* (7), 2069-2074.
75. Harrison, A. J.; Yu, M.; Gardenborg, T.; Middleditch, M.; Ramsay, R. J.; Baker, E. N.; Lott, J. S., The Structure of MbtI from *Mycobacterium tuberculosis*, the First Enzyme in the Biosynthesis of the Siderophore Mycobactin, Reveals It To Be a Salicylate Synthase. *J. Bacteriol.* **2006**, *188* (17), 6081-6091.
76. Zwahlen, J.; Kolappan, S.; Zhou, R.; Kisker, C.; Tonge, P. J., Structure and Mechanism of MbtI, the Salicylate Synthase from *Mycobacterium tuberculosis*. *Biochemistry* **2007**, *46* (4), 954-964.
77. Nagachar, N.; Ratledge, C., Roles of trpE2, entC and entD in salicylic acid biosynthesis in *Mycobacterium smegmatis*. *FEMS Microbiol Lett* **2010**, *308* (2), 159-65.
78. Hudson, A. T.; Campbell, I. M.; Bentley, R., Biosynthesis of 6-methylsalicylic acid by *Mycobacterium phlei*. *Biochemistry* **1970**, *9* (20), 3988-3992.
79. Dain, J. G.; Bentley, R., The role of malonate in the bacterial biosynthesis of 6-methylsalicylic acid. *Bioorganic Chemistry* **1971**, *1* (4), 374-379.
80. Duerfahrt, T.; Eppelmann, K.; Müller, R.; Marahiel, M. A., Rational Design of a Bimodular Model System for the Investigation of Heterocyclization in Nonribosomal Peptide Biosynthesis. *Chemistry & Biology* **2004**, *11* (2), 261-271.
81. Tateson, J. E., Early steps in the biosynthesis of mycobactins P and S. *Biochem J* **1970**, *118* (5), 747-753.
82. Frankel, B. A.; Blanchard, J. S., Mechanistic analysis of *Mycobacterium tuberculosis* Rv1347c, a lysine N ϵ -acyltransferase involved in mycobactin biosynthesis. *Archives of Biochemistry and Biophysics* **2008**, *477* (2), 259-266.
83. Moody, D. B.; Young, D. C.; Cheng, T.-Y.; Rosat, J.-P.; Roura-mir, C.; O'Connor, P. B.; Zajonc, D. M.; Walz, A.; Miller, M. J.; Levery, S. B.; Wilson, I. A.; Costello, C. E.; Brenner, M. B., T Cell Activation by Lipopeptide Antigens. *Science* **2004**, *303* (5657), 527-531.
84. Madigan, C. A.; Cheng, T.-Y.; Layre, E.; Young, D. C.; McConnell, M. J.; Debono, C. A.; Murry, J. P.; Wei, J.-R.; Barry, Clifton E., 3rd; Rodriguez, G. M.; Matsunaga, I.; Rubin, E. J.; Moody, D. B., Lipidomic discovery of deoxysiderophores reveals a revised mycobactin biosynthesis pathway in *Mycobacterium tuberculosis*. *Proc Natl Acad Sci U S A* **2012**, *109* (4), 1257-62.
85. Robinson, R.; Sobrado, P., Substrate Binding Modulates the Activity of *Mycobacterium smegmatis* G, a Flavin-Dependent Monooxygenase Involved in the Biosynthesis of Hydroxamate-Containing Siderophores. *Biochemistry* **2011**, *50* (39), 8489-96.
86. Wolpert, M.; Gust, B.; Kammerer, B.; Heide, L., Effects of deletions of mbtH-like genes on chlorobiocin biosynthesis in *Streptomyces coelicolor*. *Microbiology* **2007**, *153* (5), 1413-1423.
87. Baltz, R. H., Function of MbtH homologs in nonribosomal peptide biosynthesis and applications in secondary metabolite discovery. *J Ind Microbiol Biotechnol* **2011**, *38* (11), 1747-60.
88. Rodriguez, G. M.; Voskuil, M. I.; Gold, B.; Schoolnik, G. K.; Smith, I., ideR, an Essential Gene in *Mycobacterium tuberculosis*: Role of IdeR in Iron-Dependent Gene Expression, Iron Metabolism, and Oxidative Stress Response. *Infect. Immun.* **2002**, *70* (7), 3371-3381.
89. Gold, B.; Rodriguez, G. M.; Marras, S. A. E.; Pentecost, M.; Smith, I., The *Mycobacterium tuberculosis* IdeR is a dual functional regulator that controls transcription of genes involved in

- iron acquisition, iron storage and survival in macrophages. *Molecular Microbiology* **2001**, *42* (3), 851-865.
90. Yellaboina, S.; Ranjan, S.; Vindal, V.; Ranjan, A., Comparative analysis of iron regulated genes in mycobacteria. *FEBS Letters* **2006**, *580* (11), 2567-2576.
 91. Snow, G. A., Isolation and structure of mycobactin T, a growth factor from *Mycobacterium tuberculosis*. *Biochem J* **1965**, *97* (1), 166-175.
 92. LaMarca, B. B. D.; Zhu, W.; Arceneaux, J. E. L.; Byers, B. R.; Lundrigan, M. D., Participation of fad and mbt Genes in Synthesis of Mycobactin in *Mycobacterium smegmatis*. *J. Bacteriol.* **2004**, *186* (2), 374-382.
 93. Mitchison, D. A., Role of individual drugs in the chemotherapy of tuberculosis. *Int J Tuberc Lung Dis* **2000**, *4* (9), 796-806.
 94. Ratledge, C.; Brown, K. A., Inhibition of mycobactin formation in *Mycobacterium smegmatis* by p-aminosalicylate. A new proposal for the mode of action of p-aminosalicylate. *Am Rev Respir Dis* **1972**, *106* (5), 774-776.
 95. Nagachar, N.; Ratledge, C., Knocking out salicylate biosynthesis genes in *Mycobacterium smegmatis* induces hypersensitivity to p-aminosalicylate (PAS). *FEMS Microbiol Lett* **2010**, *311* (2), 193-199.
 96. Adilakshmi, T.; Ayling, P. D.; Ratledge, C., Mutational Analysis of a Role for Salicylic Acid in Iron Metabolism of *Mycobacterium smegmatis*. *J. Bacteriol.* **2000**, *182* (2), 264-271.
 97. Naser, S. A.; Gillespie, R. F.; Naser, N. A.; El-Zaatari, F. A. K., Effect of IS900 Gene of *Mycobacterium paratuberculosis* on *Mycobacterium smegmatis*. *Current Microbiology* **1998**, *37* (6), 373-379.
 98. Chipperfield, J. R.; Ratledge, C., Salicylic acid is not a bacterial siderophore: a theoretical study. *BioMetals* **2000**, *13* (2), 165-168.
 99. Ong, S. T.; Shan Ho, J. Z.; Ho, B.; Ding, J. L., Iron-withholding strategy in innate immunity. *Immunobiology* **2006**, *211* (4), 295-314.
 100. Gobin, J.; Horwitz, M., Exochelins of *Mycobacterium tuberculosis* remove iron from human iron-binding proteins and donate iron to mycobactins in the *M. tuberculosis* cell wall. *J. Exp. Med.* **1996**, *183* (4), 1527-1532.
 101. Wagner, D.; Maser, J.; Lai, B.; Cai, Z.; Barry, C. E., 3rd; Honer Zu Bentrup, K.; Russell, D. G.; Bermudez, L. E., Elemental analysis of *Mycobacterium avium*-, *Mycobacterium tuberculosis*-, and *Mycobacterium smegmatis*-containing phagosomes indicates pathogen-induced microenvironments within the host cell's endosomal system. *J Immunol* **2005**, *174* (3), 1491-1500.
 102. Kahnert, A.; Seiler, P.; Stein, M.; Bandermann, S.; Hahnke, K.; Mollenkopf, H.; Kaufmann, S. H. E., Alternative activation deprives macrophages of a coordinated defense program to *Mycobacterium tuberculosis*. *European Journal of Immunology* **2006**, *36* (3), 631-647.
 103. Ojha, A.; Hatfull, G. F., The role of iron in *Mycobacterium smegmatis* biofilm formation: the exochelin siderophore is essential in limiting iron conditions for biofilm formation but not for planktonic growth. *Mol Microbiol* **2007**, *66* (2), 468-483.
 104. Manabe, Y. C.; Saviola, B. J.; Sun, L.; Murphy, J. R.; Bishai, W. R., Attenuation of virulence in *Mycobacterium tuberculosis* expressing a constitutively active iron repressor. *Proceedings of the National Academy of Sciences of the United States of America* **1999**, *96* (22), 12844-12848.
 105. Hou, J. Y.; Graham, J. E.; Clark-Curtiss, J. E., *Mycobacterium avium* Genes Expressed during Growth in Human Macrophages Detected by Selective Capture of Transcribed Sequences (SCOTS). *Infect. Immun.* **2002**, *70* (7), 3714-3726.
 106. Waddell, S. J.; Butcher, P. D., Microarray analysis of whole genome expression of intracellular *Mycobacterium tuberculosis*. *Curr Mol Med* **2007**, *7* (3), 287-296.
 107. Lounis, N.; Truffot-Pernot, C.; Grosset, J.; Gordeuk, V. R.; Boelaert, J. R., Iron and *Mycobacterium tuberculosis* infection. *Journal of Clinical Virology* **2001**, *20* (3), 123-126.
 108. Gomes, M. S.; Boelaert, J. R.; Appelberg, R., Role of iron in experimental *Mycobacterium avium* infection. *Journal of Clinical Virology* **2001**, *20* (3), 117-122.
 109. Trousseau, A., *Lectures on Clinical Medicine*. 3rd ed.; The New Sydenham Society: London, 1872; Vol. 5.
 110. Gangaidzo, I. T.; Moyo, V. M.; Mvundura, E.; Aggrey, G.; Murphree, N. L.; Khumalo, H.; Saungweme, T.; Kasvosve, I.; Gomo, Z. A. R.; Rouault, T.; Boelaert, J. R.; Gordeuk, V. R., Association of Pulmonary Tuberculosis with Increased Dietary Iron. *The Journal of Infectious Diseases* **2001**, *184* (7), 936-939.
 111. Boelaert, J. R.; Vandecasteele, S. J.; Appelberg, R.; Gordeuk, V. R., The Effect of the Host's Iron Status on Tuberculosis. *J Infect Dis* **2007**, *195* (12), 1745-1753.

112. Gordeuk, V.; McLaren, C.; MacPhail, A.; Deichsel, G.; Bothwell, T., Associations of iron overload in Africa with hepatocellular carcinoma and tuberculosis: Strachan's 1929 thesis revisited. *Blood* **1996**, *87* (8), 3470-3476.
113. Timm, J.; Post, F. A.; Bekker, L.-G.; Walther, G. B.; Wainwright, H. C.; Manganelli, R.; Chan, W.-T.; Tsenova, L.; Gold, B.; Smith, I.; Kaplan, G.; McKinney, J. D., Differential expression of iron-, carbon-, and oxygen-responsive mycobacterial genes in the lungs of chronically infected mice and tuberculosis patients. *Proc Natl Acad Sci U S A* **2003**, *100* (24), 14321-14326.
114. Rachman, H.; Strong, M.; Ulrichs, T.; Grode, L.; Schuchhardt, J.; Mollenkopf, H.; Kosmiadi, G. A.; Eisenberg, D.; Kaufmann, S. H. E., Unique transcriptome signature of *Mycobacterium tuberculosis* in pulmonary tuberculosis. *Infect Immun* **2006**, *74* (2), 1233-42.
115. Matzanke, B. F.; Böhnke, R.; Möllmann, U.; Reissbrodt, R.; Schünemann, V.; Trautwein, A. X., Iron uptake and intracellular metal transfer in mycobacteria mediated by xenosiderophores. *BioMetals* **1997**, *10* (3), 193-203.
116. Macham, L. P.; Ratledge, C.; Nocton, J. C., Extracellular iron acquisition by mycobacteria: role of the exochelins and evidence against the participation of mycobactin. *Infect. Immun.* **1975**, *12* (6), 1242-1251.
117. Ratledge, C.; Patel, P. V.; Mundy, J., Iron transport in *Mycobacterium smegmatis*: the location of mycobactin by electron microscopy. *J Gen Microbiol* **1982**, *128* (7), 1559-1565.
118. Ratledge, C.; Marshall, B. J., Iron transport in *Mycobacterium smegmatis*: The role of mycobactin. *Biochimica et Biophysica Acta (BBA)-General Subjects* **1972**, *279* (1), 58-74.
119. Ratledge, C.; Ewing, M., The occurrence of carboxymycobactin, the siderophore of pathogenic mycobacteria, as a second extracellular siderophore in *Mycobacterium smegmatis*. *Microbiology* **1996**, *142* (8), 2207-2212.
120. Ratledge, C., Iron, mycobacteria and tuberculosis. *Tuberculosis* **2004**, *84* (1-2), 110-130.
121. Stephenson, M. C.; Ratledge, C., Iron transport in mycobacterium smegmatis: uptake of iron from Ferriexochelin. *J Gen Microbiol* **1979**, *110* (1), 193-202.
122. Rodriguez, G. M.; Smith, I., Identification of an ABC Transporter Required for Iron Acquisition and Virulence in *Mycobacterium tuberculosis*. *J. Bacteriol.* **2006**, *188* (2), 424-430.
123. Farhana, A.; Kumar, S.; Rathore, S. S.; Ghosh, P. C.; Ehtesham, N. Z.; Tyagi, A. K.; Hasnain, S. E., Mechanistic Insights into a Novel Exporter-Importer System of *Mycobacterium tuberculosis* Unravel Its Role in Trafficking of Iron. *PLoS ONE* **2008**, *3* (5), e2087.
124. Santhanagopalan, S. M.; Rodriguez, G. M., Examining the role of Rv2895c (ViuB) in iron acquisition in *Mycobacterium tuberculosis*. *Tuberculosis (Edinb)* **2012**, *92* (1), 60-2.
125. Siegrist, M. S.; Unnikrishnan, M.; McConnell, M. J.; Borowsky, M.; Cheng, T.-Y.; Siddiqi, N.; Fortune, S. M.; Moody, D. B.; Rubin, E. J., Mycobacterial Esx-3 is required for mycobactin-mediated iron acquisition. *Proc Natl Acad Sci U S A* **2009**, *106* (44), 18792-7.
126. Roura-Mir, C.; Wang, L.; Cheng, T.-Y.; Matsunaga, I.; Dascher, C. C.; Peng, S. L.; Fenton, M. J.; Kirschning, C.; Moody, D. B., Mycobacterium tuberculosis Regulates CD1 Antigen Presentation Pathways through TLR-2. *J Immunol* **2005**, *175* (3), 1758-1766.
127. Holmes, M. A.; Paulsene, W.; Jide, X.; Ratledge, C.; Strong, R. K., Siderocalin (Lcn 2) Also Binds Carboxymycobactins, Potentially Defending against Mycobacterial Infections through Iron Sequestration. *Structure* **2005**, *13* (1), 29-41.
128. Kjeldsen, L.; Johnsen, A.; Sengelov, H.; Borregaard, N., Isolation and primary structure of NGAL, a novel protein associated with human neutrophil gelatinase. *J. Biol. Chem.* **1993**, *268* (14), 10425-10432.
129. Kjeldsen, L.; Cowland, J. B.; Borregaard, N., Human neutrophil gelatinase-associated lipocalin and homologous proteins in rat and mouse. *Biochimica et Biophysica Acta-Protein Structure and Molecular Enzymology* **2000**, *1482* (1-2), 272-283.
130. Xu, S. Y.; Carlson, M.; Engstrom, A.; Garcia, R.; Peterson, C. G.; Venge, P., Purification and characterization of a human neutrophil lipocalin (HNL) from the secondary granules of human neutrophils. *Scand J Clin Lab Invest* **1994**, *54* (5), 365-376.
131. Kjeldsen, L.; Bainton, D.; Sengelov, H.; Borregaard, N., Identification of neutrophil gelatinase-associated lipocalin as a novel matrix protein of specific granules in human neutrophils. *Blood* **1994**, *83* (3), 799-807.
132. Flo, T. H.; Smith, K. D.; Sato, S.; Rodriguez, D. J.; Holmes, M. A.; Strong, R. K.; Akira, S.; Aderem, A., Lipocalin 2 mediates an innate immune response to bacterial infection by sequestering iron. *Nature* **2004**, *432* (7019), 917-921.

133. Goetz, D. H.; Holmes, M. A.; Borregaard, N.; Bluhm, M. E.; Raymond, K. N.; Strong, R. K., The Neutrophil Lipocalin NGAL Is a Bacteriostatic Agent that Interferes with Siderophore-Mediated Iron Acquisition. *Molecular Cell* **2002**, *10* (5), 1033-1043.
134. Pettersen, E. F.; Goddard, T. D.; Huang, C. C.; Couch, G. S.; Greenblatt, D. M.; Meng, E. C.; Ferrin, T. E., UCSF Chimera-a visualization system for exploratory research and analysis. *J Comput Chem* **2004**, *25* (13), 1605-1612.
135. Triebel, S.; Bläser, J.; Reinke, H.; Tschesche, H., A 25 kDa α 2-microglobulin-related protein is a component of the 125 kDa form of human gelatinase. *FEBS Letters* **1992**, *314* (3), 386-388.
136. Taylor, J. L.; Hattle, J. M.; Dreitz, S. A.; Troudt, J. M.; Izzo, L. S.; Basaraba, R. J.; Orme, I. M.; Matrisian, L. M.; Izzo, A. A., Role for Matrix Metalloproteinase 9 in Granuloma Formation during Pulmonary Mycobacterium tuberculosis Infection. *Infect. Immun.* **2006**, *74* (11), 6135-6144.
137. Xu, S. Y.; Pauksen, K.; Venge, P., Serum measurements of human neutrophil lipocalin (HNL) discriminate between acute bacterial and viral infections. *Scand J Clin Lab Invest* **1995**, *55* (2), 125-131.
138. Saiga, H.; Nishimura, J.; Kuwata, H.; Okuyama, M.; Matsumoto, S.; Sato, S.; Matsumoto, M.; Akira, S.; Yoshikai, Y.; Honda, K.; Yamamoto, M.; Takeda, K., Lipocalin 2-Dependent Inhibition of Mycobacterial Growth in Alveolar Epithelium. *The Journal of Immunology* **2008**, *181* (12), 8521-8527.
139. Fischbach, M. A.; Lin, H.; Liu, D. R.; Walsh, C. T., How pathogenic bacteria evade mammalian sabotage in the battle for iron. *Nat Chem Biol* **2006**, *2* (3), 132-138.
140. Abergel, R. J.; Moore, E. G.; Strong, R. K.; Raymond, K. N., Microbial Evasion of the Immune System: Structural Modifications of Enterobactin Impair Siderocalin Recognition1. *Journal of the American Chemical Society* **2006**, *128* (34), 10998-10999.
141. Abergel, R. J.; Clifton, M. C.; Pizarro, J. C.; Warner, J. A.; Shuh, D. K.; Strong, R. K.; Raymond, K. N., The siderocalin/enterobactin interaction: a link between mammalian immunity and bacterial iron transport. *Journal of the American Chemical Society* **2008**, *130* (34), 11524-11534.
142. Hoette, T. M.; Abergel, R. J.; Xu, J.; Strong, R. K.; Raymond, K. N., The Role of Electrostatics in Siderophore Recognition by the Immunoprotein Siderocalin. *Journal of the American Chemical Society* **2008**, *130* (51), 17584-17592.
143. Aposhian, H. V., DMSA and DMPS-water soluble antidotes for heavy metal poisoning. *Annu Rev Pharmacol Toxicol* **1983**, *23*, 193-215.
144. Kalinowski, D. S.; Richardson, D. R., The evolution of iron chelators for the treatment of iron overload disease and cancer. *Pharmacol Rev* **2005**, *57* (4), 547-83.
145. Dayani, P. N.; Bishop, M. C.; Black, K.; Zeltzer, P. M., Desferoxamine (DFO)-mediated iron chelation: rationale for a novel approach to therapy for brain cancer. *J Neurooncol* **2004**, *67* (3), 367-77.
146. Pahl, P.; Horwitz, M.; Horwitz, K.; Horwitz, L., Desferri-exochelin induces death by apoptosis in human breast cancer cells but does not kill normal breast cells. *Breast Cancer Research and Treatment* **2001**, *69* (1), 69-79.
147. Hodges, Y. K.; Antholine, W. E.; Horwitz, L. D., Effect on ribonucleotide reductase of novel lipophilic iron chelators: the desferri-exochelins. *Biochemical and Biophysical Research Communications* **2004**, *315* (3), 595-598.
148. Sakagami, H.; Ishihara, M.; Hoshino, Y.; Ishikawa, J.; Mikami, Y.; Fukai, T., Cytotoxicity of nocobactins NA-a, NA-b and their ferric complexes assessed by semiempirical molecular orbital method. *In Vivo* **2005**, *19* (1), 277-282.
149. Yokokawa, F.; Izumi, K.; Omata, J.; Shioiri, T., Total Synthesis of Amamistatin A, an Antiproliferative Linear Peptide from an Actinomycete. *Tetrahedron* **2000**, *56* (19), 3027-3034.
150. Fennell, K. A.; Miller, M. J., Syntheses of Amamistatin Fragments and Determination of Their HDAC and Antitumor Activity. *Organic Letters* **2007**, *9* (9), 1683-1685.
151. Fennell, K. A.; Mollmann, U.; Miller, M. J., Syntheses and Biological Activity of Amamistatin B and Analogs. *The Journal of Organic Chemistry* **2008**, *73* (3), 1018-1024.
152. Hu, J.; Miller, M. J., Total Synthesis of a Mycobactin S, a Siderophore and Growth Promoter of Mycobacterium Smegmatis, and Determination of its Growth Inhibitory Activity against Mycobacterium tuberculosis. *Journal of the American Chemical Society* **1997**, *119* (15), 3462-3468.
153. Xu, Y.; Miller, M. J., Total Syntheses of Mycobactin Analogues as Potent Antimycobacterial Agents Using a Minimal Protecting Group Strategy. *The Journal of Organic Chemistry* **1998**, *63* (13), 4314-4322.

154. Mukai, A.; Fukai, T.; Matsumoto, Y.; Ishikawa, J.; Hoshino, Y.; Yazawa, K.; Harada, K.-i.; Mikami, Y., Transvalencin Z, a new antimicrobial compound with salicylic acid residue from *Nocardia transvalensis* IFM 10065. *J Antibiot (Tokyo)* **2006**, *59* (6), 366-369.
155. Llamas, M. A.; Mooij, M. J.; Sparrius, M.; Vandenbroucke-Grauls, C. M. J. E.; Ratledge, C.; Bitter, W., Characterization of five novel *Pseudomonas aeruginosa* cell-surface signalling systems. *Mol Microbiol* **2008**, *67* (2), 458-472.
156. Walz, A. J.; Miller, M. J., β -Lactams in synthesis: short syntheses of cobactin analogs. *Tetrahedron Letters* **2007**, *48* (29), 5103-5105.
157. Nayyar, A.; Jain, R., Recent advances in new structural classes of anti-tuberculosis agents. *Curr Med Chem* **2005**, *12* (16), 1873-1886.
158. Ferreras, J. A.; Ryu, J.-S.; Lello, F. D.; Tan, D. S.; Quadri, L. E. N., Small-molecule inhibition of siderophore biosynthesis in *Mycobacterium tuberculosis* and *Yersinia pestis*. *Nat Chem Biol* **2005**, *1* (1), 29-32.
159. Somu, R. V.; Boshoff, H.; Qiao, C.; Bennett, E. M.; Barry, C. E.; Aldrich, C. C., Rationally Designed Nucleoside Antibiotics That Inhibit Siderophore Biosynthesis of *Mycobacterium tuberculosis*. *Journal of Medicinal Chemistry* **2006**, *49* (1), 31-34.
160. Vannada, J.; Bennett, E. M.; Wilson, D. J.; Boshoff, H. I.; Barry, C. E.; Aldrich, C. C., Design, Synthesis, and Biological Evaluation of β -Ketosulfonamide Adenylation Inhibitors as Potential Antitubercular Agents. *Organic Letters* **2006**, *8* (21), 4707-4710.
161. Somu, R. V.; Wilson, D. J.; Bennett, E. M.; Boshoff, H. I.; Celia, L.; Beck, B. J.; Barry, C. E.; Aldrich, C. C., Antitubercular Nucleosides That Inhibit Siderophore Biosynthesis: SAR of the Glycosyl Domain. *Journal of Medicinal Chemistry* **2006**, *49* (26), 7623-7635.
162. Qiao, C.; Gupte, A.; Boshoff, H. I.; Wilson, D. J.; Bennett, E. M.; Somu, R. V.; Barry, C. E.; Aldrich, C. C., 5'-O-[(N-Acyl)sulfamoyl]adenosines as Antitubercular Agents that Inhibit MbtA: An Adenylation Enzyme Required for Siderophore Biosynthesis of the Mycobactins. *Journal of Medicinal Chemistry* **2007**, *50* (24), 6080-6094.
163. Neres, J.; Labello, N. P.; Somu, R. V.; Boshoff, H. I.; Wilson, D. J.; Vannada, J.; Chen, L.; Barry, C. E. 3rd; Bennett, E. M.; Aldrich, C. C., Inhibition of siderophore biosynthesis in *Mycobacterium tuberculosis* with nucleoside bisubstrate analogues: structure-activity relationships of the nucleobase domain of 5'-O-[N-(salicyl)sulfamoyl]adenosine. *J Med Chem* **2008**, *51* (17), 5349-5370.
164. Gupte, A.; Boshoff, H. I.; Wilson, D. J.; Neres, J.; Labello, N. P.; Somu, R. V.; Xing, C.; Barry, C. E.; Aldrich, C. C., Inhibition of Siderophore Biosynthesis by 2-Triazole Substituted Analogues of 5'-O-[N-(Salicyl)sulfamoyl]adenosine: Antibacterial Nucleosides Effective against *Mycobacterium tuberculosis*. *Journal of Medicinal Chemistry* **2008**, *51* (23), 7495-7507.
165. Stirrett, K. L.; Ferreras, J. A.; Jayaprakash, V.; Sinha, B. N.; Ren, T.; Quadri, L. E. N., Small molecules with structural similarities to siderophores as novel antimicrobials against *Mycobacterium tuberculosis* and *Yersinia pestis*. *Bioorganic & Medicinal Chemistry Letters* **2008**, *18* (8), 2662-2668.
166. Arora, P.; Goyal, A.; Natarajan, V. T.; Rajakumara, E.; Verma, P.; Gupta, R.; Yousuf, M.; Trivedi, O. A.; Mohanty, D.; Tyagi, A.; Sankaranarayanan, R.; Gokhale, R. S., Mechanistic and functional insights into fatty acid activation in *Mycobacterium tuberculosis*. *Nat Chem Biol* **2009**, *5* (3), 166-73.
167. Gupte, A., Synthesis of deuterium-labelled 5'-O-[N-(Salicyl)sulfamoyl]adenosine (Sal-AMS-d4) as an internal standard for quantitation of Sal-AMS. *Journal of labelled compounds & radiopharmaceuticals* **2008**, *51* (2), 118-122.
168. Jayaprakash, V.; Sinha, B. N.; Ucar, G.; Ercan, A., Pyrazoline-based mycobactin analogues as MAO-inhibitors. *Bioorganic & Medicinal Chemistry Letters* **2008**, *18* (24), 6362-6368.
169. Kosterink, J. G. W., Positron emission tomography in the diagnosis and treatment management of tuberculosis. *Curr Pharm Des* **2011**, *17* (27), 2875-80.
170. Petrik, M.; Haas, H.; Dobrozemsky, G.; Lass-Flörl, C.; Helbok, A.; Blatzer, M.; Dietrich, H.; Decristoforo, C., ^{68}Ga -siderophores for PET imaging of invasive pulmonary aspergillosis: proof of principle. *J Nucl Med* **2010**, *51* (4), 639-645.
171. Hall, R. M., Mycobactins: how to obtain them and how to employ them as chemotaxonomic characters for the mycobacteria and related organisms. *Actinomycetes* **1986**, *19*, 92-106.
172. Bosne, S.; Lévy-Frébault, V. V., Mycobactin analysis as an aid for the identification of *Mycobacterium fortuitum* and *Mycobacterium chelonae* subspecies. *Journal of Clinical Microbiology* **1992**, *30* (5), 1225-1231.
173. Greatbanks, D.; Bedford, G. R., Identification of mycobactins by nuclear-magnetic-resonance spectroscopy. *Biochem. J.* **1969**, *115* (5), 1047-1050.

174. Snow, G. A., Metal complexes of mycobactin P and of desferrisideramines. *Biochem. J.* **1969**, *115* (2), 199-205.
175. Raghu, B.; Sarma, G. R., Isolation and characterization of siderophores and envelope proteins from mycobacteria. *Biochemistry and Molecular Biology International* **1993**, *31* (2), 333-339.
176. Schwyn, B.; Neilands, J. B., Universal chemical assay for the detection and determination of siderophores. *Anal Biochem* **1987**, *160* (1), 47-56.
177. Arnow, L. E., Colorimetric determination of the components of 3,4-dihydroxyphenylalaninetyrosine mixtures. *J. Biol. Chem.* **1937**, *118* (2), 531-537.
178. Lambrecht, R. S.; Collins, M. T., Inability to detect mycobactin in Mycobacteria-infected tissues suggests an alternative iron acquisition mechanism by Mycobacteria in vivo. *Microbial Pathogenesis* **1993**, *14* (3), 229-238.
179. Peyron, P.; Vaubourgeix, J.; Poquet, Y.; Levillain, F.; Botanch, C.; Bardou, F.; Daffé, M.; Emile, J.-F.; Marchou, B.; Cardona, P.-J.; de Chastellier, C.; Altare, F., Foamy Macrophages from Tuberculous Patients' Granulomas Constitute a Nutrient-Rich Reservoir for M. tuberculosis Persistence. *PLoS Pathog* **2008**, *4* (11), e1000204-.
180. Bratbak, G.; Dundas, I., Bacterial dry matter content and biomass estimations. *Appl Environ Microbiol* **1984**, *48* (4), 755-7.
181. Bakken, L. R.; Olsen, R. A., Buoyant densities and dry-matter contents of microorganisms: conversion of a measured biovolume into biomass. *Appl Environ Microbiol* **1983**, *45* (4), 1188-95.
182. Feldman, D.; Krishnan, A., Estrogens in unexpected places: possible implications for researchers and consumers. *Environ Health Perspect* **1995**, *103 Suppl 7*, 129-33.
183. Ratledge, C.; Winder, F. G., The accumulation of salicylic acid by mycobacteria during growth on an iron-deficient medium. *Biochem J* **1962**, *84*, 501-6.
184. Hall, R. M.; Ratledge, C., A simple method for the production of mycobactin, the lipid-soluble siderophore, from mycobacteria. *FEMS Microbiology Letters* **1982**, *15* (2), 133-136.
185. Messenger, A. J. M.; Ratledge, C., *Siderophores in Comprehensive Biotechnology*. Pergamon Press: Elmsford, NY, 1985; Vol. 3.
186. Luo, M.; Fadeev, E. A.; Groves, J. T., Mycobactin-mediated iron acquisition within macrophages. *Nat Chem Biol* **2005**, *1* (3), 149-153.
187. Garton, N. J.; Waddell, S. J.; Sherratt, A. L.; Lee, S.-M.; Smith, R. J.; Senner, C.; Hinds, J.; Rajakumar, K.; Adegbola, R. A.; Besra, G. S.; Butcher, P. D.; Barer, M. R., Cytological and Transcript Analyses Reveal Fat and Lazy Persister-Like Bacilli in Tuberculous Sputum. *PLoS Medicine* **2008**, *5* (4).
188. Barry, C. E., 3rd; Boshoff, H., Getting the iron out. *Nat Chem Biol* **2005**, *1* (3), 127-128.
189. Martinez, J. S.; Carter-Franklin, J. N.; Mann, E. L.; Martin, J. D.; Haygood, M. G.; Butler, A., Bioinorganic Chemistry Special Feature: Structure and membrane affinity of a suite of amphiphilic siderophores produced by a marine bacterium. *Proceedings of the National Academy of Sciences* **2003**, *100* (7), 3754-3759.
190. Cook, G. M.; Berney, M.; Gebhard, S.; Heinemann, M.; Cox, R. A.; Danilchanka, O.; Niederweis, M., Physiology of mycobacteria. *Adv Microb Physiol* **2009**, *55*, 81-182, 318-9.
191. den Hertog, A. L.; Klatser, P. R.; Anthony, R. M., Buoyant density of Mycobacterium tuberculosis: implications for sputum processing. *Int J Tuberc Lung Dis* **2009**, *13* (4), 466-71.
192. Lin, P. L.; Pawar, S.; Myers, A.; Pegu, A.; Fuhrman, C.; Reinhart, T. A.; Capuano, S. V.; Klein, E.; Flynn, J. L., Early events in Mycobacterium tuberculosis infection in cynomolgus macaques. *Infect Immun* **2006**, *74* (7), 3790-803.
193. Gadagkar, R.; Gopinathan, K. P., Growth of Mycobacterium smegmatis in minimal and complete media. *Journal of Biosciences* **1980**, *2* (4), 337-348.
194. IUPAC, *Compendium of Chemical Terminology, 2nd ed. (the "Gold Book")*. Scientific Publications: Oxford, 1997.
195. Via, L. E.; Lin, P. L.; Ray, S. M.; Carrillo, J.; Allen, S. S.; Eum, S. Y.; Taylor, K.; Klein, E.; Manjunatha, U.; Gonzales, J.; Lee, E. G.; Park, S. K.; Raleigh, J. A.; Cho, S. N.; McMurray, D. N.; Flynn, J. L.; Barry, C. E. 3rd, Tuberculous granulomas are hypoxic in guinea pigs, rabbits, and nonhuman primates. *Infect Immun* **2008**, *76* (6), 2333-2340.
196. Wilson, R.; Turner, A. P. F., Glucose oxidase: an ideal enzyme. *Biosensors and Bioelectronics* **1992**, *7* (3), 165-185.
197. Harrington, J. M.; Crumbliss, A. L., The redox hypothesis in siderophore-mediated iron uptake. *Biometals* **2009**, *22* (4), 679-689.
198. Kiema, G. K.; Aktay, M.; McDermott, M. T., Preparation of reproducible glassy carbon electrodes by removal of polishing impurities. *Journal of Electroanalytical Chemistry* **2003**, *540*, 7-15.

199. Harrington, J. M.; Park, H.; Ying, Y.; Hong, J.; Crumbliss, A. L., Characterization of Fe(III) sequestration by an analog of the cytotoxic siderophore brasilibactin A: Implications for the iron transport mechanism in mycobacteria. *Metallomics* **2011**, *3* (5), 464-471.
200. Miller, M. J.; Walz, A. J.; Zhu, H.; Wu, C.; Moraski, G.; Möllmann, U.; Tristani, E. M.; Crumbliss, A. L.; Ferdig, M. T.; Checkley, L.; Edwards, R. L.; Boshoff, H. I., Design, Synthesis, and Study of a Mycobactin-Artemisinin Conjugate That Has Selective and Potent Activity against Tuberculosis and Malaria. *J Am Chem Soc* **2011**, *133* (7), 2076-2079.
201. Boukhalfa, H.; Crumbliss, A. L., Chemical aspects of siderophore mediated iron transport. *Biometals* **2002**, *15* (4), 325-339.
202. Wirgau, J. I.; Spasojević, I.; Boukhalfa, H.; Batinić-Haberle, I.; Crumbliss, A. L., Thermodynamics, kinetics, and mechanism of the stepwise dissociation and formation of Tris(L-lysinehydroxamate)iron(III) in aqueous acid. *Inorg Chem* **2002**, *41* (6), 1464-73.
203. Randles, J. E. B., A cathode ray polarograph. Part II.-The current-voltage curves. *Trans. Faraday Soc.* **1948**, *44*, 327-338.
204. Sevcik, A., Oscillographic polarography with periodical triangular voltage. *Collection of Czechoslovak Chemical Communications* **1948**, *13*, 349-377.
205. Lennartson, A., Optical resolution and racemisation of [Fe(acac)₃]. *Inorganica Chimica Acta* **2011**, *365* (1), 451-453.
206. Klingler, R. J.; Kochi, J. K., Electron-transfer kinetics from cyclic voltammetry. Quantitative description of electrochemical reversibility. *The Journal of Physical Chemistry* **1981**, *85* (12), 1731-1741.
207. Nicholson, R. S.; Shain, I., Theory of Stationary Electrode Polarography. Single Scan and Cyclic Methods Applied to Reversible, Irreversible, and Kinetic Systems. *Analytical Chemistry* **1964**, *36* (4), 706-723.
208. Dabkowska, A. P.; Foglia, F.; Lawrence, M. J.; Lorenz, C. D.; McLain, S. E., On the solvation structure of dimethylsulfoxide/water around the phosphatidylcholine head group in solution. *J Chem Phys* **2011**, *135* (22), 225105.
209. Vladkova, R., Chlorophyll a self-assembly in polar solvent-water mixtures. *Photochem Photobiol* **2000**, *71* (1), 71-83.
210. Collins, K. D.; Washabaugh, M. W., The Hofmeister effect and the behaviour of water at interfaces. *Q Rev Biophys* **1985**, *18* (4), 323-422.
211. Reed, M. B.; Domenech, P.; Manca, C.; Su, H.; Barczak, A. K.; Kreiswirth, B. N.; Kaplan, G.; Barry, C. E., 3rd, A glycolipid of hypervirulent tuberculosis strains that inhibits the innate immune response. *Nature* **2004**, *431* (7004), 84-87.
212. Minion, J.; Leung, E.; Talbot, E.; Dheda, K.; Pai, M.; Menzies, D., Diagnosing tuberculosis with urine lipoarabinomannan: systematic review and meta-analysis. *Eur Respir J* **2011**, *38* (6), 1398-405.
213. Laemmli, U. K., Cleavage of structural proteins during the assembly of the head of bacteriophage T4. *Nature* **1970**, *227* (5259), 680-5.
214. Blankespoor, R.; Limoges, B.; Schollhorn, B.; Syssa-Magale, J.-L.; Yazidi, D., Dense monolayers of metal-chelating ligands covalently attached to carbon electrodes electrochemically and their useful application in affinity binding of histidine-tagged proteins. *Langmuir* **2005**, *21* (8), 3362-3375.
215. Capek, P.; McBride, N. S.; Dona, V.; Angrish, D.; Tahlan, K.; Saccavini, C.; Jiang, B.; Boshoff, H.; Barry, C. E., 3rd; Dickerson, T. J., Total Synthesis of Mycobactin S and T: Synthetic Revision and Biological Properties. *Submitted for publication* **2012**.
216. Walz, A. J.; Mollmann, U.; Miller, M. J., Synthesis and studies of catechol-containing mycobactin S and T analogs. *Org Biomol Chem* **2007**, *5* (10), 1621-1628.
217. Rodriguez, G.; Gardner, R.; Kaur, N.; Phanstiel, O., Utilization of Fe³⁺-acinetoferrin analogs as an iron source by Mycobacterium tuberculosis. *BioMetals* **2008**, *21* (1), 93-103.
218. Ryndak, M. B.; Wang, S.; Smith, I.; Rodriguez, G. M., The Mycobacterium tuberculosis high-affinity iron importer, IrtA, contains an FAD-binding domain. *J Bacteriol* **2010**, *192* (3), 861-9.
219. Kamin, R. A.; Wilson, G. S., Rotating ring-disk enzyme electrode for biocatalysis kinetic studies and characterization of the immobilized enzyme layer. *Analytical Chemistry* **1980**, *52* (8), 1198-1205.
220. Cass, A. E.; Davis, G.; Francis, G. D.; Hill, H. A.; Aston, W. J.; Higgins, I. J.; Plotkin, E. V.; Scott, L. D.; Turner, A. P., Ferrocene-mediated enzyme electrode for amperometric determination of glucose. *Anal Chem* **1984**, *56* (4), 667-71.
221. Ghindilis, A. L.; Atanasov, P.; Wilkins, E., Enzyme-catalyzed direct electron transfer: Fundamentals and analytical applications. *Electroanalysis* **1997**, *9* (9), 661-674.

222. Gorton, L.; Lindgren, A.; Larsson, T.; Munteanu, F. D.; Ruzgas, T.; Gazaryan, I., Direct electron transfer between heme-containing enzymes and electrodes as basis for third generation biosensors. *Analytica Chimica Acta* **1999**, *400* (1-3), 91-108.
223. Wang, J., Electrochemical glucose biosensors. *Chem Rev* **2008**, *108* (2), 814-25.
224. Wang, J.; Li, M.; Shi, Z.; Li, N.; Gu, Z., Direct Electrochemistry of Cytochrome c at a Glassy Carbon Electrode Modified with Single-Wall Carbon Nanotubes. *Analytical Chemistry* **2002**, *74* (9), 1993-1997.
225. Gooding, J. J.; Wibowo, R.; Liu, Yang, W.; Losic, D.; Orbons, S.; Mearns, F. J.; Shapter, J. G.; Hibbert, D. B., Protein Electrochemistry Using Aligned Carbon Nanotube Arrays. *Journal of the American Chemical Society* **2003**, *125* (30), 9006-9007.
226. Drummond, T. G.; Hill, M. G.; Barton, J. K., Electrochemical DNA sensors. *Nat Biotechnol* **2003**, *21* (10), 1192-9.
227. Wolff, A. C.; Hammond, M. E. H.; Schwartz, J. N.; Hagerty, K. L.; Allred, D. C.; Cote, R. J.; Dowsett, M.; Fitzgibbons, P. L.; Hanna, W. M.; Langer, A.; McShane, L. M.; Paik, S.; Pegram, M. D.; Perez, E. A.; Press, M. F.; Rhodes, A.; Sturgeon, C.; Taube, S. E.; Tubbs, R.; Vance, G. H.; van de Vijver, M.; Wheeler, T. M.; Hayes, D. F.; American Society of Clinical Oncology; College of American Pathologists, American Society of Clinical Oncology/College of American Pathologists guideline recommendations for human epidermal growth factor receptor 2 testing in breast cancer. *J Clin Oncol* **2007**, *25* (1), 118-45.
228. Kontoghiorghes, G. J.; Neocleous, K.; Kolnagou, A., Benefits and risks of deferiprone in iron overload in Thalassaemia and other conditions: comparison of epidemiological and therapeutic aspects with deferoxamine. *Drug Saf* **2003**, *26* (8), 553-84.
229. Allain, P.; Chaleil, D.; Mauras, Y.; Beaudeau, G.; Varin, M. C.; Poignet, J. L.; Ciancioni, C.; Ang, K. S.; Cam, G.; Simon, P., Pharmacokinetics of desferrioxamine and of its iron and aluminium chelates in patients on haemodialysis. *Clin Chim Acta* **1987**, *170* (2-3), 331-8.
230. Limenta, L. M. G.; Jirasomprasert, T.; Jittangprasert, P.; Wilairat, P.; Yamanont, P.; Chantharaksri, U.; Fucharoen, S.; Morales, N. P., Pharmacokinetics of deferiprone in patients with β -thalassaemia: impact of splenectomy and iron status. *Clin Pharmacokinet* **2011**, *50* (1), 41-50.
231. Piga, A.; Galanello, R.; Forni, G. L.; Cappellini, M. D.; Origa, R.; Zappu, A.; Donato, G.; Bordone, E.; Lavagetto, A.; Zanaboni, L.; Sechaud, R.; Hewson, N.; Ford, J. M.; Opitz, H.; Alberti, D., Randomized phase II trial of deferasirox (Exjade, ICL670), a once-daily, orally-administered iron chelator, in comparison to deferoxamine in thalassemia patients with transfusional iron overload. *Haematologica* **2006**, *91* (7), 873-80.
232. Raymond, K. N.; Dertz, E. A.; Kim, S. S., Enterobactin: an archetype for microbial iron transport. *Proc Natl Acad Sci U S A* **2003**, *100* (7), 3584-8.
233. Ramanaviciene, A.; Ramanavicius, A., Molecularly imprinted polypyrrole-based synthetic receptor for direct detection of bovine leukemia virus glycoproteins. *Biosens Bioelectron* **2004**, *20* (6), 1076-82.
234. Blanco-López, M. C.; Lobo-Castañón, M. J.; Miranda-Ordieres, A. J.; Tuñón-Blanco, P., Voltammetric sensor for vanillylmandelic acid based on molecularly imprinted polymer-modified electrodes. *Biosens Bioelectron* **2003**, *18* (4), 353-62.
235. Youn, S. W.; Takahashi, M.; Goto, H.; Maeda, R., Microstructuring of glassy carbon mold for glass embossing-Comparison of focused ion beam, nano/femtosecond-pulsed laser and mechanical machining. *Microelectronic Engineering* **2006**, *83* (11-12), 2482-2492.
236. Dai, L.; Griesser, H. J.; Mau, A. W. H., Surface Modification by Plasma Etching and Plasma Patterning. *The Journal of Physical Chemistry B* **1997**, *101* (46), 9548-9554.
237. Schrodinger, LLC, The PyMOL Molecular Graphics System, Version 1.5.0.1. 2012.

Appendix 1: Matlab Programs for Processing Electrochemical Data

The following are Matlab programs that were written for analysis of the electrochemical data produced during this project. Note that `hdrload.m` is also required for some of these programs and was downloaded from the Mathworks website at <http://www.mathworks.com/support/tech-notes/1400/1402.html>.

High-Speed Cyclic Voltammogram PicoScope Data Processing 'PicoScope_binning_v11.m'

```
% This file was written by Nicholas McBride to process cyclic voltammetry
% data acquired using the PicoScope 6 oscilloscope software. Please refer
% to the accompanying protocol document to see details on data acquisition.

clear;

% Gets all the .mat file names in the specified directory and current range
DirName = uigetdir('', 'Please select the directory containing .mat files to
be processed');
InputFiles = dir(fullfile(DirName, '*.mat'));
CurrentRange = input('Current range (mA): ')/1000;
BinSize = 4000;

for FileNum = 1:length(InputFiles)

    % Load data from PicoScope.mat file
    % This file will contain the single column arrays 'A' and 'B'
    containing
    % the channel A and B data and the variables 'Length' 'Tinterval' and
    'Tstart'
    FileName = InputFiles(FileNum).name;
    disp(' ');
    disp(['Loading "', FileName, '"']);
    load(fullfile(DirName, FileName));

    % Determine the number of binned untrimmed samples from the bin size
    NumBins = floor(Length/BinSize);

    % Separates the bins into different columns
    ColBinsA = zeros([BinSize, NumBins]);
    ColBinsB = zeros([BinSize, NumBins]);
    for BinNum = 1:NumBins
        BinBottom = (BinNum-1)*BinSize+1;
        BinTop = BinNum*BinSize;
        ColBinsA(:, BinNum) = A(BinBottom:BinTop);
        ColBinsB(:, BinNum) = B(BinBottom:BinTop);
    end
    clear('A', 'B');

    BinA = mean(ColBinsA)';
    BinB = mean(ColBinsB)';
    clear('ColBinsA', 'ColBinsB');
```



```

% Post-bin processing

% Scaling current range = 200mV for Solartron instrument
BinB = BinB.*(CurrentRange/0.2);

% Find minimum and maximum potentials to the nearest 10mV
MinPot = round(100*min(BinA))/100;
MaxPot = round(100*max(BinA))/100;

% Finds scan speed using linear fit
BinTinterval = Tinterval*BinSize;
Time = [0:BinTinterval:(NumBins-1)*BinTinterval]';
Fit =
polyfit(Time(round(0.35*NumBins):round(0.45*NumBins)),BinA(round(0.35*NumBi
ns):round(0.45*NumBins)),1); % Watch out for these numbers causing trouble
ScanSpeed = abs(Fit(1));

% Determines whether vertex 2 is the minimum or maximum potential
if Fit(1) >= 0
    Vertex1Pot = MinPot;
    Vertex2Pot = MaxPot;
    [unused, Vertex2Index] =
max(BinA(round(0.45*NumBins):round(0.55*NumBins)));
else
    Vertex1Pot = MaxPot;
    Vertex2Pot = MinPot;
    [unused, Vertex2Index] =
min(BinA(round(0.45*NumBins):round(0.55*NumBins)));
end
Vertex2Index = Vertex2Index+round(0.45*NumBins)-1; % Corrects for
limited range used to find vertex 2 index in previous line

% Trims the data to include only the center cycle from the data
% acquisition period and check if an entire cycle is included
SweepLengthBins = round((MaxPot-MinPot)/(ScanSpeed*BinTinterval));
CycleStartIndex = Vertex2Index-SweepLengthBins;
if CycleStartIndex < 1
    CycleStartIndex = 1;
end
CycleEndIndex = Vertex2Index+SweepLengthBins;
if CycleEndIndex > NumBins
    CycleEndIndex = NumBins;
end

TrimA = BinA(CycleStartIndex:CycleEndIndex);
TrimB = BinB(CycleStartIndex:CycleEndIndex);

% Display statistics. The nasty was done by more than two elephants.
disp(['Vertex potential 1: ', num2str(Vertex1Pot), ' V']);
disp(['Vertex potential 2: ', num2str(Vertex2Pot), ' V']);
disp(['Calculated scan speed: ', num2str(ScanSpeed), ' V/s']);
disp(['Original data points: ', num2str(Length)]);
disp(['Bin size: ', num2str(BinSize)]);
disp(['Final resolution: ', num2str(SweepLengthBins/((MaxPot-MinPot))),
' bins/V']);

% Write the stats and binned, trimmed data to a .csv file
NewFileName = regexprep(FileName,'.mat','_binned.csv');
disp(['Writing 1 cycle of binned data to "', NewFileName, '"']);

dlmwrite(fullfile(DirName, NewFileName), {'Original file name',
FileName}, 'delimiter', '');

```

```

    dlmwrite(fullfile(DirName, NewFileName), {'Modified',
InputFiles(FileNum).date}, '-append', 'delimiter', '');

    dlmwrite(fullfile(DirName, NewFileName), {'Processed file name',
NewFileName}, '-append', 'delimiter', '', 'roffset', 1);
    dlmwrite(fullfile(DirName, NewFileName), {'Processed', datestr(now)},
'-append', 'delimiter', '');

    dlmwrite(fullfile(DirName, NewFileName), {'Original data points',
num2str(Length)}, '-append', 'delimiter', '', 'roffset', 1);
    dlmwrite(fullfile(DirName, NewFileName), {'Bin size',
num2str(BinSize)}, '-append', 'delimiter', '');
    dlmwrite(fullfile(DirName, NewFileName), {'Final resolution (bins/V)',
num2str(SweepLengthBins/((MaxPot-MinPot)))}, '-append', 'delimiter', '');
    dlmwrite(fullfile(DirName, NewFileName), {'Vertex potential 1 (V)',
num2str(Vertex1Pot)}, '-append', 'delimiter', '');
    dlmwrite(fullfile(DirName, NewFileName), {'Vertex potential 2 (V)',
num2str(Vertex2Pot)}, '-append', 'delimiter', '');
    dlmwrite(fullfile(DirName, NewFileName), {'Calculated scan speed
(V/s)', num2str(ScanSpeed)}, '-append', 'delimiter', '');

    dlmwrite(fullfile(DirName, NewFileName), 'Potential (V),Current (A)',
'-append', 'delimiter', '', 'roffset', 1); % Write data headers
    dlmwrite(fullfile(DirName, NewFileName), [TrimA,TrimB], '-append'); %
Write data
end

% Seven more words to finish eights.

```

Appendix 2: Mycobactin Masses for HRMS Screening

Table 14: Carboxymycobactin masses.

ID	C	H	N	O	Fe	C in Fatty Acyl	Unsat	Exact Mass	M + H+	M + H+ (Fe54)
CM1	28	34	5	12	1	2	0	688.15533	689.16261	687.16728
CM2	29	36	5	12	1	3	0	702.17098	703.17826	701.18293
CM3	30	36	5	12	1	4	1	714.17098	715.17826	713.18293
CM4	30	38	5	12	1	4	0	716.18663	717.19391	715.19858
CM5	31	38	5	12	1	5	1	728.18663	729.19391	727.19858
CM6	31	40	5	12	1	5	0	730.20228	731.20956	729.21423
CM7	32	40	5	12	1	6	1	742.20228	743.20956	741.21423
CM8	32	42	5	12	1	6	0	744.21793	745.22521	743.22988
CM9	33	42	5	12	1	7	1	756.21793	757.22521	755.22988
CM10	33	44	5	12	1	7	0	758.23358	759.24086	757.24553
CM11	34	44	5	12	1	8	1	770.23358	771.24086	769.24553
CM12	34	46	5	12	1	8	0	772.24923	773.25651	771.26118
CM13	35	46	5	12	1	9	1	784.24923	785.25651	783.26118
CM14	35	48	5	12	1	9	0	786.26488	787.27216	785.27683
CM15	36	48	5	12	1	10	1	798.26488	799.27216	797.27683
CM16	36	50	5	12	1	10	0	800.28053	801.28781	799.29248
CM17	37	50	5	12	1	11	1	812.28053	813.28781	811.29248
CM18	37	52	5	12	1	11	0	814.29618	815.30346	813.30813
CM19	38	52	5	12	1	12	1	826.29618	827.30346	825.30813
CM20	38	54	5	12	1	12	0	828.31183	829.31911	827.32378
CM21	39	54	5	12	1	13	1	840.31183	841.31911	839.32378
CM22	39	56	5	12	1	13	0	842.32748	843.33476	841.33943
CM23	40	56	5	12	1	14	1	854.32748	855.33476	853.33943
CM24	40	58	5	12	1	14	0	856.34313	857.35041	855.35508
CM25	41	58	5	12	1	15	1	868.34313	869.35041	867.35508
CM26	41	60	5	12	1	15	0	870.35878	871.36606	869.37073
CM27	42	60	5	12	1	16	1	882.35878	883.36606	881.37073
CM28	42	62	5	12	1	16	0	884.37443	885.38171	883.38638
CM29	43	62	5	12	1	17	1	896.37443	897.38171	895.38638
CM30	43	64	5	12	1	17	0	898.39009	899.39736	897.40203
CM31	44	64	5	12	1	18	1	910.39009	911.39736	909.40203
CM32	44	66	5	12	1	18	0	912.40574	913.41301	911.41768
CM33	45	66	5	12	1	19	1	924.40574	925.41301	923.41768
CM34	45	68	5	12	1	19	0	926.42139	927.42866	925.43333
CM35	46	68	5	12	1	20	1	938.42139	939.42866	937.43333
CM36	46	70	5	12	1	20	0	940.43704	941.44431	939.44898
CM37	47	70	5	12	1	21	1	952.43704	953.44431	951.44898
CM38	47	72	5	12	1	21	0	954.45269	955.45996	953.46463
CM39	48	72	5	12	1	22	1	966.45269	967.45996	965.46463
CM40	48	74	5	12	1	22	0	968.46834	969.47561	967.48028
CM41	49	74	5	12	1	23	1	980.46834	981.47561	979.48028
CM42	49	76	5	12	1	23	0	982.48399	983.49126	981.49593
CM43	50	76	5	12	1	24	1	994.48399	995.49126	993.49593
CM44	50	78	5	12	1	24	0	996.49964	997.50691	995.51158

Table 15: Mycobactin T masses.

ID	C	H	N	O	Fe	C in Fatty		Exact Mass	M + H+	M + H+ (Fe54)
						Acyl	Unsat			
MT1	29	36	5	10	1	3	1	670.18115	671.18843	669.19310
MT2	29	38	5	10	1	3	0	672.19680	673.20408	671.20875
MT3	30	38	5	10	1	4	1	684.19680	685.20408	683.20875
MT4	30	40	5	10	1	4	0	686.21246	687.21973	685.22440
MT5	31	40	5	10	1	5	1	698.21246	699.21973	697.22440
MT6	31	42	5	10	1	5	0	700.22811	701.23538	699.24005
MT7	32	42	5	10	1	6	1	712.22811	713.23538	711.24005
MT8	32	44	5	10	1	6	0	714.24376	715.25103	713.25570
MT9	33	44	5	10	1	7	1	726.24376	727.25103	725.25570
MT10	33	46	5	10	1	7	0	728.25941	729.26668	727.27135
MT11	34	46	5	10	1	8	1	740.25941	741.26668	739.27135
MT12	34	48	5	10	1	8	0	742.27506	743.28233	741.28700
MT13	35	48	5	10	1	9	1	754.27506	755.28233	753.28700
MT14	35	50	5	10	1	9	0	756.29071	757.29798	755.30265
MT15	36	50	5	10	1	10	1	768.29071	769.29798	767.30265
MT16	36	52	5	10	1	10	0	770.30636	771.31363	769.31830
MT17	37	52	5	10	1	11	1	782.30636	783.31363	781.31830
MT18	37	54	5	10	1	11	0	784.32201	785.32928	783.33395
MT19	38	54	5	10	1	12	1	796.32201	797.32928	795.33395
MT20	38	56	5	10	1	12	0	798.33766	799.34493	797.34960
MT21	39	56	5	10	1	13	1	810.33766	811.34493	809.34960
MT22	39	58	5	10	1	13	0	812.35331	813.36058	811.36526
MT23	40	58	5	10	1	14	1	824.35331	825.36058	823.36526
MT24	40	60	5	10	1	14	0	826.36896	827.37623	825.38091
MT25	41	60	5	10	1	15	1	838.36896	839.37623	837.38091
MT26	41	62	5	10	1	15	0	840.38461	841.39188	839.39656
MT27	42	62	5	10	1	16	1	852.38461	853.39188	851.39656
MT28	42	64	5	10	1	16	0	854.40026	855.40753	853.41221
MT29	43	64	5	10	1	17	1	866.40026	867.40753	865.41221
MT30	43	66	5	10	1	17	0	868.41591	869.42318	867.42786
MT31	44	66	5	10	1	18	1	880.41591	881.42318	879.42786
MT32	44	68	5	10	1	18	0	882.43156	883.43883	881.44351
MT33	45	68	5	10	1	19	1	894.43156	895.43883	893.44351
MT34	45	70	5	10	1	19	0	896.44721	897.45448	895.45916
MT35	46	70	5	10	1	20	1	908.44721	909.45448	907.45916
MT36	46	72	5	10	1	20	0	910.46286	911.47013	909.47481
MT37	47	72	5	10	1	21	1	922.46286	923.47013	921.47481
MT38	47	74	5	10	1	21	0	924.47851	925.48578	923.49046
MT39	48	74	5	10	1	22	1	936.47851	937.48578	935.49046
MT40	48	76	5	10	1	22	0	938.49416	939.50143	937.50611
MT41	49	76	5	10	1	23	1	950.49416	951.50143	949.50611
MT42	49	78	5	10	1	23	0	952.50981	953.51708	951.52176
MT43	50	78	5	10	1	24	1	964.50981	965.51708	963.52176
MT44	50	80	5	10	1	24	0	966.52546	967.53273	965.53741
MT45	51	80	5	10	1	25	1	978.52546	979.53273	977.53741